University of Sussex

Fabrication and Application of Structured Graphene/Polymer Based Composites

By

Manuela Meloni

Submitted for the degree of Doctor of Philosophy in Physics

Acknowledgements

Firstly, I would like to thank my supervisor Prof. Alan Dalton for the support, patience and motivation in these 3 years. His guidance helped me in all the time. I wish to thank Dr Alice King for the immense help and support during all my PhD. Probably the words are not enough to explain how grateful I am towards you. Thanks for understanding every single time all my doubts, my problems. Thanks for giving guidance to the thesis writing and for patience to correct it. I could not have done it without you. Thanks to the good company and the help I had in the Materials Physics group. Especially I would like to say thanks to Dr Matthew Large for his immense help in paper writing and to other people of the group: Giuseppe, Sean, Aline, Marcus, Annie, Dr Peter Lynch, Dr Manoj Tripathi, Dr Yuanyang Rong, Frank and Abdullah for the time spent in the lab for their suggestions and encouragement. Thanks to the Enabling Excellence Group and especially to Mario, Ana, Ruben, Antonia, Yuman, Dr Sebastian Nufer, Dr Emin Istif, Dr Lorenzo Vallan, Daniel and Dominik for having made this experience enjoyable during the secondments and workshops. Thanks also to the other people of the network like Elodie, Dr Chris Ewels, Dr Wolfgang Maser, Dr Ana Benito, Dr Alejandro Ansón, Dr Raul Arenal for their help and support. My old and new friends thanks for always being there. Most importantly, I thank my parents for the love they give me every single day despite we are separated from many kilometres, thanks for always believing me and for the moral and emotional support.

Abstract

Despite there being a significant development in polymer composites for multiple applications over the past few decades, there are still many difficulties relating to the effective distribution of nanoparticles such as Graphene and other 2D materials in preparing structure and minimising aggregation. To overcome these obstacles a simple method for modulating the properties of the composites by controlling the organization of the fillers, using an ordered lattice of polymer particles as a template, is described. This technique can facilitate the self-assembly of nanomaterials while preserving their useful properties and allows well-defined interface between the polymer and the nanomaterial resulting in a honeycomb-like arrangement. The ideal case would be to obtain a segregated percolating network whereby low loadings of nanoparticles are added to obtain high performance systems and thus reduce the cost for possible industrial applications. The enhancement of the mechanical and electrical properties of the composites suggests the use of these materials for different applications such as transport applications, where the combination of high strength and lightweight is required. Moreover, to reinforce systems that are very delicate such as membranes or fibres or for possible applications in sensor technology, molecular electronics, supercapacitors, electrochromic devices and pressure sensitive adhesives materials. The physical properties of these composites can be tailored using different matrices such as natural rubber, or a bimodal particle system, to create materials with high density and low void fractions, and hence very low percolation threshold. Furthermore, the combination of excellent monolayer fraction and homogenous dispersion of the GO within the polymer dispersion leads to highly uniform films, with good distribution of the filler throughout, in a segregated network. A reduction in situ proceeds to improve the innate properties of the GO, but also to modify the polymer in close proximity through and exothermic process, thus providing a much improved interface between filler and matrix, improving both the electrical and mechanical properties. The advantage of this method to organize the graphene nanoparticles in a segregated pathway does not require the use of expensive equipment or materials, and it is a promising way to open up pathways to tunable electronic composite materials on a large scale.

Contents

Abbreviations

PNCs: Polymeric Nanocomposites

CNTs: Carbon Nanotubes

CB: Carbon Black

rGO: reduced Graphene Oxide

GO: Graphene Oxide

NLR: Natural Latex Rubber

CVD: Chemical Vapour Deposition

PECVD: Plasma Enhanced CVD

NMP: N-Methyl-Pyrrolidone

SDBS: Sodium Dodecylbenzene Sulfonate

TBA: Tetrabutylammonium Hydroxide

CCG: Chemically Converted Graphene

FGS: Functionalized Graphene Sheets

Rs: Sheet Resistance

ET: Electron Transfer

MWI: Microwave Irradiation

ITO: Indium Tin Oxide

UV: Ultraviolet

SC: Supercritical

TMDs: Transition Metal Dichalcogenides

MoS_2: Molybdenum Disulfide

WS_2: Tungsten Disulfide

$MoSe_2$: Molybdenum Diselenide

WSe_2: Tungsten Diselenide

TiO_2: Titanium Dioxide

ZnO: Zinc Oxide

HI: Hydroiodic Acid

$NaBH_4$: Sodium Borohydride

H_2SO_4 : Sulphuric Acid

$KMnO_4$: Potassium Permanganate

$NaNO_3$: Sodium Nitrate

PVA: Poly (Vinyl Alcohol)

SRGO: PVA/Sulfonated Graphene Oxide

PAN: Polyacrylonitrile

PAA: Polyacrylic Acid

PS: Polystyrene

PE: Polyethylene

PMMA: Poly(Methyl Methacrylate)

f-GO: functionalized GO

ARG: Aqueous Reduced Graphene

DMF: Dimethylformamide

TPU: Thermoplastic Polyurethane

A-NFC: Amine-modified Nano-Fibrillated Cellulose

PEN: Poly (Ethylene-2,6-Naphthalate)

IPA: Isopropyl Alcohol

PLA/EG: Polylactide/Exfoliated Graphite

PLA: Poly (Lactic Acid)

CTAB: Cetyl Trimethylammonium Bromide

AA: Acrylic Acid

PANI: Polyaniline

NanoGs: Nano Graphene sheets

PPy: Polypirrole

PBT: Poly (Butylene Terephthalate)

CPCs: Conductive Polymer Composites

NR: Natural Rubber

SWNTs: Single Walled CNTs

PC: Polycarbonate

PP: Polypropylene

BA: Butyl Acrylate

AAEM: Acetoacetoxyethyl Methacrylate

PSAs: Pressure-Sensitive Adhesives

SEM: Scanning Electron Microscopy

SE: Secondary Electrons

BSE: Backscattered Electrons

TEM: Transmission Electron Microscopy

AFM: Atomic Force Microscopy

CCD: Charge-Coupled Device

FTIR: Fourier-Transform Infrared Spectroscopy

ATR: Attenuated Total Reflectance

DSC: Differential Scanning Calorimetry

TGA: Thermogravimetry Analysis

T_g: glass Transition Temperature

T_m: melting Temperature

T_c: crystallization Temperature

XRD: X-Ray Diffraction

XPS: X-Ray Photoelectron Spectroscopy

ESCA: Electron Spectroscopy for Chemical Analysis

DLS: Dynamic Light Scattering

PL: Polymer Latex

MFFT: Minimum Film Formation Temperature

AA: Acrylic Acid

MAA: Methacrylic Acid

H_2O_2: Hydrogen Peroxide

DI water: purified water

$Na(NO_3)_2$: Calcium Nitrate

FEG-SEM: Field Emission Gun Scanning Electron Microscope

EDS: Energy-dispersive X-ray Spectroscopy

KPFM: Kelvin Probe Force Microscopy

NVP: N-vinylpyrrolidone

PA6: Polyamide 6

PET: Polyethylene Terephthalate

THF: Tetrahydrofuran

DR: Double Resonance

AAT: Avery Adhesive Test

CPD: Contact Potential Difference

List of Figures

Chapter 2

Chapter 3

Chapter 4

Chapter 5

aqueous dispersion to a uniform brown solid composite, to the final reduced composite after thermal treatment. The composite is conductive enough to allow current to flow and illuminate the LED light of the microscale device. B. Conductivity vs work function for different electrode metals. We observe the highest conductivities using gold in either a planar or embedded format (inset), which has a work function almost matching that of thermally rGO at the temperatures investigated here.

Figure 5.16 a.b.c. Conductivity vs time for 0.2, 0.5, 2 wt.% of composites during the reduction process at 120 and 150 °C.

Figure 5.17 A. Bubble plot illustrating the wt.% of different filler which the maximum conductivity is achieved B. Absolute conductivity vs the percolation threshold for different polymer matrices.

Chapter 6

Figure 6.1 ln [time] vs 1/ T graph. (inset) photographs illustrating the colour change (brown to black) of the composite before and after reduction for a. NLR-rGO based composite and b. Latex 2-rGO based composite.

Figure 6.2 FTIR spectra of NLR-GO before and after the treatment at 130 for 30 min.

Figure 6.3 A. Absolute conductivity of NLR-rGO composite for reduction at 130 °C. B. Plot on log-log axes of electrical conductivity as a function of $(\varphi-\varphi_c)$ of the NLR-rGO composite.

Figure 6.4 DLS analysis of the particle size in the natural latex dispersion and the data are presented on a logarithmic x-axis.

Figure 6.5 AFM image in topography of the NLR-rGO based composite. b. DMT-modulus (related to the Young's Modulus and it is showing different interaction between the NLR polymer and the fillers. In principle the darkest part is the polymer and the brighter part is the filler). c. Adhesion showing again the different probe interaction with the polymer and with the rGO flakes. Figure 6.6 Electron micrograph of uncoated composite surface at different order of magnification.

Figure 6.6 a.b.c.d. Electron micrograph of uncoated NLR/rGO based composite surface at different orders of magnification. They do not show any structured morphology in the matrix surface.

Figure 6.7 Schematic illustration of the formation of conductive networks for the polymer latex system and for the NLR system.

Figure 6.8 Absolute conductivity of NLR-graphene based composite.

Figure 6.9 Graphene volume fraction in wt.% vs solid content of the composite dispersion for the GO and graphene fillers.

Figure 6.10 NLR-Graphene based glove.

Figure 6.11 Permeation test: weight percent increase vs time for ▲ NLR-graphene_Acetone; ◆ NLR_Acetone; ◆ NLR-graphene_IPA and ▲ NLR_IPA.

Chapter 7

Chapter 8

List of Tables

Appendix

Table 1 Electrical Conductivity of polymer nanocomposites with different conductive fillers.

Table 2 Mechanical properties of graphene-based composites.

Chapter 1

Introduction

Over the past few decades, polymer materials have been substituted for many conventional materials that are currently used in various applications from kitchenware to mechanical components. This is possible as a result of the advantages that polymers can offer over conventional materials. Some of these advantages include cost reduction, processability, ease of processing, low density, sound and vibration damping, corrosion resistance, mechanical toughness etc. There are some drawbacks however, such as poor thermal stability; they can be oxidised at high temperatures. In their saturated form, they typically possess low conductivity and strength. Therefore, polymeric nanocomposites have been an area of intense research for the past 30 years. Conducting composites are of particular interest, as advantages in anti-static coatings and flexible electronics can be easily identified over traditional metal and rare earth element devices. Research has led to the development of new types of polymer composites that are electrically conductive by adding conductive filler to the polymer matrix such as carbon nanotubes (CNTs), carbon black (CB), metals etc. Carbon-based nanoparticles such as graphene, reduced graphene oxide (rGO) and CNTs are considered as ideal candidates for the next generation of filler because they offer the potential to combine several properties, such as electrical conductivity, good mechanical properties and thermal stability among others. Although remarkable advances have been brought by this intensive research, there are still challenges to overcome; the difficulties with manufacture and achieving stable and homogeneous dispersion of the filler in the matrix. These inhomogeneities result from filler aggregation which may require more filler loading to create a conductive network but detrimentally limit the mechanical performance of the composite. According to Velev and Kaler [1] colloidal crystalline templates are three-dimensional close-packed crystals of submicrometer spheres, whose ordered structure is replicated in a solid matrix, to

produce materials with ordered pores. In this work it is shown that using the self-assembly method it is possible to overcome the problem with filler distribution. Indeed, when carbon-based materials are mixed with colloidal spherical particles, they are able to self-organize into a honeycomb-like arrangement. It is also presented that by using this technology it is possible to obtain highly conductive composites with lower electrical percolation compared to other polymer composites reported in literature. The properties of these composites can be modulated by changing the particle size (although the percolation threshold will be independent of this), the particle glass transition and also the fillers.

1.1. Objectives and Aims

The purpose of this research is to take advantage of the properties of carbon-based nanoparticles such as graphene and rGO; including their electrical conductivity, good mechanical properties in applications in the field of polymer composites. Composites provide a crucial route to transform these nanomaterials into nanocomposites that can be used for applications such as supercapacitors, sensors and pressure-sensitive adhesives. The main thesis aims are as follows:

1. To produce a highly conductive rGO-latex based nanocomposite. The self-assembly of GO into a honeycomb-like arrangement within a latex matrix and the inherent GO properties are optimised in this composite fabrication. Subsequent to this, the conductivity is enhanced with a simple low temperature, heating step.
2. To study the possible interaction between the latex polymer matrix and the GO nanoparticles and the mechanism governing the reduction in situ of GO.
3. To tailor the physical properties of these composites using different matrices such as natural rubber, or a bimodal particle system, to create materials with high density and low void fractions, and hence very low percolation threshold.
4. To explore the mechanical properties of the composites as a function of GO, rGO, graphene concentration and the varying of the matrix.

1.2. Outline of the thesis

Chapter 1: Introduction

In this chapter the aims and the objectives of this thesis are introduced, and the problems related to the research work. An outline is also presented in which a brief explanation of each chapter is given.

Chapter 2: Structured composites

A general review of the current state of the art and the physics of the structure and properties of graphene, GO and rGO and composite materials, including electrical and mechanical properties.

Chapter 3: Methods and materials

In this chapter, all the methods of investigation used in this research project are shown. The procedures for materials preparation and for composite fabrication are also described.

Chapter 4: Developing matrix structures and optimizing fillers

It contains the characterisation and optimisation of the polymer and the materials used to prepare the composite and the packing of particles resulting from the use of different fillers.

Chapter 5: Latex Based Nanocomposites: study of the electrical properties

A completely novel highly conductive composite is fabricated and characterised using an in-situ reduction of the optimised GO polymer.

Chapter 6: Electrical Properties of natural rubber-rGO-based composites

This chapter demonstrates the generality of the approach by applying the reduction in situ of GO in a natural latex rubber (NLR) matrix and then studying the electrical properties of the NLR based composite with different filler.

Chapter 7: Apollonian packing using a bimodal system

The focus of this chapter is in the combination of particle packing and percolation thresholds of binary particle systems using different fillers such as graphene and CNTs.

Chapter 8: Studies of the modification of mechanical properties

In this chapter, the mechanical properties of the different composites are investigated and interpreted.

Chapter 9: Conclusions and future work

In this chapter, the results are summarised and the possible future work outlined.

Chapter 2

Structured composites

In this chapter a literature review on composite materials, graphene, GO and 2D materials is provided, describing their structure and properties. It includes the various production methods for graphene-based composites and their electrical and mechanical performance.

2.1 Composites in general

Composite materials are made by the combination of two or more materials with different properties, giving a final material with unique features. Composites are present in nature either in animals and plants [2] (Figure 2.1). For example, wood is a composite made by cellulose fibres held together by lignin, the two substances if taken individually are weaker, but when they are combined together in a structure they form a much stronger material. The most common approach is the support of a hard material filler which provides mechanical integrity, within a softer matrix that allows for deformation and energy absorption. Another example is the bone in our body that is also a composite. Bones are a composite of hydroxyapatite (calcium phosphate) that is a hard and brittle material and from collagen that is a soft and flexible material, that together give bones the properties that are needed to support the body. For many thousands of years, people have been making composites. An example can be given by mud bricks, that can be used as a building material. The mud can be dried out into a brick shape and by mixing it with straw it is possible to create bricks that are more resistant. Another example is concrete, which consists of a mixture of small stones, cement and sand. When metal rods or wires are added its tensile strength can increase, and the latter composite is called reinforced concrete. The first modern composite material was fibreglass discovered by Herman Hammesfahr in 1880, that is a mixture of a plastic matrix and glass fibres, and it is still used for boat hulls, sports equipment, building panels etc.

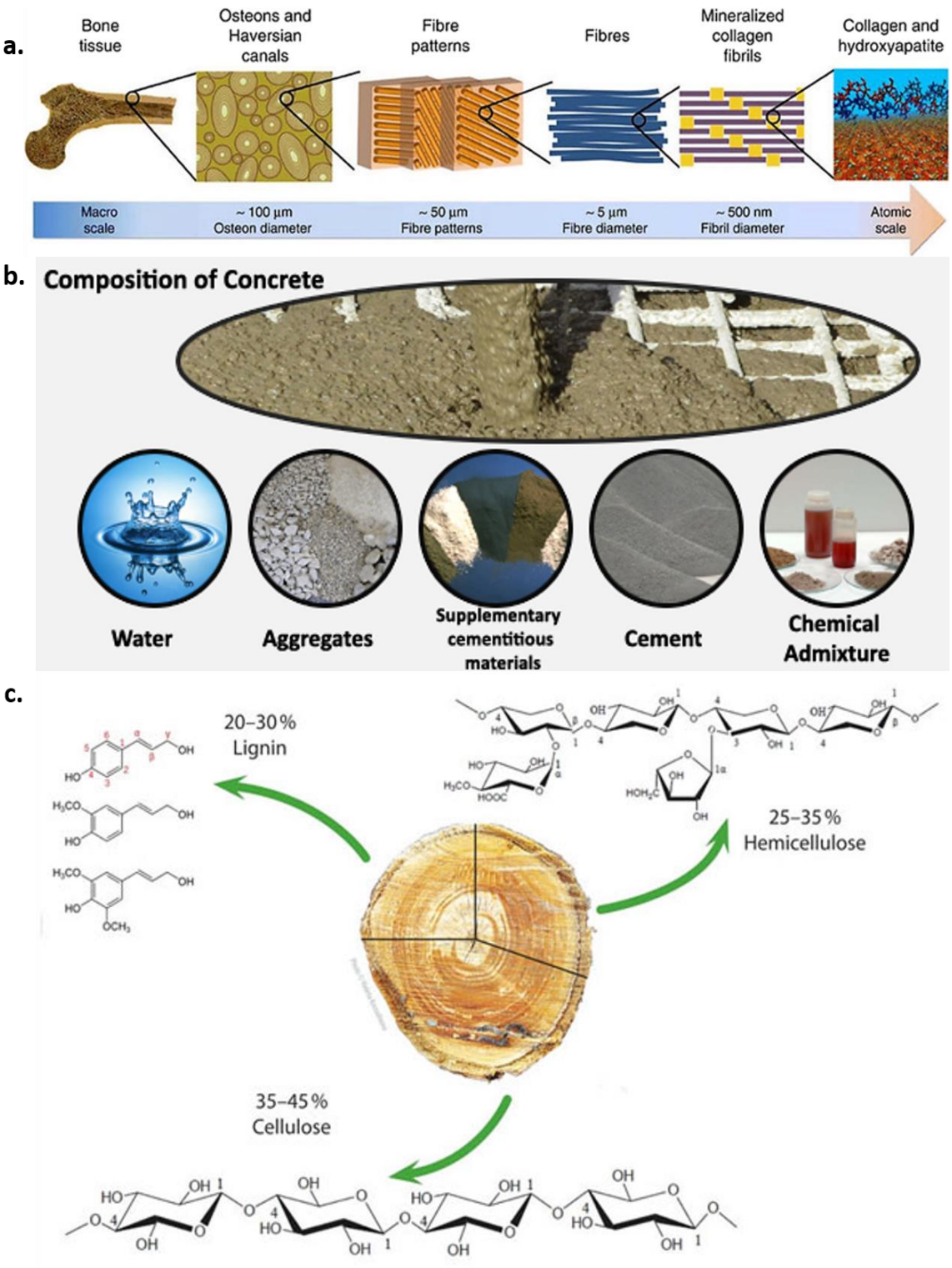

Figure 2.1 Some examples of composites such as bone tissue (a.), concrete (b.) and wood (c.) [3].

Nowadays modern materials such as polymer-based composites are used instead of many conventional materials in various applications due to easy processing, productivity and

the reduction of the cost. They have the advantage of being light and strong whilst at the same time, being flexible, and mouldable into complex shapes.

2.2 Nanoparticle Fillers

2.2.1 2D materials

2D materials are crystalline materials consisting of a single or bi-layer of atoms that can generally be categorised as either 2D allotropes of various elements or compounds, consisting of two or more covalently bonding elements. In Figure 2.2 a top and side view of some typical 2D materials is shown. Layered combinations of different 2D materials are generally called van der Waals heterostructures. With the liquid exfoliation technique, it is possible to obtain individual crystal sheets from a variety of layered materials [4] [5]. Research on two-dimensional materials has grown in an exponential way since the first report of graphene isolation in 2004 [6] becoming the flagship in many fields of research such as materials science and nanoscience. Since then, diverse 2D compounds have been identified, including semiconducting transition metal dichalcogenides (TMDs) such as molybdenum disulfide (MoS_2), tungsten disulfide (WS_2), molybdenum diselenide ($MoSe_2$) and tungsten diselenide (WSe_2), boron nitride (BN), several transition metal carbides, nitrides-based materials, and phosphorene.

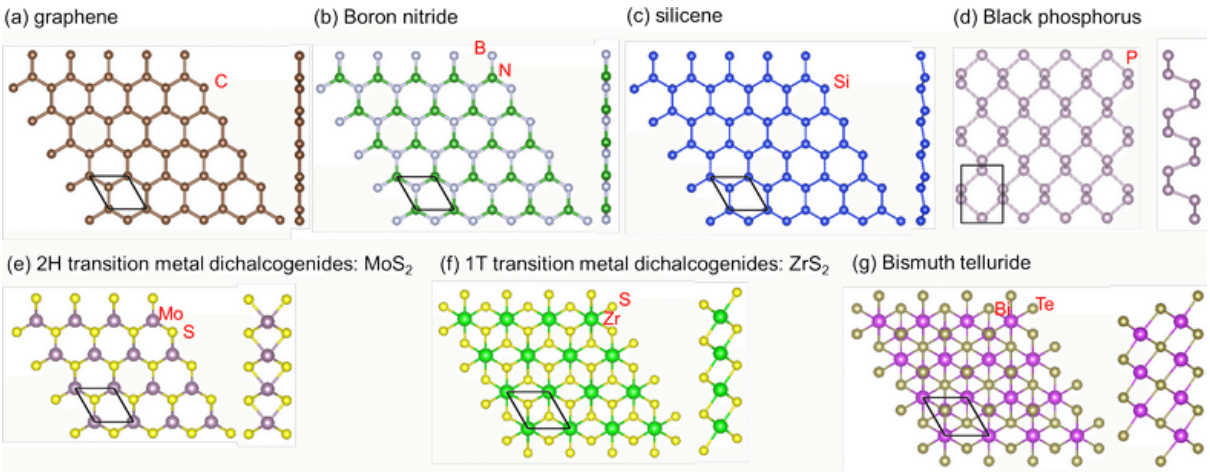

Figure 2.2 Top view and side view of some typical 2D materials. The primitive unit cell of each material is indicated by black lines in the top view [7].

They have attracted enormous attention due to their chemical and physical properties, such as high mechanical strength, high conductivity, high mobility and long spin diffusion length for spintronics devices [8]. 2D materials can also be used in diverse areas such as spintronics, semiconductor devices, catalysts and batteries [8]. Furthermore, they can be tailored for non-covalent interaction with various chemical species, making them interesting for fabricating devices that exhibit high sensitivity towards detection of gases, ions and small molecules [9]. The fact that it is possible to combine their electrical, optical and mechanical properties make them ideal components for the fabrication of new generation of high-performance chemical sensors, energy generation and storage, and for opto-electronic devices.

2.2.2. Graphene

Graphene is a single-layer carbon sheet with a hexagonal lattice structure, that exhibits extraordinary thermal [10] and electrical conductivity [11] and remarkable mechanical [12] strength superior to steel. As such, it can be considered promising for sensing applications, is impermeable [13] in its pristine form making it an ideal barrier material to prevent liquid and gas permeation or to shield metallic surfaces against corrosion. There are different methods used to produce graphene and its derivates that are generally classified as the bottom-up and the top-down approaches (Figure 2.3).

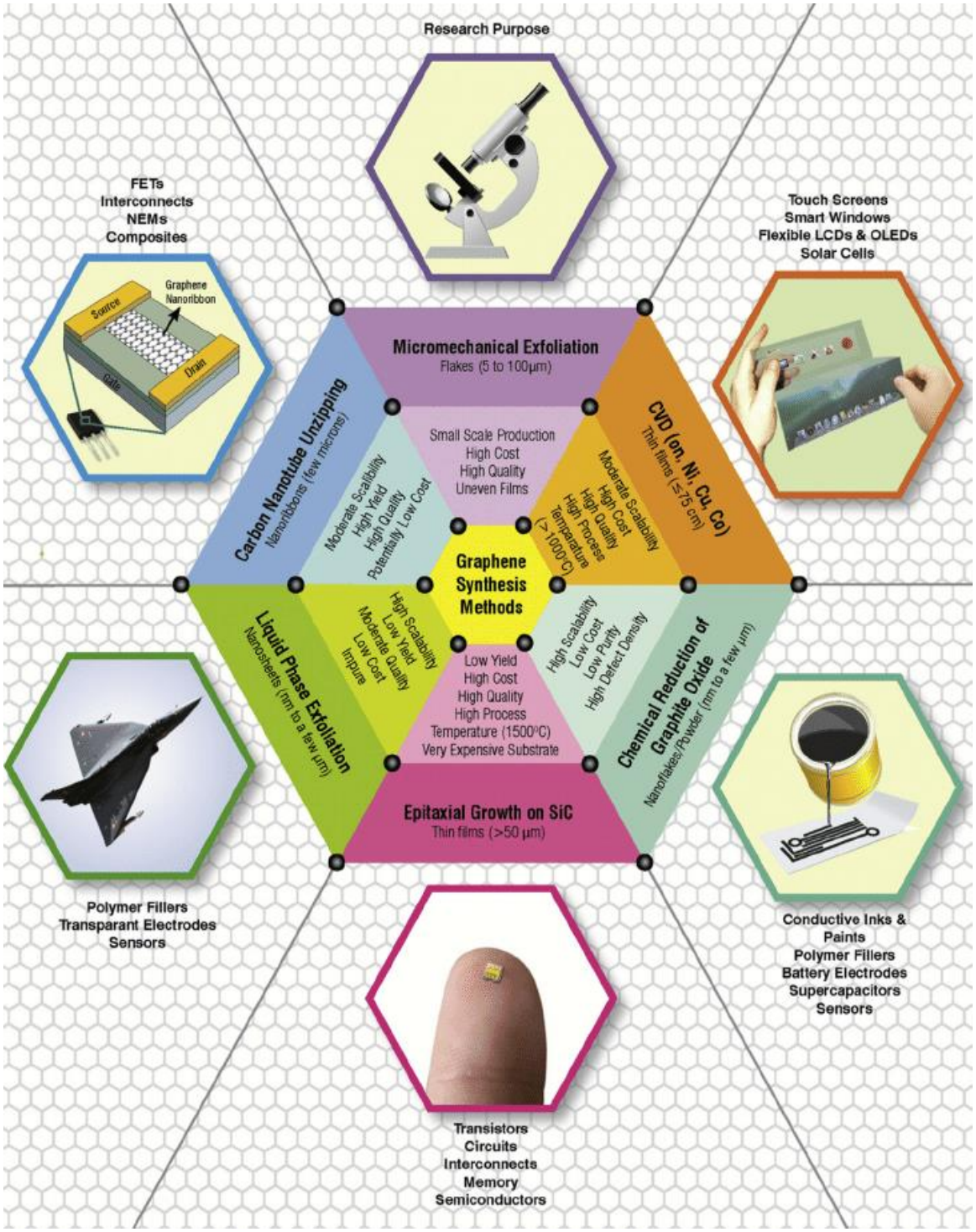

Figure 2.3 A schematic showing the conventional methods commonly used for the synthesis of graphene along with their key features, and the current and future applications[14].

The bottom-up approach involves the direct synthesis of graphene materials from carbon sources. For example, chemical vapor deposition (CVD) is used to grow large area of single, and few layer graphene sheets on metal substrates such as Ni and Cu [15] [16]. In

this method, graphene is grown on metal foils at temperatures approaching or exceeding 1000 °C using a mixture of carbon sources such as methane and hydrogen. Another technique is plasma-enhanced CVD (PECVD) [17] that allows the production of single-layer graphene. Compared to the normal CVD, the advantages are that the reaction time (< 5 min) is markedly reduced and the reaction takes place at a lower growth temperature of 650 °C. Graphitization of carbon-containing substrates such as SiC can also give single and few layer graphene films using high temperature annealing of 1280 °C [18]. Graphene is also obtainable by a solvothermal method [19] using ethanol and sodium followed by pyrolysis or through organic synthesis [20] to give graphene like polyaromatic hydrocarbons. Alternatively, top-down approaches are more convenient in terms of processability, ease of implementation (intercalation and chemical functionalization) and higher yield. The liquid exfoliation method of graphite allows the isolation and the dispersion of graphene sheets by using solvent intercalates such as N-methyl-pyrrolidone (NMP) [21] or detergent stabilization such as sodium dodecylbenzene sulfonate (SDBS) [22]. Another way to obtain single-layer graphene sheets is by thermal exfoliation [23] at 1000 °C using oleum (fuming sulphuric acid with 20% free SO_3) and tetrabutylammonium hydroxide (TBA). Using this method, it was possible to have a yield of ~90% after purification. Furthermore, electrochemical exfoliation of graphite can be used to produce graphene nanosheets with the assistance of an ionic liquid and water [24]. An alternative method is the reduction of GO sheets from the exfoliated graphite oxide [25]. The latter is used to prepare rGO, chemically converted graphene (CCG) or functionalized graphene sheets (FGS).

2.2.3 GO

GO consists of a one-atom-thick planar sheet comprised of mostly sp^2-bonded carbon interspersed by sp^3 regions due to the addition of oxygen based functional groups. In 1958 Hummers and Offeman [26] developed an oxidation method, for producing graphite oxide. It is easy to perform and consists of using a mixture of potassium permanganate ($KMnO_4$), concentrated sulphuric acid (H_2SO_4), and sodium nitrate ($NaNO_3$) reacting with graphite. Subsequently, GO is prepared by dispersion and exfoliation of the graphite oxide in water or a suitable organic solvent. These interact with the various oxygen containing functional groups in the GO.

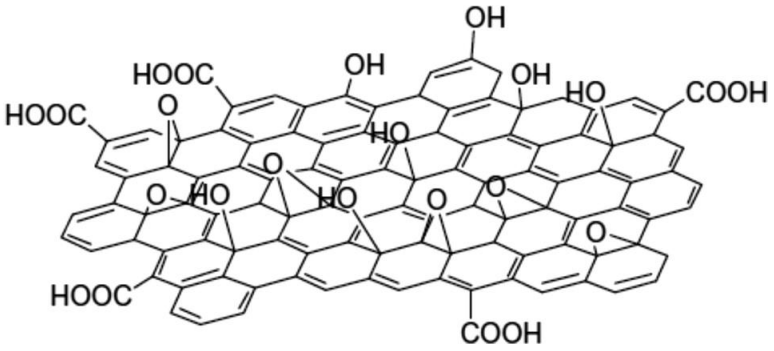

Figure 2.4 GO structure [27].

The oxygen functional groups are mostly in the form of hydroxyl and epoxy groups on the basal plane, with smaller amounts of carboxy, carbonyl, phenol, lactone, and quinone at the sheet edges (Figure 2.4). The oxygenated groups in GO can strongly affect its electronic, mechanical, and electrochemical properties. Moreover, the polar oxygen functional groups of GO render it highly hydrophilic and this gives good dispersibility in many solvents, particularly in water. The resulting GO dispersion can be subsequently deposited on various substrates, or incorporated into composites, coatings etc. Therefore, the chemical composition of GO, which can be chemically, thermally, or electrochemically engineered, allows the tunability of its physicochemical properties. The study of GO-based materials in recent years has been popular and extensive, particularly with respect to electrochemical applications. These include its facile synthesis, high dispersibility in a range of solvents, capability of coupling electroactive species onto the surface, and unique optical properties (through the establishment of fluorescently active sp^2 domains). Electronic properties, such as the conductivity of the GO sheets, depend strongly on their chemical and atomic structure. They depend upon the degree of structural disorder arising from the presence of a substantial sp^3 carbon fraction. In general, “as-synthesized” GO films are typically insulating with a large band gap in the electron density of states [28] exhibiting sheet resistance (R_s) values of about 1000 Ω/sq or higher [29]. The intrinsic insulating nature of GO is strongly correlated to the amount of sp^3 C−O bonding. This, in turn, produces in-plane transport barriers, leading to the absence or disruption of electron percolation pathways among the sp^2 carbon clusters, which allows classical carrier transport to occur. However, the reduction of GO (i.e., the

incremental removal of oxygen) using a variety of chemical and thermal treatments, can result in a decrease in Rs by several orders of magnitude and hence transform the material into a semiconductor and ultimately into a graphene-like semimetal [30]. The conductivity of the rGO samples can reach ~1000 S/m [25]. In addition to these interesting electronic characteristics, GO is also expected to exhibit unique optical properties as evidenced by the recent demonstration of photoluminescence from GO [31]. GO luminescence was found to have distinct features existing over a wide spectral window (from the near-UV-to-blue visible (vis) to near-infrared (IR)). This is due to the establishment of local sp^2 domains of varying size depending on the level of chemical modification of the graphene basal plane. This property should prove useful for biosensing, fluorescence tagging and for a range of other optoelectronics applications. Recently, it has become popular to explore the electrochemical properties of GO at electrode surfaces [32]. Due to its favourable electron mobility and unique surface properties, such as one-atom thickness and high specific surface area, GO can accommodate the active species and facilitate their electron transfer (ET) at electrode surfaces. GO exhibits enhanced chemical activity compared with pristine graphene because of the presence of a large number of oxygen-containing functional groups and structural defects. Another important chemical reactivity of GO is its capacity for chemical functionalization. This involves adding other groups to GO platelets using various chemical reactions. Typically, GO can be covalently functionalized using specially selected small molecules or polymers through activation and amidation/esterification of either the carboxyls or hydroxyls in GO via coupling reactions.

2.2.4 Reduction of GO

As mentioned previously, GO lacks the exceptional electronic properties of graphene due to structural disorder. Therefore, an important area of research is on the reduction of GO, which partly restores the structure by removing the oxygen-containing groups, resulting in the emergence of an extended conjugated structure and also the properties correlated with the graphene (Figure 2.5). The rGO sheets are usually considered as one kind of chemically derived graphene.

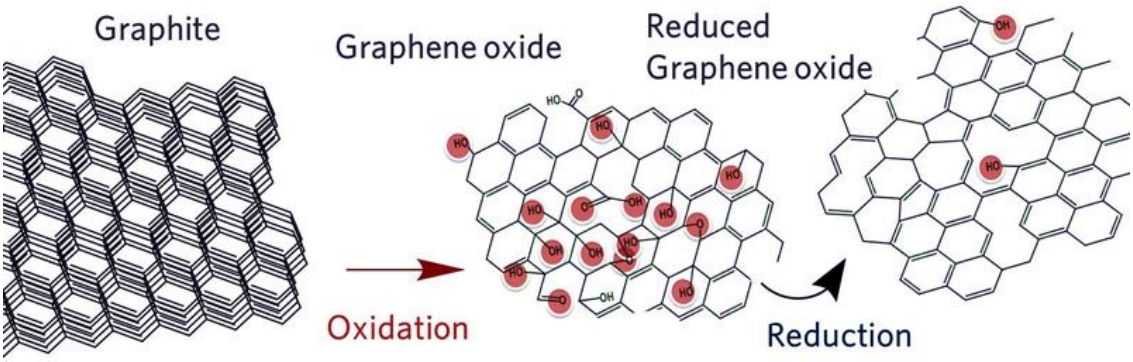

Figure 2.5 Illustration of rGO synthesis [33].

Various techniques have been developed to perform the reduction step in the past few years. There have been reports of reducing GO in the solution phase using various reducing agents such as hydrazine hydrate [34]. The process involves the addition of the reagent to a GO aqueous dispersion, producing an electrically conductive black powder containing graphene-like sheets. Much effort have been made to change the charge state of rGO sheets by adding soluble polymers such as poly(sodium 4-styrenesulfonate) [35] or ammonia [25] to assemble macroscopic structures by simple solution processes (Figure 2.6). In organic chemistry metal hydrides such as sodium borohydride ($NaBH_4$), sodium hydride and lithium aluminium hydride are considered as strong reducing reagents, and they have a slight to very strong reactivity with water, which is the main solvent for the dispersion of GO. Recently, $NaBH_4$ was demonstrated to be more effective than hydrazine [36], for the chemical reduction of GO. $NaBH_4$ has a moderate efficiency in the reduction of epoxy and carboxylic groups, but unfortunately, after the reduction, many alcohol groups remain [37].

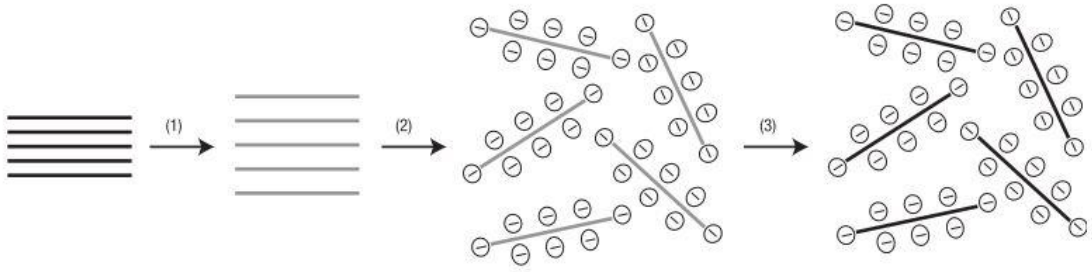

Figure 2.6 Schematic that shows the chemical route to the synthesis of aqueous graphene dispersions. 1. Oxidation of graphite (black blocks) to graphite oxide (lighter coloured blocks) with greater interlayer distance. 2. Exfoliation of graphite oxide in water by sonication to obtain GO colloids that are stabilized by electrostatic repulsion. 3. Controlled conversion of GO colloids to conducting graphene colloids through deoxygenation by hydrazine reduction [25].

Due to the high toxicity of these reducing agents, in 2010 Fernandez-Merino et al. [38] suggested an alternative method to reduce GO using Ascorbic acid (Vitamin C). Indeed, AFM images (Figure 2.7) confirm the formation of single-layer sheets of rGO using ascorbic acid as a reducing agent. This study has opened the perspective of replacing hydrazine with an agent that is environmentally friendly and safe to use for graphene-based materials in large-scale applications. This method was also found to be more stable in water compared to $NaBH_4$. Another strong reducing agent that can be used for the GO reduction is HI (hydroiodic acid) [39][40]. In this case, the reduction can occur at room temperature. The resulting GO films have good flexibility and improved tensile strength, that makes HI a good candidate for GO film reduction. There are also other reductants like strong alkaline solutions (KOH, NaOH) [41], urea and thiourea that can be used but they tend to be inferior compared to the strong reductants such as hydrazine, $NaBH_4$ and HI. Another approach to reduction is by thermal annealing [42][43] using rapid heating at high temperatures (> 2000 °C/min) to exfoliate graphite oxide to obtain graphene. The rapid increase of the temperature results in decomposition into gases of the oxygen-containing functional group in the GO, that create an incredibly high pressure between the stacked layers. This method allows not only for the exfoliation of graphite oxide but also reduces the GO functional groups giving small size and wrinkled graphene sheets [44], because the decomposition of oxygen-containing groups also removes carbon atoms from the carbon plane, and cuts the graphene into small pieces. An alternative way is to do the reduction process when the GO is already in powders or films, by simply annealing

in vacuum [29], inert [45] or a reducing atmosphere [46]. In these approaches, the heating temperature and the presence of oxygen can play a significant role in the reduction of GO.

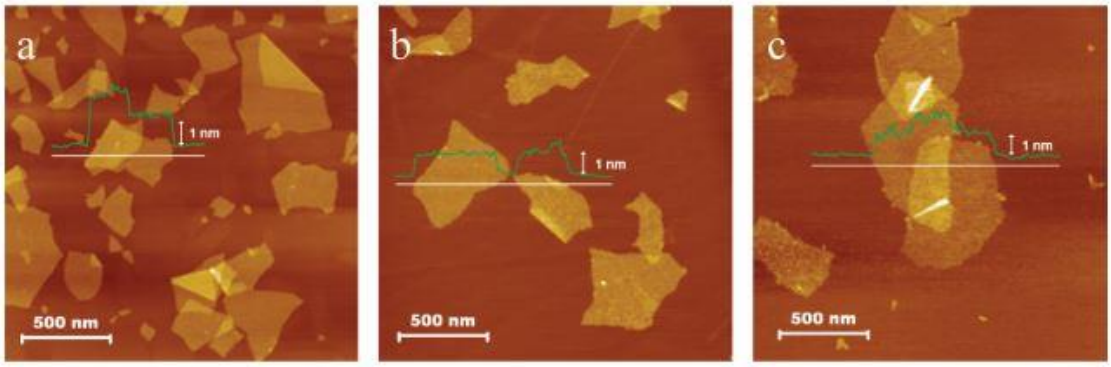

Figure 2.7 a. Representative AFM images of unreduced, hydrazine-reduced b. and vitamin C-reduced c. GO sheets deposited onto HOPG substrates from their corresponding suspensions. Lines profiles are superimposed onto each image, showing that single-layer sheets are obtained in all cases [38].

As an example, Becerril et al. [29] used a temperature of 1000 °C under vacuum. Interestingly, in the presence of a reduction gas like H_2 the reaction can be realized at much lower temperatures such as ~ 600 °C [47]. The results using this method are very effective, but it requires large energy consumption, critical treatment conditions and implicit control of the heating conditions to prevent excessive expansion of the GO structure. If the heating rate is too high, the resulting explosion deleteriously damages the flakes. On the other hand, slow heating makes it a time-consuming process. An alternative process involves the use of thermal irradiation using different heating resources such as microwave irradiation (MWI) [48][49][50] that allows uniform and rapidly heating or a photo-irradiation method [51] that can produce rGO films with higher conductivity. A possible alternative for the reduction of GO is the electrochemical removal of the oxygen functional groups. This can be carried out using an electrochemical cell using an aqueous solution at room temperature [52][53][54]. The reduction is caused by the electron exchange between GO and the electrodes and could avoid the use of dangerous chemicals such as hydrazine as well as eliminating by products. The GO film can be deposited on a substrate, in general on ITO glass, and then placed in the electrochemical cell and then an inert electrode is placed in the opposite side of the GO film. The reduction takes place during the charge of the cell using the cyclic voltammetry method. Ramesha and Sampath

have found that the reduction began at –0.6 V and reached a maximum at –0.87 V [55]. GO can also be reduced by photo-chemical reactions with the assistance of a photocatalyst such as titanium dioxide (TiO_2) under ultraviolet (UV) irradiation [56][57][58]. Upon UV-irradiation, charge separation occurs on the surface of TiO_2 particles. In the presence of ethanol, the holes are scavenged and ethoxy radicals are produced, allowing for the accumulation of electrons within the TiO_2 particles. The electrons interact with the GO sheets to reduce the functional groups. The carboxyl groups can also interact with the hydroxyl group on the TiO_2 surface producing a hybrid between TiO_2 nanoparticles and GO sheets and retained after reduction. Other groups have tried to use the same method to do the reduction of GO using other materials that possess photocatalytic activity like ZnO [59][60], $BiVO_4$ [61]. In Figure 2.8 is shown the photocatalytic reduction of GO using ZnO nanowires.

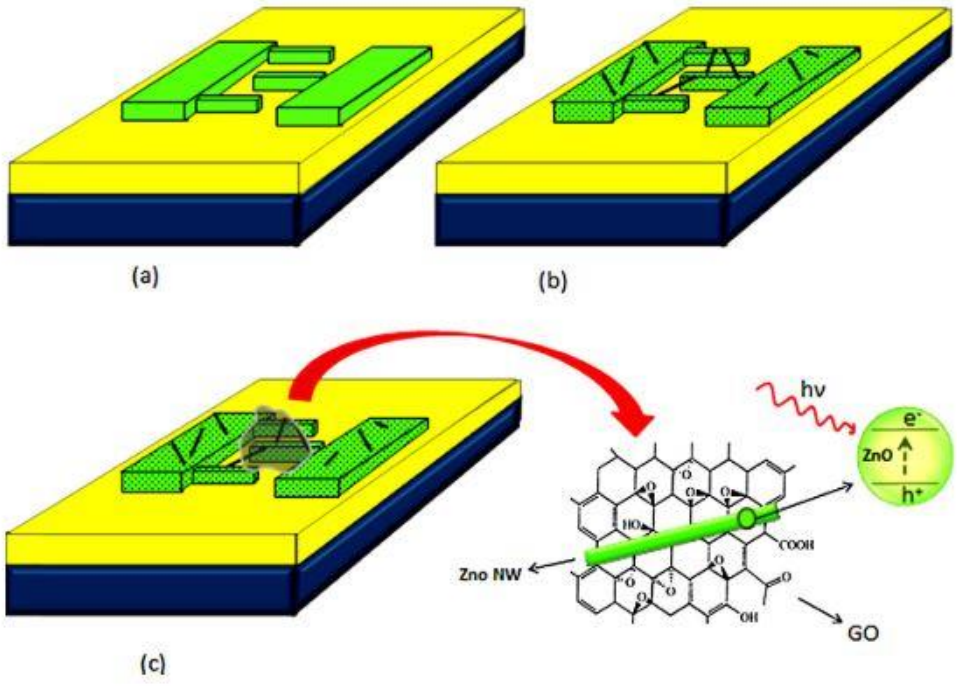

Figure 2.8 Scheme showing the process flow to achieve GO-ZnO based sensor. a. Patterning the comb-like Zn electrodes, b. oxygen plasma bombardment to form ZnO nanowires, c. coating the GO sheets on the obtained structure, and d. photo-catalytic reduction of GO using ZnO nanowires [60].

Another approach that can be used to obtain a stable dispersion of rGO is the solvothermal method. In this method, a sealed container is used in order to bring the solvent above its boiling point by the increase of pressure resulting from the heating [62]. The overheated supercritical (SC) water can also play the role of reducing agent in a GO solution as shown by Zhou et al [63]. The SC water can partly remove the functional groups on the GO and also recover the aromatic structure in the carbon lattice. There is also the possibility to use another solvent, such as NMP [64], the reduction is not performed in a sealed container and the heating temperature (200 °C) is lower than the boiling point of NMP (202°C, 1 atm). The deoxygenation of GO can happen thanks to the thermal annealing and NMP acting as an oxygen-scavenger at high temperature.

2.2.5 Carbon Nanotubes

CNTs were first synthesised by Iijima in 1991 [65] and since their discovery, they have stimulated the interest of many researchers in different areas such as material sciences, physics and chemistry. They are a class of nanomaterials that consist of graphene sheets that have been rolled into a tube [66]. There are two main structures, single-walled nanotubes (SWNTs) and multi-walled nanotubes (MWNTs). SWNT is a single graphene sheet wrapped into a cylindrical tube, whereas MWNTs are a collection of concentric SWNTs. MWNTs have diverse length and diameter compared to SWNTs, and indeed their properties are different [67]. The CNTs are described by a chiral vector, $\vec{C}$, and the chiral angle, θ. The vector is defined in equation 2.1.

$$\vec{C} = n\vec{a_1} + m\vec{a_2} \qquad \text{(Equation 2.1)}$$

where n and m are integers and $\vec{a_1}$ and $\vec{a_2}$ are unit vectors. When $n=m$ the tubes are described as armchair, when n or $m=0$ they are zig zag and all other combinations are chiral. The zig zag and armchair nanotube structures are shown in Figure 2.9. The difference in the integers also determines if tubes are metallic or semiconducting.

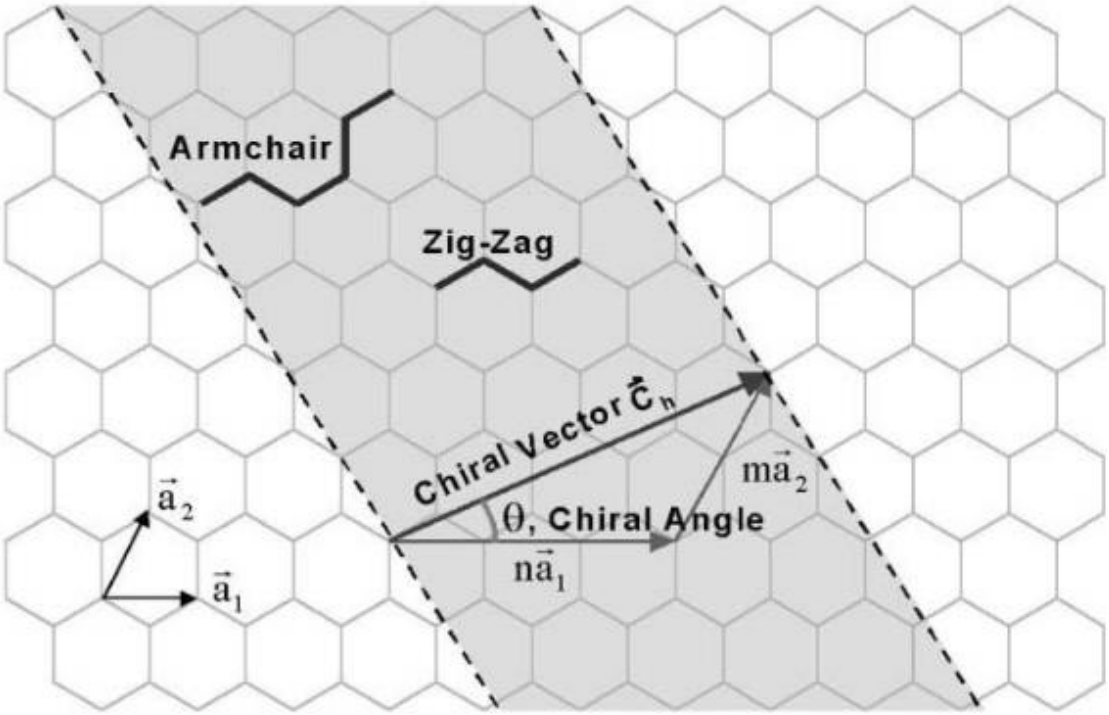

Figure 2.9 Schematic diagram showing how a hexagonal sheet of graphene is 'rolled' to form CNTs [66].

There are various methods that have been used to produce CNTs resulting in different growth and properties of CNTs. In Arc discharge technique [68][69] two graphite electrodes are used as anode and cathode. They are held a short distance apart under helium (He) atmosphere. In general, at high temperatures (> 1700 °C) CNTs grow with fewer defects compared to other methods. Another method used to produce SWNTs with high quality and purity is the laser ablation method [70]. A laser vaporises a graphite target in high temperature reactor with the presence of inert gas into the chamber. The most widely used method for the production of CNTs is the CVD method [71] in which the CNTs grow directly on the desired substrate such as Nickel (Ni), Cobalt (Co) or Iron (Fe), or a combination [72]. This method is the most promise for industrial-scale deposition. CNTs have unique optoelectronic and mechanical properties primarily from their effective one-dimensional structure. Therefore, they can offer enormous opportunities for the development of new material systems. CNTs can be used as potential reinforcement in nanocomposites because they have high elastic modulus, greater than 1 TPa and strengths 10–100 times higher than the strongest steel at a fraction of the weight [66]. Furthermore, CNTs are thermally stable up to 2800 °C in vacuum, and possess

higher thermal conductivity as diamond and electrical conductivity is 1000 folds higher than copper wires [73]. These properties can be used in various devices such as scanning probe microscopy and microelectronic devices [74] etc.

2.3 Aqueous colloidal polymer dispersions

Polymer latex dispersions prepared by emulsion polymerisation can exhibit a vast range of properties due to their compositions and phase morphological features. They have been widely used in industry due to their possibility to be obtained in higher concentrations and using more conventional equipment [75]. They can be used for several applications such as adhesives, coatings, synthetic rubbers, thermoplastics, binders, plastic pigments and rheological modifiers [76]. This type of polymerisation allows the formation of polymer species with high molecular weight and high reaction rates. Furthermore, this polymerisation is environmentally friendly because it does not use toxic solvents. Generally, the properties of polymer latex dispersions are dictated by the monomers properties and their polymerisation process. Indeed, the morphology of the latex particles is affected by the particle size, the sequence and also the hydrophilicity of the monomers used in the emulsion polymerisation process [75]. Acrylics are probably the most versatile family. Their properties can vary greatly, and for this reason, they can be used to produce polymers with flexible, rigid, nonionic, ionic, hydrophilic and hydrophobic properties [77]. In recent decades, acrylic monomers have been used for the production of copolymers with broad properties for a variety of applications such as emulsifiers, wetting agents, compatibilisers, dispersion stabilisers and coating materials [78]. They are formed by emulsion polymerisation of acrylic monomers, such as alkyl esters of methacrylic and acrylic acid [79]. These monomers have been extensively used in industry due to their reactivity, in fact, they can copolymerise very well with each other providing an enormous variety of physical properties and attainable compositions [80]. Furthermore, acrylic polymers possess different functional groups into the polymer chain which can supply some sites for compatibility with other polymers, for crosslinking, adhesion, etc [81]. In addition, these polymer particles can be synthesised to own various sizes from 50 to 500 nm, morphology such as spherical and non-spherical, with heterogeneous or homogeneous polymer compositions [82]. Free radical monomers are required in order to perform emulsion polymerisation. In general, in this kind of polymerisation vinyl monomers are used such as acrylate ester, methacrylate ester monomers, acrylic acid

(AA) [76]. Figure 2.10 shows the chemical structure of some monomers used to create the polymer latex dispersion (block-copolymer) used in this thesis to create graphene-based composites, such as methyl methacrylate (MMA), butyl acrylate (BA), AA and methacrylic acid (MAA).

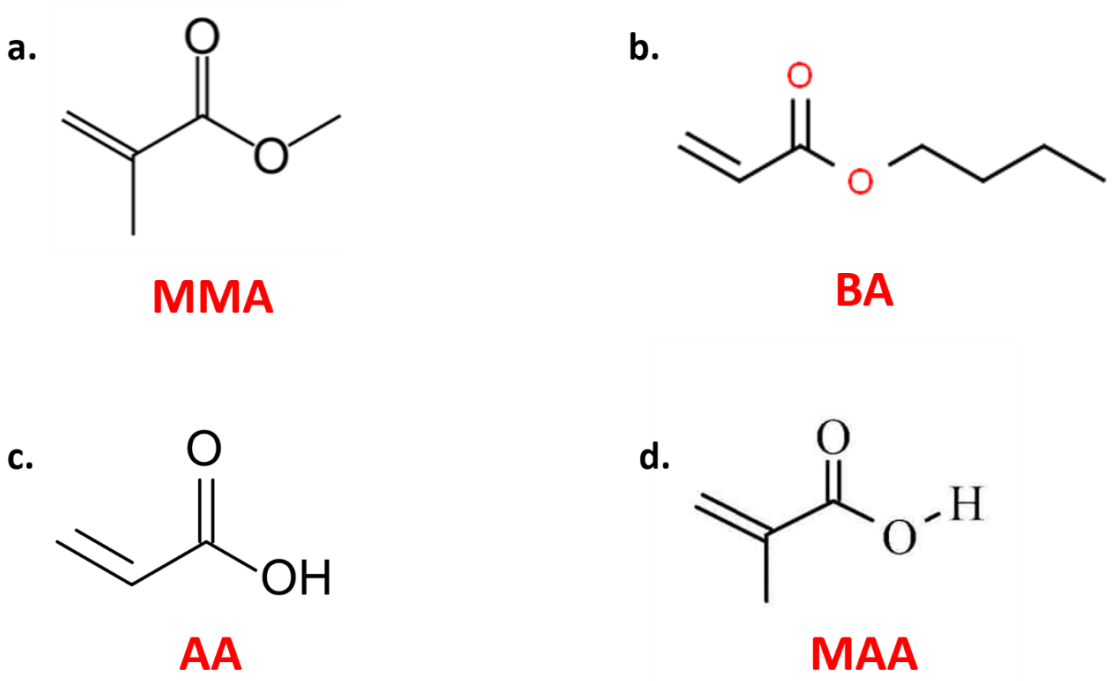

Figure 2.10. Chemical composition of different monomers such as a. MMA, b. BA, c. AA, d. MAA.

In the block copolymer MMA:BA:AA, or BA:MMA:MAA, the MMA monomer (Figure 2.10 a.) acts as hardening monomer and the other monomers such as BA (Figure 2.10 b.), AA (Figure 2.10 c.), and MAA (Figure 2.10 d.), are added to introduce some functional groups like carboxyl and hydroxyl group in the copolymer matrix. These functional groups are important to improve solvent resistance, adhesion, toughness and water resistance [77]. Another type of polymer latex that can be used to prepare composites materials is the natural latex rubber (NLR). NLR is a milk-like fluid which comes from an amazonian rubber tree called Hevea Brasiliensis [83]. It is a stable colloidal suspension

of rubber latex particles in water, which mainly consists of high molecular weight of isoprene (2-methyl 1,3-butadiene) [84] as shown in Figure 2.11. At the end of its macromolecules, there are also non-isoprene units such as amino acids, proteins and phospholipids that are surrounded by a surface of rubbery particles which gives them a negative charge, guaranteeing colloidal stability [85]. In the natural state, the rubber molecules are long chains that are tangled up and only linked together by a weak bond. Thus, it is very easy to pull them apart, and this explains why the rubber is elastic and stretchy.

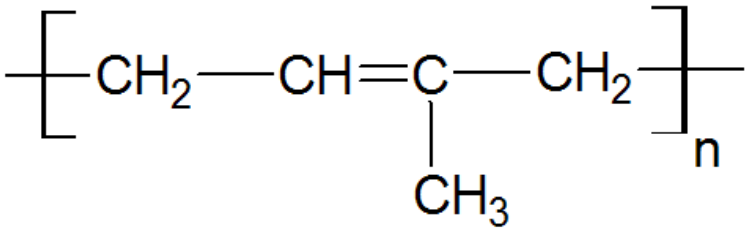

Figure 2.11. Chemical structure of NLR.

NLR is widely used in technological and industrial areas, such as vibration isolation systems and as pneumatic tires. The properties of NLR can be modified by using various nanoparticles to suit the desired application [84]. In order to harden the NLR a vulcanisation process is used. In general, sulphur is the most used to form cross-links between the polymer chains. The vulcanisation process brings better durability and rigidity and other changes in the mechanical properties of the rubber. During the process, the sulphurs react with the allylic hydrogen atoms adjacent to the double bond in the NLR. These allylic hydrogen atoms are called “cure sites” and some of these C-H bonds are replaced by chains of sulphur atoms.

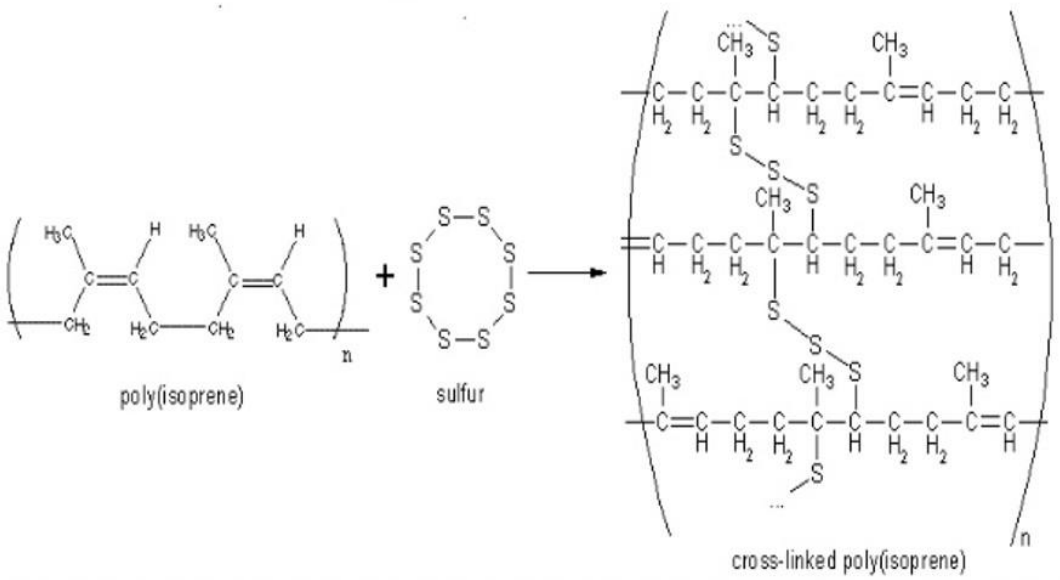

Figure 2.12. Vulcanisation reaction between the poly(isoprene) and sulphur [86].

Therefore the sulphur acts as a cross-linking agent which link with a cure site of another polymer chain as shown in Figure 2.12. These bridges contain between one and several atoms and the physical properties of the final NLR are strongly influenced by the number of sulphur atoms in the cross-link. Indeed, a higher number of sulphur atoms give good dynamic properties and bad heat resistance.

2.4 GO based composites

The key aspects for designing polymer-based composites is to make sure that the filler is well dispersed within the matrix. If the dispersion is homogeneous then the probability to enhance the properties of the polymer with the filler is higher [87]. Many methods exist to incorporate nanofillers into a polymer matrix such as solution mixing, melt blending, latex technology and in situ polymerisation among others.

Solution mixing

The solution method [88][89] is a facile and fast procedure and for this reason, it has been exploited widely. It involves the mixing of a graphene-based dispersion with a polymer matrix that can be already in a solution or mixed with the graphene dispersion by

ultrasonication or high-speed shearing combined with ice-cooling [90]. In order to achieve good dispersibility between the polymer and the filler, it is important to pay attention to solvent compatibility. For instance, a critical aspect of nanoparticle dispersion involves the understanding of the relationship between the cohesive energy density of the liquid and the surface energy of the particle. This interaction is typically defined using a Hansen parameter approach. The dispersion can be cast onto a substrate and the solvent can subsequently be removed, with the possibility of re-aggregation of the filler. Alternatively, the dispersion can be precipitated using a non-solvent for the polymer, activating encapsulation of the filler within the polymer molecules during precipitation. In general, this method provides a good dispersion of the filler and it is quite versatile because it is possible to use several solvents to dissolve the polymer and disperse the nanoparticles. GO can be mixed directly with water soluble polymers such as poly (vinyl alcohol) (PVA) due to the presence of oxygen functional groups in its structure. Zhao *et al.* [91] have prepared nanocomposites based on exfoliated aqueous dispersions of GO nanosheets and PVA. PVA powders were added into the GO dispersion and then stirred at 85 °C for 6h. They have shown that most of the GO sheets are well dispersed in the polymer matrix, with minimum restacking (Figure 2.13). Mo *et al.* [92] prepared PVA/sulfonated GO (SRGO) composites, slowing adding the SRGO in the polymer dispersion and stirred for 30 min to obtain a homogeneous solution. The mechanical properties of PVA improved due to the strong interaction between the -SO_3H groups on the SRGO sheets and PVA chains. To improve the solubility and interaction of GO and the polymer matrix, chemical functionalization can be an option. Numerous kinds of polymers such as PAN, PAA, PS, PE and PMMA have been successfully mixed with functionalized GO (f-GO), for example, GO with amino, cyano and isocyanate functional groups [93]. The functionalisation allows the dispersion in both water and organic solvents reducing the agglomeration of the nanoparticles and helping to obtain higher loadings of graphene in the composites [94].

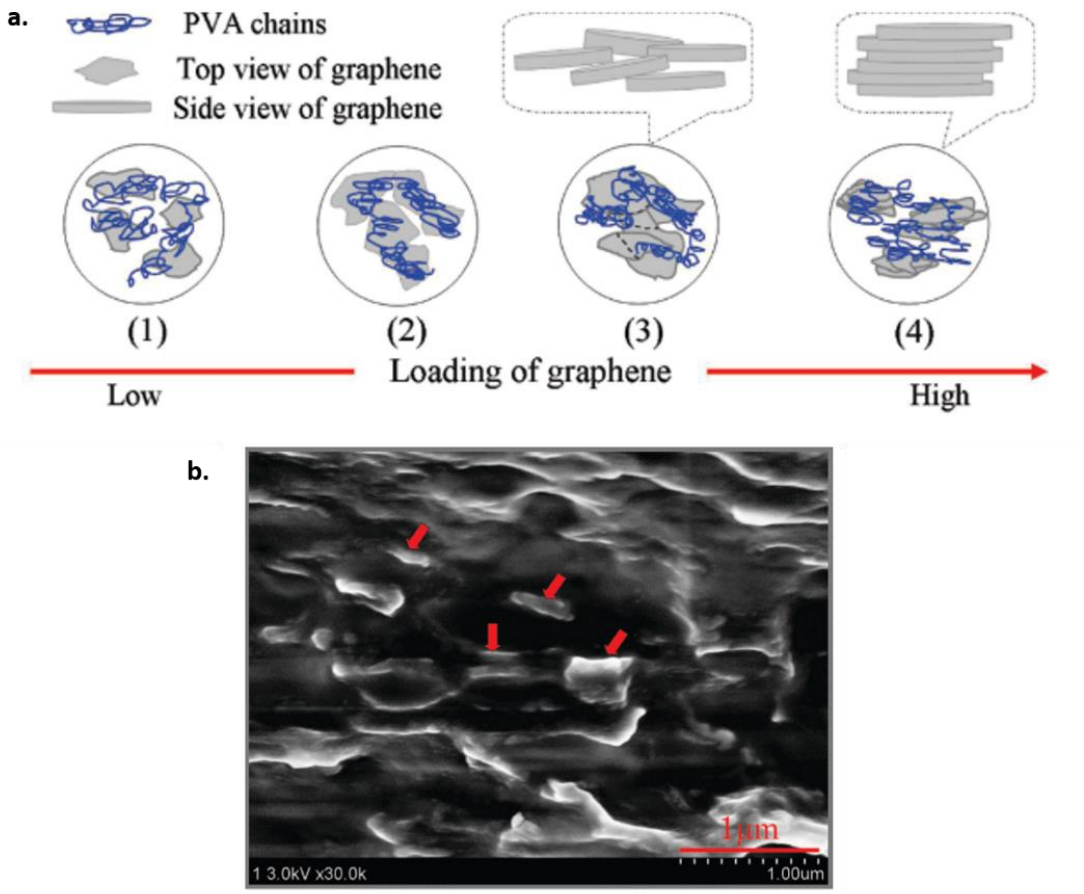

Figure 2.13 a. Schematic models of various dispersion types of graphene nanosheets in PVA matrix: (1) GO nanosheets are individually dispersed in the matrix at intervals. (2) The edges of GO nanosheets just join together side by side. (3) Some of GO nanosheets are overlapping with each other. (4) GO nanosheets are restacking together by layers. As increasing graphene content, the resulting dispersion form gradually changes. b. FESEM image of cross section of composite sample with a loading of 1.8 vol %graphene in PVA. The rows point to the graphene nanosheets dispersed in the PVA matrix [91].

Liao *et al.* [89] have proposed a co-solvent mixing method which avoids the complete drying of aqueous rGO (ARG). The ARG is kept in a wet state by removing about 90% of the water in the ARG-water suspension in order to prevent aggregation. After that, an aqueous miscible organic solvent dimethylformamide (DMF) has been added, to have a solution of ARG-water-DMF. The polymer matrix is then added to the latter solution and a uniform dispersion is achieved. In this work, they have chosen thermoplastic polyurethane (TPU) as the matrix. The resulting ARG-TPU composites show good mechanical and electrical properties. The solvent blending method has also been used for the preparation of amine-modified nano-fibrillated cellulose (A-NFC) and chemically

converted graphene composite [95], resulting in electrical conductivity of 71.8 S/m with a 10 wt.% of graphene.

Melt blending

Melt blending is a technique [96][97] most widely used in industry to produce thermoplastic nanocomposites due to the fact that it is inexpensive and quite simple. It requires melting the polymer at elevated temperatures and then mixing the graphene powders using a shear force. High temperatures are used to make the polymer matrix soft in order to allow easy dispersion of the reinforcement phase. One disadvantage of this process is that the associated shear forces required are sometimes too high and can cause a buckling or breakage of the graphene sheets. This technique is less effective in dispersing graphene sheets compared to the solvent blending due to the higher viscosity of the composite at increased sheet loading [98]. Kim *et al.* [99] prepared composites of GO and poly (ethylene-2,6-naphthalate) (PEN) by melt blending using a temperature of 250 °C and a twin-screw extruder. The composite has shown good performances in suppressing gas permeability. Kalaitzidou *et al.* [100] managed to obtain polypropylene nanocomposites reinforced with exfoliated graphite nanoplatelets by melt mixing polymer solution followed by compression or injection moulding and coating. They have done the sonication in the presence of isopropyl alcohol (IPA) to improve dispersion and to obtain electrically conductive composites with low percolation threshold ~ 0.3 vol.%. Kim *et al.* [96] have prepared a series of polylactide-exfoliated graphite (PLA-EG) composites obtaining a homogeneous dispersion using melt blending. They found Young's moduli of the resulting composites increased with EG content up to ~2 wt.%. and observed an electrical resistivity of 10^{16} Ω cm^{-1} at 2 wt.%. Bao *et al.* [101] have developed a master-batch strategy to disperse graphene into poly(lactic acid) (PLA) by melt bending (Figure 2.14). The graphene was well dispersed, and the obtained nanocomposites present markedly improved crystallinity, rate of crystallization, mechanical properties, electrical conductivity and fire resistance. The properties are dependent on the dispersion and loading of graphene, showing a percolation threshold at 0.08 wt.%.

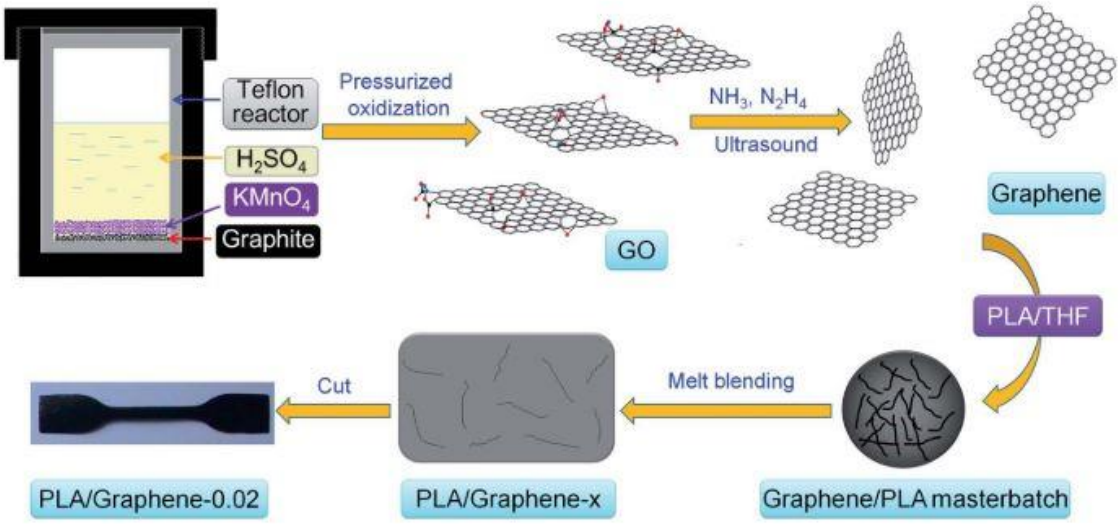

Figure 2.14 Illustration for the preparation of graphene and PLA-graphene nanocomposites. The graphite is oxidized by pressurized oxidization and then reduced to single-atom-thick graphene by a multiplex reduction method. The graphene-PLA masterbatch (20 % graphene) is prepared by solvent blending from PLA and graphene in THF media. The ‘‘x’’ in ‘‘PLA-Graphene-x’’ is the percentage of the graphene. The black sample is PLA-graphene-0.02 which contains 0.02 % graphene [101].

Latex Technology

Latex-based processing is an increasingly common way to produce polymer-nanomaterial composites because it gives control of the structure at the nanoscale using an environmentally friendly process compared to the solvent-based alternatives as no volatile organic species are released during the film formation. The latex route exhibits two major advantages compared to the melting route or solution blending method. First, it is sustainable as latex is made of polymer micro/nanospheres in a water suspension without using organic solvent. Second, it favours the build-up of a tunable architecture of fillers. This architecture promotes the formation of a percolating network of fillers at lower filler content defined as a segregated network, because of the excluded volume created by the polymer particles that forces the filler into interstitial spaces between the polymer particles during the drying process. This methodology leads the fillers to arrange in the polymer matrix in a very specific way. The morphology of the segregated network depends on the relative dimensions of the fillers and of the polymer particles. If the lateral size of the filler (w_G) is smaller than the latex diameter (d_{latex}) then the segregated network is obtained [102] [103] (Figure 2.15).

As a result, the final composite microstructure consists of two interpenetrated networks, one made of the polymer matrix and the other one made of percolating fillers [104]. Specifically in the literature relating to graphene, there are many examples of conductive composite fabricated using the self-assembly mechanism, and the two main strategies are: 1) the GO flakes are blended with the latex followed by reduction to get back to the electrical properties, or 2) rGO is blended with the latex, and the reduction step occurs prior to the blending step [105]. Both strategies have advantages and drawbacks. Regarding the choice of the matrix, there are a large variety available including elastomers, thermoplastics, epoxies, block copolymers and hydro-aerogels. Each has unique properties, which can be tuned for various applications and specific needs [106]. For example, elastomers are highly stretchable polymers consisting of lightly cross-linked chains. In contrast, epoxy resins have rigid segments and are heavily cross-linked, so they show high mechanical strength, stiffness and high brittleness. Thermoplastic polymers exhibit lower mechanical properties but can be reinforced using crystalline domains and are not chemically cross-linked so can be easily processed, shaped, melted and recycled. Thereafter, the polymer choice also has an impact in the final properties of the composites. Yousefi *et al.* [107] produced polyurethane (PU)-based composites films containing highly aligned graphene sheets using the latex method. The dispersion of GO is reduced in situ using hydrazine, resulting in a fine dispersion and a high degree of orientation of the graphene sheets. The resulting composites have shown an electrical conductivity of 10^{-3} S/cm at 5 wt.% and a percolation threshold of 0.078 vol. %.

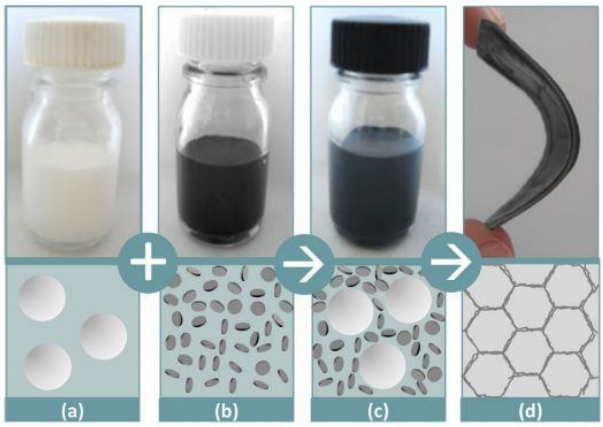

Figure 2.15 Processing steps of the nanocomposite materials: (a) blank latex, (b) NMG suspension, (c) NMG-latex blend, and (d) flexible and conductive material obtained after water evaporation and film formation [102].

Zhang *et al.* [108] prepared PMMA-GO composites, with the aid of a cationic surfactant cetyl trimethylammonium bromide (CTAB), through electrostatic attraction. The GO-PMMA particles showed better thermal stability than the pure PMMA. Zhao *et al.* [109] have produced graphene filled polystyrene (PS) nanocomposites by latex technology. The PS was synthesized first via disperse polymerisation in an ethanol-water medium by using a cationic co-monomer, and then directly co-assembled with GO, due to electrostatic adsorption and $\pi - \pi$ interaction, with the GO nanosheets gradually wrapping the surface of the cationic PS particles. The fabricated nanocomposites show a conductivity of 25.2 S/m at 1.22 vol.% and a percolation threshold of 0.09 vol.%. Gudarzi *et al.* [110] have developed a method for the fabrication of polymer-graphene composites based on the assembly of colloidal polymer particles and graphene sheets. By choosing an appropriate colloidal core (hydrophobic core of PMMA and hydrophilic shell of acrylic acid), they have managed to prevent the aggregation of rGO nanolayers in aqueous media, but also guaranteeing a good interfacial interaction due to the strong bond between polar segments of polymer chains and the oxygen groups of graphene. The composite also remained stable during the GO reduction, resulting in the molecular level dispersion of graphene in the final polymeric composite. They have found an enhancement in modulus and hardness and also in the T_g shift toward higher temperatures with the addition of rGO.

In-situ polymerization

In-situ polymerisation [111][112] involves the polymerisation of hydrophobic monomers in the presence of graphene nanosheets. In this approach, graphene or its derivative is first swollen in the liquid monomer, and then a suitable initiator is dispersed. Either heat or radiation can be used to initiate the polymerization. It is possible to obtain well-dispersed graphene in polymer matrix after polymerisation due to intercalation of monomers into the layered structure of the graphite that increases the interlayer spacing and exfoliates graphene platelets. During the polymerisation process, some difficulties are associated with the increase of the viscosity, that limits the loading fraction and the processing of the composites. Some groups [113] have tried to functionalize the GO with amine groups to promote the dispersion of the flakes and take advantage of the functional groups. They have found that the functionalization allows the formation of strong interfaces between the filler and the matrix, enhancing the mechanical properties of the matrix at small filler loading. In some cases, the process is carried out in the presence of solvents, thus solvent removal is a critical issue similarly in the solvent blending. Tang *et al.* [114] have used this technique to fabricate graphene nanosheets/epoxy nanocomposites, and have improved the thermal conductivity of the composites through the non-covalent functionalization of pyrene molecules with a functional segmented polymer chain on the thermally exfoliated graphene. The pyrene on the surface of graphene nanosheets plays an important role in inhibiting their aggregation and facilitating dispersion within polymer matrix homogeneously. Instead, Mo *et al.* [115] prepared the same type of composite using the in situ polymerisation of pyrrole in the presence of nano graphene sheets (NanoGs), obtaining a maximum conductivity of 1.56 S/m at 15.2 wt. % of PPy-NanoGs and flexural strength of 18 MPa at the same amount. Other people have used the same method to prepare graphene polymer composites using Nylon 6 [111][116], PMMA [112] [117], PU [118], poly (butylene terephthalate) (PBT) [118] etc.

2.5 Main Applications

Nowadays a major industrial effort has focused on producing wearable, corrosion-resistant, conducting and flexible materials. The main applications of these materials are in power generation and storage to power-sources for equipment and computers.

Therefore, extensive work on producing new materials that are suitable for this kind of application has been carried out. The key parameters to increase the electrical conductivity are the morphology and the structure of the conductive network. Conductive polymer composites (CPCs) are obtained by mixing an insulating polymer with conductive fillers such as carbon fibres, carbon nanotubes, carbon black or any filler, which can give a conducting pathway[119]. CPCs can be used in various applications like sensors, some components in circuit devices, battery and fuel cell electrodes.

Percolation theory- Correlation of structure with conductive properties of the composites

An important aspect to consider in order to have conductive composites is the concentration of the conductive filler that must be above the percolation threshold as described in detail by the percolation theory. The idea of segregated and percolating networks was described for the first time by Kusy in the 70s [120]. He described that the possible arrangement of the filler particles in a polymer matrix can be random or segregated. In the region below the percolation threshold, the electrical conductivity is equivalent to the electrical conductivity of the polymer matrix at low filler loading. The overall composite conductivity approaches zero because the conductive channels based on the uninterrupted contact between the particles are not formed yet. As the filler concentration increases, continuous conductive pathways are developed until a certain critical volume fraction known as the percolation threshold is reached. After that, the conductive network continues to increase as the particles concentration increases until the electrical conductivity plateau is achieved [121]. There are some factors that can affect the electrical conductivity of the resulting polymer composites such as shape and size of filler, aspect ratio, the inherent conductivity of the filler, the spatial distribution of the filler in the polymer matrix and the interaction among the polymer and the filler. The equation that explains this phenomenon is:

$$\sigma = \sigma_0 (\phi - \phi_c)^t \quad \text{for } \phi > \phi_c \qquad \text{(Equation 2.2)}$$

where σ is the conductivity of the composite, σ_0 is a proportionality constant (intrinsic conductivity of the filler), t is the critical exponent, whereas ϕ is the filler and ϕ_c is the

percolation threshold concentration, respectively. The critical exponent, *t* is important to understand the dimensionality of the system. According to the literature [122], a theoretical value for the critical exponent is t = 1-1.33 for a two-dimensional system and t = 2 for a three dimensional percolating network [123][124].

2.5.1. Conductive Polymer Composite Materials

A large amount of effort has been devoted to improve and enhance the electrical properties of an insulating matrix by combining it with conductive fillers, such as graphene, CB, CNTs and so on. In particular, highly insulating systems such as NR would have many applications if it could be made conductive. For many filled polymer composites the critical concentration of conductive filler is around 15% by volume, Grunlan has shown that the percolation threshold for CB-filled conductive composites can be reduced when latex is used as the composite matrix starting material. However, in such composites, the CB content needs to be high in order to provide sufficient electrical conductivity due to its inherently low aspect ratio [125]. High filler loadings can lead to some difficulties in processing and in the loss of the mechanical properties of the system. Afterwards, they managed to obtain a model matrix starting material for CB-filled electrically conductive polymer composites using monodisperse P(MMA-co-BA) lattices [126]. Creating composites with lattices that have glass transition temperatures at or below room temperature allows for the formation of low percolation threshold material without using heat or pressure because in the former individual polymer strands are sufficiently mobile to allow for full film coalescence. In these composites, the percolation threshold is reduced by an order of magnitude compared to conventional melt or solution-based systems. In situ- polymerisation of MMA in the presence of graphite [127] has proved to be a successful approach to the fabrication of conductive materials with a percolating network occurring at ~0.3 vol. %. Another way to reduce the percolation threshold is to use high aspect ratio particles such as SWNTs. In PVAc-SWNTs based composites, the polymer particles create excluded volume and push the filler into the interstitial space between them. SWNTs have therefore restricted organization into the polymer matrix resulting in the reduction of the percolation threshold [128]. With this method, we can get some advantages in terms of processing and the cost as the nanotubes are relatively expensive.

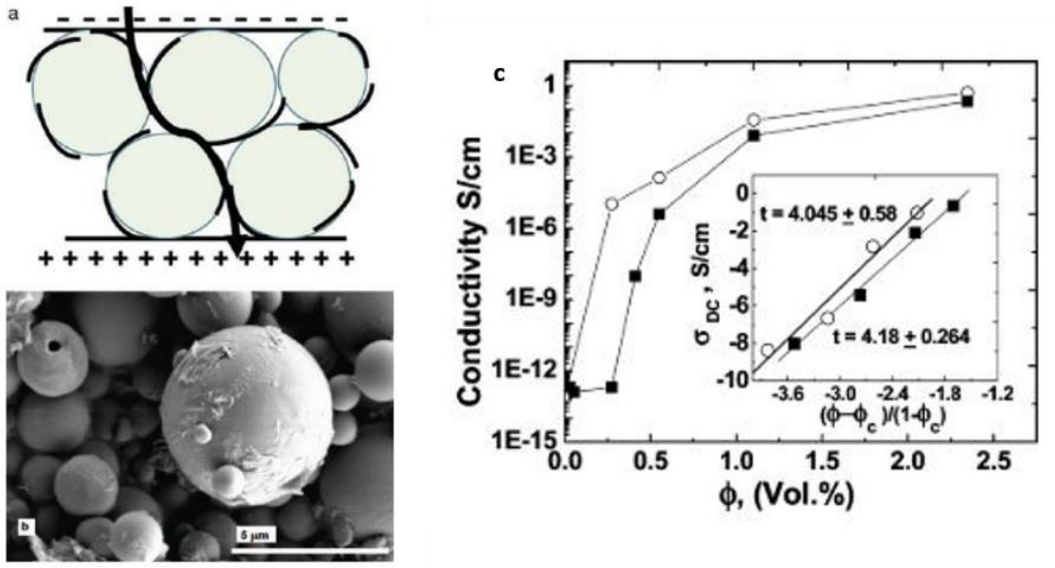

Figure 2.16 a. Schematic of the directed assembly of graphene nanosheets on the polymer microspheres to generate an electron transport path. b. SEM micrograph of graphene nanosheets on the PC microspheres. c. Direct current conductivity percolation data of graphene PC nanocomposite prepared by (a) emulsion mixing (○) and (b) solution mixing (■) [129].

Jurevicz *et al.* [130][131] designed a robust, stretchable and electrically conducting thin film with significantly improved transparency and lattice percolation at very low CNTs inclusion (~ 0.1 wt. %) with important implications for several applications in flexible and stretchable electronics. The latex technology concept has also been applied for the preparation of graphene-PS nanocomposites [132]. The percolation threshold for conduction in these systems is below 1 wt. % and the maximum conductivity of about 15 S/m can be achieved for 1.6-2 wt.% of graphene. Certainly, there are some advantages to using graphene instead of CNTs such as the cost because graphene can be obtained from cheap graphite by some simple chemical treatments. Furthermore, all the induced carriers are mobile and there are no trapped charges in pristine graphene. When the graphene nanosheets are mixed with bisphenol-A polycarbonate [129] using solution blending the conductivity becomes very high for this kind of composites reaching ~50 S/m with 2.2 vol. % of graphene and showing a percolation threshold around 0.14 vol.% (Figure 2.16). Pham *et al.* [133] have used positively charged PMMA latex particles and negatively charged graphene oxide sheets through electrostatic interactions, followed by hydrazine reduction to produce PMMA-rGO based composites. The obtained PMMA-rGO composite exhibited excellent electrical properties with a percolating threshold as low as 0.16 vol. % and electrical conductivity of 64 S/m at 2.7 vol. %. The highest conductivity

result is reached through the self-assembly of PS and ethylene-vinyl acetate (EVA) with graphene sheets [134]. The obtained PS-EVA-Graphene sheets composite exhibited excellent electrical properties with a percolating threshold as low as 0.3 wt.% and electrical conductivity of 1024 S/m at 9.6 wt. %.

2.5.2. Mechanical properties

The introduction of graphene fillers into the polymer matrix greatly enhances the properties of the original polymer, including elastic modulus, tensile strength, adhesion and so on. The enhancement of the mechanical properties of the composites suggests the use of these materials in transport applications, where the combination of high strength and lightweight is required. It is also possible to reinforce systems that are very delicate such as membranes or fibres to create smart fabrics and woven materials or even foams that are quite versatile. Therefore, they can be used in transport, construction, packing or biomedical applications [135].

Percolation theory- Correlation of structure with mechanical properties of the composites

The percolation approach can be used also for mechanical properties, but it is more complex compared to the electrical one [104]. In this approach, the fillers used in the composite can be described using two types of clusters: the infinite clusters and the finite clusters, comprising the dangling bond and the backbone as seen in Figure 2.17.

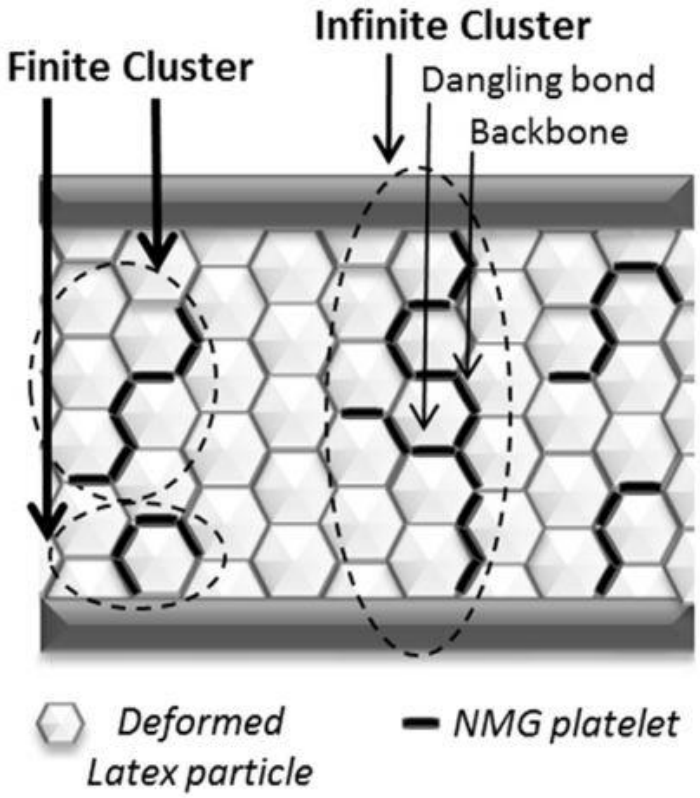

Figure 2.17 Percolation behaviour in a latex-based graphene nanocomposite [104].

While for conductivity the finite and infinite clusters can conduct, or either they do not, in the case of the mechanical properties, both (backbone and dangling bond) clusters can affect the final mechanical performance. In general, the finite cluster has a lower reinforcing effect compared to the infinite. To describe this effect of the filler percolation on the mechanical properties of the composites a model has been proposed of springs in series and parallel. Therefore, in finite clusters, the reinforcement due to fillers is associated in series with the polymer matrix while in the infinite clusters the fillers are associated in parallel. In the case where $\phi < \phi_c$, the volume fraction of the infinite cluster ϕ_∞ is zero. For $\phi \geq \phi_c$, ϕ_∞ is defined using equation 2.3:

$$\phi_\infty = \left(\frac{\phi - \phi_c}{1 - \phi_c}\right)^b \qquad \text{(Equation 2.3)}$$

The critical exponent value b is between 0.4 and 1.6. When b has a lower value, it means that the interaction between the fillers and matrix is very strong. Therefore, it would be beneficial to use a functionalised filler, such as GO, whereby the associated chemistry potentially enhances the interaction with the matrix.

Enhancement of the mechanical properties of polymer matrix/graphene composites:

An enormous amount of research has been focused on the mechanical properties of graphene nanocomposites as the presence of graphene that has a high modulus in a low modulus matrix can lead to substantial reinforcement. The evaluation of the reinforcement is most frequently made by the study of the stress-strain curves obtained during tensile testing. Mechanical properties can be affected by several parameters such as the preparation method, the graphene structure, the dispersion filler in the matrix, the orientation of the filler and the interaction of the latter with the matrix. The tensile strength is strongly affected by aggregation of the filler and this is the reason why often there is a linear increase of the tensile modulus with increasing filler content, while tensile strength saturates at lower filler percentages. In the literature, there is an incredible amount of papers that discuss the mechanical properties of graphene-based nanocomposites. As mentioned before, to have a significant improvement of these properties, it is essential to have a homogeneous dispersion of the filler in the polymer matrix and it is necessary to obtain a strong interaction between the filler and the matrix at the interface. This is particularly important for non-polar polymers like PP and PE that are the most widely used plastics. Typically for graphene filled composites, there is an increase in the modulus and tensile strength by several orders. In general, with non-polar polymers, the solution mixing technique becomes almost impossible because PP and PE are only soluble in some solvents like xylene and trichlorobenzene. Thus, the melt mixing method appears to be the most suitable to use. Song *et al.* [136] reported an eco-friendly strategy for fabricating the polymer composites with well-dispersed graphene sheets in the matrix via first coating graphene using PP latex and then melt-blending the coated graphene with the PP matrix. By only adding 0.42 wt.% of graphene sheets into the polymer matrix they have increased the Young's modulus of ~74 % and the tensile strength of 50%. Zhou *et al.* [137] achieved a 40% increase in tensile strength with the addition of only 0.7 wt.% of RGO using two simple steps. First the synthesis of GO based

PVA composite film and then the immersion of the latter into a reducing agent aqueous solution of sodium hydrosulfite (Figure 2.18). Instead, Kashyap *et al.* [138] managed to obtain an increase of ~ 150 % in both tensile strength and modulus using only 0.3 wt.% of GO in the PVA matrix, which is unprecedented. They also noted that adding hydrazine to reduce GO, leads to a decrease of the modulus to values close to that of pure PVA. The reducing agent, in this case, is not only reducing the GO platelets but it is also changing the polymer matrix.

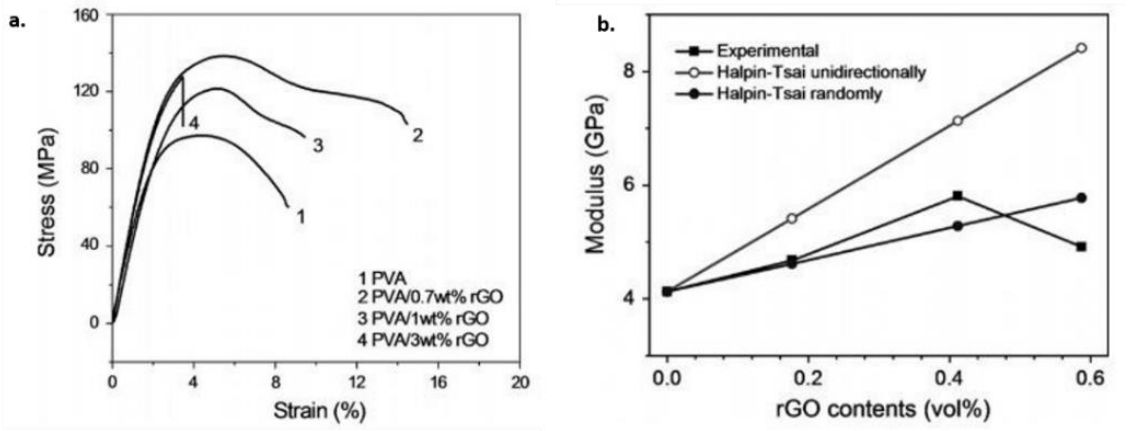

Figure 2.18 a. Stress–strain curves of PVA and PVA-rGO film. b. Young's modulus of nanocomposites [137].

In the case of poly(methyl methacrylate) PMMA as a matrix, different methods can be used such as melt mixing [139], emulsion polymerisation [140] and in situ polymerisation [112] to obtain nanocomposites in the presence of graphene. The best results have been achieved using a facile approach via in situ free-radical polymerisations, Wang *et al.* got an enhancement of 150% in the modulus and ~115 % in the tensile strength adding 0.5 wt.% of exfoliated graphene. Another important mechanical property that is worth investigating is known as tackiness. Day to day examples are numerous and in general, involve polymer films. Controlling this property is important in many applications such as sealants, coatings and also in pressure-sensitive adhesives (PSAs) in which it is desirable to have a high tackiness, whilst for paints and coatings, the tackiness is not required. Tacky polymer-based materials are typically soft with a modulus value around 10^5 Pa [141]. The adhesion energy can be described as the work needed to separate the objects, depending on the dimensions and the properties of the film itself. The force

needed to separate two objects strongly depends on the mechanical properties of the film. Nowadays, when producing polymer matrix composites is important to consider environmental issues. Hence, when making composites there is a drive to eliminate the use of organic solvents and try to substitute them with a waterborne matrix that is environmentally friendly. Consequently, they require performance that relies on solvent technology. Therefore, the present study is aimed at investigating the performance of graphene-based composites, fabricated using latex technology.

2.6. Summary

In this chapter, a general review of the current state of the physics and the structures of 2D materials such as graphene, GO, rGO and CNTs, polymer latex and composite materials are described. In the beginning, some examples of composites present in nature are given to explain the general meaning of composite materials and to give an idea that composite materials are everywhere. Afterwards, the fillers used to create nanocomposites are introduced. 2D compounds have attracted enormous attention due to their properties such as high mechanical strength, high conductivity, high mobility and so on. Since the first report of graphene isolation in 2004, they became the flagship in many research fields such as materials science and nanoscience. They are considered ideal components for the fabrication of new generation of high performance chemical sensors because of their electrical, mechanical and optical properties. Graphene has attracted the attention of many researchers due to its unique physical properties such as high thermal and electrical conductivity, remarkable mechanical strength etc. Other family members of carbon-based materials are GO, rGO and CNTs. Their physicochemical properties can be tuned due to their chemical composition which allows their use in various research areas such as nanocomposites, energy storage, biosensing, nanoelectronics etc. The physical properties of these nanomaterials can be tailored using some polymer matrix such as NLR and polymer latex dispersions. Polymer-based composites have been an area of research for the past 30 years. Especially conducting composites are of particular interest for flexible electronics and anti-static coatings. Researchers have developed a new type of polymer composites that are electrically conductive by adding conductive fillers such as CNTs, rGO, graphene etc. Although several preparation methods exist to incorporate nanofillers into the polymer matrix, latex technology seems to be the best candidate. It has major advantages compared to the solution mixing, melt blending and in situ polymerisation. First of all, it is a sustainable method because the polymer nanoparticles are suspended in water and not in an organic solvent. It also favours the build-up of a tunable architecture of fillers, promoting the formation of a percolating network of fillers at lower filler content defined as a segregated network. This methodology allows the fillers to arrange in the matrix in a very specific way. In the literature, there are many examples of graphene-based composites fabricated using the self-assembly method and are reported in Table 1 in the Appendix. These conductive composites can be used for the creation of sensors, some components in circuit devices,

battery, fuel cell electrodes and supercapacitors etc. Certainly, it is important to underline that for better understanding the electrical properties of these composites is essential to consider the percolation theory. In order to obtain conductive composites, the filler concentration must be above the percolation threshold. The percolation threshold is the lowest concentration of nanofiller at which electrical pathways are created through a specimen. That means that the insulating material is turned into a conductive material. In many cases, the critical concentration of conductive filler is around 15% by volume. In 2004 Grulan *et al.* [128] have demonstrated the possibility to obtain a percolating network with a percolation threshold less than 0.1 wt.% for the SWNTs-PVAc based composites using the self-assembly method. As well, Jurevicz *et al.* [130][131] have designed a robust, stretchable and electrical conducting thin film at very low CNTs wt% (∼ 0.1 wt%) with important implications for several applications in flexible and stretchable electronics. More polymer-carbon-based composites examples that show how the percolation threshold and the conductivity can change using different filler and matrix can be found in Table 1 in the Appendix. The mechanical properties of polymer-carbon-based composites have been also described. In this particular case, carbon fillers are used to modulate the mechanical properties of the polymer matrix and enhance the elastic modulus, tensile strength, adhesion etc. Enhancing the mechanical properties can give the possibility of using these materials for transport application, where the combination of high strength and light weight is required. Another possibility is to use them for the reinforcement of systems for smart fabrics, foams for packing, biomedical application and construction. Here again it is essential to understand the correlation between the structure and the mechanical properties. It is shown that the percolation theory can be also applied to study the mechanical properties of these materials. In literature there are many examples of polymer-based composites in which the filler has modified the mechanical properties of the matrix. For example, for the system PMMA-graphene [112] there is an increase of ∼150 % in the modulus and in the tensile strength when 0.5 wt.% of graphene is added in the PMMA matrix. Another mechanical property to take in account is the tackiness. It is useful to create materials for PSAs, sealants in which is desirable to have high tackiness whilst for paint and coating tackiness is not required.

Chapter 3

Methods and materials

3.1 Experimental techniques

3.1.1 Structural Characterisation

It is a fundamental need to study structure at the atomic or nanometre level to develop structure-property relationships in nanocomposites. Electron microscopies use highly energetic beams of electrons and electromagnetic lenses, and are used in order to increase the resolution to the Å level [142]. In this section, the two basic types of electron microscopes are described, mainly SEM and TEM.

Scanning Electron Microscopy (SEM)

This method involves rastering a focused electron beam over a surface to create an image, the electrons in the beam interact with the sample, producing various signals that can be used to obtain information about the surface topography and composition [143]. To create an SEM image, the incident electron beam is scanned in a raster pattern across the sample's surface. The interaction volume can be described as the 3- dimensional space in the sample that the primary electrons penetrate the specimen and interact within (Figure 3.1.). The accelerating voltage is responsible for the amount of energy carried by the primary electrons. A larger interaction volume is produced by electrons with higher energy and indeed generates higher energy signals, while a low accelerating voltage provides information from the surface of the specimen. SEM technique cannot resolve any features smaller than the spot size, so the resolution limit can be as small as 5 nm. Furthermore, the sample's atomic number and the beam penetration can also affect the resolution limit. It is possible to obtain the analytical information of a sample by detecting

secondary electrons (SE) and backscattered electrons (BSE) which are normally primary in nature. Secondary electrons (SE) are produced by inelastic interactions of high-energy electrons with low energy electrons of atoms in the specimen, which cause the ejection of the electrons from the atoms. They are originated within a few nanometers from the surface and they have low energy (<50 eV). SE are important because they provide high-resolution imaging of the surface morphology. Backscattered electrons (BSE) are elastically scattered from atoms in the solid, due to the elastic collisions with the nucleus of the atom. There is an interaction between the negatively-charged electrons with the electrostatic field of the positively charged nuclei and with the individual electrons. They are characterised by their high energy which varies directly with the specimen's atomic number and thus provides elemental composition analysis, as well as surface topography imaging.

Energy Dispersive Spectroscopy (EDS)

This technique is used for qualitative analysis of materials and is performed in conjunction with SEM [144]. Secondary and backscattered electrons are used to get information about the morphological analysis and X-rays are used to identify and quantify chemicals contained within the specimen. EDS can detect elements with atomic numbers from Be to U and with a concentration between 1-10 wt%. It fails when the concentration is below 0.01 wt%, indeed it can not detect trace elements. [144].

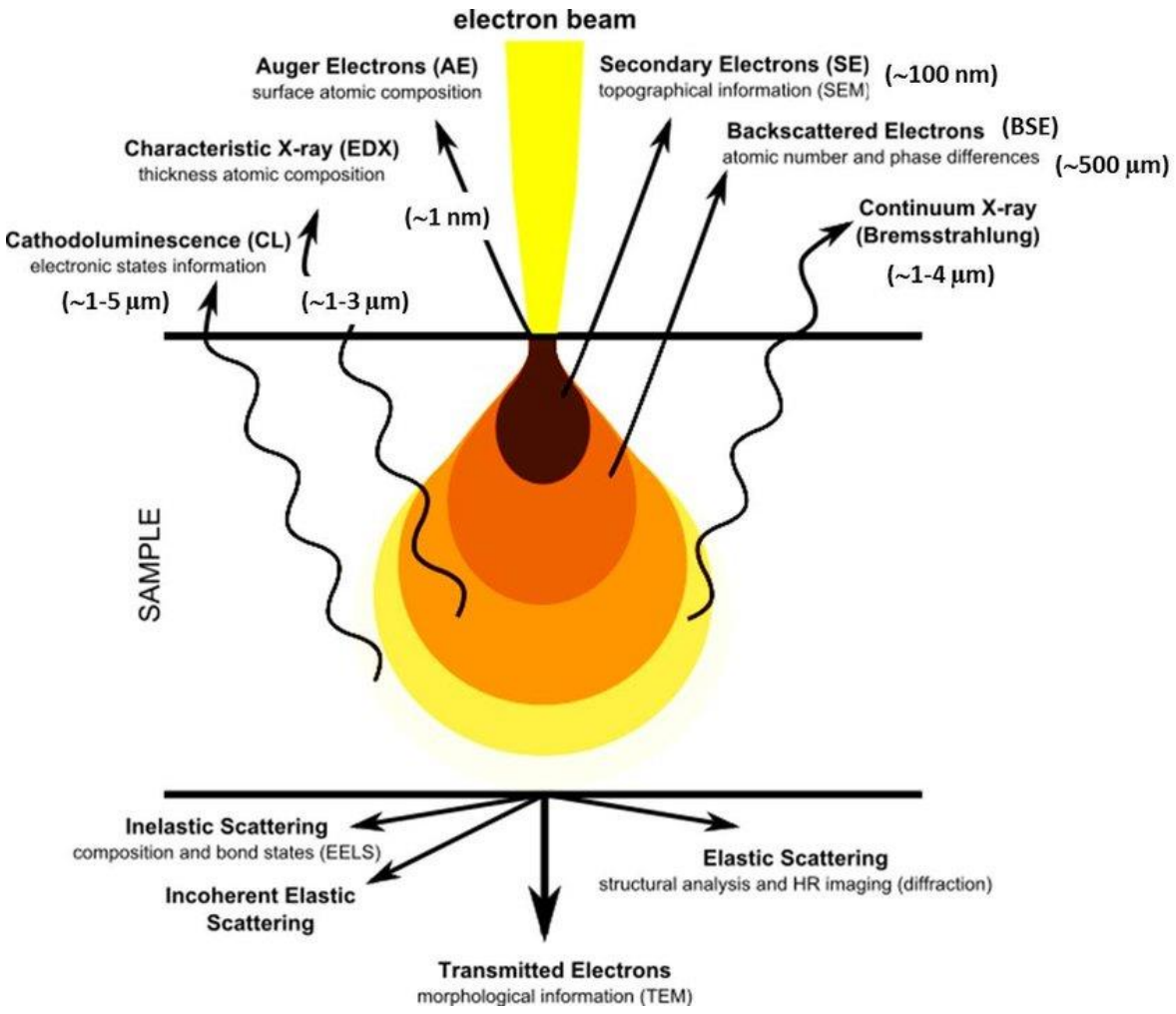

Figure 3.1. Schematic representation of different type of electron beam-sample interactions and their specific volumes of interaction [145].

In TEM a beam of electrons is passed through a specimen, and when the electrons are accelerated up to high energy levels (few 100 keV) and focused on a material, they can scatter [146]. As said before, the scattering event of electrons travelling through the interaction volume can be separated into two classes: 1) Inelastic scattering in which the electrons scatter within the target material, changing direction with each atomic interaction and losing energy. During this event secondary electrons, X-rays, heat and light maybe produced as shown in Figure 3.1. Elastic scattering in which the high energy electrons are reflected or back-scattered out of the specimen interaction volume are defined as backscattered electrons.

Atomic Force Microscopy (AFM)

AFM is a method used to investigate the shape of a surface in three-dimensional (3D) detail down to the nanometre scale. It can be used to give an image of all materials, hard or soft, synthetic or natural including biological structures such as cells and biomolecules [147]. It is a powerful tool and consists of a cantilever (typically silicon or silicon nitride) with a sharp tip (probe) on the end that is used to raster scan the surface of the specimen (Figure 3.2). The tip is held at a close distance from the sample, and when it is brought into proximity of the sample's surface, the forces between one atom at the tip and one atom on the surface is measured in accordance with Hooke's Law, equation 3.1.

$$F = -kz \qquad \text{(Equation 3.1)}$$

Where k is the spring constant of the cantilever, which depends on the dimensions and the materials, and z is the cantilever deflection produced by the interaction with the surface [148].

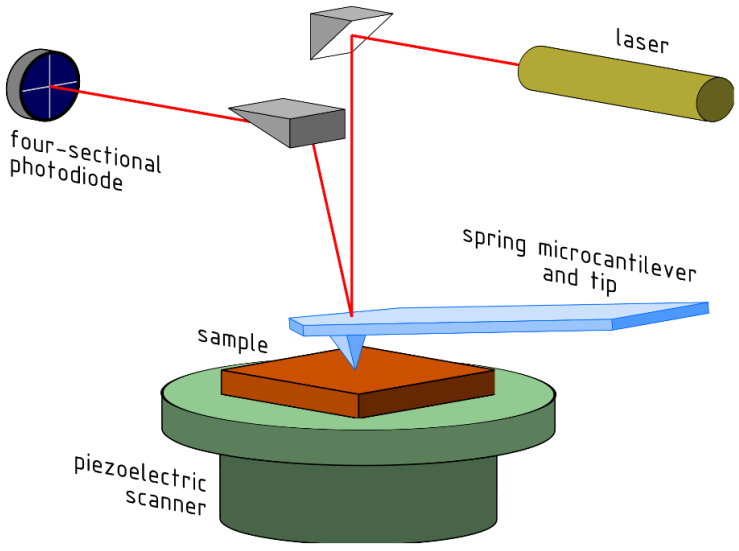

Figure 3.2. Schematic illustration of the core components of AFM [149].

With the AFM it is possible to measure several forces such as van der Waals forces, contact force, capillary forces, chemical bonding, electrostatic forces and magnetic forces among others. The AFM can be operated in different modes, depending on the application. In general, possible imaging modes are divided into three modes: static (known as contact) mode, semi-contact (tapping) mode and non-contact mode. Contact mode can be executed using a constant force or at a constant average distance. In constant force, the cantilever bends in response to the force $\bar{F}$ which acts on the tip until the static equilibrium is established. While scanning the surface the deflection can be kept constant by regulating the height of the sample relative to the tip. This mode is called equiforce mode and is the most common one. The height profiles of a homogeneous sample measured with the coulombic interaction deriving from the Pauli exclusion principle that dominates are interpreted as topography. An alternative way is to keep the height constant and the variation of cantilever deflection is recorded. This mode is called variable deflection mode and allows high scanning speeds. Usually, this mode is used for scanning hard samples as the tip directly touches the surface during scanning and it is not suitable for scanning soft samples such as polymers, biological materials because it can cause tip breakage or sample damage [150]. Instead, semi-contact mode can be used to study soft materials such as polymers and thin films, biological samples and also samples that are weakly bound to the matrix. In this mode, known as tapping mode, the cantilever oscillates at a frequency that is near to its free resonant frequency (v) given by equation 3.2 below:

$$v = \frac{1}{2\pi}\sqrt{\frac{k}{m}} \qquad \text{(Equation 3.2)}$$

where k is the spring constant, m is the mass of the cantilever. In tapping mode, the oscillation amplitude is monitored, and in phase mode imaging, the phase shift of the oscillation cantilever relative to the driver electronics is monitored. A qualitative characterisation of material properties, for example, adhesion, elasticity, chemical composition and friction can be provided by the phase shift of the cantilever oscillation. In non-contact mode, the tip does not contact the surface of the sample and the cantilever is oscillated above the surface of the specimen, operating in the attractive regime of the

inter-molecular force curve. This mode does not suffer from tip or sample degradation effects that are sometimes observed after taking several scans with contact AFM. This mode is suitable to image soft surfaces, biological samples and organic thin films, but it is also very sensitive to the condensed water laying on the surface of the sample and to external vibrations. When the AFM is operating in contact mode the liquid layer is penetrated in order to image the surface, whereas in non-contact mode, it oscillates above the adsorbed fluid layer and it gives an image of the liquid and the surface. Kelvin probe force microscopy (KPFM) is a hybrid version of AFM within contact mode and tapping mode, also known as surface potential microscopy. It is used to measure the contact potential difference (CPD) between the tip and the surface of the specimen when the two are electrically connected. The CPD (V_{CPD}) is defined as:

$$V_{CPD} = \frac{\phi_{tip} - \phi_{sample}}{-e} \qquad \text{(Equation 3.3)}$$

where ϕ_{tip} is the work function of the tip and ϕ_{sample} is the work function of the sample, and e is the electronic charge. In this mode when the tip is brought close proximity to the specimen surface, an electrical force is generated between the tip and the specimen surface, due to the differences in their Fermi energy levels. If an external bias (V_{DC}) is applied between the probe and the sample, the surface charge in the contact area is eliminated. The magnitude of this bias is a direct measurement of the CPD; therefore the work function of the sample can be calculated when the probe work function is known [151].

3.1.2 Spectroscopy techniques

This section is focused on the interaction between matter and low energy radiation often identified as optical spectroscopy [152]. It covers Raman, FTIR and UV-Vis Spectroscopy.

Raman Spectroscopy

Raman spectroscopy is a scattering technique that relies on the inelastic scattering of photons. It usually involves the inelastic scattering of monochromatic radiation in the visible part of the spectrum. When the monochromatic light interacts with a specimen it interacts with molecules or atoms and polarises (distorts) the clouds of electrons round the nuclei to form a "virtual state" [153].

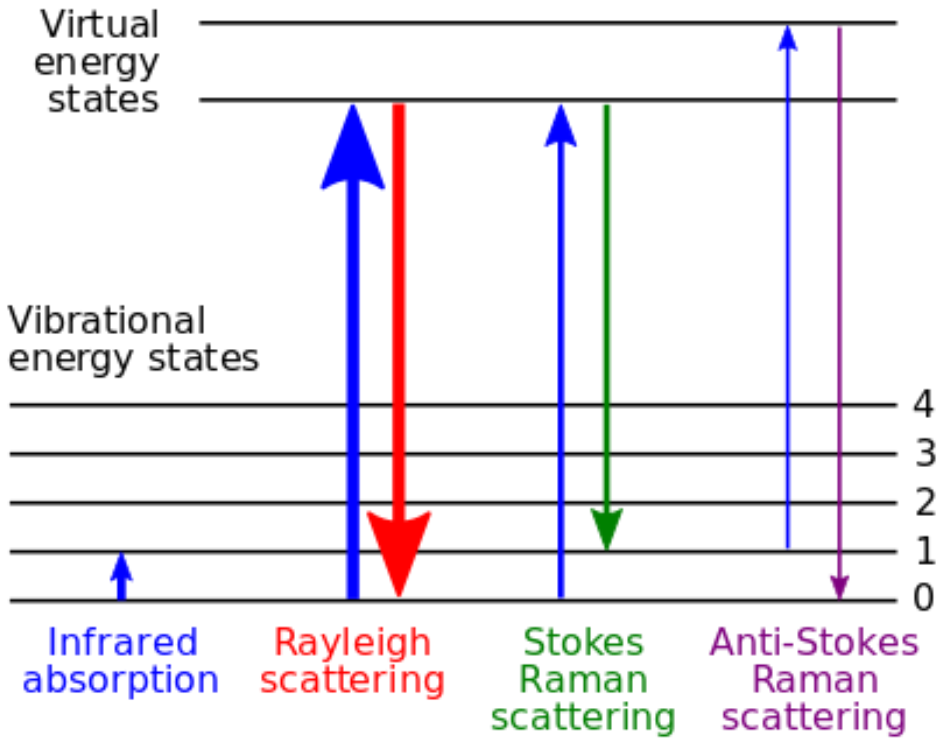

Figure 3.3. Energy-level diagram showing the states involved in Raman spectra [154].

Alternatively, Rayleigh scattering is an elastic collision between the incident photon and the molecule, the energy and therefore the frequency of the scattered photon is the same as that of the incident photon, and this is the strongest part of the scattered radiation. The Raman effect can be looked on as an inelastic collision between the incident photon and the molecule where as a result of the collision the vibrational or rotational energy of the molecule is changed by an amount ΔE_m. In order that energy may be conserved, the

energy of the scattered photon, hv_s, must be different from the energy of the incident photon hv_i by an amount equal to ΔE_m:

$$hv_i - hv_s = \Delta E_m \qquad \text{(Equation 3.4)}$$

If the molecule gains energy, then ΔE_m is positive and v_s (scattered photon) is smaller than v_i (incident photon), giving rise to Stokes lines in the Raman spectrum. If the molecule loses energy, then ΔE_m is negative and v_s is larger than v_i, giving rise to anti-Stokes lines in the Raman spectrum [155]. A schematic diagram of all the possible scattering processes are shown in Figure 3.3. A Raman system consists of a laser source, which is transferred through mirrors, a filter and polariser to the beam expander that adjusts the laser beam. The laser beam is directed onto a notch filter that acts as a band filter. Subsequently, the laser passes through a microscope lens in order to be focused on the specimen in the sample stage. The beam that is reflected from the specimen is passed back through the microscope optics and the monochromator. A charge-coupled device (CCD-camera) is used to detect and analyse the Raman shifted radiation and a software is used to analyse the data. Raman spectroscopy has become a powerful, non-invasive method to characterise graphene and related materials [156].

Fourier-Transform infrared spectroscopy (FTIR)

This is a powerful technique that allows the acquisition of spectra from a wide range of solids, liquids and gases. It is used to determine the molecular composition and the structure of a molecule through the detection of vibrational transitions. This technique collects all wavelengths, from middle IR (4000-400 cm^{-1}) to near IR (4000-10000 cm^{-1}). In infrared spectroscopy, the IR radiation is passed through the specimen as molecules absorb specific frequencies matching the transition energies of bonds and chemical groups. IR spectroscopy probes molecular motions that involve a change in a bond's dipole moment. Another option is the Attenuated Total Reflectance (ATR) mode that combats the most challenging aspects of IR analysis, the sample preparation and the spectra reproducibility. The IR beam enters the ATR crystal at the angle of typically 45º

(relative to the crystal surface) and is totally reflected at the crystal to the sample interface. Because of its wave-like properties, the light is not reflected directly by the boundary surface but by a virtual layer within the optically less dense sample. The fraction of the light reaching into the sample is known as evanescent wave. Its penetration depth depends on the wavelength, the refractive indices of the ATR crystal and the sample and the angle of the entering light beam as shown in Figure 3.4:

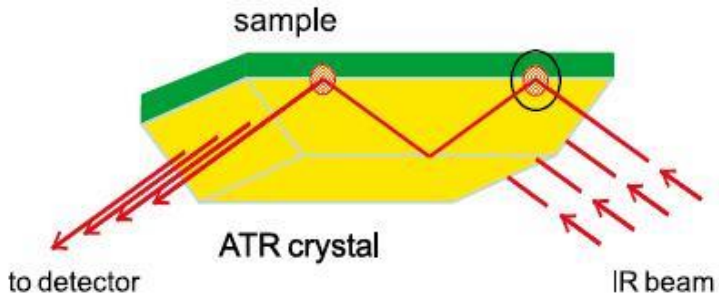

Figure 3.4. Schematic of ATR principle [157].

This evanescent wave is typical of a few microns (0.5 µm - 3 µm) beyond the crystal surface and into the sample. Thus, there must be good contact between the sample and the crystal surface. The refractive index of the crystal must be significantly higher than that of the sample, in general, the typical refractive indices for ATR crystals are between 2 and 4 and typical values for organic substances such as polymers range from ca. 1.2 to 1.5, hence many IR-active samples can be measured.

UV-Visible Absorption Spectroscopy

It is a common procedure for the identification of a compound and for measuring the concentration of the dispersion. In this technique, the intensities of the input $I_{in}(\lambda)$ and output $I_{out}(\lambda)$ light are measured to identify the absorption. The absorbance is directly proportional to the path length through the sample, b, and the concentration, c, of the absorbing species. The measurement is based on Beer's Law shown in Equation 3.5:

$$A = -\log\left(\frac{I_{in}}{I_{out}}\right) = \varepsilon bc \qquad \text{(Equation 3.5)}$$

Where ε is the molar absorptivity or extinction coefficient of the solution, and it is a proportionality constant [158].

3.1.3 Thermo- analytical techniques (DSC, TGA)

These techniques are used to determine the physical and chemical properties of a substance as a function of temperature and time. This section covers Differential Scanning Calorimetry (DSC) and Thermogravimetry Analysis (TGA).

Differential Scanning Calorimetry (DSC)

It is the simplest and most widely used thermal analysis to study polymer transitions, mainly to determine the glass transition temperature (T_g), melting and boiling point, crystallization, oxidative stability and liquid crystalline transitions. DSC measures the heat flow (energy) required to maintain the sample and the reference material at the same temperature ($\Delta T = T_s - T_r \approx 0$), as both are placed in the same environments and temperature conditions [159]. In Figure 3.5. a schematic representation of the DSC device is shown.

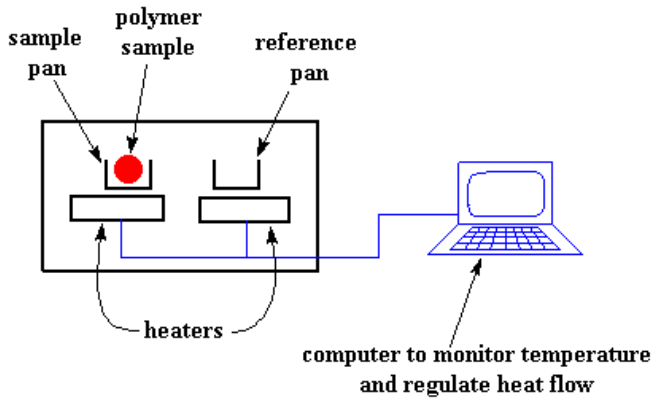

Figure 3.5. Schematic representation of DSC apparatus. Both the sample and reference are maintained at nearly the same temperature throughout the experiment. Generally, the temperature program for a DSC analysis is designed such that the sample holder temperature increases linearly as a function of time [160].

The heat flow is equivalent to enthalpy changes at constant pressure:

$$(\frac{dq}{dt})_p = \frac{dH}{dt} = Q \qquad \text{(Equation 3.6)}$$

The heat flow difference (ΔQ) between the sample and the reference measured by thermocouple is given as:

$$\Delta Q = \Delta\frac{dH}{dt} = (\frac{dH}{dt})_{sample} - (\frac{dH}{dt})_{reference} \qquad \text{(Equation 3.7)}$$

For example, in an exothermic process heat is released and ΔQ is negative. For an endothermic process, the sample absorbs energy during heating, hence more heat flow goes to the sample than to the reference and ΔQ becomes positive. Equation 3.8 can be used to describe the heat flow signal in DSC experiments [161]:

$$\frac{dH}{dt} = C_p \frac{dT}{dt} + f(T,t) \qquad \text{(Equation 3.8)}$$

Where C_p is the heat capacity, $^{dT}/_{dt}$ is the heating rate, $f(T,t)$ is the heat flow due to kinetic processes, T and t are the temperature and the time respectively. The DSC technique is typically used to characterise the thermoplastic properties of polymers including the glass transition temperature (T_g), the melting temperature (T_m) and the crystallization peak (T_c) as shown in Figure 3.6. The glass transition (T_g), plays a crucial role in defining the physical properties of polymers. It is a second-order transition and no enthalpy is therefore associated with such a transition. Below the T_g temperature, amorphous polymers are in a glassy state, they are hard and rigid, and the polymer chain movement is dramatically reduced. Above the T_g temperature, the polymer behaves as if it is liquid or in a rubbery state. Polymers have higher heat capacity above T_g and they

can absorb more heat, therefore and the T_g is in an endothermic process as shown in Figure 3.6. In polycrystalline samples, the crystallization temperature T_c is a temperature above the T_g (second peak in Figure 3.6.) in which the molecules can arrange themselves into a crystalline form if they gain enough mobility. It is an exothermic process because they release heat during this transition. Instead, the melting point (T_m) is the highest temperature peak in Figure 3.6. and at this temperature, the ordered polymer regions break up and become disordered. In this case when the polymer crystals melt they absorb heat and indeed is an endothermic process [162].

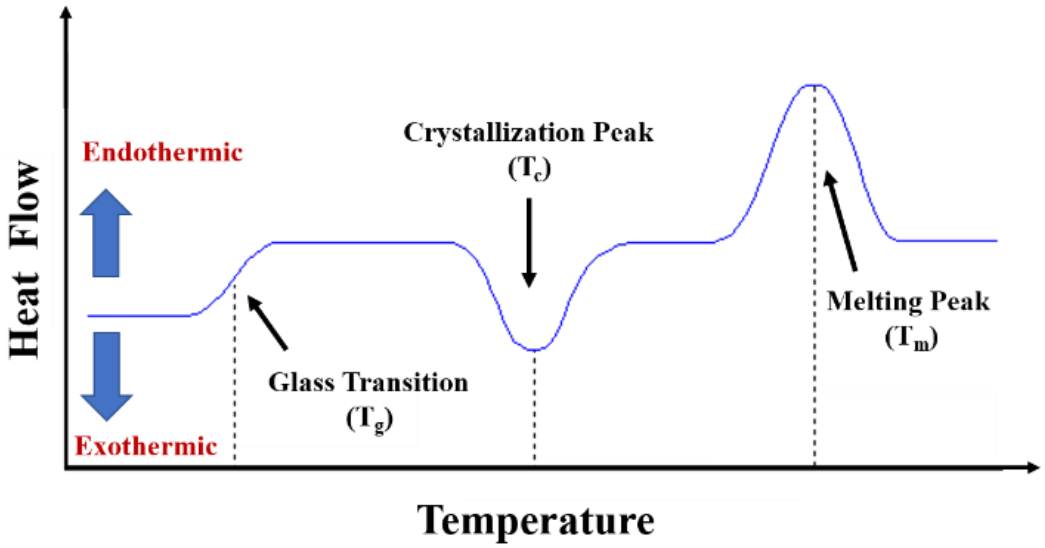

Figure 3.6. A typical DSC curve for a semi-crystalline polymer.

Thermogravimetric Analysis (TGA)

This simple technique can be used for several materials including plastics, polymers, composites, etc. to determine degradation temperatures, composition of multi-component systems, the residue level of a solvent, the moisture content and also the amount of the filler in a composite material. It measures the change in weight of a material as a function of increasing temperature, or isothermally as a function of time. The measurement can be performed in air, oxygen or in an inert atmosphere such as Argon, Nitrogen, Helium, or in vacuum.

3.1.4 X-Ray diffraction and X-Ray photoelectron spectroscopy (XRD, XPS)

X-Ray Diffraction (XRD)

It is one of the most important non-destructive techniques that provides detailed information about the crystallographic structure, chemical composition, and physical properties of materials. Diffraction is a physical phenomenon that occurs when electromagnetic radiation interacts with a comparable sized object to its wavelength. As the X-ray wavelength is comparable to the dimension of chemical bonds or interatomic distances in crystals, their diffraction is an ideal method to probe the atomic/molecular structure of a range of chemical systems. These X-rays are generated by a cathode ray tube, filtered to produce close-to monochromatic radiation directed toward the sample. The interaction of the incident rays with the sample produces constructive interference (and a diffracted ray) when conditions satisfy Bragg's Law (Equation 3.9) and a schematic representation is shown in Figure 3.7.

$$n\lambda = 2d \sin\theta \qquad \text{(Equation 3.9)}$$

where n is a positive integer, called the order of reflection, λ is the wavelength of the incident wave, d is the spacing between the crystal planes of a given specimen and θ is the angle between the incident beam and the normal to the reflecting lattice plane. By measuring the angles, θ, under which the constructively interfering rays leave the crystal, the interplanar spacings, d, of every single crystallographic phase can be determined [163].

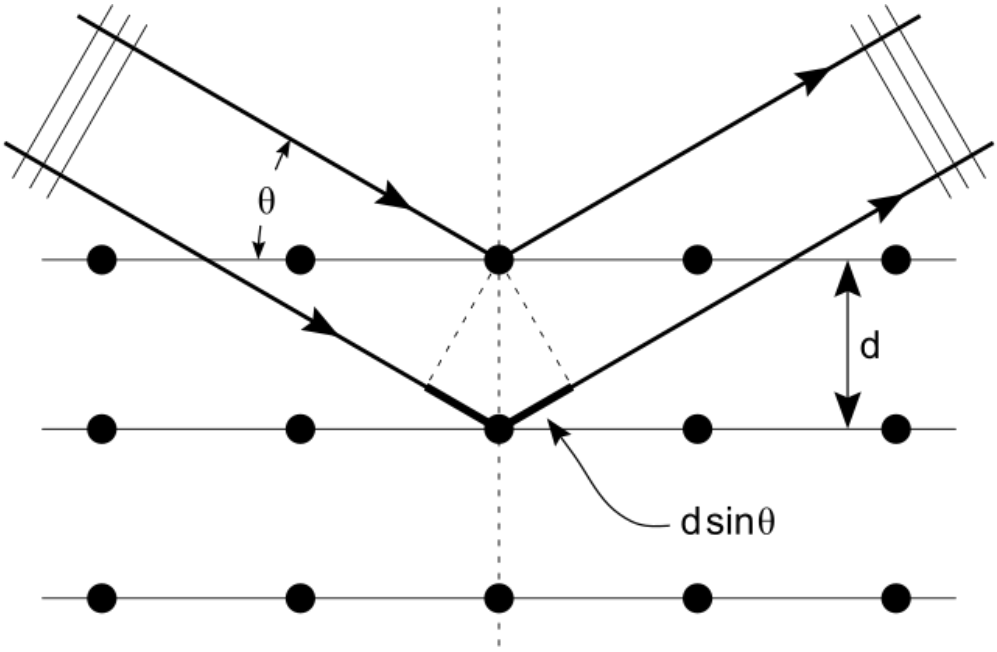

Figure 3.7. Schematic representation of Bragg's Law [164].

In order to identify an unknown substance and the content of such sample, the powder diffraction pattern is recorded with the help of a diffractometer and then compared with the patterns simulated by the Rietveld method [165].

X-Ray Photoelectron Spectroscopy (XPS)

This is a surface-sensitive quantitative spectroscopic technique that measures the elemental composition of a material. Put more simply, XPS is a useful measurement technique because it not only shows what elements are within a film but also what other elements they are bound to and it allows to find the ratio of the elements based on modifications to electron binding energies. By irradiating a specimen with a ray beam an XPS spectrum can be obtained. This technique is based on the photoelectric effect whereby the ionization energy of an electron from a sample after an X-Ray photon is absorbed can be directly related to the electrons initial state binding energy in the atom effectively supplying a chemical fingerprint. This technique requires high vacuum (10^{-8} mbar) conditions. XPS is also known as ESCA (Electron Spectroscopy for Chemical Analysis), to emphasize the chemical information that the technique provides. It can detect all elements with an atomic number (Z) of 3 (lithium) and above, therefore it can

not easily detect hydrogen (Z = 1) or helium (Z = 2). The ability to produce chemical state information makes XPS a unique and valued tool for understanding the chemistry of any surface. Subtle variations in the binding energies can be used to identify the chemical state of the materials being analysed [166]. In particular, it is extremely useful to identify the hybridization (or changes to) of carbon-containing species such as GO or pristine graphene.

3.1.5. Dynamic light scattering, DLS

Dynamic light scattering DLS also known as Photon correlation spectroscopy or Quasi-elastic light scattering is used to determine the size distribution profile of small particles (< 10 nm) in a polymer solution. The specimen is illuminated by a laser beam and the fluctuations of the scattered light are detected at a known scattering angle θ by a fast photon detector [167]. Autocorrelation analysis of the time-varying detector signal allow an estimate of the diffusion time of particles through the laser beam, and therefore models such as the Einstein equation can be used to estimate particle diameter from their measured diffusion coefficient [168].

3.1.6. Evaluation of mechanical properties

There are several techniques that can be used to study the mechanical behaviour of polymers and composites. Most of the tests are performed under controlled conditions because the mechanical properties can be affected by temperature and environmental changes. Mechanical testing includes: static testing (strength, stiffness, toughness, tensile, compressive and shear properties, etc) creep and stress, relaxation tests (creep and viscoelastic properties, time-dependent elongation behaviour, time-dependent stress) and dynamic mechanical analysis (temperature and frequency-dependent modulus and stiffness determination, thermal transition). This section includes the techniques that I have been using in this work: tensile testing and adhesion.

Tensile test

This test consists of applying a load at a constant rate along the longitudinal axis of a sample that is clamped in a loading frame, and the elongation is measured. The sample response is sensitive to its dimension, therefore it is important to normalise the force applied and also the elongation, by dividing the force by the area and Δl by the original length which gives stress (σ) and strain (ε) respectively [169]:

$$\sigma = \frac{F}{A} \qquad \text{(Equation 3.10)}$$

$$\varepsilon = \frac{l - l_0}{l_0} = \frac{\Delta l}{l_0} \qquad \text{(Equation 3.11)}$$

where F is the applied force, A is the original cross-sectional area, l_0 is the original length before a load is applied and Δl is the change in length compared to the original length. Good mechanical performance for a polymer is required for possible industrial and structural applications, indeed the characterisation of stress-strain curves of solid polymers is crucial. The mechanical properties depend on the strain (rate) and the temperature. At low strain, most polymeric materials exhibit an elastic response on applied load and the deformation is completely recovered when the load is removed. In this regime, the stress is directly proportional to the elastic strain through Hooke's law relationship [170] [171].

$$\sigma = E\varepsilon \qquad \text{(Equation 3.12)}$$

where E is the modulus of elasticity, also known as Young's Modulus. The maximum stress up to which the stress and strain remain proportional is called the proportional limit. If the material is loaded beyond its elastic limit, it does not return to its original shape and size and a permanent deformation occurs. This point is called the yield point, and a further increase in strain occurs without an increase in stress [172]. Figure 3.8. shows typical

stress-strain curves for various types of polymers. Brittle materials show very little or no yield point and brittle failure behaviour. Ductile polymers show characteristic yield stress, followed by yielding deforming associated with necking and ductile failure in this case the polymer chains become oriented under conformational changes.

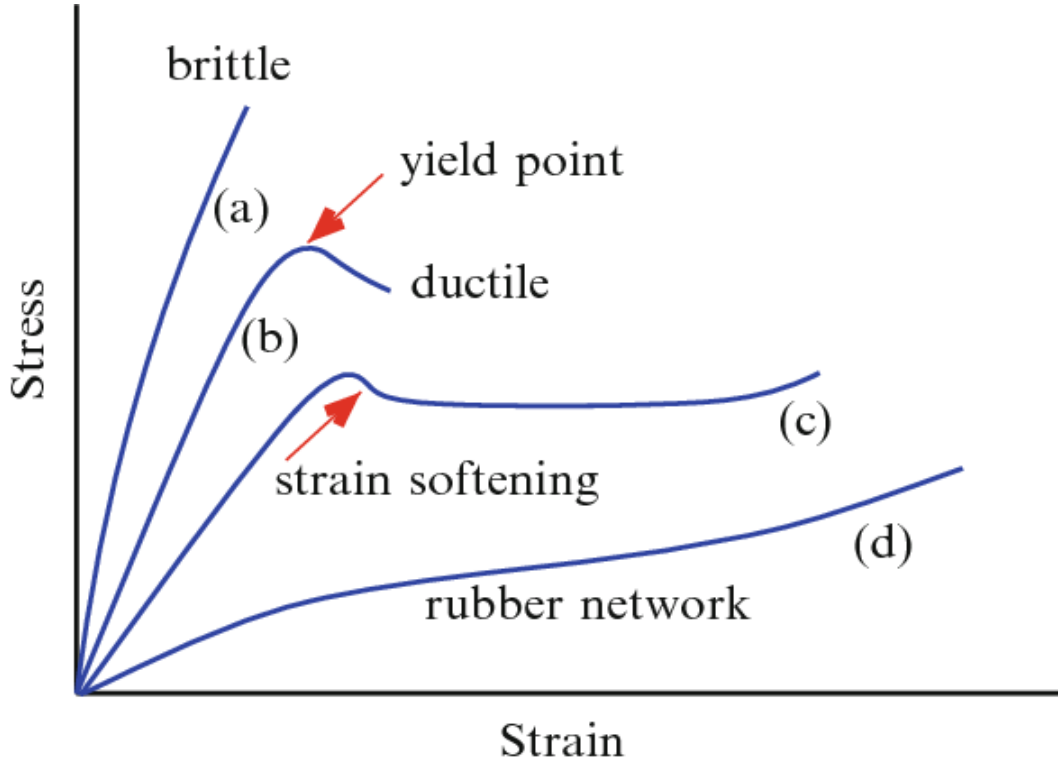

Figure 3.8. Typical stress–strain curves of polymers tested at different temperatures: curves (a), (c) represent glassy polymers. The curve (d) corresponds to the rubber state. Ends of the curves indicate the points of material failure: (a) brittle and (b),(d) ductile [173].

However, if the neck stabilizes, no further reduction in the cross-section area takes place, followed by strain-hardening. The chains that are not perfectly oriented become more aligned due to the elastic behaviour and the stress will increase until the rupture. In the rubber-like state, the polymer can experience large and reversible elastic deformation. This kind of materials do not show any yield point but there is a presence of a close to constant load regime followed by the strain hardening region. The plateau region is a consequence of the molecular chains that start to align or orientate in a manner coincident with the applied stretch state, and due to the release of energy as heat while straining the material. For rubber like materials, there exists a material model called the neo-Hookean

model that is an extension of Hooke's law that differs from the linear elastic material for moderate strains [174]. It allows us to predict strain-softening and strain hardening that occurs in the material during the deformation by:

$$\sigma = G(\lambda - \lambda^{-2}) \qquad \text{(Equation 3.13)}$$

where σ is the nominal stress, λ is the extension ratio defined as new length divided by the original length ($^{l}/_{l_0}$) and is the modulus $G = nkT$. G is directly proportional to the number of polymer chains per unit volume (n) at a given temperature (T- Kelvin), where k equals Boltzmann's constant.

Adhesion test

Self-adhesive materials and products, called pressure sensitive-adhesives (PSAs) are becoming popular for industrial applications and they do not require great mechanical strength [175]. These types of materials are characterised by instantaneous adhesion upon application of light pressure. The most common products that use PSAs are tapes, labels and protective films [176]. The test consists of having a stainless steel spherical probe connected to a force transducer, where the transducer measures the force acting on the probe. The probe is moved up and down and its displacement is measured through the motor rotation. The specimen is bonded to the test platform using double-sided tape. During the test, the displacement and the load on the probe are recorded by a computer. This measurement involves two processes: bonding and debonding as shown in Figure 3.9. A.B. During the bonding process, the probe moves down and compresses the specimen to a pre-determined force (compression force). In response, the specimen deforms and wets the probe surface. During the debonding process, the probe ascends and separates from the adhesive surface at a pre-determined test speed, then the specimen is elongated and exerts a tensile force on the transducer as the probe moves up. At this point, the adhesive begins to separate from the probe surface and the debonding strength of the adhesive is measured.

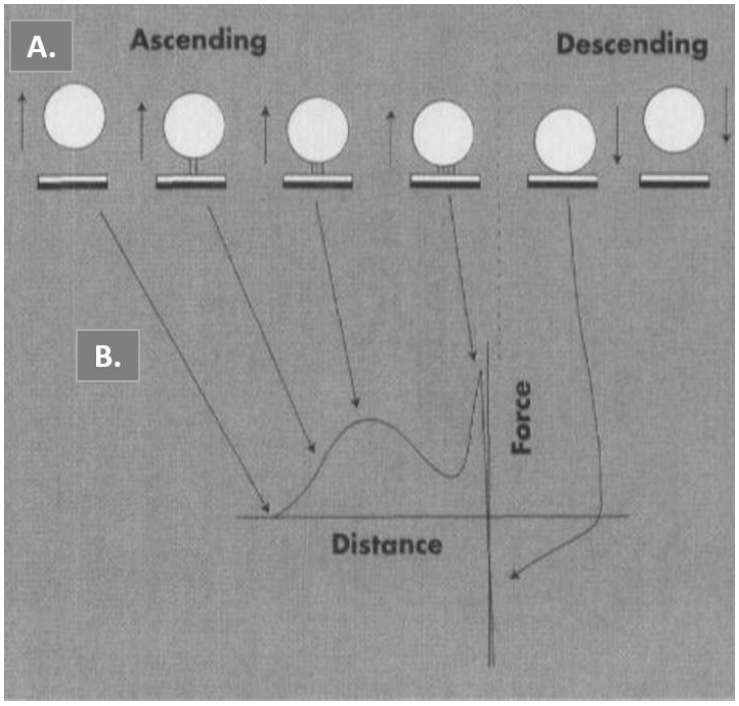

Figure 3.9. A. B. Illustration of the force vs distance profile and the corresponding bonding and debonding processes [177].

Figure 3.10 A. shows the typical avery adhesive test (AAT) profiles for PSA samples. The first peak is called the initial peak and its height is related to the tack performance of the adhesive sample. When the sample is stretched the probe starts to ascend and a tensional force is exerted on the probe by the specimen. The force increases with the probe displacement following Hooke's law (Equation 3.12) to a yield point where the sample starts to partially detach from the probe surface and forms adhesive filaments. For example, for soft adhesive materials, the bonding is very quick, and less strength against the debonding, whereas for the hard one, while the bonding is poor they have good strength against the tension. In both cases, the corresponding peak will be low. In order to have a higher peak, the specimen needs to have viscoelastic properties, with low bonding rate and high debonding rate.

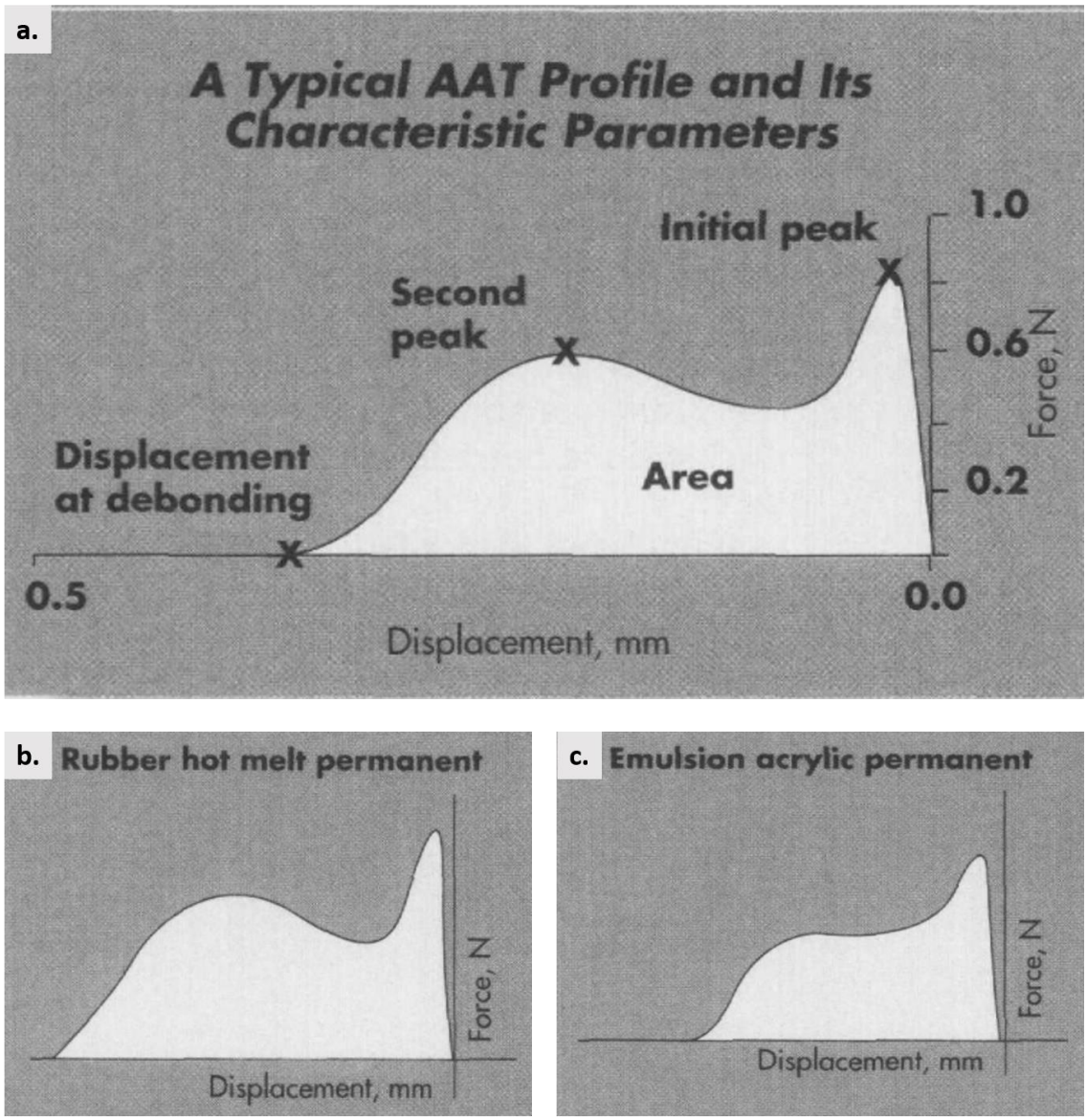

Figure 3.10. A. Typical AAT profiles for PSAs. B. Profile of the rubber hot melt permanent PSAs. C. Profile of the emulsion acrylic permanent PSAs [177].

After the yielding point, the force starts to decline, and the adhesive filaments are stretched at the molecular level, and they continue to elongate. At this point if the adhesive is stretched beyond this point, more resistance will be encountered, and the second peak will be generated (Figure 3.10 B. rubber-based permanent PSAs). Instead, if the bonding strength between the adhesive and probe is weaker than the force needed to straighten the polymers chains the filaments will detach from the probe surface before the second peak evolves (Figure 3.10.C. emulsion-permanent PSAs). The height of the second peak is proportional to the degree of crosslinking. The last part of the profile is

the displacement that measures the distance that the adhesive can elongate before it detaches from the probe. The area under the profile represents the energy required to separate the adhesive from the probe, indeed large area means more work needed to separate the probe from the sample [177].

3.2. Experimental section

3.2.1 Materials

Polymer Latex

Latex is an example of colloidal dispersion in a liquid matrix, prepared by a reaction called emulsion polymerisation. Latex particles may be synthesised from a range of monomers but the typical ones are acrylates (MMA, BA, ethylhexyl acrylate), styrene, vinyl acetate and butadiene and associated copolymer monomers. The molar ratio of the monomers in the copolymers determines its glass transition temperature (T_g), the point at which the solid polymer changes into a liquid-like polymer because long range motion of the molecule's backbone is enabled [178]. Latex films are used for a wide range of applications including coatings, paints, inks, PSAs, drug delivery systems and thin films. The easiest way of film forming used in industry is the drop-casting of the latex aqueous dispersion onto a substrate. Particle assembly, due to the attractive capillary forces and convective particle flux is facilitated by the controlled evaporation of water [179]. This is followed by particle deformation and inter-diffusion leading to transparent thin films. Jiang *et al.* [180] have used spin-coating as a means to apply uniform thin films onto a substrate. The colloidal dispersion, in this case, is spread on the substrate by centrifugal forces while the latter rotates at high speed. This method can be used to produce antireflective coatings. The process, from a stable dispersion of colloidal polymer particles into a continuous film, is called latex film formation, and it involves several steps from a dilute to a concentrated dispersion, into a packed array of particles to a continuous polymer film [181] as shown in Figure 3.11. In the first stage, that corresponds to the wet initial stage, as a result of surface tension (water-air interfacial tension) and capillary forces [182], the distance between the particles is reduced and the concentration increases until a dense packing of spheres is achieved. In the second stage, the particles start deforming and this part is essential for the film formation. The latex has to dry above the minimum film formation temperature (MFFT), in order to obtain a uniform void free film. After that, the spherical particles deform into rhombic dodecahedra structures, due to the reduction of the interfacial energy and capillary forces. However, if the latex dries below the MFFT, polymer particles do not deform, and the interstices are filled with air resulting in non-transparent powdery film. In the last stage, called coalescence, the inter-

diffusion of polymers across particle-particle boundaries occurs producing a homogeneous transparent film [183].

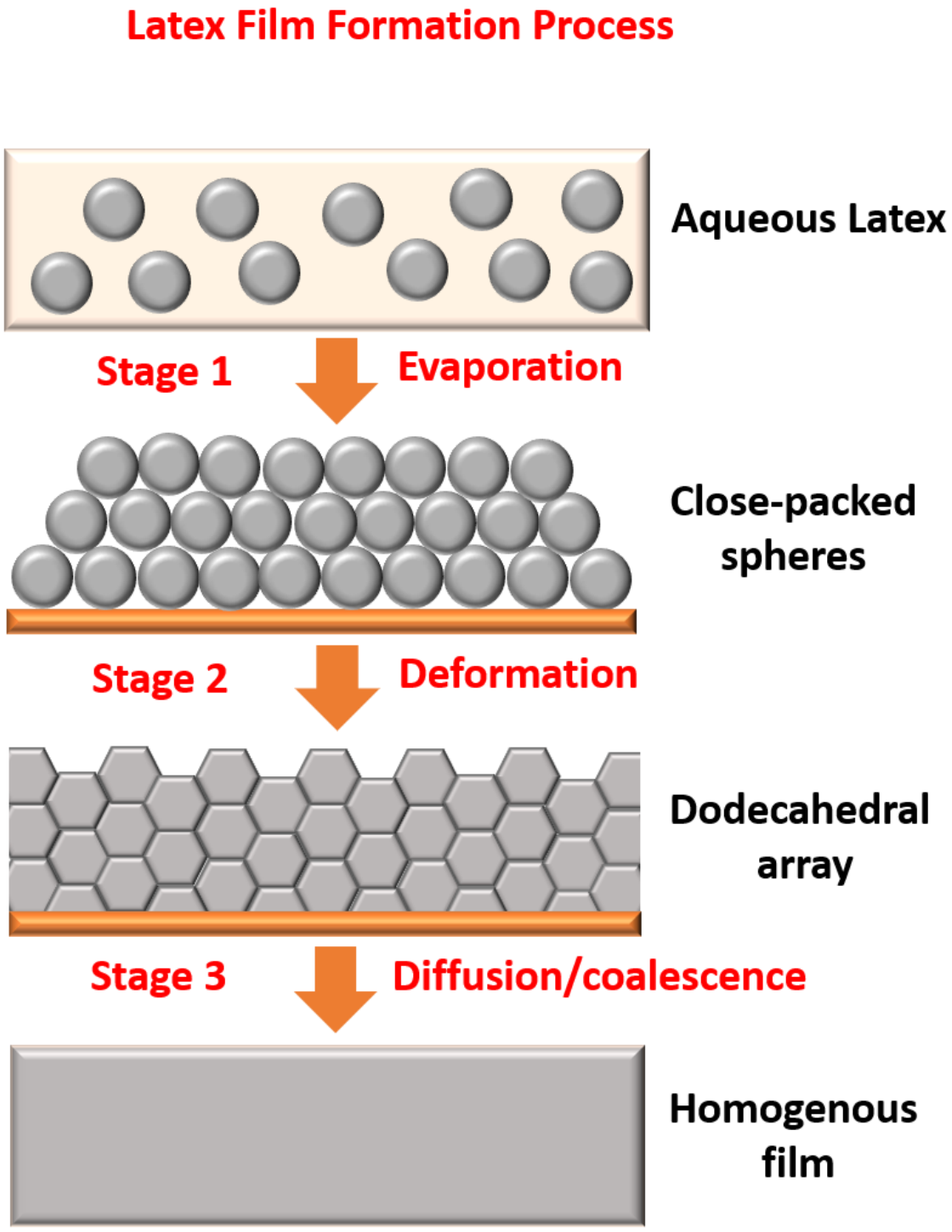

Figure 3.11 Stages of the latex film formation process: Stage 1: concentration of the colloidal suspensions and the formation of a closed packed array of spherical particles, Stage 2: dense packing and deformation of the particles forming a honeycomb-like structure, Stage 3: polymer inter-diffusion between adjacent particles and formation of the film.

Three different polymer latex samples, prepared by emulsion polymerization, and a Natural Latex rubber sample were used in this work and are summarised in Table 3.1 given below.

Table 3.1 The range and type of latex materials used in this work and their morphological parameters.

	Composition	**Solids Content* /wt. %**	**Particles size** /nm**	**T_g *** /°C**
Latex 1	BA: MMA: MAA	24,82	270	39.24
Latex 2	MMA:BA: AA	54	172, 80	19.53
Latex 3	BA: MMA: MAA	30	253, 50	40.9
Latex 4	Natural Latex Rubber	60	400, 60	-70¤

*The solids content (SC) determined by wet and dry weighting of approximately of 2g of latex dispersion placed onto a petri dish and dried at 45°C for 24h. The values reported are the average of 10 measurements.

** Latex sphere sizes (measured by AFM and dynamic light scattering technique).

***T_g experimentally measured by DSC.

¤ T_g taken by [184].

Two monodispersed, polymer latex samples (called here “Latex 1” and “Latex 2”) prepared by emulsion polymerisation provided by DSM NeoResins (Waalwijk, The Netherlands) and Cytec Surface Specialties, respectively, were used and are summarised in Table 3.1. The components used in forming the high-T_g latex (latex 1) include: random copolymer of BA, MMA and MAA. MMA is used to enhance colloidal stability and the properties of the resulting films. Latex 2 includes a random copolymer of MMA, BA, and AA: in a molar ratio of MMA:BA: AA of 49:49:2. Latex 3 was formed by combining two types of latex that had the same composition but different particle sizes 253 and 50 nm. The two latexes were combined in different concentrations, from 0.01 to 0.5 weight fraction, of the small latex particles in to the big. Films were then cast and dried in the

oven at 45 degrees for 5 hours. 45 degrees was used as this is above the glass transition temperature and so a continuous film is formed, but it is not so hot as to have completely broken down the particle barriers. Latex 4 is the pre-vulcanized NLR purchased from Liquid Latex Direct with a solid fraction of 60 wt.%. It mainly consists of a high molecular weight polyisoprene (2-methyl 1,3-butadiene)[84]. The NLR was pre-compounded with crosslinking agents such as sulphurs, in this way it is possible to have an enhancement of the elasticity of the NLR by creating sulphur bonds between the polymer chains upon curing at 130°C.

GO Preparation

In 1958 Hummers and Offeman [26] developed an oxidation method as a safer, faster and more efficient method of producing graphite oxide. The method is really easy to perform, and it consists of using a mixture of $KMnO_4$ and H_2SO_4, and $NaNO_3$ reacting with graphite. The schematic representation of the modified Hummers method is shown in Figure 3.12. For the preparation of the GO polymer composites, I have used the GO made by modified Hummers method as reported elsewhere [185][186]. In detail, 5 g of graphite flakes were put into a mixture of 170 mL H_2SO_4 and 3.75 g $NaNO_3$ and the mixture was cooled in an ice bath and stirred for 30 minutes. Thereafter, 25 g of $KMnO_4$ were slowly added and stirred for another 30 minutes. Then, the ice bath was removed, and the mixture was warmed up to 35-40 ºC and stirred for 2 h. The reaction was terminated by adding slowly 250 mL of distilled water and then 20 mL H_2O_2 (30 %) solution. The mixture was stirred for 2h, 4h or overnight depending on the oxidation degree, filtered and the obtained powders were repetitively washed with 400 mL of HCl: H_2O (1:10 v/v) to remove metal ions followed by distilled water to remove the acid. In the end, the graphite oxide obtained was dried at room temperature.

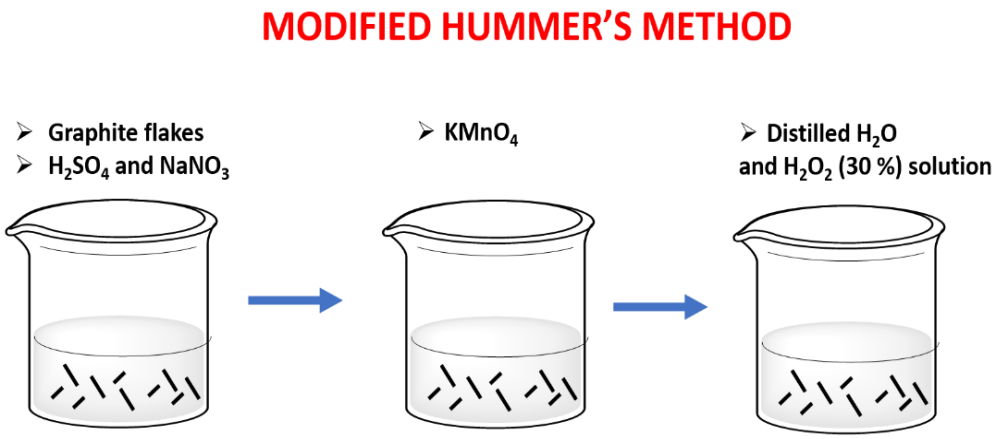

Figure 3.12 Schematic representation of the modified Hummer's method.

GO Preparation

GO was obtained by bath sonication of an aqueous graphite oxide dispersion (2 mg/mL) for 2 hours, followed by centrifugation at 4500 rpm for 60 minutes, obtaining a brown-coloured dispersion of exfoliated GO with a final concentration of 1 mg/mL. The GO solution was then diluted in DI water to achieve 0.5 mg/mL of GO concentration. In order to investigate the differences of the interactions, dependent upon the size of the sheets as well as the density and type of functional groups present I have characterised the particle size distribution using AFM as shown in Chapter 4 in Figure 4.7 c.f.i., and the content and type of oxygen functionality using XPS.

Liquid exfoliated Graphene

Dispersions of liquid-exfoliated graphene in water-surfactant have been supplied by Advanced Material Development Ltd. The concentration of graphene was 0.3 mg/mL, stabilised with Triton X-100.

As-produced Graphene

Elicarb Premium grade graphene powders were purchased from Thomas Swan, which have been produced using a top-down graphite exfoliation approach. The particle sizes are between 0.5 μm and 1.0 μm.

Fabrication of composite dispersions

Different aqueous, composite dispersions, containing various weight fractions of GO and Graphene were prepared and studied in this thesis. These were prepared by mixing the respective nanoparticle dispersions with polymer latex dispersions, followed by low energy homogenisation to ensure good mixing. Their composition is given in Table 3.2 below.

Latex 1,2-GO composites

Depending on the desired GO concentration in the final composite mixture (ranging from 0 wt. % to 2 wt. %) latex dispersion was combined with aqueous GO dispersion. All the samples were then sonicated in the water bath for 10 min to ensure good mixing. Calculation of the amount of GO in weight percent was based on the assumption that GO is in solution and on the basis of the weight of the latex solids content.

Latex 3-graphene composites

Exfoliated graphene dispersion in water and Triton-X-100 was added to different latex mixtures, then bath sonicated for 10 min to guarantee a good mixing. Then, the samples were deposited onto a substrate and then characterised.

Latex 4-GO and graphene composites

GO dispersion was mixed with the latex dispersion by simple magnetic stirring and then diluted to reduce their viscosity. The samples were prepared using a coagulation dipping method to obtain thin films.

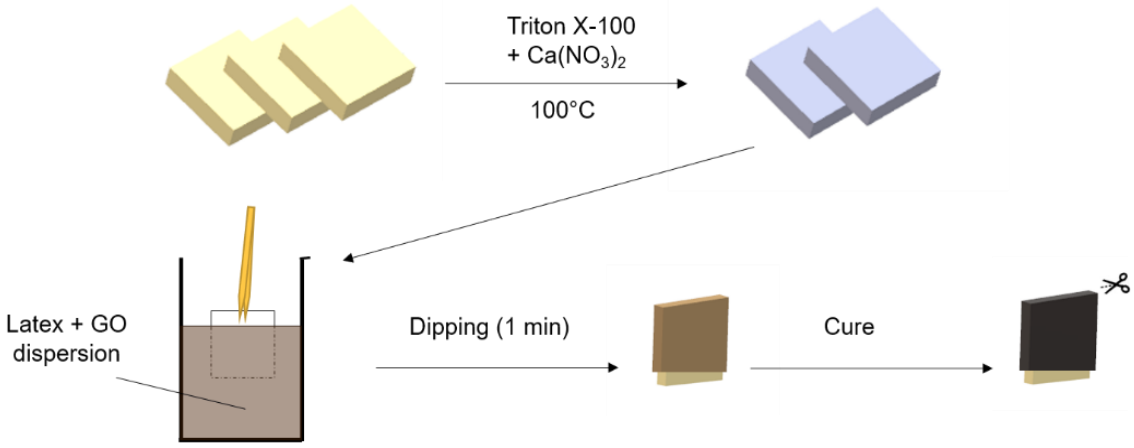

Figure 3.13 Schematic representing the preparation of the NLR-GO based composites.

The support used to create a thin film is a square domino of 2 cm. The square domino was immersed in a solution of Triton X-100 (0.1 mg / mL) and then in a solution of $Na(NO_3)_2$ (30% m). Triton X-100 serves to obtain a homogeneous dispersion of the salt ($Na(NO_3)_2$) on the surface of the domino. After that, the domino is immersed into the NLR-GO dispersion for 1 min and then finally cured in the oven at 100 °C. (Figure 3.13).

Table 3.2 Composition of composites studied in this thesis.

	Composition	**GO/Gr or CNTs / wt. %**
Comp.1	Latex 1: GO	From 0 to 2wt.%
Comp.2	Latex 2: GO	From 0 to 2wt.%
Comp.3	Latex 3: graphene- Triton-X-100	From 0 to 1 wt%
Comp.4	Latex 4-GO	From 0 to 0.6 wt%
Comp.5	Latex 4-graphene	From 0 to 5 wt%

Reduction of latex-GO based composites

The reduction in situ of GO has been done in order to obtain conductive composites and study the electrical properties of the Comp. 1,2,4. The reduction of Comp. 1,2 have been done using different temperatures starting from 40 °C to 200 ° C, changing the reduction time as shown in Table. 3.3. while the reduction of Comp.4 has been done at 130 °C for 30 min.

Table 3.3 The range of different temperatures and times used to do the reduction in situ of GO in the latex 1,2-GO based composites.

Temperature / °C	Time / h
40	456
60	240
80	72
120	35
135	20
150	5
180	0.25
200	0.0833

3.2.2 Experimental Procedures

In this section are described the experimental procedures for each technique that has been used in this thesis. TEM analysis of latex-GO dispersion has been done by a collaborator at the Institute of Nanoscience of Aragon (INA) in Zaragoza (Spain). SEM analysis of composite materials has been performed at the University of Brighton. TGA, DSC, XRD and XPS analysis have been done at the Instituto de Carboquímica (ICB) in Zaragoza (Spain). AFM measurements and Raman mapping of the liquid exfoliated graphene have been done by some colleagues at the University of Sussex. Raman and

FTIR analysis, DLS, conductivity, adhesion, stress-strain and permeation measurements have been done by myself.

Imaging conditions and sample preparation for AFM-based studies

For topological studies, a Bruker Dimension ® Icon AFM positioned in an isolated box over an anti-vibration stage to minimise environmental noise and building vibrations was employed. Bruker Scan Assist-Air AFM probes silicon tip on silicon nitride lever have an average spring constant of 0.4 N/m and a tip radius of 2 nm (resonance frequency of 70 kHz). Scan Assist-Air AFM probes were used to acquire surface topographic images. The latex dispersion and the composites dispersions were drop casted onto a glass slide and depending on the type of the latex investigated, the solution was left to dry for 24 h at room temperature (for latex with T_g around room temperature) or dried in the oven for few hours at 45 °C for the latex with higher T_g values. The dry samples were then placed on the AFM stage. KPFM measurements were performed with the same Dimension Icon system, using a PFQNE-AL tip with spring constant calibrated with standard contact calibration on silica at around 0.6 N/m. These tips are pure silicon super sharp tips with tip radius around 5 nm and proprietary reflecting coating on the backside. The samples were studied using KPFM. The magnitude of the CPD is governed by the properties of both the tip and the sample surface. When the AFM probe is brought into close proximity to the sample surface, upon electrical connection, the Fermi levels align. Both the probe and the surface of material are now charged (by the formation of an electric double layer). Due to the charging of the probe and the sample surface, an electrostatic force develops due to the V_{CPD}. This force can then be nullified by applying an external bias (V_{DC}) between the probe and the sample. The CPD measurement was obtained during the interleave passage following the previously measured line topography at a set distance of 80 nm in air. The latex dispersion was drop casted onto a glass slide and it was left drying for 24 h at room temperature. Subsequently, the GO dispersion was spin-coated onto the latex substrate followed by the reduction step using 150°C for 5h. The samples were then placed on the AFM stage for KPFM measurement.

SEM analysis

Microstructural investigations of composite materials were made using a Zeiss SIGMA field emission gun scanning electron microscope (FEG-SEM) at an accelerating voltage of 1-1.5 kV with a working distance of 2.1 mm. Samples were imaged in high vacuum conditions and a secondary electron detector was used for image acquisition. Owing to the relatively high electrical conductivity of the samples, they were imaged without sputtering metal onto their surface. Energy-dispersive X-ray spectroscopy (EDS) analysis were performed using an accelerating voltage of 5 kV in a working distance of 8.4 mm.

TGA studies

TGA experiments were performed under N_2 atmosphere (60 mL/min flow) and registered with a SETARAM 'Setsys Evolution 16/18' device at a heating rate of 10 °C/min, in the range from room temperature to 800 °C on samples of average mass around 10 mg.

DSC analysis

Measurements were made in a Mettler DSC-823e instrument, calibrated using an indium standard (heat flow calibration) and an indium-zinc standard (temperature calibration). The experiments were performed on samples of about 4-5 mg, exactly weighed, placed into standard 40 μL Aluminium crucibles, under a 100 mL/min flow of N_2. A first heating isotherm (50 °C for 5 min and cooling down to room temperature at -10 °C/min) was applied in order to erase the thermal history of the polymer matrix. Then, a heating program was performed from room temperature to 250 °C (at 10 °C/min) and back down to room temperature (at -10 °C/min). This program was executed for up to three consecutive cycles.

X-ray analysis

X-ray photoelectron spectroscopy (XRD) of the powder materials was performed in an ESCAPlus Omicron spectrometer provided with an Mg anode (1253.6 eV) working at 225 W (15 mA, 15 kV) and the peaks were calibrated with C1s peak (284.5 eV).

XPS analysis

XPS analysis were performed in an ESCAPlus Omicron device, provided with an aluminium anode (1486.7 eV) and 225W power (15 mA, 15 kV). Survey spectra (not shown) were acquired with 0.5 eV step scanning, 0.2 s dwell time and 50 eV pass energy, while high resolution C1s orbitals were recorded at 0.1 eV steps, 0.5 s dwell time and 20 eV pass energy. The sample analysis area was 1.75 x 2.75 mm. All spectra were treated with CasaXPS software. In all cases, Shirley-type backgrounds were applied, and all deconvoluted components were Gaussian/Lorentzian mixed shape (with 70% Lorentzian character), except for C=C sp^2 components, which were treated with an asymmetry function typical of graphitic structures [187].

Raman analysis

The Raman measurements were carried out with a Renishaw inVia confocal Raman microscope with a 660 nm solid-state laser (model: RL660C100) and ×100 objective lens. Variation in the laser power was achieved with a series of neutral density (ND) filters. The Raman spectrum for the three types of GO is shown in Chapter 4 in Figure 4.8 and has been obtained using a 660 nm laser at 0.5 % of power, exposure time 10 seconds and 5 accumulations. The fluorescence background for each GO spectra was subtracted using the Wire 2.0 Renishaw software. Raman spectra of the commercial GO was obtained using 532 nm laser with x100 objective, 10% of intensity for 10 seconds and 2 accumulations and is shown in Chapter 4 in Figure 4.5 A. Raman mapping of the liquid exfoliated graphene was performed using 405 nm laser with a 100x objective lens. A xyz scanning stage was used to move the sample with a step size of 250 nm and a Raman spectrum was recorded at every point with an exposure of 10 seconds. The images obtained are 81x81 pixels and 20x20 μm.

TEM analysis

The Latex-GO dispersion was deposited onto the substrate-mounted holey carbon TEM grid followed by a room temperature drying process to evaporate the aqueous solvent.

TEM images were acquired in a JEOL microscope model 2000 FXII at an acceleration potential of 200 kV.

FTIR analysis

The FT-IR measurements were performed using PerkinElmer Spotlight 400 FT-IR Microscope System. The system uses a dual-mode single point and MCT array (mercury cadmium telluride) detector standard with InGaAs array option for optimised NIR imaging. All the measurements were done using the mid-IR (4000-500 cm^{-1}). For the free-standing specimens, all the measurements have been done using the ATR mode in reflectance (from 3500- 700 cm^{-1}).

Conductivity measurement

The measurements were performed in two ways: a) using a multimeter and b) using a two point probe system (Keithley 2614B) and the IV characteristics were measured through the gold electrodes or gold wires for the free-standing sample. The final specific conductivity was calculated from the resistance and thickness of the film. The polymer films were prepared by casting the composite dispersion onto the gold electrodes or casting in the free-standing mould adding gold wires. In both cases, the sample was then dried for 24 h at room temperature.

Stress-strain measurements

Tensile stress-strain tests were carried out on the rectangular-shaped GO-polymer latex composite samples using a TA.XTplus Texture Analyser in combination with analysis software from Exponent. In preparation for each stress-strain measurement, the sample being tested was placed into the clamps of the texture analyser using abrasive sand paper grips to avoid slippage. Next, the sample was pulled taut using the automated controls built into the device. Once the samples were sufficiently taut and secured in place, the dimensions of the cross section, the length before deformation were measured using a digital calliper of precision 0.01mm. The test was then launched using the control software, with an acceleration of 2 mm/sec.

Adhesion measurements

The measurements have been done by placing the specimen on the Texture Analyser's platform using a flat circle metal probe with 12.57 mm^2 surface area. The force applied was changed from 0.5 to 4 N. For each sample, the measurement was repeated 15 times. Test speed and time was fixed constant at 0.1mm/s and 10 s.

Permeation test

The measurement was performed cutting a square (2cm x 2cm) of the glove made by NLR itself and with NLR-graphene based composite with 4 wt.% of graphene content. Subsequently, the sample was put in contact with different solvent to see if the inclusion of graphene modifies the permeability of the NLR glove. The weight (g) was measured every 30 min.

3.4. Summary

This chapter introduced the experimental techniques used in this work for the characterisation of the nanomaterials and the composites. In the first section the operation of the techniques used were described. There were reported the two basic types of electron microscopes, such as SEM and TEM. AFM was also explained in detail because it gives information about the topography of the specimen surface in detail down to the nanometre scale. After that, a section focused on the interaction between matter and low energy radiation identified as optical spectroscopy was also described. It covers Raman, FTIR and UV-Vis spectroscopy. Furthermore, thermo-analytical techniques were presented such as DSC and TGA. They were used to determine the physical and chemical properties of a substance as a function of the temperature and time. Then XRD and XPS to get information about the crystallographic structure, chemical and elemental composition of materials. The DLS technique used to determine the size distribution of small particles (< 10 nm) in a solution or dispersion was discussed. A section related to the evaluation of the mechanical properties of polymers and composites was also explained. The mechanical tests include tensile and adhesion test. In the second part of the chapter, a full description of the experimental methodologies, mainly the latex film formation process, GO preparation, and fabrication of the polymer-GO or graphene based composites is also presented. The experimental procedures used for AFM, SEM, TEM, Raman, TGA, DSC, XRD, XPS, FTIR analysis are also included. In the end, there is also a section related to conductivity, adhesion, stress-strain, permeation measurements.

Chapter 4

Developing matrix structures and optimizing fillers

This chapter provides a description of the techniques used to characterise the polymer latex materials and the nanofillers for the fabrication of structured composites. AFM height sensor images of the polymer latex highlight the difference in morphology of the matrices due to their composition, particle size and T_g. Morphology change influences the final properties of the composites when GO or graphene are added into the polymer matrix. In order to understand the possible interfacial interaction between GO or graphene sheets with the polymer spheres, FTIR and Raman spectroscopy are used to characterise their chemical structures. AFM is also used to characterise the lateral size and the thickness of the fillers. In fact, in order to obtain a structured composite it is important to vary the particle size and the concentration of the fillers, as they affect its morphology. The filler has to be small enough to be placed into the interstitial space between the polymer spheres, but also big enough to prevent phase separation due to stratification. The main goal is to reach the best electrical and mechanical properties of the system using the lowest concentration of filler. As a result, efficient and cheap composites can be developed for industrial applications such as sensors, circuit devices, battery, and pressure sensitive adhesives.

4.1. Characterisation of Latex Polymer

Owing to differences in composition, particle size and T_g, latex polymer matrices, characterised in this thesis, exhibit distinctive morphology that can affect the properties of final composites when mixed with GO and Graphene. As said previously in Chapter 3, Latex 1 is formed from a random copolymer of BA, MMA and MAA. Figure 4.1 a.b. shows representative AFM height sensor images on a thick Latex 1 film. A dense monodispersed packing is seen with some visible defects, in the form of misalignment in the colloidal structure and empty lattice sites.

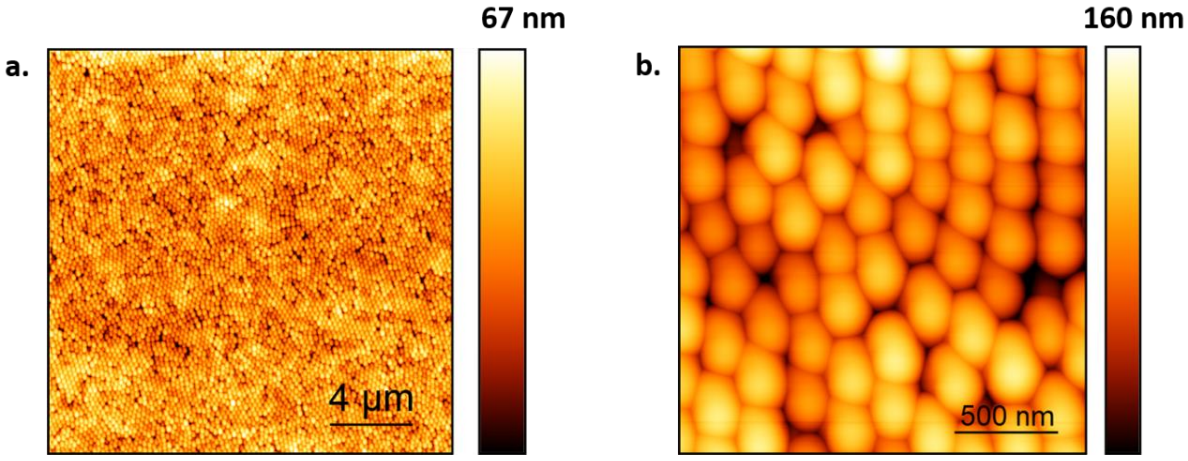

Figure 4.1 a.b. AFM height sensor images of Latex 1, using different scan size. Particle size is 270 nm.

Latex 2 is based on MMA:BA:AA. It exhibits a distribution of small and big particles (diameter of 80 and 172 nm, respectively), as seen in Figure 4.2 A.B. The small particles are filling the interstices of the larger particles. A few regions present ordered packing over short ranges, otherwise, packing is mostly random. The particle size ratio is too large to have good packing between the particles, and this aspect is investigated later in Chapter 7.

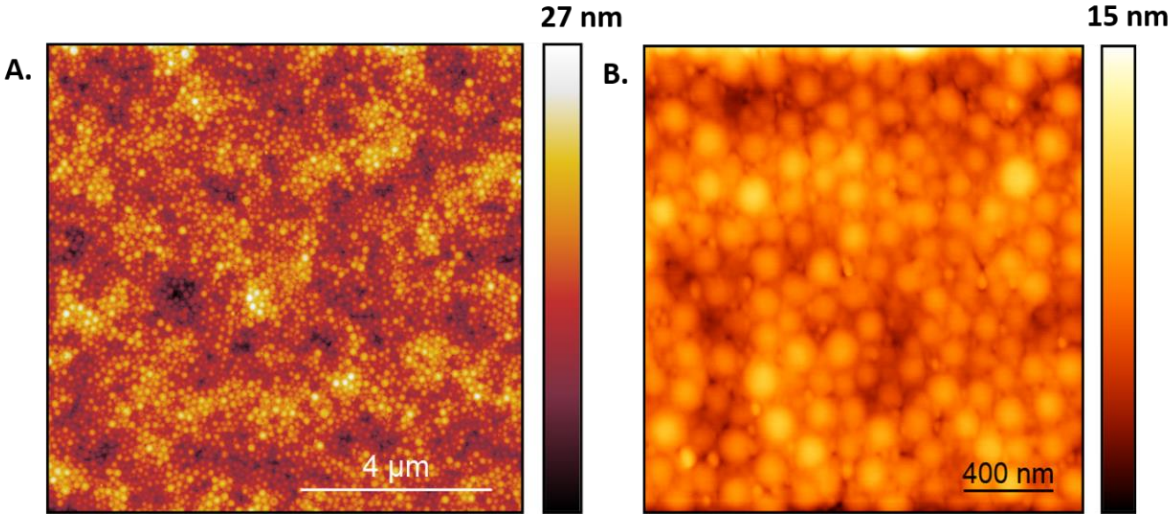

Figure 4.2 A.B. AFM topography images of latex 2 spheres deposited on glass slide, taken using Scan Asyst®-Air AFM probes using different scan sizes.

Latex 3 is the result of a mixture between big (253 nm) and small particles (50 nm). The size ratio used is ~5 and so there should be little or no expansion of the system. In this size regime, it is predicted that the small particles will fill the interstices of the larger particle without affecting the overall system, i.e. there will be no volume expansion and so the void fraction is reduced. This is clearly seen up to 10% of small particles added to the mixture. For 20% of small particles, it is clear that the small particles are filling the interstices between the larger particles, as shown in Figure 4.3 a.b. The overall hexagonal ordering is still maintained; however, the small particles appear to have pushed the larger particles apart, indicating that there is actually a volume expansion of the system.

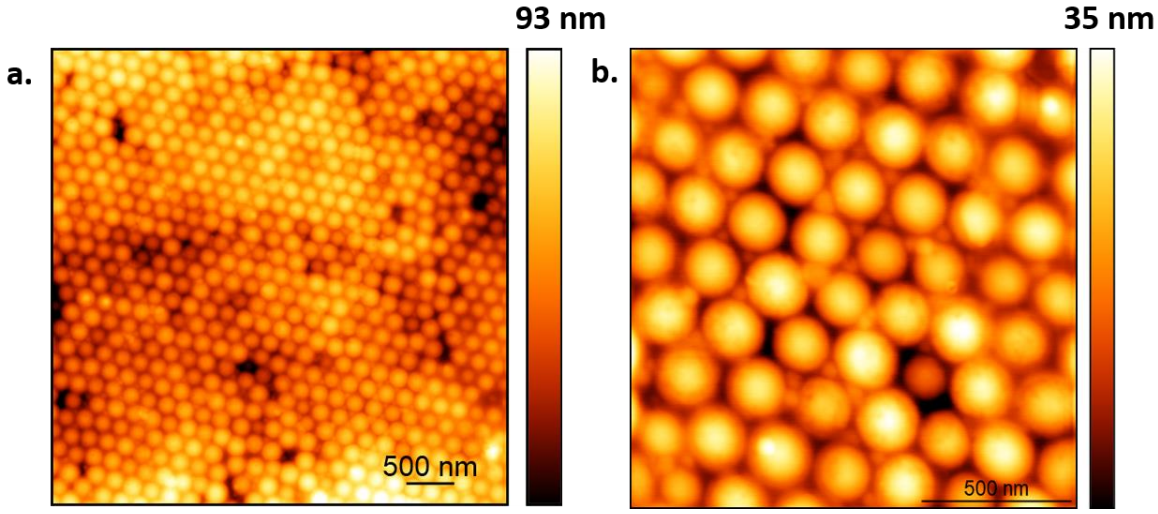

Figure 4.3 a.b. AFM topography images of latex 3 film formed using 20% of small particles mixture.

The AFM images of Latex 4, the pre-vulcanized NLR are displayed in Figure 4.4 a.b. The surface morphology of the sample appears flat, inhomogeneous and it is not possible to see the bimodal particle arrangements. This is due to the fact that in order to dry the sample, it was cured at 100°C in the oven. Such temperature is well above the T_g (-70°C, as shown in Chapter 3), meaning that the particles have coalesced due to the thermal activation of the chains.

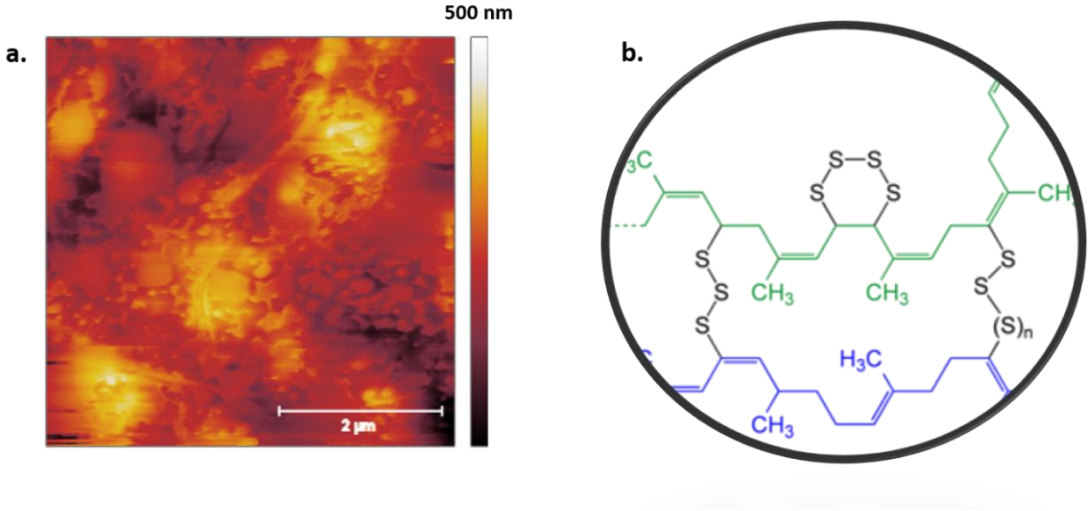

Figure 4.4 a. AFM topography image of the NLR system. b. chemical structure of NLR after the vulcanisation process [188].

4.2. GO

Due to the hydrophilicity and therefore the ease of incorporation into waterborne polymers, GO has been focussed on for the composite fillers. Variation of preparation methods and purification techniques result in a highly inhomogeneous GO product. Therefore, it is necessary to characterise and optimise parameters in order to improve the interfacial interaction of GO and the resulting composite properties.

4.2.1. Commercial GO

Physical chemical characterisation of GO is not often easy to interpret due to the presence of different oxygen functional groups. Raman spectroscopy is a powerful technique to identify and characterise every member of the carbon family. The main features in the Raman spectra of GO are the so-called G and D peaks, which lie at around 1560 and 1360 cm^{-1} respectively [189][190]. Figure 4.5 A. shows the Raman spectra of commercial GO. The G band is found at 1604 cm^{-1} and is attributed to the in-phase vibrations of ordered crystal structure while the D band is found at 1352 cm^{-1} and is assigned to the disordered crystal structure [191]. This fact loosely correlates the G band to the sp^2 carbon and the D band to the presence of sp^3, hence, to oxygenated domains [192]. The commercial GO has a G/D ratio of 0.12 and the linewidth of the G peak is comparatively narrow, indicating that the sample contains large domains of sp^2 carbon in the flakes. This can

also be an indication that the flakes are very large, as the edges (which contribute to the D peak) are a smaller percentage of the sample.

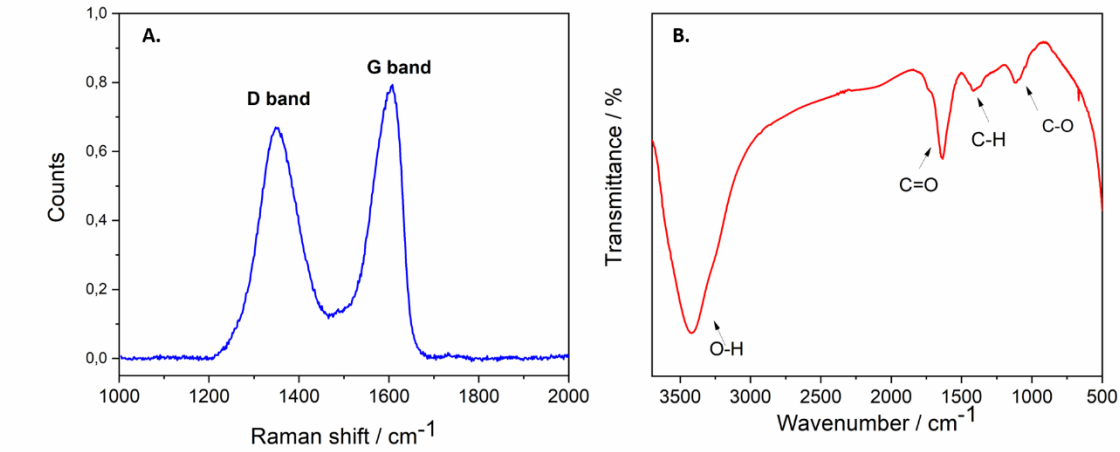

Figure 4.5 A. Raman and B. FTIR spectra of commercial GO.

FTIR was performed to investigate the structure and functional groups of GO, such as hydroxyl (-OH), epoxy (-C-O-C), and ketone (C=O) groups. The FTIR spectrum of GO is reported in Figure 4.5 B. and shows the typical vibration frequencies as shown by Bagri *et al.*[193]. The hydroxyl stretching mode band appears at 3419 cm^{-1}, whereas at 1631 cm^{-1} there is the carboxyl band and at 1100 cm^{-1} there is another band that corresponds to ethers/epoxides groups. The C=O feature is the strongest oxygen functionalisation for this sample, with these groups being found across the basal plane rather than just at the edges. At this point, it was possible to infer that commercial GO flakes are relatively large, as indicated by Raman and FTIR characterisation. Moreover, IR analysis indicates that the basal plane of the GO sheets have an abundant array of chemical functionalities ranging from acidic to epoxy groups. The relatively large disorder feature in the Raman spectrum indicates that there are a range of non-conjugated sites on the sheet which confirms the existence of various chemical functionalities determined by FTIR. AFM was used to characterise the lateral size and the thickness of the GO layer. The AFM topography image in Figure 4.6 a. shows the presence of GO sheets that have a mean lateral size of 4.0 ± 1.3 μm as shown in the histogram in Figure 4.6 b. The thickness varies from 1.0 to 1.5 nm. However, as seen in the histogram, there is still a significant population of very

large flakes, up to 20 μm, and these will often dominate the spectra due to their disproportionate representation in a standard focal area. Similar results have been found by Yang *et al.* [194]. In fact, the AFM height profile image reveals a thickness of 1.0 to 1.2 nm in good agreement with our results. They have also noted that the lateral size of a GO single layer can range from 500 nm to 50 μm. This lateral size change depends on the synthesis and the post-synthesis treatment, e.g. sonication.

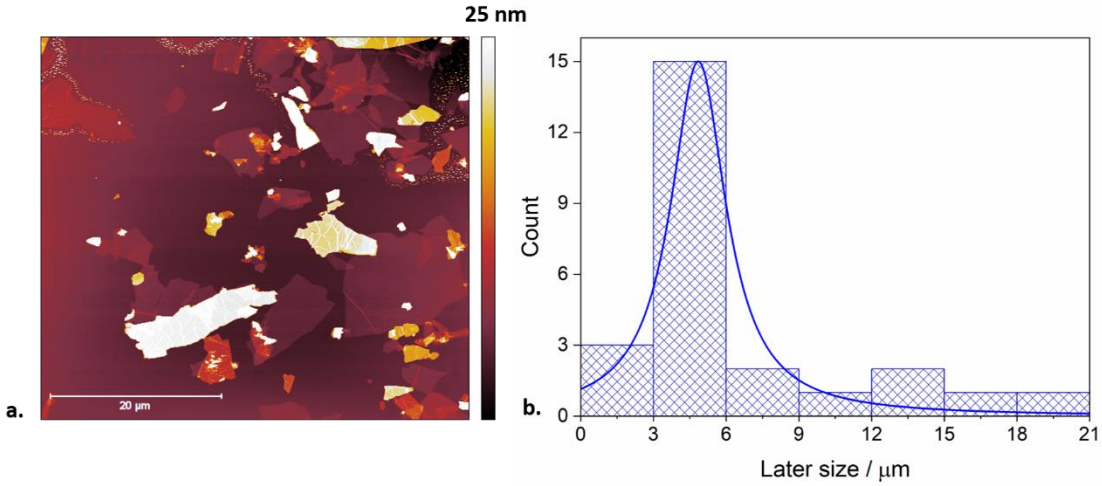

Figure 4.6 a. AFM image in topography of commercial GO and b. particle size distribution.

4.2.2. GO prepared by Hummer's method

In order to control its properties, GO flakes were fabricated using the Hummer's method [186], as described in Chapter 3 in the experimental section. By varying the oxidation time, it is possible to modify the structure and oxygenation of the GO. Longer oxidation times lead to more oxygen groups, but also scission of the flakes and a greater fraction of monolayers, as there is increased separation of the layers with the oxygen intercalation [195] [196]. GO1 is produced with an oxidation time of 2 h and they are displayed in Figure 4.7 a. The mean lateral size of GO1 flakes is $\sim 2.0 \pm 1.2$ μm as shown in the histogram in Figure 4.7 c. The thickness varies from 1.0 to 1.2 nm. XPS measurements that have been done by a collaborator [197] show that the C/O ratio for this type of GO is 4.8. In the histogram in Figure 4.7 c. is also possible to notice that there is a presence of flakes that are bigger ~ 20 μm as seen before for commercial GO. GO2 is instead obtained after an oxidation time of 4 h (Figure 4.7 d.) and the flakes have a mean lateral size of 1.5 ± 0.8 μm (Figure 4.7 f.). The thickness is around 1.0 to 1.2 nm and the C/O

ratio of 4.6. Oxygen functional groups have not increased substantially with the oxidation time, but scission of the flakes has occurred, with a significant decrease in the mean lateral size. Finally, GO3 is formed after 16 h (Figure 4.7 g.) and in this case, the particle size and the C/O ratio significantly decreased when compared to the other two samples. It has a mean lateral size of 1.0 ± 0.6 μm (Figure 4.7 i.) with the flakes being prevalently monolayers with an average thickness of 1.5 nm and the C/O ratio of 0.9. The differences between the three samples are substantial and are summarised in Table 4.1.

Table 4.1 XPS data, C/O ratio for the three kinds of GO samples and particle size distribution from AFM measurements.

	GO1	**GO2**	**GO3**
C/O ratio	4.8 ± 0.5	4.6 ± 0.5	0.9 ± 0.5
Particle size	2.0 ± 1.2 μm	1.5 ± 0.8 μm	1.0 ± 0.6 μm

We can see from the C/O ratios that the oxidation is not radically different between 2 h and 4 h but there is a significant reduction in the flake size, as energy is used to separate layers and cut flakes. After 16 h of oxidation, however, there is a dramatic increase in the oxygen functionalisation, without a corresponding reduction in flake size, so greater addition of functional groups occurs without further destruction of the flake geometry. Following the observed difference in GO particle size, Raman spectroscopy has been performed for the GOs flakes to evaluate if there were any differences in the chemical structure. In Figure 4.8 the Raman spectra of the 3 types of GO is shown. We can see that there is a downshift in the defect feature for GO2 and 3, without significant change in the graphitic feature or the intensity ratio compared to the other GOs. This implies that the increased functionality of GO does not affect the sp^2 regions, but rather to add edges states to the already established defects.

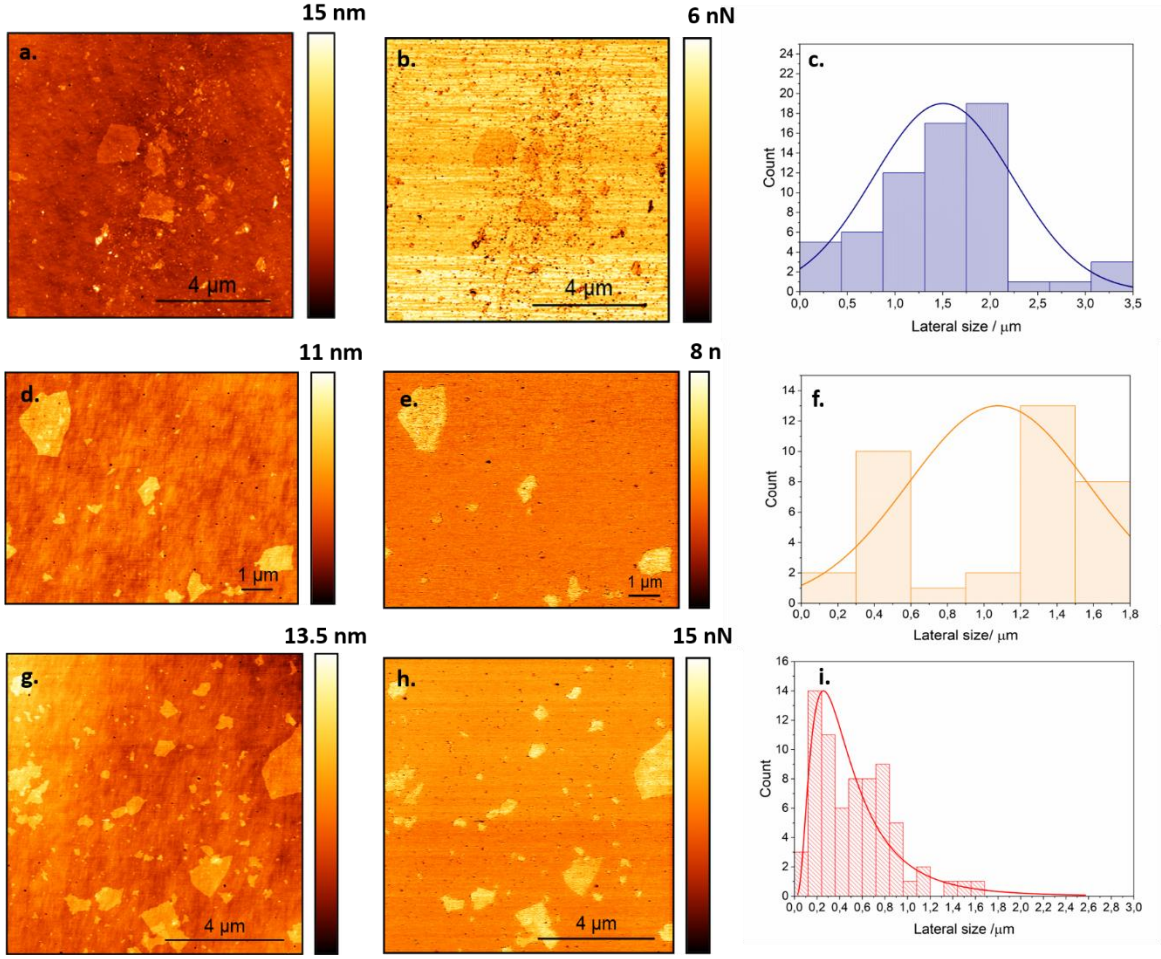

Figure 4.7 a.d.g AFM image in topography of the GO1, GO2 and GO3 flakes respectively. b.e.h. AFM image in adhesion of the three kinds of GO and c.f.i respectively size distribution.

GO tends to consist of regions of high concentration defects and regions of sp^2 rather than homogeneously dispersed defects. The increase in oxygen concentration in these defect regions, and the increase in edges states due to size reduction, can explain the change in the D peak without a corresponding perturbation of the G peak.

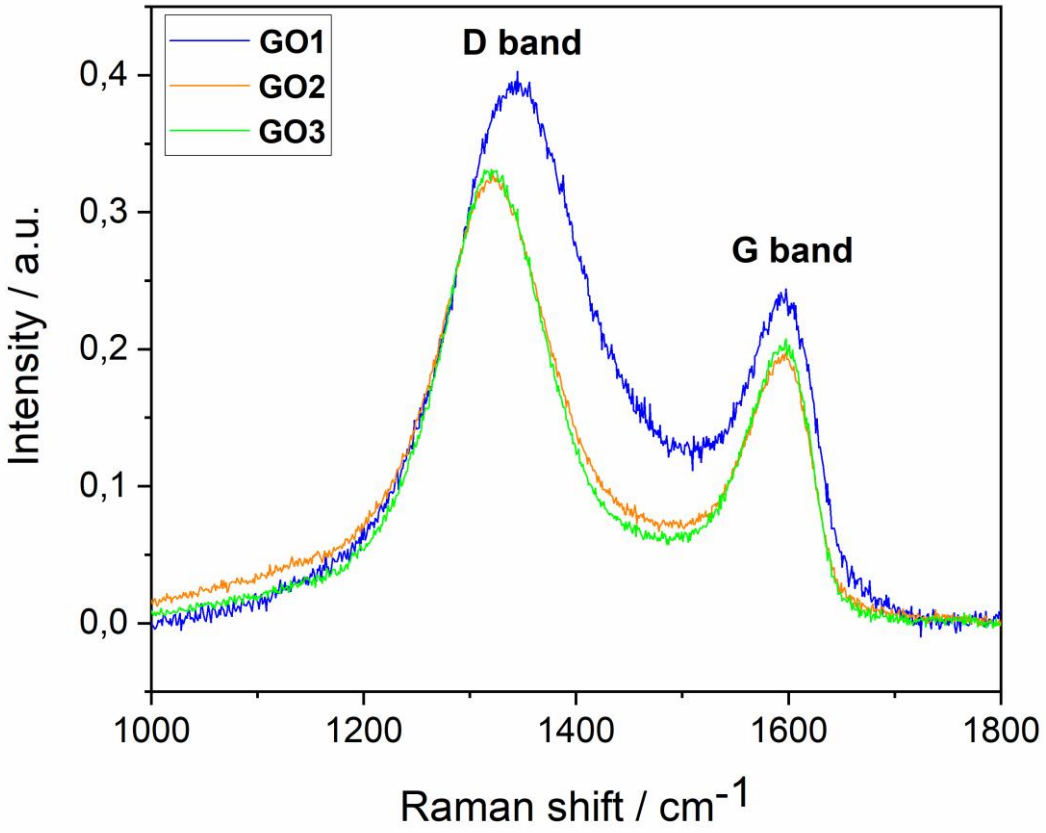

Figure 4.8 Raman spectra of GO1, GO2 and GO3.

At this point after all the measurements, it was important to decide which GO was more suitable to get a better interaction with the latex spheres in order to create an optimised polymer/GO based composites. For the creation of the Latex 1 and 2 based composites (described in Chapter 3 in the experimental section), GO3 flakes were chosen due to the fact that it contains more oxygen and the particle size is smaller compared to the other two options. This way, the flakes should not interfere with the particle packing and the increased oxygen functionalisation should improve the aqueous dispersion of the flakes, leading to a more homogenous composite. This choice has also been crucial in order to obtain a better interaction with the latex and also to increase the conductivity after the thermal reduction. The strong interaction between Latex 1 and GO3 sheets has been confirmed by TEM as shown in Figure 4.9 a.b.c.d.e.f. The morphology of the polymer latex sphere and GO sheets in water dispersion is displayed in Figure 4.9 a.b. The TEM images prove how the polymer spheres are tightly wrapped by the GO3 flakes even in the

dispersion, before film formation. GO3 sheets are big enough to wrap the polymer spheres as displayed in Figure 4.9 c.d. This strong interaction has also been demonstrated using higher magnification (Figure 4.9 e.f.).

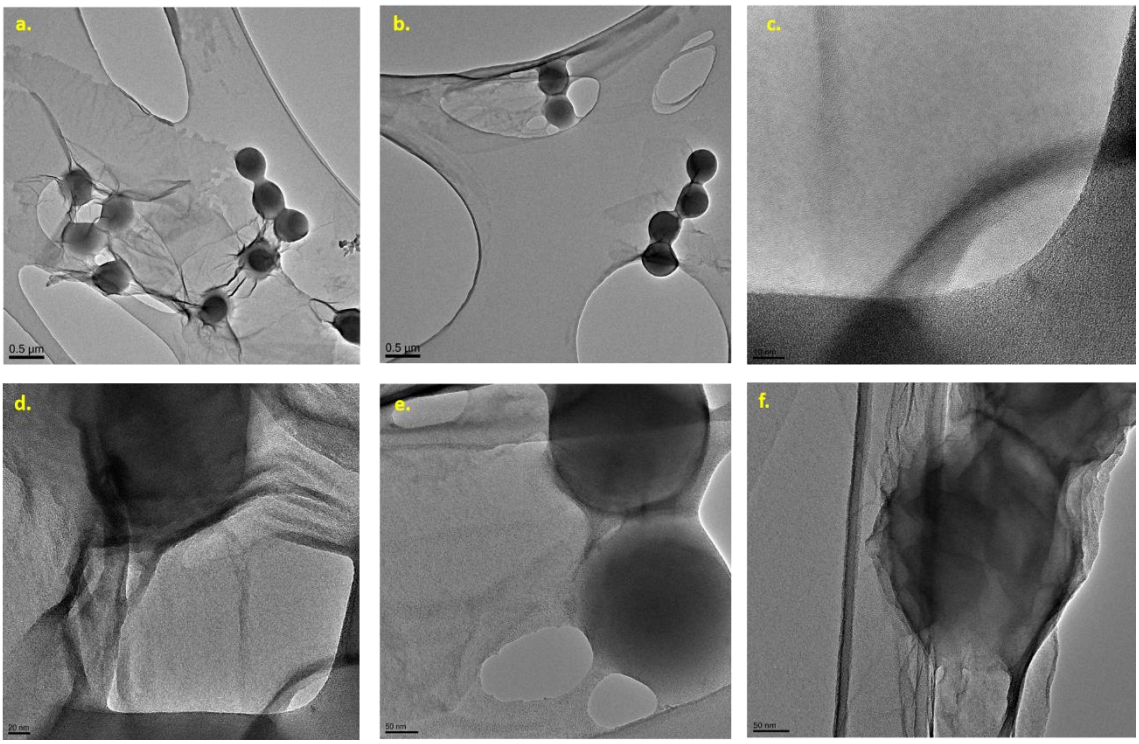

Figure 4.9 a.b.c.d.e.f. TEM images of GO3 sheets interacting with the Latex 1 spheres at different orders of magnification.

4.3. Liquid exfoliated graphene

In order to determine how the morphology and the physical properties of the matrices can change by modifying the filler, liquid exfoliated graphene was used to create NLR and Latex 3 based composites (as shown in the experimental section in Chapter 3). As shown before for GO flakes, characterisation techniques have been used in order to characterise particle size and chemical information about the liquid exfoliated graphene. In Figure 4.10 a. an AFM height sensor image of the liquid exfoliated graphene flakes is displayed and it shows the average lateral dimension of the graphene flakes of 156.42 nm (Figure 4.10 b.) and a thickness of ~10 nm.

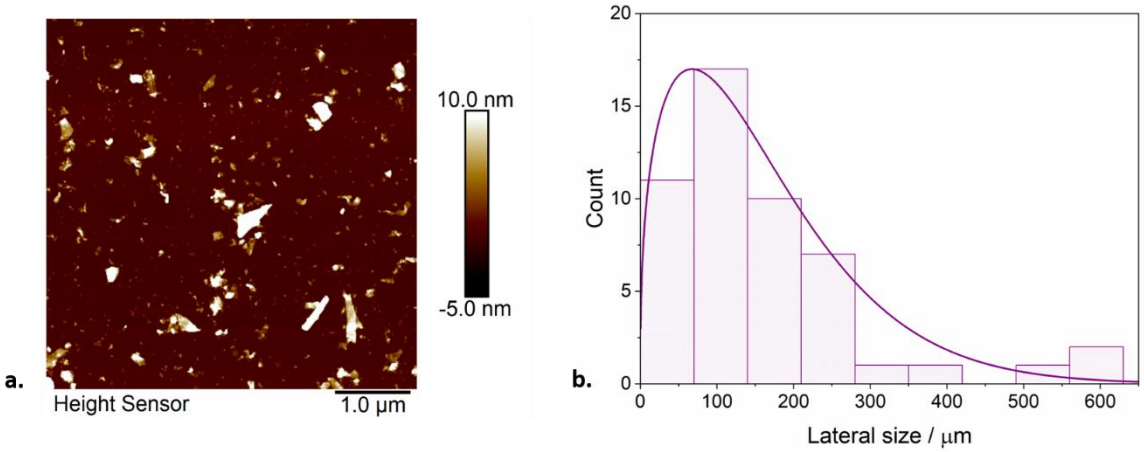

Figure 4.10 a. AFM image in topography and b. particle size distribution of exfoliated graphene.

Figure 4.11 displays the Raman spectrum obtained for the liquid exfoliated graphene, showing the most intense features of a D peak at 1360 cm^{-1}, G peak at 1580 cm^{-1} and 2D mode at 2700 cm^{-1}.

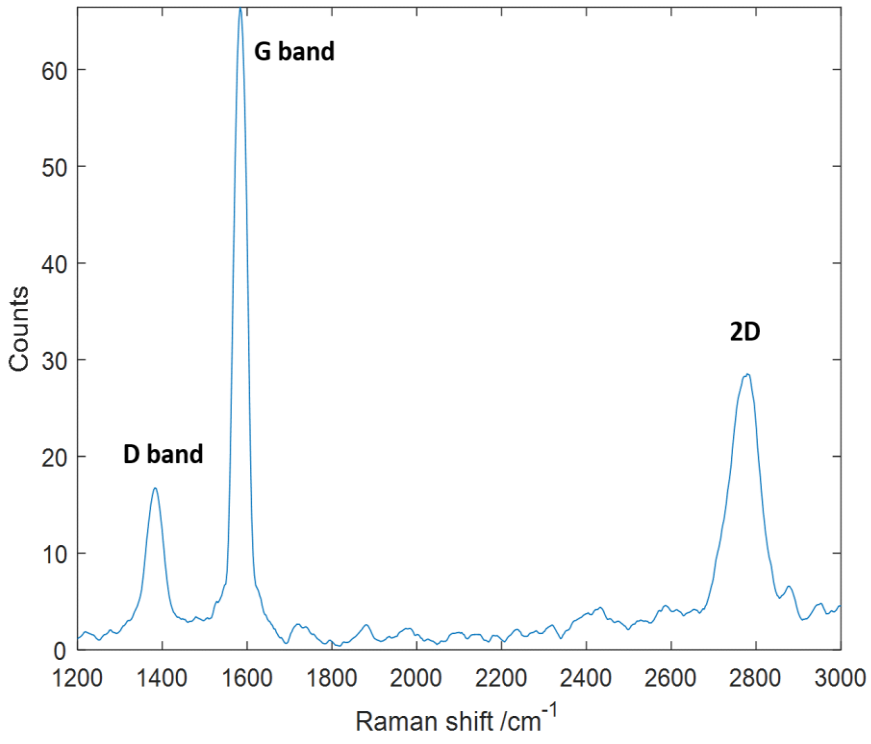

Figure 4.11 Single Raman spectra of liquid exfoliated graphene.

The D peak in general, in the pristine graphene, is not visible because of the crystal symmetries [198], and as described before, indicates defects [199] and edges. As we have small nanosheets, in this case, we expect the edges to play a significant role in the Raman spectrum. The G peak is due to the doubly degenerate zone center E_{2g} mode, that are Raman active as fundamentals [199]. The 2D mode of graphene has been detailed by Ferrari *et al.* as the results of a double resonance (DR) process arising from the special electronic band structure of graphene [200]. In order to obtain detailed information about compounds in a composite, Raman mapping is known to be an effective technique [201]. Each pixel in the mapping corresponds to the position of the D, G and 2D peaks, as shown in Figure 4.12 a.b.c. respectively. For the D peak, there is a homogeneous distribution of a peak position at 1385 cm^{-1}, for G peak at 1585 cm^{-1} and for the 2D mode, the position is scattered between 2750 to 2790 cm^{-1}. The 2D peak can be measured using a metric [202] to indicate the number of layers, so the spread of 2D positions and the intensity at those positions indicates that there are differences in layer number between particles, and when statistically averaged over a large map, the average is ~ 7 layers, in agreement with the AFM images.

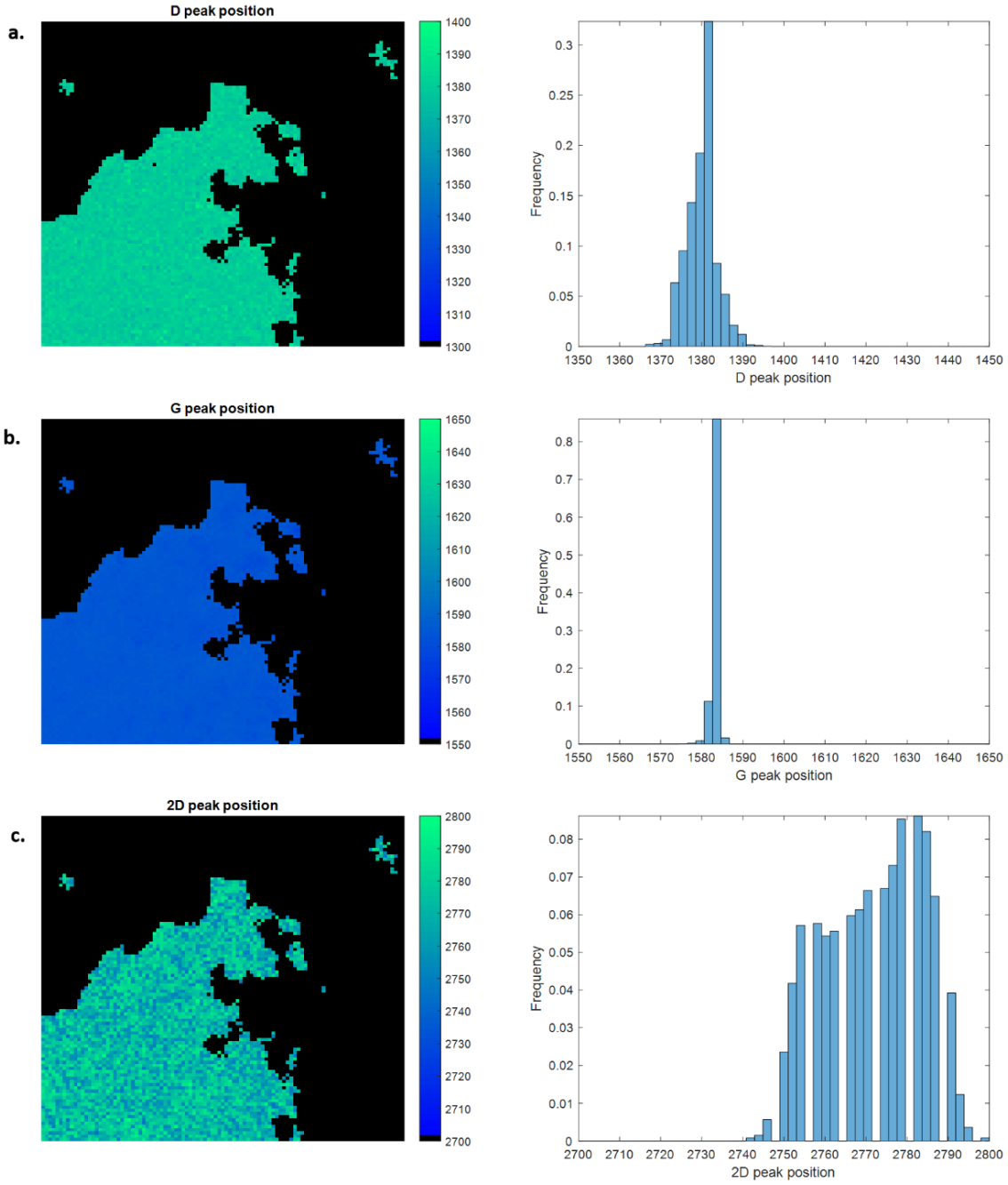

Figure. 4.12 Raman mapping of the liquid exfoliated graphene, showing peak position and corresponding histograms associated with a. D, b. G and c. 2D peaks.

Similarly, in Figure 4.13 a.b. is possible to map the ratio of D over G peak intensity (I_D/I_G) and the ratio of 2D over G peak intensity ratio (I_{2D}/I_G) ratio, respectively. The I_D/I_G ratio is between 0.2 and 0.3 and it means a low number of defects in the structure. The I_{2D}/I_G ratio average is ~ 0.4 and it means that the number of graphene layers is around 8.7.

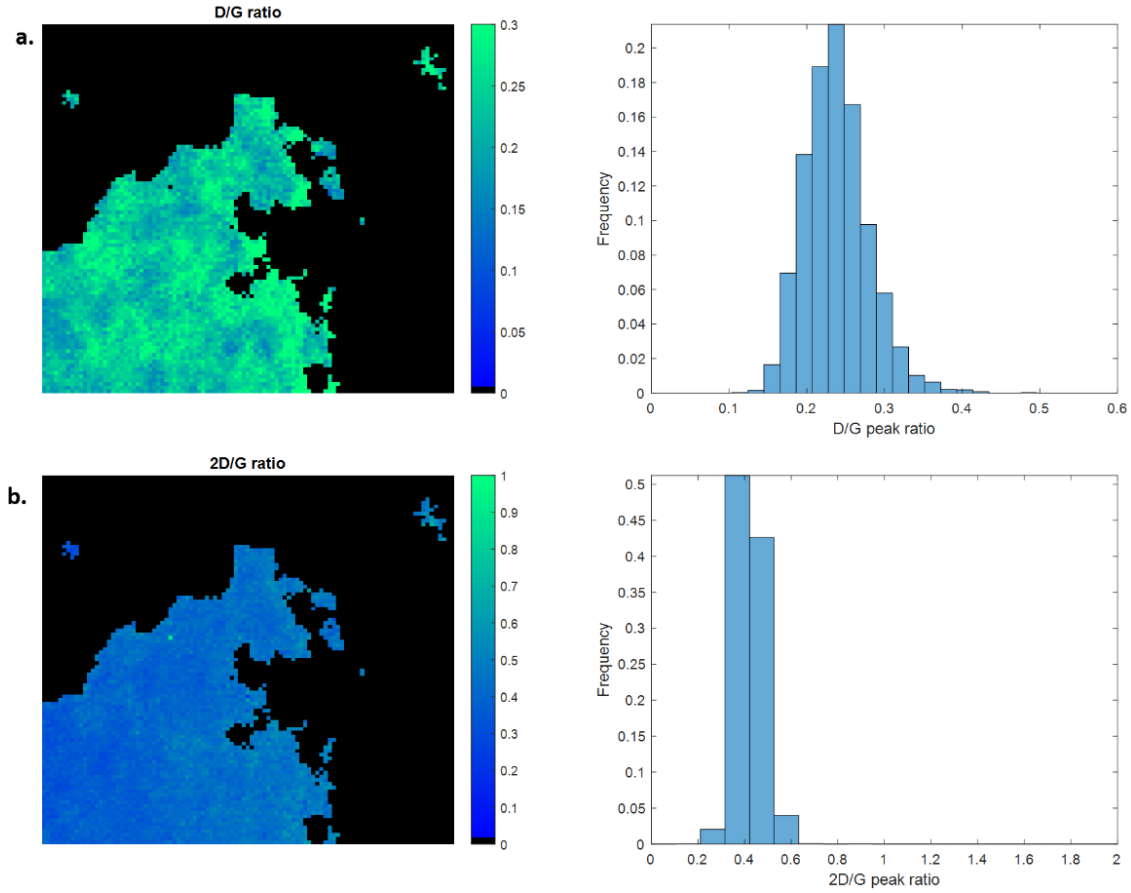

Figure. 4.13 a. Raman mapping of liquid exfoliated graphene representing a. the I_D/I_G ratio and b. the I_{2D}/I_G peak ratio.

4.4. Particle packing results using different fillers

In order to reach a particle pathway, it is important that the filler is small enough to be placed into the interstitial space between the polymer latex spheres but big enough in order to prevent phase separation due to stratification. To illustrate the importance of size, Figure 4.14 A.B. shows representative AFM images of the latex 1 with Ag triangles system. The Ag nanoparticles are not forming any segregated nanostructure between the latex spheres, and appear to aggregate at the surface as displayed in the AFM images. The KPFM image in Figure 4.14 C. shows the excellent electronic contrast of the particles. If it was possible to form a network structure, it would provide interesting materials.

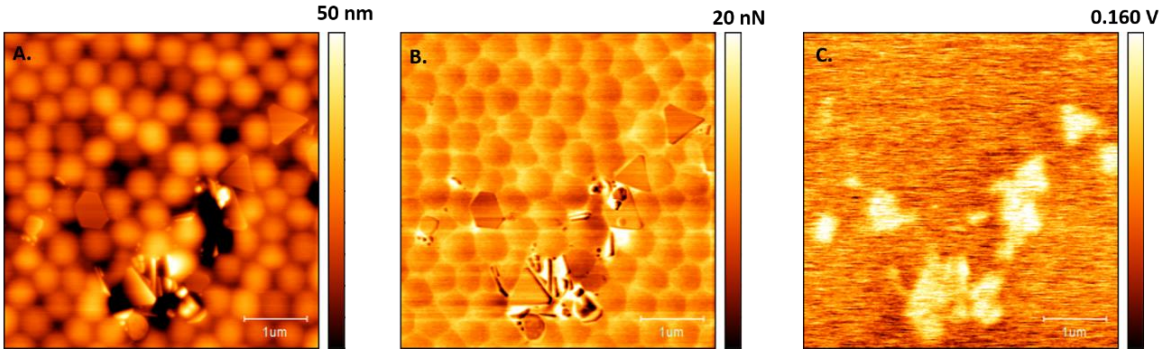

Figure 4.14 A. AFM height sensor image of Latex 1-Ag triangles composite, B. in adhesion and C. KPFM.

This is probably due to the Ag particle size, as they are too big to exist at the interstitial space of the latex (~300 nm), or due to their rigidity. SEM image from the top part of the composite shown in Figure 4.15 A. confirms that the Ag nanoparticles are not forming any structured pathway but rather are creating a random like composite. Analysing the electron micrograph images displayed in Figure 4.15 B.C. taken from the bottom part of the composites it is also possible to see that the Ag triangles sedimented, because of a large density mismatch between the triangles and latex particles.

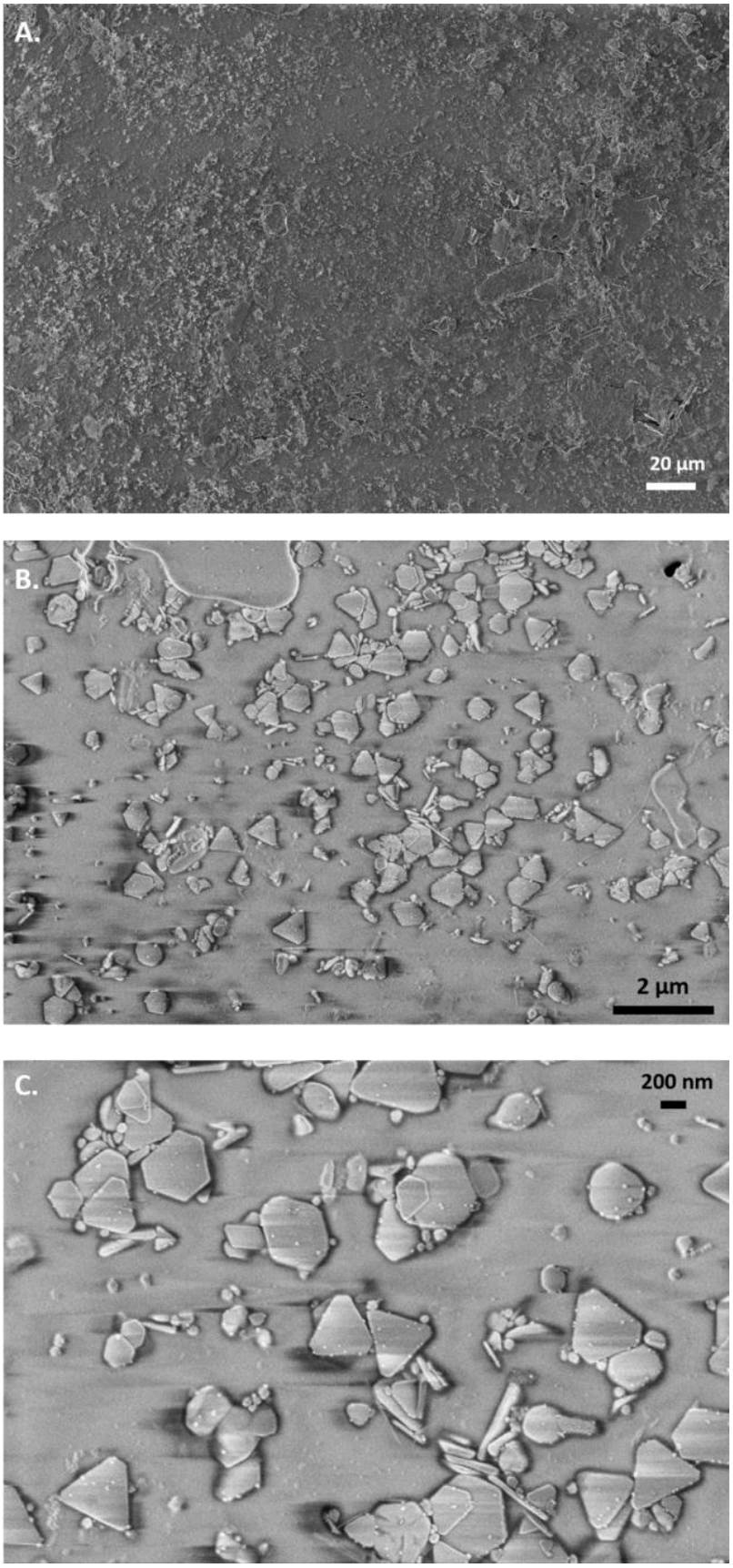

Figure 4.15 SEM images of the Latex 1-Ag triangles composite. A. The top part of the composites and B.C. bottom side of the nanocomposite.

In order to get a homogeneous structure it is important to ponder the possible interaction among the polymer latex spheres and the filler, the dimension of the filler particle and its shape. In Figure 4.16 a. is shown the structure of Latex 2-GO based composite formed by a bimodal latex and the GO flakes at a low concentration (0.01 wt.%). From AFM image in adhesion mode, shown in Figure 4.16 b., it is visible that the GO flakes are not forming any pathway because of the low concentration and most of the particles are accumulated in a small area of the sample. It is evident that they are starting to form localised connections.

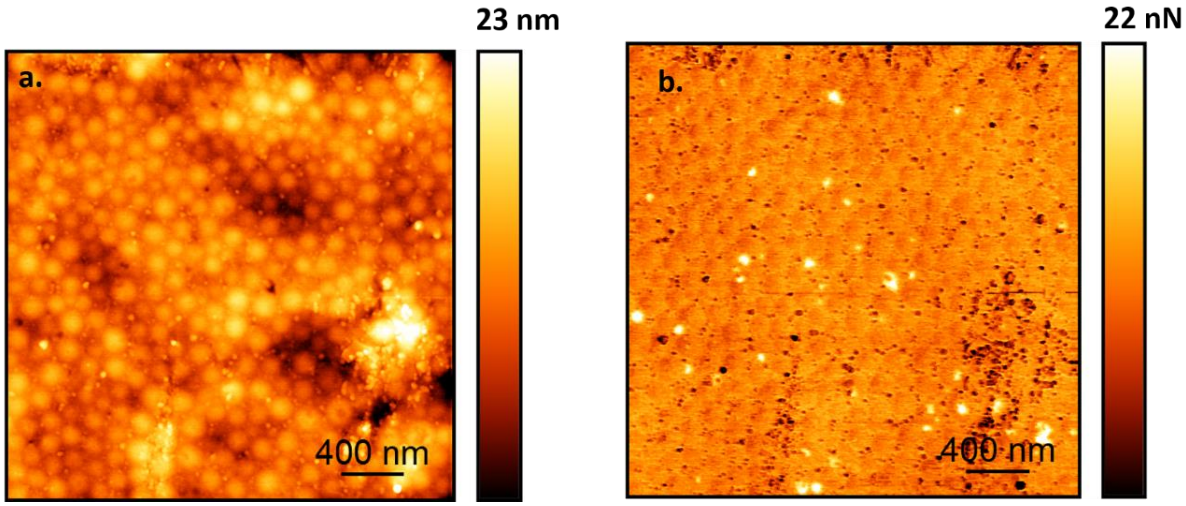

Figure 4.16 a. AFM topography image of the Latex 2-GO based composite at 0.01 wt.% of GO and b. in adhesion.

The best results in terms of achieving a segregated network are obtained when the GO concentration is high enough to reach the percolation threshold and the flakes can be interconnected to each other. Figure 4.17 a. represents the structure of Latex 1-GO based composite which illustrates the segregated network concept. From the Adhesion image shown in Figure 4.17 b. is it possible to notice the different interactions between the polymer and the GO flakes, because of the strong contrast between them. The GO flakes are locked into the latex structure forming a honeycomb-like arrangement due to the fact that the GO content was at 2 wt.% and hence above the percolation threshold. Obtaining this kind of system is a starting point in order to obtain functional and cheap

nanocomposites. As said in previous chapters, it is important to attain the best electrical and mechanical properties of a system whilst minimising the amount of filler. It can be useful for possible interconnection with the industries and commercialisation of the composites.

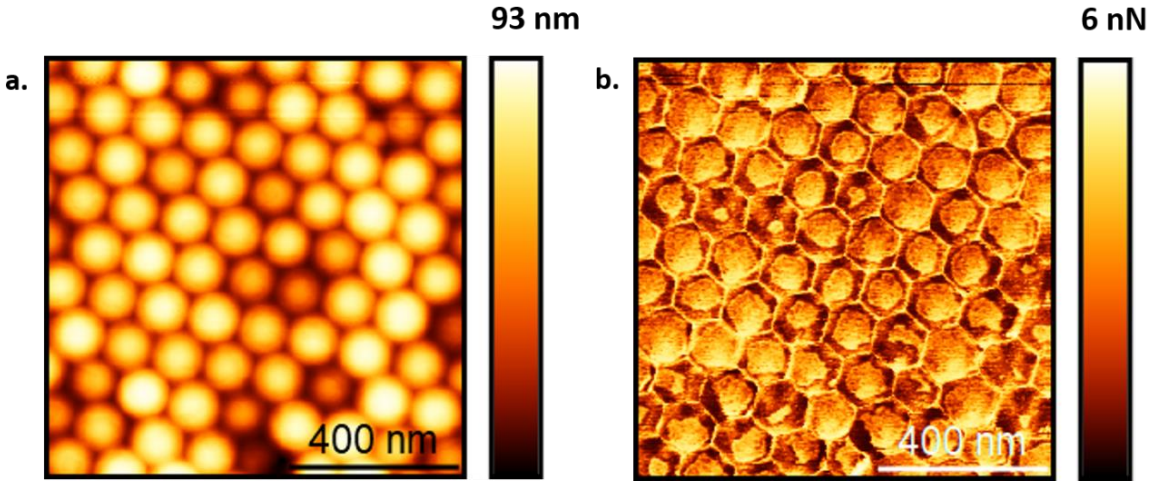

Figure 4.17 a. AFM height sensor image of the Latex 1-GO based composite at 2 wt.% of GO and b. in adhesion mode.

4.5. Conclusions

This chapter presents essential information to understand which parameters have been taking into account in order to develop optimised composite systems. While creating a nanocomposite using the latex assembly method, it is important to play with the particle size of the filler and also with their concentration. The polymer matrix itself can also influence the final properties of the composite. The latex matrices used in this thesis possess different morphologies after the drying process due to their particle size, T_g and composition. At the beginning of the chapter, AFM is used to indicate clear differences in the morphology of the four types of latex matrices used to prepare the nanocomposites. Then, there is a description of the nanoparticles used to prepare the composites such as commercial GO, synthesised GO and liquid exfoliated graphene. GO has been chosen as a potential candidate for the formation of structured composites due to its hydrophilicity and indeed the facile incorporation into water-dispersed polymers. AFM, Raman and FTIR spectroscopy have been used in order to have a better understanding of GO particle size and investigate the structure and the functional groups of GO. Subsequently, GO3 has been chosen as a perfect candidate for the creation of highly structured GO based nanocomposites due to the fact that it contains more oxygen and is smaller in size compared with the other fillers. The increased functionalisation should improve the aqueous dispersion of the flakes, leading to a more homogenous composite. This choice has been crucial to obtaining a better interaction with the latex. This strong interaction is confirmed by TEM images in which GO sheets are strongly interacting with the latex spheres and wrap the particles even in the dispersion, before film formation. After discussing the fillers, there is a description of how the fillers can influence the particle packing during film formation. As discussed previously, in order to obtain a better interaction among the polymer latex matrices and the fillers it is fundamental to take into account the dimension, shape and concentration of the fillers. In fact, the nanoparticles are able to self-organize into three-dimensional hexagonal patterns only if they are small enough to be placed into the interstitial space between the polymer spheres but also big enough to prevent phase separation due to stratification. Some examples are given to demonstrate that there is a level of complexity in creating homogenous composites. In the first example, Latex 1-Ag triangles-based composites are described. In this particular case, the Ag particles are too big and rigid to exist at the interstitial space of the latex and because of that are not forming any structured pathways but rather are creating a random

like composite. In the second example, Latex 2-GO based composites are reported. In this case, GO concentration is too low to reach the perfect pathway. The best results in terms of achieving a segregated network are obtained when GO concentration is high enough to reach the percolation threshold and the flakes can be interconnected to each other. Thus, it is a starting point for developing efficient and cheap composites for industrial applications such as pressure sensitive adhesives, sensors, circuit devices, and battery.

Chapter 5

Latex Based Nanocomposites: study of the electrical properties

The introduction section of Chapter 2 briefly reviewed recent progress in the fabrication and properties of various polymer composites. It has been shown that the percolation threshold can be successfully lowered using GO instead of graphene, because of the presence of oxygen functional groups that make GO more dispersable in the polymer matrix. In this section, the segregated network concept is introduced as a more efficient method for formation of conductive pathways, resulting in a further lowering of the electrical percolation threshold without sacrificing mechanical properties coupled with ease of fabrication. As already mentioned in Chapter 2, the segregated network concept is not novel but has been explored extensively as the need for new light-weight conductive composites increases. Kusy [120] was the first researcher investigating the continuity of a network when a filler is dispersed into another, and he denoted the term segregated as a dispersion of particles that are restricted into the boundaries of larger particles. In his work, he showed that the distribution of the fillers in a polymer matrix can be random or segregated [120]. A segregated network occurs when the particles occupy only the interstitial volume along the boundaries of the matrix. Therefore, he developed a model which connects the volume fraction of the dispersed phase to the particles size ratio, to create a continuous connected pathway. In 2001, Grunlan and co-workers [203] prepared segregated network composites using CB as a conductive filler. Afterwards, Jurewicz *et al.* [130] developed a novel preparation method which allows the organization of CNTs into highly ordered structures which utilizes an ordered lattice of polymer particles as a template. Inspired by these previous findings, a structured composite prepared using GO is presented.

5.1. Segregated network concept in polymer-GO composites

Composite formation is achieved through direct mixing of aqueous polymer latex and GO dispersions as shown in Chapter 3. The mixed dispersion is cast onto a substrate (such as a glass slide or a free-standing mould), dried, and subsequently treated at elevated temperature under vacuum in order to reduce the GO in situ. In Figure 5.1 a schematic illustration of the formation process of the segregated network is represented. During drying, as a result of surface tension and capillary forces, the interparticle distance is reduced and the concentration rises until a dense packing of spheres is achieved.

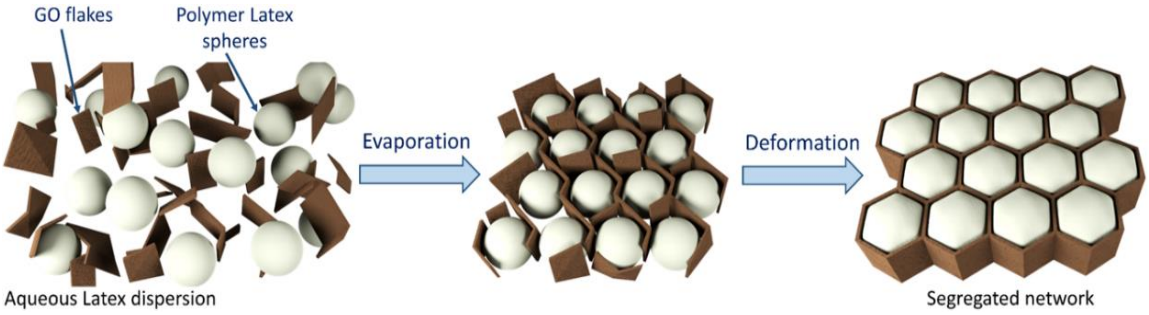

Figure 5.1 A schematic illustration of the formation of segregated networks.

In order to produce a uniform void-free film, it is necessary to dry the latex in ambient conditions. After water evaporation, the latex particles are progressively deformed to fill the voids left by the water due to the reduction of interfacial energy and capillary forces. At this point, the nanoparticles can exist only at the interstitial spaces because they are excluded from the volume occupied by the polymer and are locked into the crystal lattice formed by the latex particles. AFM height sensor image (Figure 5.2 a.) shows how the structure of a Latex 1-GO based composite is arranged after drying, confirming that a segregated structure is achieved. After thermal treatment at 150 ºC, the latex spheres are deformed as can be seen from Figure 5.2 b. but the rGO particles are still in the segregated structure.

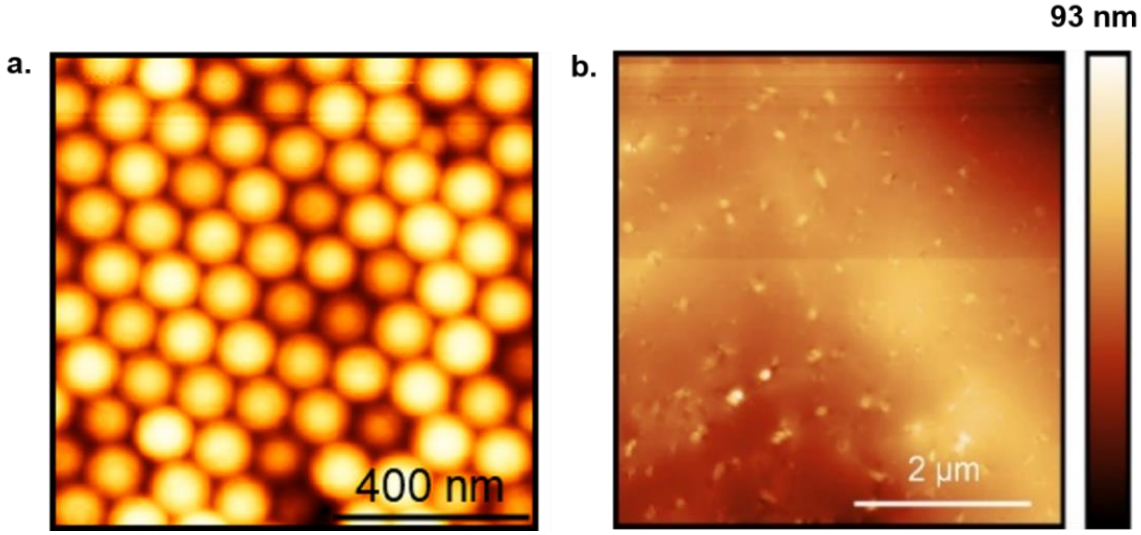

Figure 5.2 a. AFM image in topography for Latex 1-GO based composite at 2 wt.%. b. AFM height sensor image for Latex 1-GO based composite at 2 wt.% after reduction at 150 °C for 5h.

We have two separated processes, in the first one we form the GO composite that is brown, and is not conductive, in the second step after treatment we have the reduction in situ of GO, and the composite becomes black and also conductive. It is visible by eye that the composites are changing colour after the treatment in the vacuum oven. Morphological studies of the composites with 2 wt. % of GO content, are presented in Figure 5.3 From the electron micrograph images in Figure 5.3 F., it is clear there is an organisation of the particles on the surface of the composite, and if we have a look at the structure closely is also possible to see that the honeycomb-like array is maintained even after the reduction. It is possible to see the coalescence space of the polymer spheres that is ~ 250 nm and matches with the particle size of Latex 1 and the rGO flakes network around this space. So, there is a conductive network of rGO throughout the entire structure of the composite. The presence of the large flakes of rGO can be seen at the surface as well (Figure 5.3 A.B.C.D.E.), and there is almost no charging of the polymer under the electron beam, as the network is conductive enough to dissipate the charge.

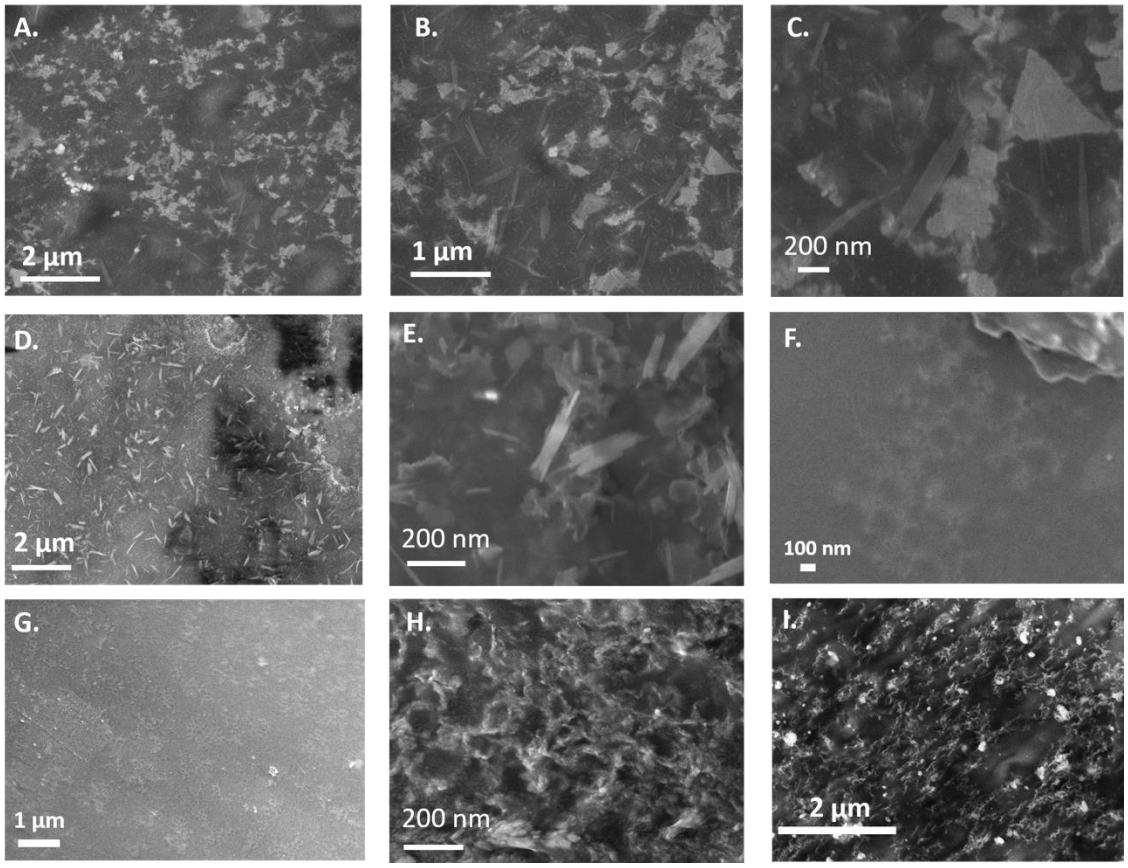

Figure 5.3 A. B. D. G. Low magnification electron micrograph of uncoated composite surface, with rGO particles visible. C.E.F. high magnification electron micrograph showing the formation of local conducting networks structured by the original latex template. H.I. Electron micrograph of an uncoated composite cross-sectional surface.

5.2. Activation energy related to GO exothermic reaction

As the colour change is clearly visible as an indicator of reduction, this provides a simple mechanism to rapidly identify the change as a function of time and temperature. The Arrhenius equation relates a reaction rate constant k to the activation energy E_A for an activated chemical process;

$$k = Ae^{-\frac{E_A}{k_B T}} = Ae^{-\frac{E'_A}{RT}} \qquad \text{(Equation 5.1)}$$

Where A is a temperature-independent scaling constant, k_B is the Boltzmann constant, T is the absolute temperature, R is the ideal gas constant. The two forms of the expression

simply relate the activation energy E_A (in eV) and E_A' (in J/mol) to the thermal energy in the respective units. The rate constant k can be treated as reciprocal to a characteristic time scale for a process (which is more directly measurable in many cases). Since we observe a well-defined colour change after a period of thermal treatment in the composites, t_{cc}, we posit that this can be identified as proportional to the characteristic time $1/k$ such that;

$$t_{cc} = \frac{\alpha}{k} = \frac{1}{A} e^{\frac{E_A}{k_B T}} \qquad \text{(Equation 5.2)}$$

Taking the logarithm of the expression above gives;

$$\ln t_{cc} = \ln \alpha - \ln k = \frac{E_A}{k_B T} - \ln A \qquad \text{(Equation 5.3)}$$

Plotting the logarithm of the time taken for a colour change to be observed *vs* the reciprocal of the absolute temperature $(1/T)$ is predicted to produce a straight-line plot. This is how rate data for chemical processes might normally be processed, however here we have modified the Arrhenius expression to relate to the variables we can directly measure. It can be seen that the gradient of an $\ln t_{cc}$ vs $1/T$ plot is still uniquely defined by the process activation energy E_A. Terms relating the units t_{cc}, as well as the constants A and α, combine into a single additive constant;

$$\ln t_{cc} = \frac{E_A}{k_B T} - C \qquad \text{(Equation 5.4)}$$

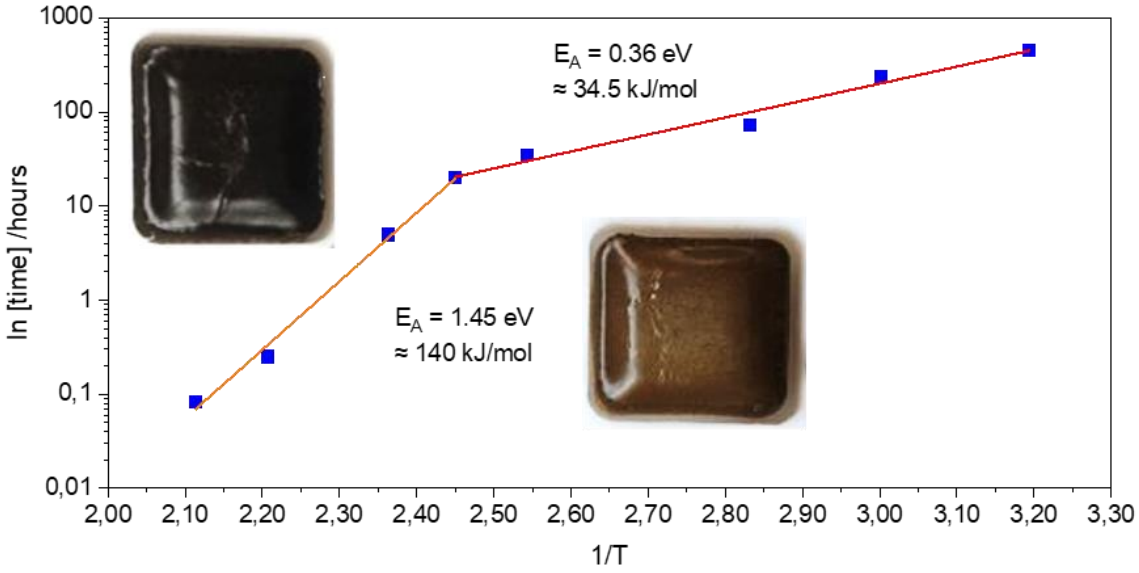

Figure 5.4 ln [time] vs 1/T graph. Two processes are shown.

When we plot ln [time] versus 1/T we have linear behaviour, indeed from the slope of the curve, the E_a is obtained. From the graph it is clear that there are two processes, one that occurs in the low temperature regime that corresponds at 0.36 eV (from 40 °C to 135 °C) then there is a more energetic process in the high temperature regime, E_a is 1.45 eV (from 150 °C to 220 °C), because at this temperature the GO can be involved in an exothermic reaction [204][205]. In the second process, the activation energy coincides with the expected activation energies for bulk GO thermal decomposition reported here [206]. The low temperature regime most likely corresponds to the thermal reduction of GO as reported in several cases [207]. The higher temperature process is a more complex process, that involves the direct chemical interaction of the polymer with the GO and is discussed later in this chapter. The full DSC cycles are shown in Figure 5.5 a. and it shows the presence of an endothermic peak that appears after heating the samples at 50 ºC, which is ascribable to the thermal release of the weakly bonded oxygen groups.

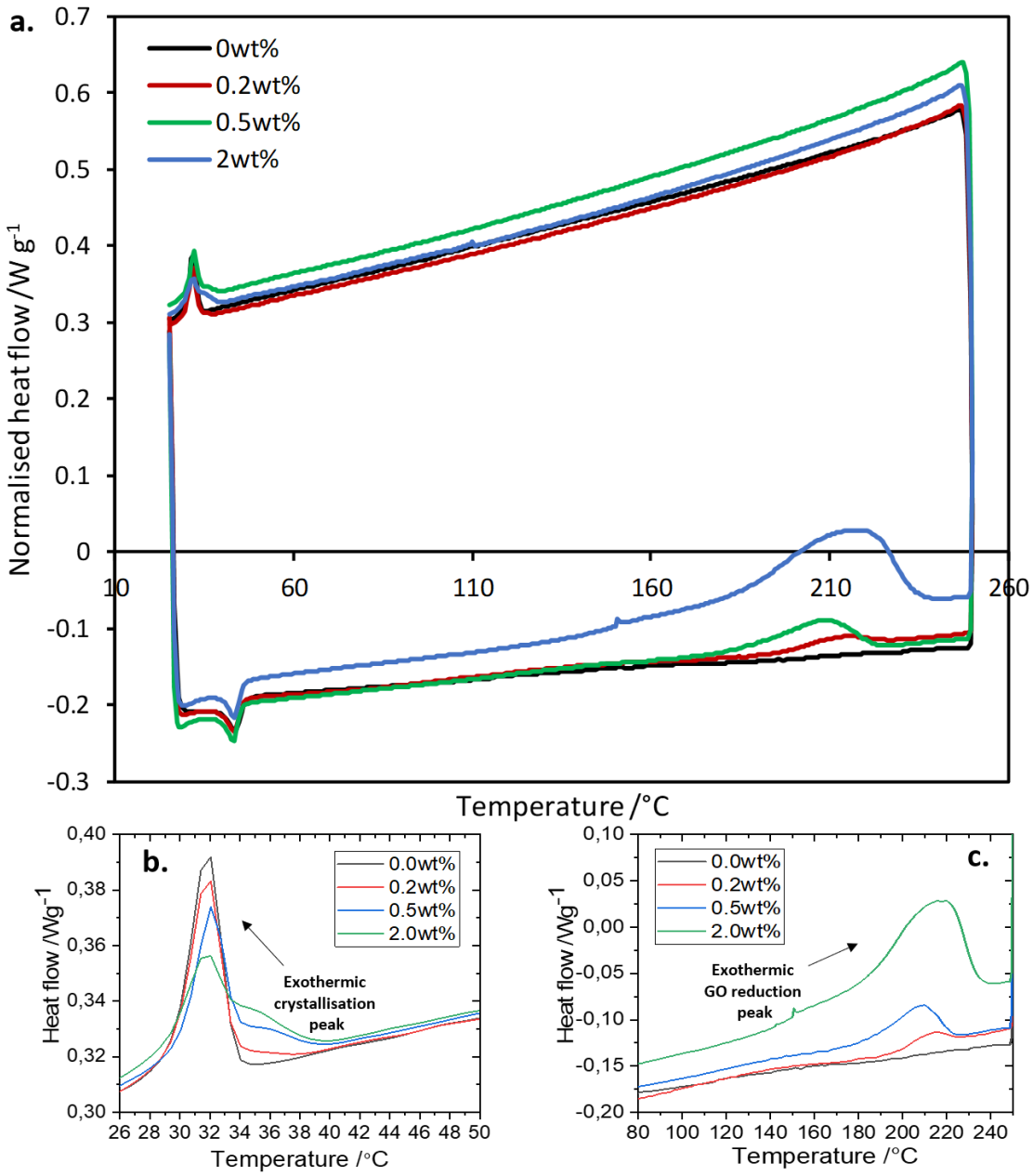

Figure 5.5 a. DSC study for Latex 2-GO based composites at different wt. %. b. Heat flow vs temperature for different wt. % of Latex 2-GO based composites, showing the exothermic crystallisation peak. c. Heat flow vs temperature for different wt. % of Latex 2-GO based composites, showing the exothermic GO reduction peak.

Then, between 150 and 220 ºC, there is an exothermic peak that is getting larger with increasing GO concentration. Moreover, after the cooling, there is also the presence of another exothermic peak that is attributable to the crystallization peak. In Figure 5.5 b. the crystallization peak for different rGO content is displayed, and it shows that there is a peak decrease from the pristine latex to the sample with higher concentration.

Conversely, in Figure 5.5 c. is shown the exothermic peak for different rGO concentration. The graph confirms that there is an exothermic process that appears only in the composites that contain GO and not in the polymer alone. And this can be explained by the fact that when GO is heated at 150 ºC it can undergo an exothermic reaction, and this strengthens the activation energy results calculated by the Arrhenius relationship discussed before. The exothermic peak visible in Figure 5.5 c. matches that observed for GO reduction observed elsewhere [204]. From the thermogravimetric data in Figure 5.6 a. the thermal degradation of the polymer is clearly visible, with a maximum rate of degradation at 400 ºC. There appears to be a shift to a higher temperature for the peak degradation rate with increasing GO content above the percolation threshold (Figure 5.6 a. inset), though the shift is perhaps too small to be conclusive. The ash fraction plotted in Figure 5.6 b. increases monotonically with the GO content but is not proportional. This can give the idea that the GO reduction process is resulting in the formation of an additional system component (suggested to be aromatic material by the XPS data discussed later in the chapter), which has properties significantly different from the base polymer.

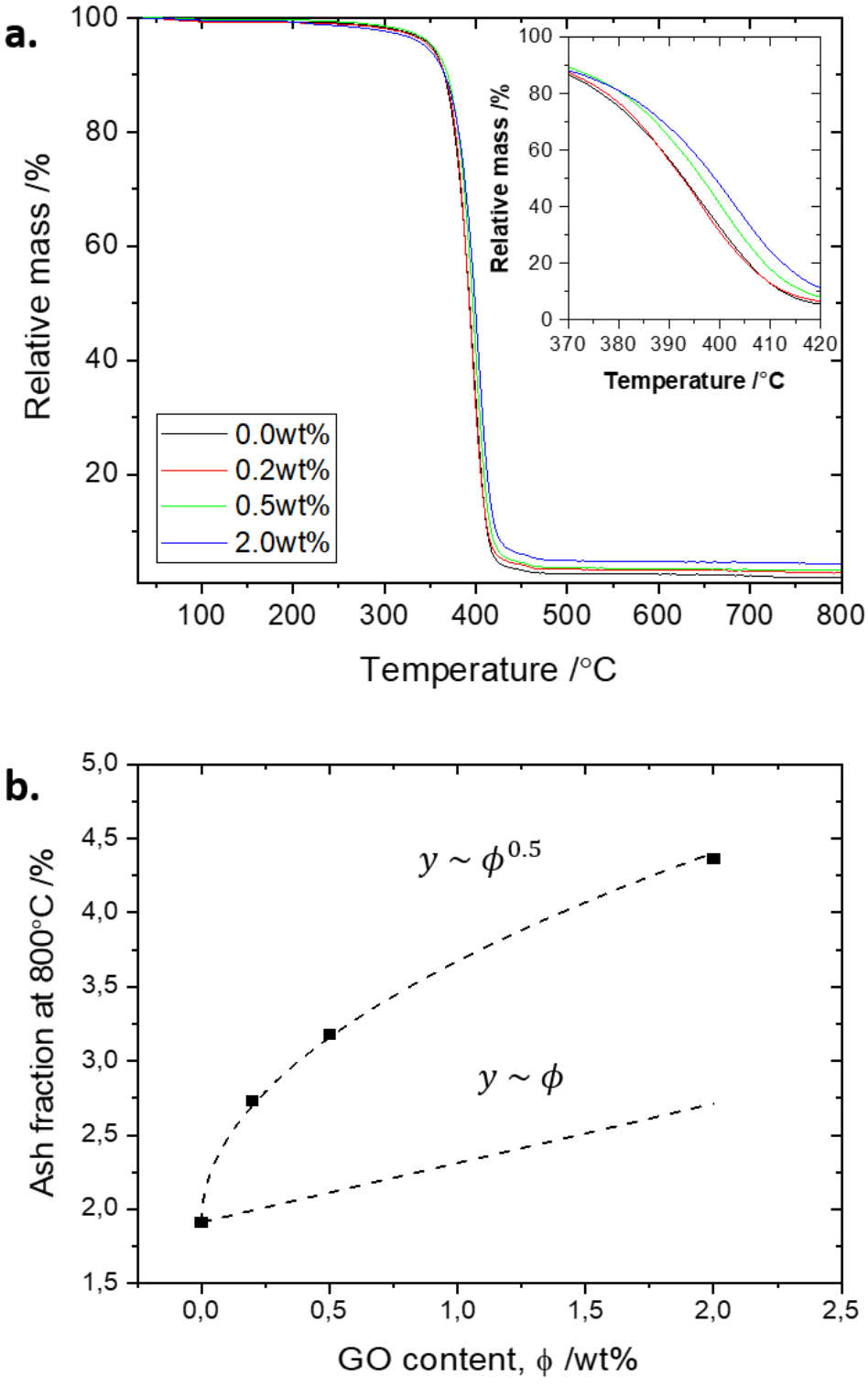

Figure 5.6 a. Thermogravimetric graph of Latex 2-GO based composites and the latex 2 itself. b. Ash fraction at 800 °C/% vs the GO content/wt. %.

5.3. Morphological and chemical characterisation of the latex composites

To have a better understanding of the composite I have done some measurements that confirm the presence of rGO flakes into the matrix, such as KPFM, SEM, XRD, XPS analysis and FTIR spectroscopy. In the KPFM technique we measure the work function of the surface of the sample, since it requires a conductive sample grounded to the metallic base when the sample is not reduced no particular features are shown in the KPFM images (Figure 5.7 b.) while after reduction the composites are now electrically conductive and we can see the contrast between the surface and the rGO flakes (Figure 5.7 d.). From the AFM height sensor image in Figure 5.7 c. can be noticed some depressions on the surface of the specimen that are around 100 nm. The main KPFM signal seems to arrive from the latter area (Figure 5.7 d.).

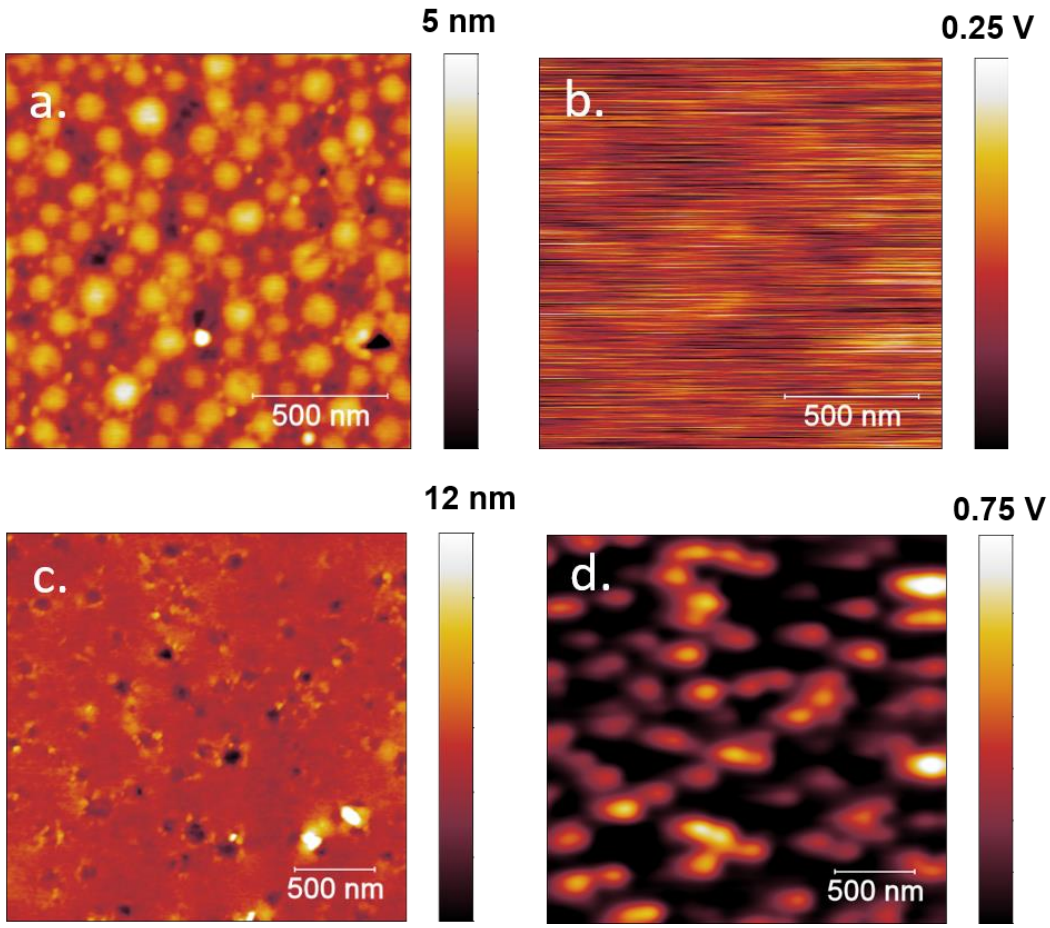

Figure 5.7 a. AFM image in topography for Latex 2-GO based composite at 2wt. %. b. KPFM image Latex 2-GO based composite at 2wt. %. c. AFM height sensor image for Latex 2-GO based composite at 2wt. % after reduction at 150 °C. d. KPFM image of Latex 2-GO based composite at 2wt. % after reduction.

A confirmation of what is shown in the AFM height sensor images is given by the electron micrograph pictures at a different order of magnification observable in Figure 5.8 a.b.c.d.e.f which perfectly show the presence of the rGO flakes within the matrix. In big areas of the specimen (Figure 5.8 d.e.) all the cavities appear exhibiting a similar pattern as in the KPFM. The flakes are homogeneously spread in all the surface of the specimen proving that rGO particles pathway is formed. However, it is also interesting to notice that GO flakes seem to be more concentrated into these cavities. This could explain why in the KPFM the most intense features come from that part of the composite. The presence of pitting in the polymer indicates that in regions of high GO concentration we have polymer degradation from the evolved heat of this exothermic reaction. This highlights the fact that there is a direct interaction between GO and the polymer system when higher temperature is used. In fact, the thermal treatment not only brings to the production of highly reduced GO but it also induces the aromatisation of the polymer (as explained later in chapter). This points to a strongly synergetic effect between both elements.

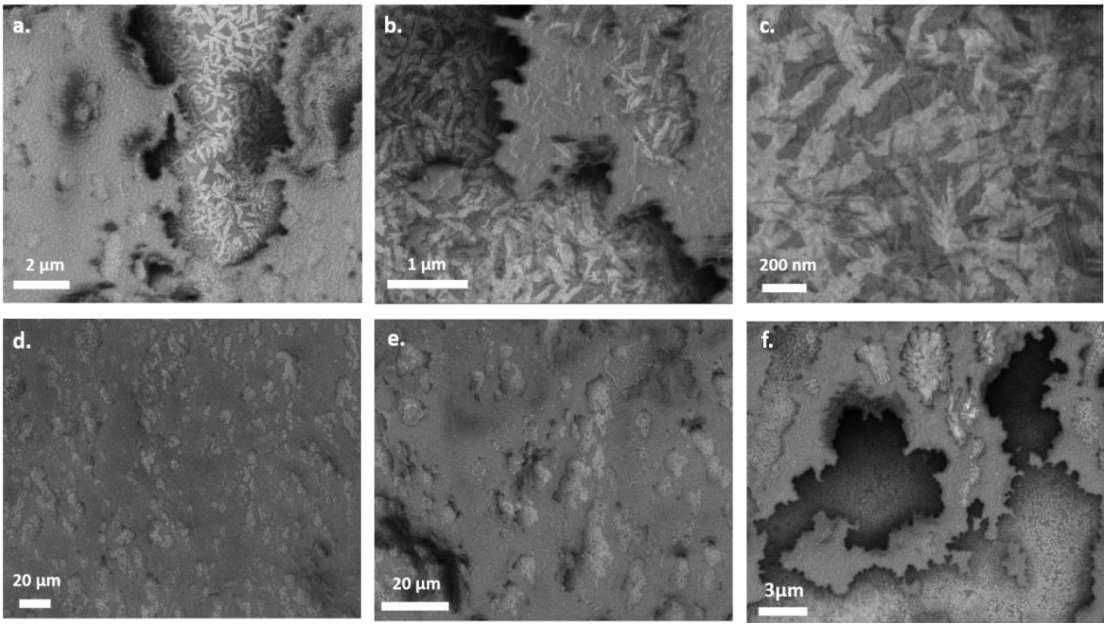

Figure 5.8 a.b.c.d.e.f. Micrograph images of Latex 2-rGO based composite at 2 wt.% of rGO at different orders of magnification.

Subsequently, EDS analysis has been done in order to confirm that the flakes displayed in the SEM images are rGO and no other species. It is important to point out that this technique is used for qualitative analysis of the material [144], hence it can not give the

exact amount of the different elements present into the specimen. However, it is a powerful technique that can give an idea of the chemical composition of the sample. From Figure 5.9 A. is visible the same morphology of the composite, but in this case, with a charging effect due to higher voltage used to obtain the spectrum. Therefore, the image does not look as clear as before because the sample was further away to perform the measurement. Furthermore, spectrum 4 displayed in Figure 5.9 B., show the only presence of carbon and oxygen into the sample cavity. This is a further confirmation with the one mentioned before that inside the cavities of the sample there is a presence of rGO flakes.

Table 5.1 EDS results regarding the wt. % and atomic % of Carbon and Oxygen for Comp.2 with 2 wt.% of rGO.

Element	wt. %	atomic %
Carbon	73.50	78.70
Oxygen	26.50	21.30
Total	100.00	100.00

Similarly, in Figure 5.9 C. and D., EDS spectrums show carbon and oxygen peaks with the same intensity meaning that rGO flakes are homogeneously dispersed in the surface of the specimen. This measurement proves the argument previously done. All the EDS results are reported in Table 5.1.

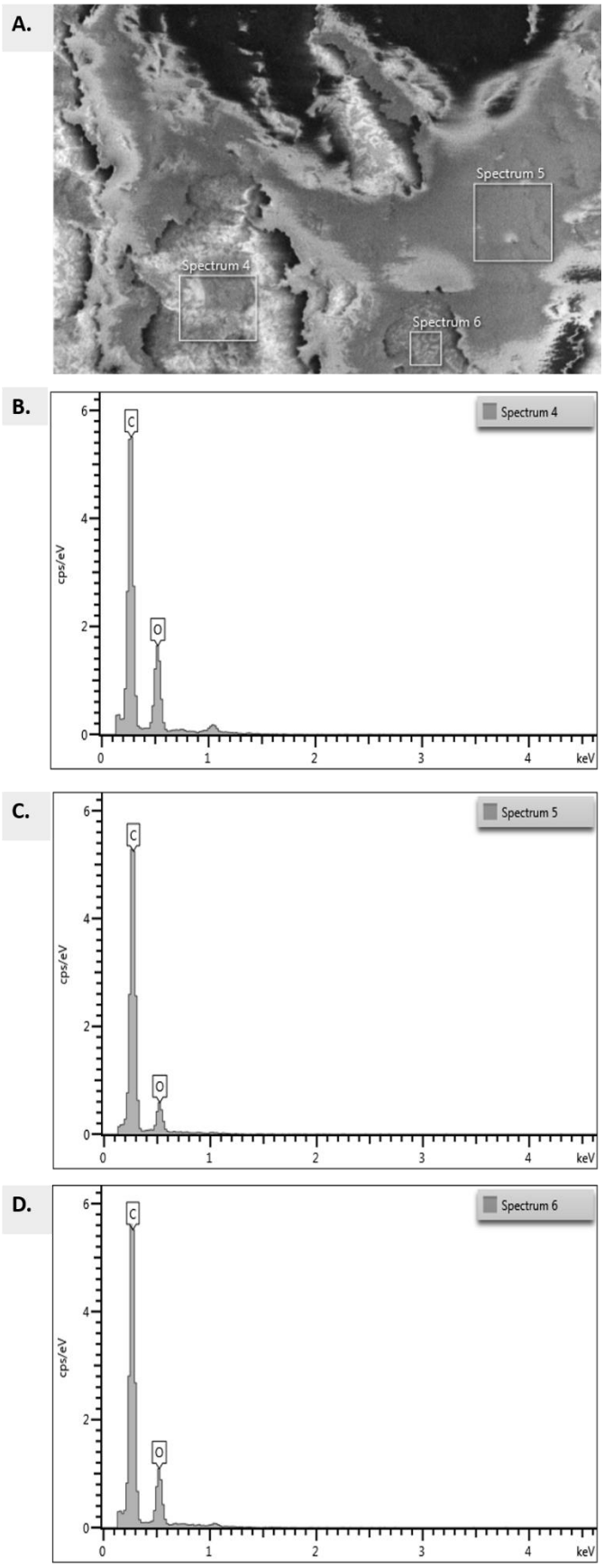

Figure 5.9 A. Electron Micrograph image of Latex 2-rGO based composite at 2 wt.% of rGO with B.C.D EDS spectrum results of Latex 2-rGO based composite with rGO concentration of 2 wt.%.

Afterwards, XRD and XPS analysis were performed in order to understand the chemical interaction among the polymer matrix and the GO nanoparticles. In Figure 5.10 a.b. are shown the XRD data for Latex 2-GO based composites before and after reduction respectively. Small and sharp satellite peaks are widely present in all the samples, possibly it can be ascribable to the impurities in Latex 2-GO based composites. The background has not been subtracted in order to maintain the visibility of all the observed features. The pristine polymer Latex 2 shows a broad band centred at around $2\theta = 20°$, very similar to those reported for NLR [208]. This band is maintained in all GO-based nanocomposites. The presence of GO is visible in the form of a shoulder at its most characteristic angle ($2\theta \sim 11°$). In particular, non-treated samples show clear evidence of the presence of GO. The treated samples show a somewhat different behaviour, particularly at higher GO loadings. The most interesting feature is a knee and progressive step increase of the background with increasing GO content, observed at low diffraction angles ($2\theta \sim 7°$), which could correspond to a long-range arrangement generated by the thermal treatment. Indeed, after the thermal treatment the crystallization peak turned into a two-feature peak, meaning that at least two different species are simultaneously crystallising, but only when the reduction has taken place, indicating a new species of aromatised polymer, most likely only in close proximity to the GO flakes, where the reaction is centred, creating a modified polymer junction between the filler and the bulk of the polymer matrix.

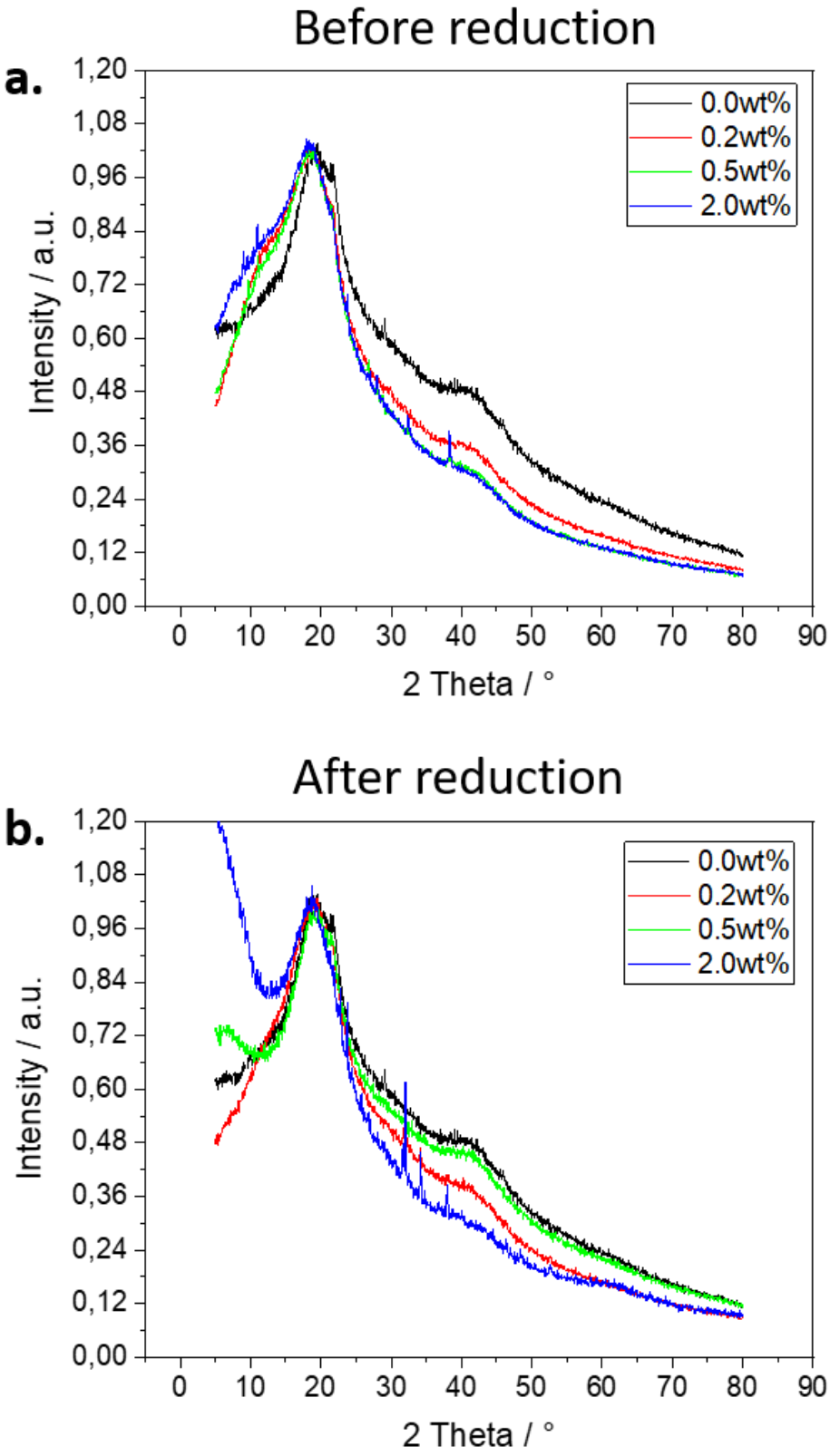

Figure 5.10 a.b. XRD patterns for Latex 2-GO based composites at different GO weight fraction before and after thermal reduction.

After that, the XPS was performed and the overall atomic surface composition obtained for all samples is displayed in Table 5.2 In general, samples contained C-O-S and K. The ash sample obtained after the TGA measurements contained also fluorine, but could be due to contamination from external materials, probably Teflon. In all the spectra (Figure 5.11 A.B., Figure 5.12 A.B. and Figure 5.13) the grey dots are the experimental measurements, while the red line is the envelope function (the sum of all deconvoluted components, which we tried to adjust as best as possible to the experimental data). Every component has always a particular colour, in order to facilitate the visual assignment.

Table 5.2 The overall atomic surface composition obtained for all samples.

	% C	% O	% S	% K	%F	Total
Pristine PL2	51.75	22.31	21.11	4.83	N/A	99.999
PL2 treated	52.31	41.59	4.94	1.16	N/A	99.998
PL2-2wt.% GO	44.78	46.75	7.84	0.62	N/A	99.995
PL2-2wt.% rGO	47.67	42.19	8.56	1.58	N/A	100.001
TGA residue	21.92	36.86	20.39	7.41	13.42	100

In Figure 5.11 A. the C 1s spectrum of the pristine Latex 2 is displayed, it is visible how the majority of carbon bonds are aliphatic sp^3, and also some oxygen bonds, corresponding to C-O and O-C=O, compatible with the latex composition (acrylates). Apparently, no C=C sp^2 component is noticed. After the thermal treatment seems that there is an incrementation of the oxygen groups, maybe due to the formation of polymer bonds and aromatisation and degradation of the GO into highly conductive, polymer bound rGO bridges.

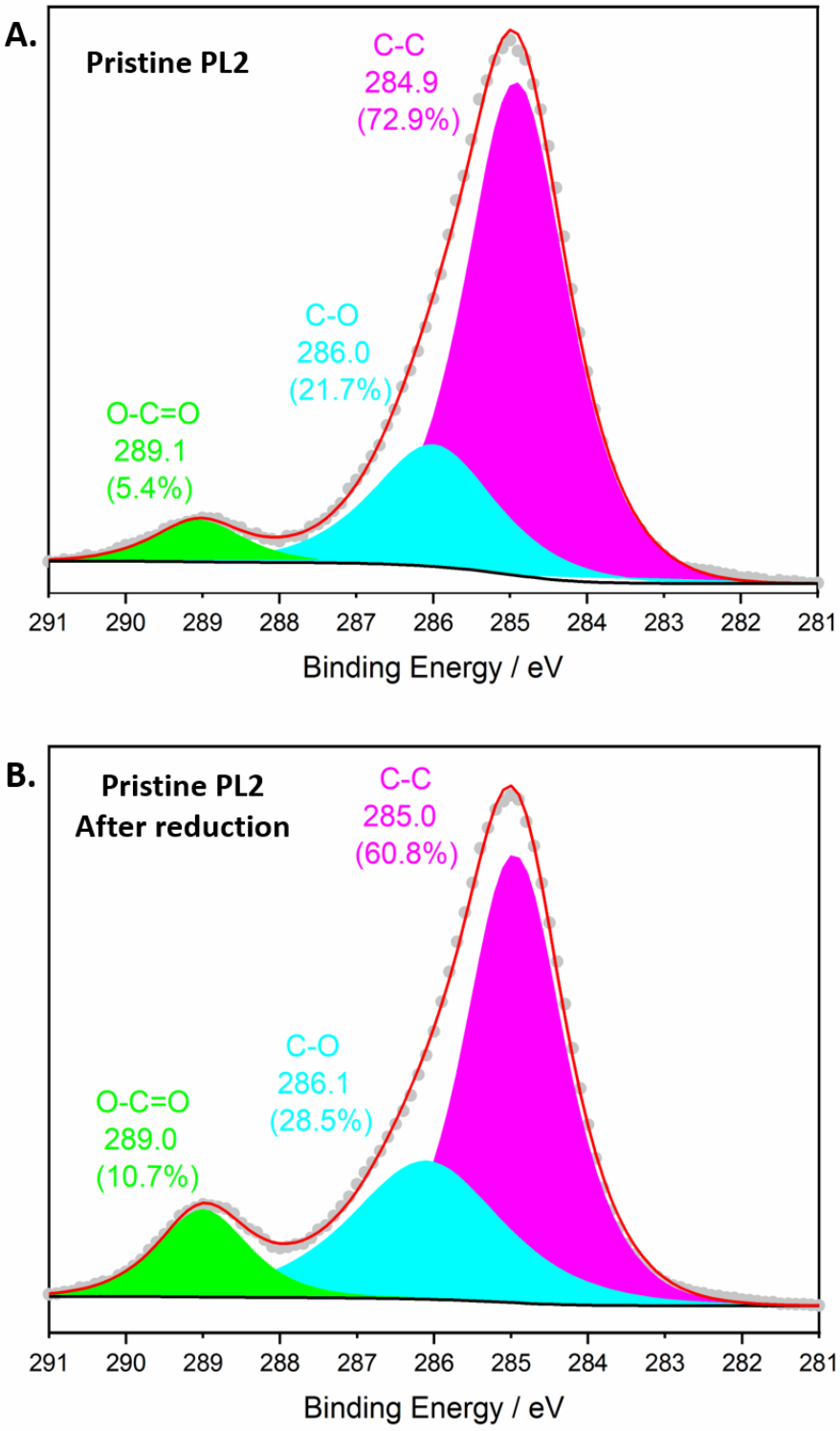

Figure 5.11 A.B. XPS of the pristine Latex 2 before and after reduction respectively.

Instead, when GO is incorporated into the matrix (Figure 5.12 A.), there is also a general increase of oxygen groups as it happens after the heating treatment of the pristine polymer. As XPS is a surface technique (~50 Å deep), we cannot distinguish if the treated Latex 2 has this oxygen only in surface or in the whole sample (as 2wt% GO is expected to be). When the GO composite is heated, it is clearly seen that a new C=C sp^2 component arises in the reduced sample compared to the untreated one as shown in Figure 5.12 B., proving that the in-situ reduction of GO has taken place. Another component also appears, at 290.8 eV, ascribable to π-π* shakeup of aromatic sp^2 carbons, and points that there is an aromatisation of the structure. Further, the C sp^3 component experience a significant upshift (now at 1.8 eV higher than its precursor sample), is compatible with aliphatic carbon bonds in benzene-containing polymers. Indeed, the signals are perfectly compatible with the equivalent carbons in Polyethylene Terephthalate (PET) polymers [209][210].

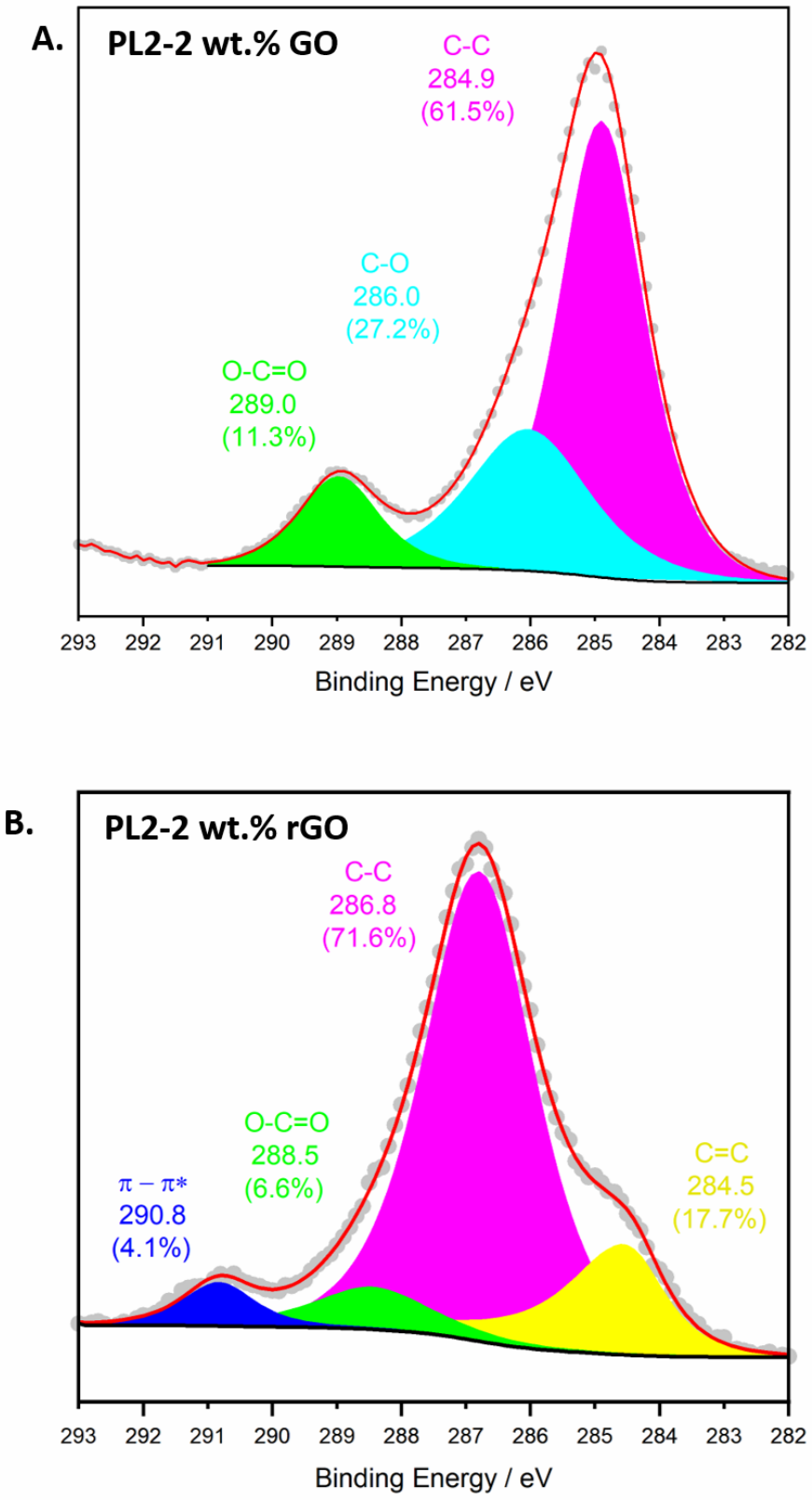

Figure 5.12 A.B. XPS of Latex 2-GO based composite at 2 wt. % of GO before and after reduction respectively.

PET has a similar structure to those acrylate polymers in Latex 2 but with additional benzene rings in the backbone chains. This would support the fact that not only GO experiences a thermal reduction but also that the polymer matrix experiences an aromatisation, which only happens in the presence of GO. The ash residue of the TGA measurement (Figure 5.13) is a much more complex profile. It presents a prominent C=C sp^2 component, the majoritarian feature, and no visible carbon-oxygen groups or sp^3 carbons, as could be expected for a fully pyrolysed sample. The high oxygen content in the survey composition of this sample could come from oxidized residual metals (such as K). Again, the π-π* shakeup can be assigned. The whole C 1s orbital in this sample can be visualised as the same situation for the 2wt% rGO (treated) sample but brought to the extreme. The presence of fluorine in the TGA residue, seen in the survey spectrum, is here denoted by a small component corresponding to aliphatic carbons bound to $–CF_2$-groups, perfectly compatible with fluorinated acrylates. Finally, the carbon signals are merged with the K signals. We can perfectly notice the two main components of the K 2p orbital. This did not happen in former samples, but an easy explanation could be that the TGA pyrolysis have altered the proportions of all elements, as it has removed a lot of carbon.

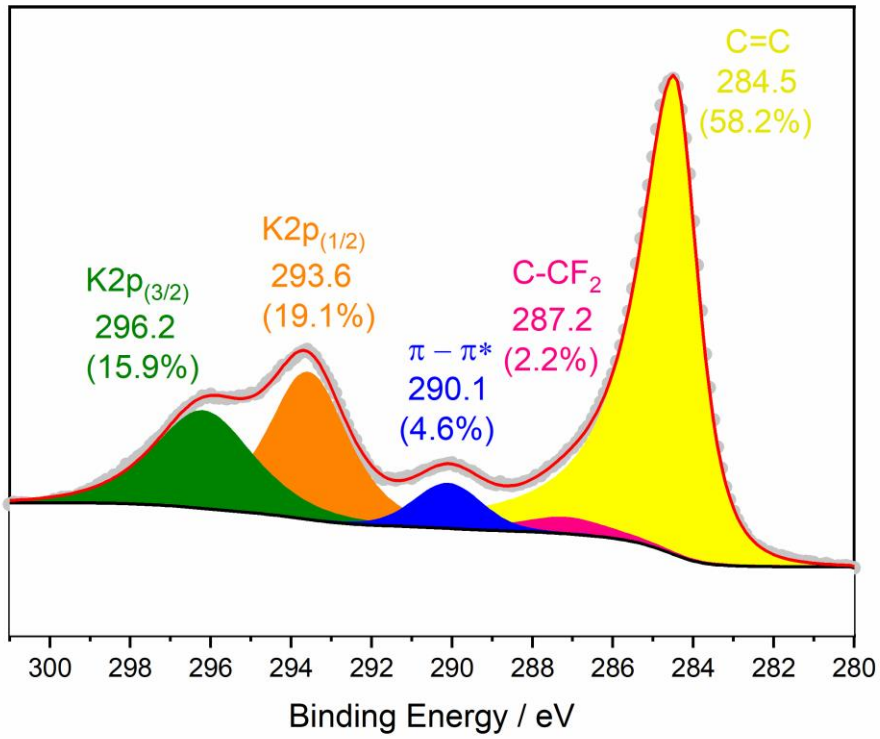

Figure 5.13 XPS of ash residue of the TGA measurement of Latex 2-rGO based composite with 2wt. % of rGO.

FTIR spectra (Figure 5.14) gives the confirmation as well that there is a formation of C=C sp^2 structure in Latex 2-GO based composite at 2wt.% after reduction, due to the presence of the C=C bond band at 1595 cm^{-1}.

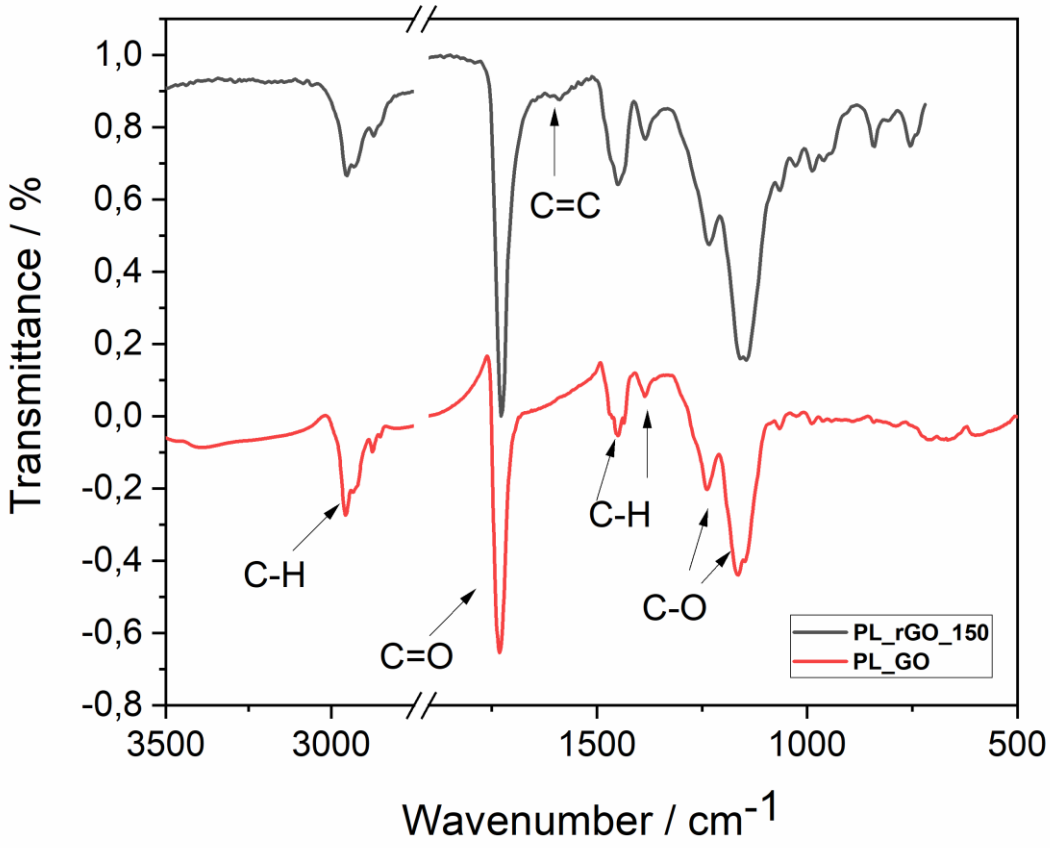

Figure 5.14 FTIR of Latex 2-GO based composite at 2 wt.% of GO before and after thermal reduction.

5.3.1 Proposed mechanism

For such a reduction to be occurring at low temperatures we infer that the latex itself is interacting with the functional groups on the GO. The evidence comes from the XRD, XPS and FTIR data shown before, that support the fact that not only GO experiences a thermal reduction but also that the polymer matrix experiences an aromatisation, which only happens in the presence of GO. Since GO contains various chemical functional groups on its edges and basal plane, it is difficult to predict a possible reaction mechanism between GO and polymer latex (MMA:BA: AA).

5.4 Electrical characterisation of the polymer-rGO based composites

After understanding the possible mechanism behind the reduction in situ of GO using a mild temperature, the next step was to examine the electrical properties of these systems. It is well known that when you have nanoparticles distributed in a polymer matrix there is a threshold at which the current can flow through the composite if the fillers are interconnected [211]. This phenomenon is governed by the percolation threshold theory as in Equation 5.5:

$$\sigma = \sigma_{\mathrm{PL}} + \sigma_0 \, (\phi - \phi_c)^t \quad for\ \phi > \phi_c \qquad \text{(Equation 5.5)}$$

Where σ is the conductivity of the composite, σ_{PL} is the conductivity of the matrix polymer, σ_0 is a proportionality constant (intrinsic conductivity of the filler), *t* is the critical exponent, whereas ϕ is the filler and ϕ_c is the percolation threshold. concentration, respectively. Electrical properties of the composites were investigated as a function of the rGO wt.% as shown in Figure 5.15 A. In the region below the percolation threshold, the system is not conductive, the electrical conductivity related to the polymer is shown, the nanoparticles are not enough to build conductive channels. As the filler concentration increases, continuous conductive pathways are developed until a certain critical volume fraction known as the percolation threshold. Beyond the threshold, the conductive network increases as the particle concentration increases until the electrical conductivity plateau remains flat. The composites are extremely conductive after the reduction process (10^3 S/m) indicating that we have a high level of reduction and a well segregated network within the composite. The conductivity is much higher compared to the rGO buckypaper treated at the same conditions as shown in the graph (Figure 5.15 A.).

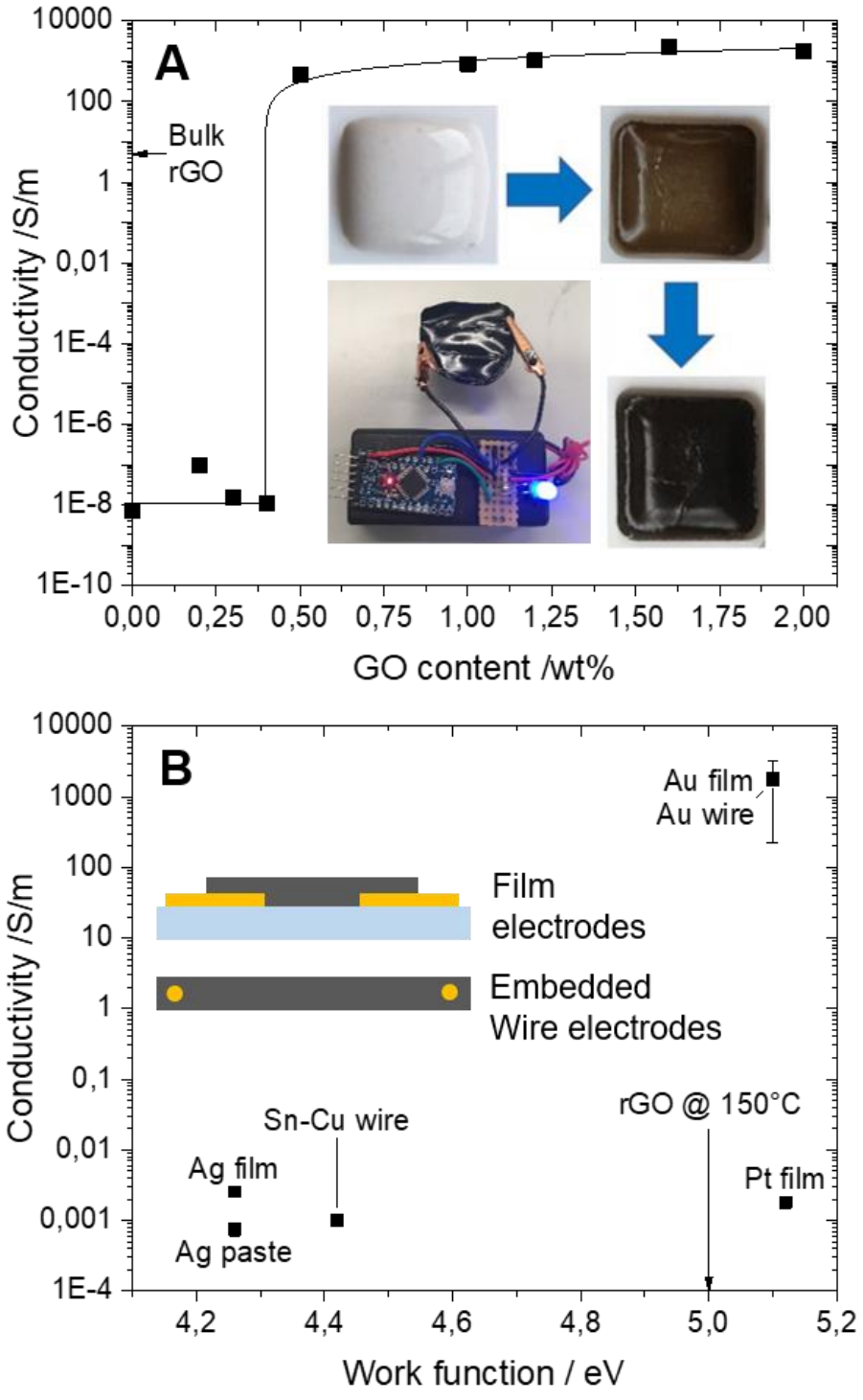

Figure 5.15 A. Absolute conductivity of polymer latex-rGO composites vs GO inclusion for reduction at 150ºC. (inset) photographs illustrating composite formation from aqueous dispersion to a uniform brown solid composite, to the final reduced composite after thermal treatment. The composite is conductive enough to allow current to flow and illuminate the LED light of the microscale device. B. Conductivity vs work function for different electrode metals. We observe the highest conductivities using gold in either a planar or embedded format (inset), which has a work function almost matching that of thermally rGO at the temperatures investigated here [212].

The thermal treatment applied here is much milder than is typically used to achieve high-quality graphene materials from GO. Despite this, it is surprising that the conductivities of the composites achieve relatively high values; especially considering the low filler content of the system. Curiously, it has been observed that the conductivity obtained is sensitive to the electrode material chosen, as shown in Figure 5.15 B. The highest conductivities are measured for gold electrodes, which we attribute to work function matching of the electrodes with the conducting network [212]. By fitting the measured conductivity data to Equation 5.5, it is found that the percolation threshold ϕ_c appears at 0.4 wt.% of rGO in good agreement with the theoretical value reported here, for particles of similar shape and aspect ratio [213]. The value of the critical exponent, t, is 0.7. The expected value depends on factors such as dimensionality, breadth of the distribution of conductivities in the network, and whether the filler is isotropically distributed [122]. Further, one may consider that GO reduction is a strongly exothermic process [206]; it is conceivable that strong, localised heating promotes the reduction of adjacent GO particles. In this model, the conductive network elements are no longer isotropically distributed but are spatially correlated. Such a scenario would be better described by "explosive" percolation [214][215], which typically is associated with much smaller scaling exponents.

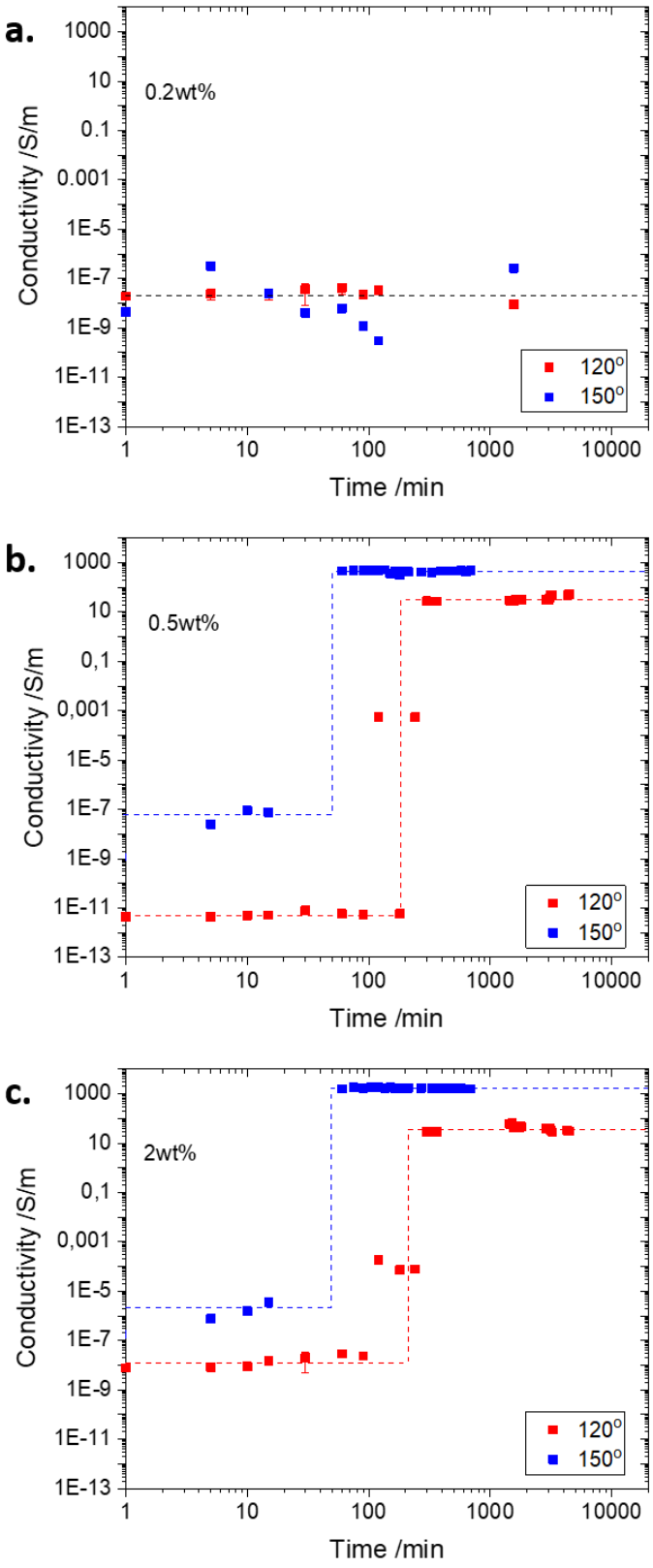

Figure 5.16 a.b.c. Conductivity vs time for 0.2, 0.5, 2 wt.% of composites during the reduction process at 120 and 150 °C.

The conductivity vs the time for various wt.% of rGO is presented in Figure 5.16 a.b.c. It is shown how the conductivity is changing with the time for the sample at 0.2wt. %, being below the percolation threshold, and indeed, the conductivity is very low because there is not enough filler to create a segregated network as mentioned before. In Figure 5.16 b. the 0.5 wt.% composite is shown; after 1 h of thermal treatment, the sample starts to be conductive, keeping the same value for longer treatment times. The same happens for the 2 wt.%, above the percolation threshold. It was also noticed that the change in conductivity happens before 150ºC, and then the systems follow the same behaviour.

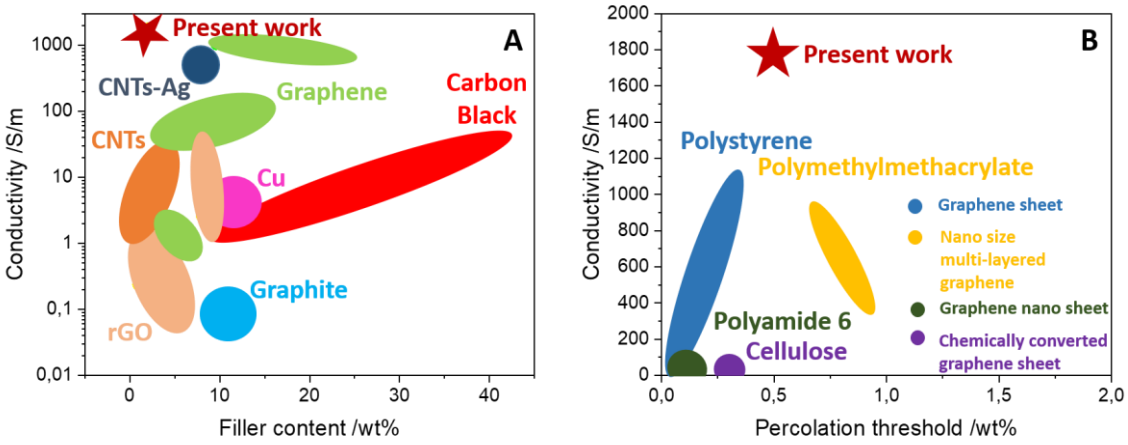

Figure 5.17 A. Bubble plot illustrating the wt.% of different filler which the maximum conductivity is achieved B. Absolute conductivity vs the percolation threshold for different polymer matrices.

The bubble plot in Figure 5.17 A.B. shows the absolute conductivity achieved beyond the percolation threshold vs weight fraction for a series of different fillers such as graphene, CNTs, CB, Cu, rGO etc and also compare to different matrices such as cellulose [95], PS [104][109][134], PMMA [216], polyamide 6 (PA6) [217]etc. All the references to build the bubble plot are shown in Table 1 in the Appendix at the end of the thesis. Our composites show the highest conductivity value of 1808 S/m with a percolation threshold of 0.4 wt.% of rGO.

5.5. Conclusions

In this chapter, the self-assembly method is described as more efficient for the formation of conductive pathways, resulting in lowering of the percolation threshold. The segregated network concept is not novel but has been explored extensively for conductive composites development [120] [130] [203]. Inspired by these previous findings, in this chapter, polymer Latex 2-GO based composites are presented. AFM image in Figure 5.2 a. confirms the achievement of the segregated structure for this system, in which GO nanoparticles are locked into the crystal lattice formed by the latex particles. After that, the reduction in situ of GO within a polymer latex matrix to produce highly conductive composites, after film formation is described. Taking advantage of GO properties is important from a processing perspective to produce well defined composites in aqueous dispersions, but then regain much of the electrical properties of graphene in a simple reduction step (Figure 5.15 A.). Moreover, these composites show the highest conductivity value of 1808 S/m with a percolation threshold of 0.4 wt.% of rGO. The conductivity is much higher than GO buckypaper treated at the same conditions (Figure 5.15 A., labelled as "Bulk rGO"), indicating some influence of the polymer matrix on the reduction process. The thermal treatment applied here is much milder than is typically used to achieve high-quality graphene materials from GO [42][43]. In spite of this, it is surprising that the conductivities of the composites achieve relatively high values, especially considering the low filler content of the system. Moreover, the reduction of GO is an exothermic process [206], and therefore, it is conceivable that strong, localised heating promotes the reduction of adjacent GO particles and may modify the polymer latex. Indeed, network formation may propagate from spontaneous initiation sites, in a manner typical of explosive percolation more so than the usual isotropically distributed filler case. XPS data strongly suggest that the reduction of the GO induces an aromatization of the matrix polymer. Localised aromatisation due to the highly exothermic GO reduction could explain the high conductivity of the composites. This points to a strong synergistic effect between the rGO and aromatised polymer latex 2. The thermal treatment can be modified to control the reduction. Higher temperatures can be used to increase the rate of reduction, or an almost room temperature process can be used over a longer period, where heating may be undesirable. This time and temperature dependence of the composites can make them excellent sensors (time-temperature indicators) (Figure 5.4). The fact that the temperatures are low and the time scales span

from minutes to several days, also makes them very practical sensors for the food industry for example. The other advantage of such a sensor is the ‘switch on’ effect of the reduction, the composites become conductive at a certain time and/or temperature and so could be used for direct display indicators for future applications as time/temperature sensors.

Chapter 6

Electrical properties of NLR-rGO-based composites

NLR is one of the most attractive elastomers and is extensively used in industrial areas, such as pneumatic tyres and vibration isolation systems. Depending on the desired applications the properties of the NLR can be modulated by using several reinforcing fillers such as CB, silica, CNTs etc [218] [219] [220] [221]. It is known that there are difficulties in dispersing exfoliated graphene in the rubber matrix, due to their smaller thickness and strong van der Waals interaction forces. To deal with these issues, researchers tried to use GO instead, in order to obtain uniform dispersion with the matrix, followed by reduction of the GO to restore the electrical properties of graphene. Zhan *et al.* [222] proposed an ultrasonically assisted latex mixing and in situ reduction process to prepare graphene-NR composites. GO was first ultrasonically dispersed into NLR and then reduced in situ by hydrazine hydrate, followed by latex coagulation, to obtain the graphene-NLR masterbatch. Afterwards, they managed to obtain graphene-NLR composites [223] with a conductive segregated network exhibiting an electrical conductivity of 0.03 S/m at 3.56 wt.% of graphene and a percolation threshold of 1.24 wt.%. The reduction of GO has been done by the use of hydrazine and subsequently they have added a crosslinking agent to obtain the graphene-NLR composite. However, they could not avoid the flocculation and re-stacking of the rGO platelets. Hernández *et al.* [224] prepared FGS-NLR composites, reducing the GO at 1000 °C under inert atmosphere, and then directly mixing the filler and rubber in an open two-roll laboratory mill. Inspired by these previous findings, NLR-rGO and graphene-based composites are presented. In this chapter, the electrical properties of both systems are provided. Afterwards, starting from the idea that graphene could provide the opportunity to act as an impermeable barrier, its possible application is also described.

6.1. Reduction in situ of GO in NLR composite and time-temperature study

In this work, the reduction of the GO has been done in situ, simplifying the process and using a much milder thermal treatment, after the dipping method as discussed in Chapter 3 in the experimental section. In order to investigate the process energetics, a study of time-temperature dependence of colour and conductivity was performed. As described in section 5.2 of Chapter 5, it is possible to see that the system follows the Arrhenius relationship for time and temperature identifying the colour onset. In Figure 6.1 a. is displayed the plot of ln [time] vs 1/T for NLR-rGO based composite. A linear behaviour is shown and the inset images illustrate the colour change before and after reduction of the system. The maximum temperature reached for this system is 130 °C due to the degradation of the NLR at higher temperatures. This is a result of the breakdown of the carbon-sulphur bonds, which limit the temperature range that can be investigated and make the high temperature exothermic regime, shown for the synthetic latex 2, beyond reach.

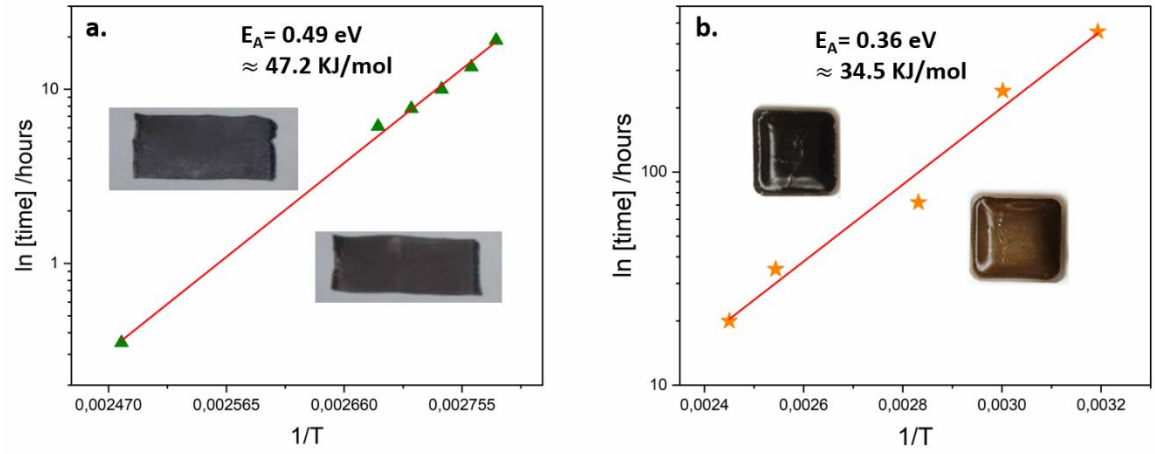

Figure 6.1 Ln [time] vs 1/ T graph. (inset) photographs illustrating the colour change (brown to black) of the composite before and after reduction for a. NLR-rGO based composite and b. Latex 2-rGO based composite.

Conversely, the minimum temperature that could be reached was 85 °C due to the fact that under this value the composite was still wet and indeed it was impossible to measure the respective conductivity and the colour change. At this point it was important to start comparing results for the NLR-rGO system to the results found for the Latex 2-rGO

system, previously discussed in Chapter 5. In this chapter section, only the process that occurs in the low temperature regime due to the degradation of NLR polymer while using higher temperatures is described. In Figure 6.1 b. the plot ln[time] vs 1/T Latex 2-rGO based composite is shown. In this case, it was possible to conduct the same experiment from 40 °C to 135 °C due to the T_g of Latex 2. In fact, the T_g value of Latex 2 is approximately room temperature, and this means that the drying process happens at lower temperatures. Comparing the two systems, it is possible to prove that E_a values for both processes are very similar, 0.49 eV for NLR composite and 0.36 eV for the synthetic one (Latex 2). The fact that in both systems the E_a values are comparable for analogous temperatures means that there is something related with GO properties and the interaction with the polymer matrix. In fact, GO can act as a initiator and react with the polymer species even using low temperatures (40-135°C) [225]. However, using these conditions slows down the speed of the reaction because higher E_a values can be reached only using higher temperatures (>150 °C) when GO exhibits an explosive reaction [204] as shown in Chapter 5. The main difference in the two systems is ascribable to the different chemical composition of the polymer. The Latex 2 is much more reactive than the NLR due to the presence of monomers such as MMA, BA, AA that introduce some functional groups such as carboxyl and hydroxyl groups in the copolymer matrix. The chemical structure of these monomers is reported in Figure 2.10 in Chapter 2. These functional groups are reactive, and as discussed before in Chapter 5, they can polymerise with the GO nanoparticles leading to an aromatisation of the structure. In contrast, NLR is by definition highly stable, and it mainly consists of high molecular weight isoprene (2-methyl 1,3-butadiene) [84] as shown in Figure 2.11 in Chapter 2. At the end of its macromolecules, there are also non-isoprene units such as amino acids, proteins and phospholipids that are surrounded by a surface of rubbery particles which gives them a negative charge, guaranteeing the latex stability [85]. In order to harden the NLR matrix, a vulcanisation process is used. The vulcanisation brings better durability and rigidity in the mechanical properties of the rubber. In general, sulphurs are the most used and they react with the allylic hydrogen atoms adjacent to the double bond in the NLR, and therefore some of these C-H bonds are replaced by chains of sulphur atoms. The most probable mechanism behind the reduction in situ of GO can be explained by a redox reaction. It is likely that the sulphurs can oxidise and the GO in turn reduces. The redox reaction is shown below.

$$GO_x + S \rightarrow SO_x + G \qquad (6.1)$$

It is possible that sulphur oxidation happens due to its bond breaking that may happen easily with light or with a thermal treatment at 60 °C. The FTIR spectra in Figure 6.2 shows some important features that confirm this argument. Before the thermal treatment, the FTIR spectra shows features related to the GO flakes such as the O-H stretching mode at 3428 cm^{-1}, the C-H stretching mode at 3012 cm^{-1}, the carboxyl band at 1828 cm^{-1} and a band that corresponds to the ether/epoxide groups at 1060 cm^{-1}. After the thermal treatment a sharp band appears at 1390 cm^{-1}, related to the sulphur-oxygen bond formation due to the oxidation of the sulphur group. A band also appears at 1512 cm^{-1}, ascribable to the C=C sp^2 due to the reduction *in-situ* of GO.

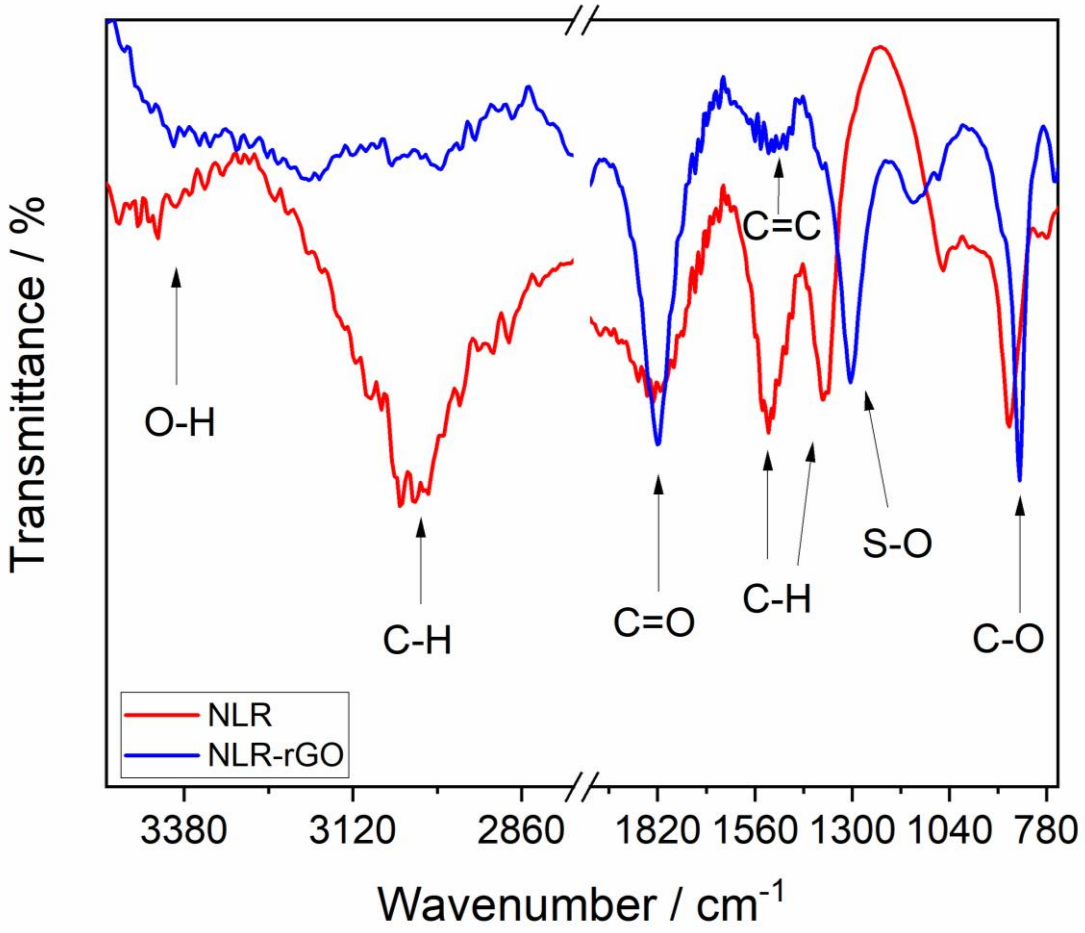

Figure 6.2 FTIR spectra of NLR-GO before and after the treatment at 130 °C for 30 min.

6.2. Evaluation of electrical conductivity and the determination of the percolation threshold for natural rubber-rGO based composites

The electrical conductivity measurements were performed as described in the experimental procedures section in Chapter 3. Figure 6.3 A. shows clear percolation behaviour for the NLR-rGO based composite post thermal treatment at 130 °C for 30 min.

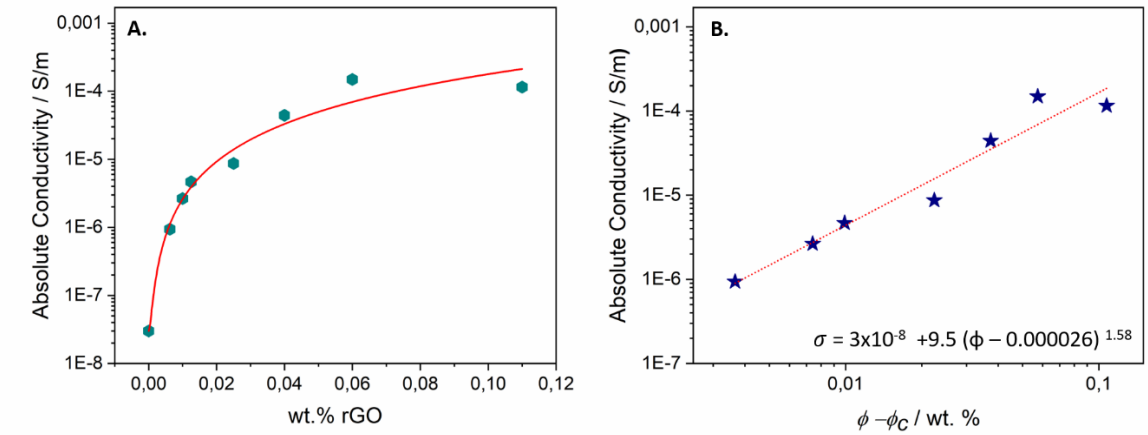

Figure 6.3 A. Absolute conductivity of NLR-rGO composite for reduction at 130 °C. B. Plot on log-log axes of electrical conductivity as a function of (φ-φ_c) of the NLR-rGO composite.

A significant conductivity enhancement (over 4 orders of magnitude greater than the latex matrix) was observed indicating the formation of a percolating rGO network at very low concentrations of rGO. The electrical conductivity reached 10^{-4} S/m and by fitting the measured conductivity data with Equation. 5.5 in Chapter 5, the percolation threshold appears at approximately 0.002 wt.%. The electrical conductivity value at such mass fraction is very low, near to Apollonian packing. The maximum conductivity reached is less than the reported 0.03 S/m [6], but the percolation threshold in this work is significantly lower than predicted. The explanation appeared after taking DLS measurements, as shown in Figure 6.4. The results show that our NLR dispersion is a bimodal system and contains small particles of 60 nm and big particles of 400 nm. This gives a size ratio of 6.7, which is the theoretical value for the perfect filling of the voids between the large particles with the small particles. This feature allows the rGO flakes to form a conductive pathway in the composite [226] [227] [228]. In order to investigate the dimensionality of the conductive rGO network, a least-squares linear regression on log-transformed data was performed (Figure 6.3 B). Because the density of rGO can be only

approximated, the mass fraction of rGO is preferred, rather than the volume fraction, for fitting the experimental data. A value of 1.58 was obtained for the critical exponent (t).

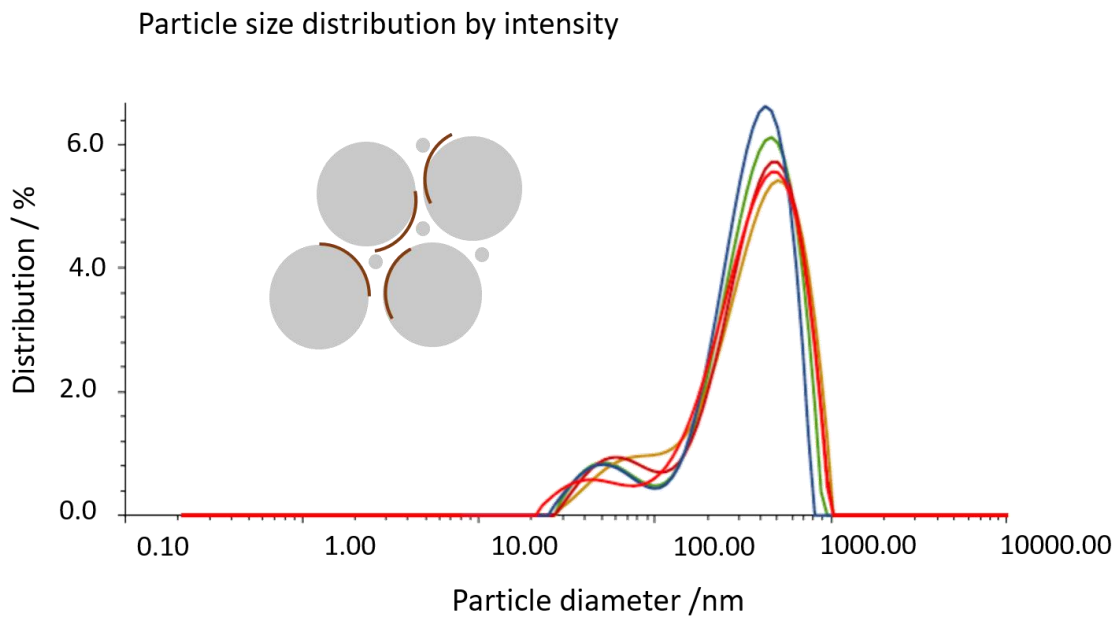

Figure 6.4 DLS analysis of the particle size in the natural latex dispersion. The data are presented on a logarithmic x-axis.

According to the literature, a theoretical value of $t \approx 2$ was estimated for a percolation network in three-dimensions [123] [124] and between 1-1.33 for a two-dimensional system [122]. The value obtained in the present work closely match the theoretical predictions for the critical exponent (t) in three-dimensional networks. Theoretically, the value of the constant σ should approach the conductivity of rGO. For a bimodal polymer packing arrangement, the minimum percolation threshold is posed at 0.03 [229] [230]. The fact that there exists a universal minimum percolation means that there is a limit due to the shape of the structure and the void space among the particles. This is significant when combining the percolation with the particle packing, which affirms that the void structure of a system is strongly dependent on the size and the shape of the particles and how the latter can pack after drying. Brouwers [226][227][228] defined a function for how the void fraction would vary for all the lattice systems and this is reported in Chapter 7 (Equation 7.1). The NLR-rGO system has a percolation threshold value that is much

lower compared to the universal one calculated by Brouwers. This may be due to the evolutionary optimised system of NLR, or may be a result of a limitation to the network that we have not taken into account, perhaps due to the coalescence of the particles (described below in section 6.3).

6.3. Morphology evaluation of NLR-rGO based composites

AFM and SEM investigations, in Figure 6.5 a.b.c and Figure 6.6 a.b.c.d. respectively, show that the solid composite does not display any structured morphology. This means that the packing must happen when the NLR particles are dispersed with the GO flakes, before the film forming and the fillers are trapped. The contrast in the SEM images in Figure 6.6 a.b.c.d indicates that there is conductivity within the system, as otherwise there would be charging. This means there must be some conductive network within the matrix that is not visible as the particles coalesce. In the synthetic system shown in Chapter 7, the particle boundaries remain even after film formation due to the presence of a surface modification, so the network is clearly present throughout.

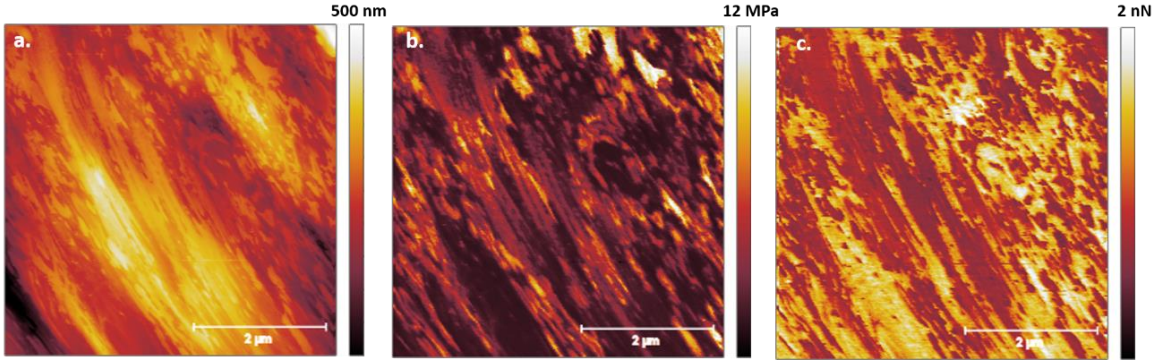

Figure 6.5 a. AFM image showing topography of the NLR-rGO based composite. b. DMT-modulus (related to the Young's Modulus, showing different interactions between the NLR polymer and the fillers. In principle the darkest part is the polymer and the brighter part is the filler). c. Adhesion showing again the different probe interaction with the polymer and with the rGO flakes.

This is well explained in the schematic picture shown in Figure 6.7, which illustrates the formation of conductive networks in both systems. In the polymer latex system, after the polymer deformation, the rGO flakes fill the interstices between the small and the big

spheres of the latex and the conductive network is clearly visible in the sample surface using AFM and SEM measurements (Figure 7.6 a.b. and 7.7 A.B.C. in Chapter 7). Contrary to this, for NLR system, the conductive network is not visible in the matrix surface (as shown before) due to particle coalescence.

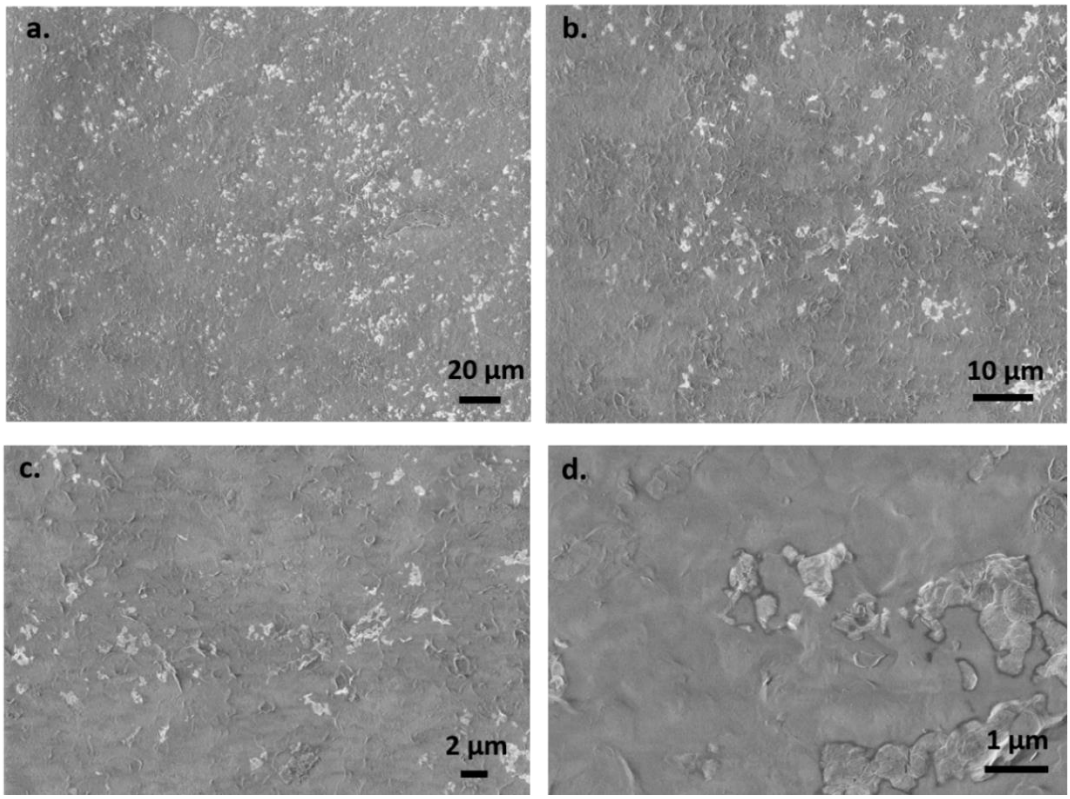

Figure 6.6 a.b.c.d. Electron micrograph of uncoated NLR-rGO based composite surface at different orders of magnification. They do not show any structured morphology in the matrix surface.

This phenomenon can be explained by the fact that the polymer latex has a T_g ~40°C, and after the deformation step, the latex particles start to deform in the dodecahedral array. In the NLR system, instead, a polymer diffusion across the particle-particle boundaries takes place, and the rGO flakes diffuse into the latex particles due to the low Tg (-70 °C) of the NLR. So, after deformation, it diffuses and coalesces and does not preserve the same array as the synthetic latex matrix (as shown in Figure 6.7). However, the low percolation implies there must be a segregated network of some sort.

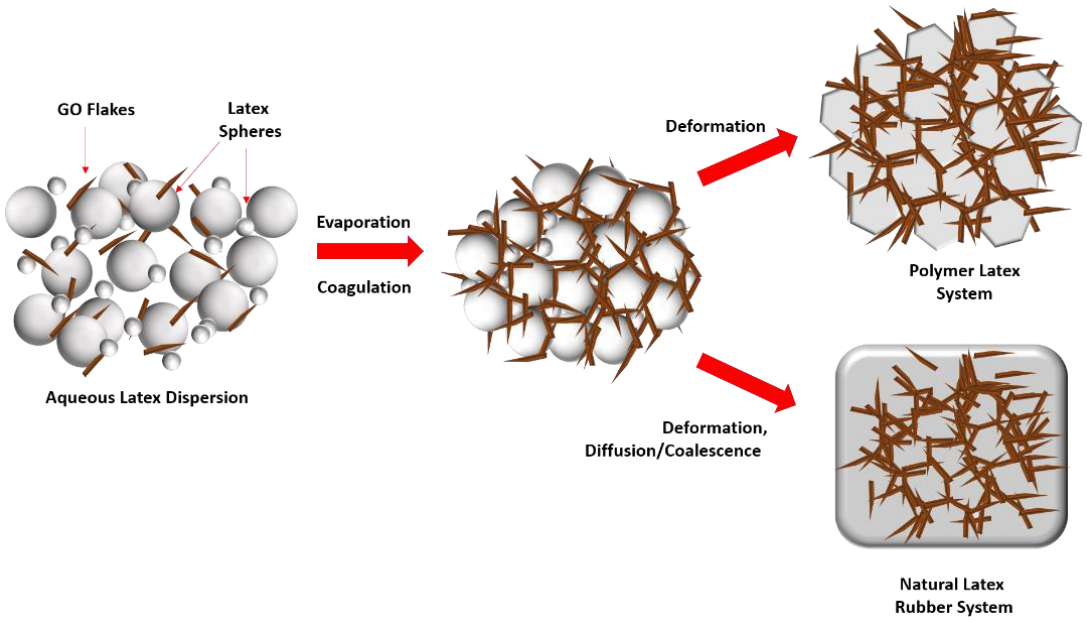

Figure 6.7 Schematic illustration of the formation of conductive networks for the polymer latex system and for the NLR system.

6.4. Electrical characterisation of NLR-graphene based composites

In this section, the electrical properties related to the NLR-graphene based composites are described. The idea is to compare the electrical properties of the NLR-rGO and graphene-based composites in order to understand how these properties change as the filler is changed. Exfoliated graphene is used in order to obtain a homogeneous dispersion. The sample preparation is explained in Chapter 3. In Figure 6.8 the absolute conductivity vs the wt.% of graphene for the NLR-graphene based composite is shown. As discussed in Chapter 2, graphene possesses a high conductivity of ~1 x 10^2 S/m [231], but when added into NLR matrix the maximum conductivity reached is 3.67 x 10^{-4} S/m at 5 wt. %. The value does not seem to deviate a lot from the value obtained using rGO. Indeed, the electrical conductivity for NLR/rGO based composites is 10^{-4} S/m with 0.06 wt.%. It is clear that in order to obtain a similar value with graphene it is necessary to use more material as shown in Figure 6.9. This implies that the reduction of the GO in situ is a highly effective method of creating conductive rubber composites. There are two possible reasons for the graphene composite not outperforming the rGO composite. Firstly, the homogeneity of the dispersion within the composite is not as high, due to the hydrophobicity of the graphene compared to the water dispersibility of the GO.

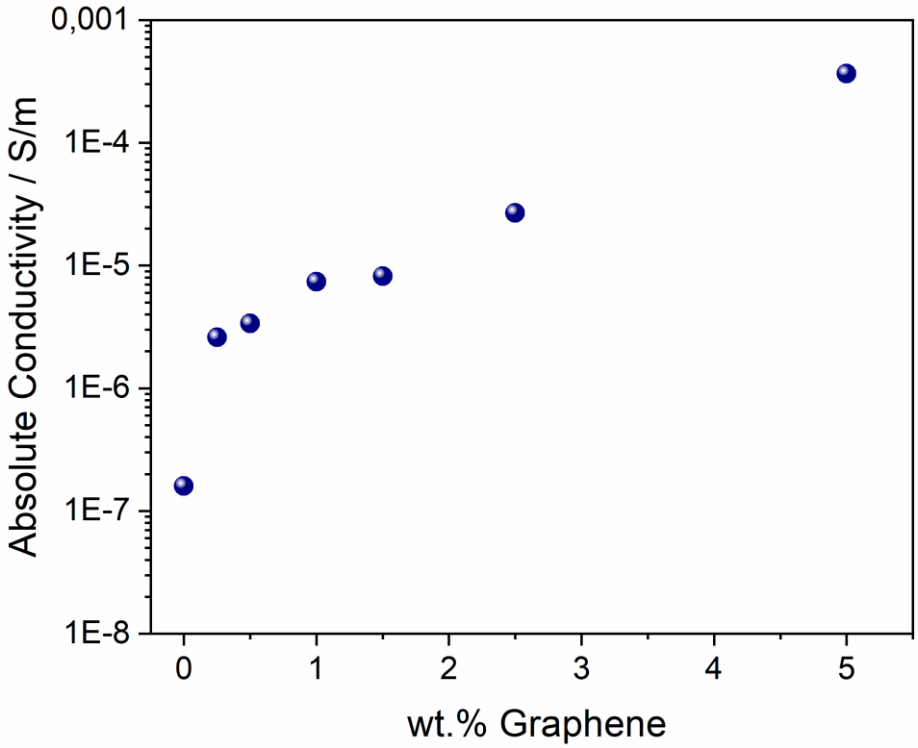

Figure 6.8 Absolute conductivity of NLR-graphene based composite.

Secondly, the reduction process creates an intimate bond between the matrix and the filler, with this interface being the usual failure point for composites. The intimate interaction due to the reduction process provides better pathways for electron transport. The higher solid content for the GO shown in Figure 6.9 will aid in the homogeneity of the composite, as there is less opportunity for aggregation of the filler in the excess water, and a tighter contact of the fillers with the polymer particles.

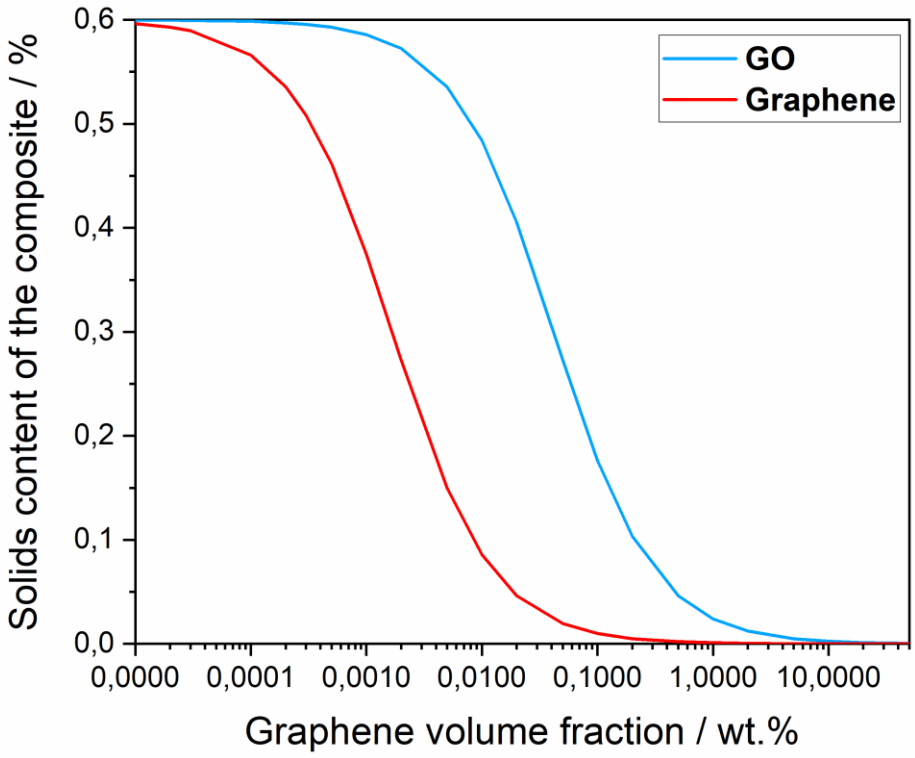

Figure 6.9 Graphene volume fraction in wt.% vs solid content of the composite dispersion for the GO and graphene fillers.

6.5. Prevention of liquid permeation in graphene-NLR composites

It is well known that graphene can provide advantages beyond just electrical conductivity. It is chemically inert and provides the opportunity to act as an impermeable barrier and thus reduce the material permeation. For this reason, it was proposed to use graphene to create a glove in order to increase the permeability of normal NLR while using different solvents such as acetone and isopropanol (IPA). In Figure 6.10 the graphene glove prepared using 4 wt.% of graphene in NLR dispersion is displayed. The permeation test is described in Chapter 3 and the results are shown in Figure 6.11.

Figure 6.10 NLR-Graphene based glove.

Unfortunately, the permeability of the graphene glove gets worse with both solvents (acetone and IPA) compared to the NLR glove. When acetone is used as a solvent, there is a huge difference in terms of permeability compared to the NLR itself. Conversely, there is a minimal difference while using IPA as a solvent. In both cases, better permeability is achieved using the NLR glove instead of the graphene glove. The permeation values are reassumed in Table 6.1 below.

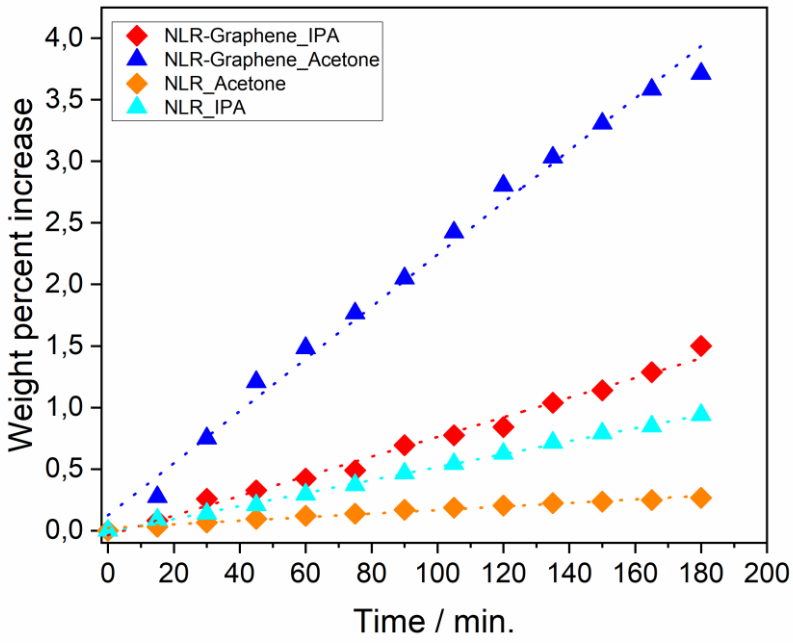

Figure 6.11 Permeation test: weight percent increase vs time for ▲ NLR-graphene_acetone; ◆ NLR_acetone; ◆ NLR-graphene_IPA and ▲ NLR_IPA.

At this point, it is worth providing an explanation for why graphene-NLR based composites do not give high conductivity results and do not increase the permeability of the NLR glove. Probably, in this case, the graphene is more rigid than required to conform to the particle packing. Therefore pores are created within the structure, rather than the graphene forming a continuous network as desired. It is also important to point out that to create an impermeable barrier, a much higher fraction of graphene is required but this brings difficulties in terms of composite processing.

Table 6.1 Permeability values for NLR and NLR-rGO based composites for different solvent.

Sample	Permeability/ g x 100/min
NLR_Acetone	$0.001 \pm 6.3 \times 10^{-5}$
NLR-rGO_Acetone	$0.021 \pm 5.7 \times 10^{-4}$
NLR_IPA	$0.005 \pm 6.3 \times 10^{-5}$
NLR-rGO_IPA	$0.008 \pm 2.4 \times 10^{-4}$

6.6. Conclusions

In this chapter the electrical properties of NLR- based composites using rGO and liquid exfoliated graphene as a filler were reported. The reduction in-situ of GO using a mild treatment after the dipping process was described. The time-temperature relationship to the conductivity based on colour change was also investigated. The colour change study was then compared to the one done for the Latex 2-rGO system described previously in Chapter 5. NLR-rGO based composites also follow Arrhenius behaviour. The two systems possess similar E_a values, 0.49 eV for NLR based composite and 0.36 eV for the synthetic (Latex 2) composite. The fact that in both systems the E_a values are comparable for analogous temperatures means that the dominant factor is something related to the GO properties and the interaction with the NLR. In fact, GO can act as a initiator and react with the polymer species even using low temperatures (40-135°C) [225]. However, using these conditions slows down the speed of the reaction because higher E_a values can be reached only using higher temperatures (>150 °C) when GO exhibits an explosive reaction [204] as shown in Chapter 5. The main difference in the two systems is ascribable to the different chemical composition of the polymer. The Latex 2 is much more reactive than the NLR due to the presence of monomers such as MMA, BA, AA that introduce some functional groups, like carboxyl and hydroxyl groups, in the copolymer matrix. These functional groups are reactive, and they can polymerise with the GO nanoparticles leading to an aromatisation of the structure. Another difference is related to the T_g value and this affects the surface morphology of the samples. Indeed, for NLR systems, AFM and SEM images (Figure 6.5 a.b.c. and Figure 6.6 a.b.c.d.) do not display any structured morphology. The packing must happen when the GO flakes are dispersed in NLR matrix. This is because after deformation the GO particles diffuse into the NLR particles due to low T_g, and coalesce without preserving the array structure. Instead in the synthetic system, the particle boundaries remain even after film formation due to the presence of a surface modification, so the network is clearly present throughout. The differences in polymer properties are reflected in the electrical conductivity performance. In fact, NLR-rGO composite does not reach the same level of conductivity reached for the synthetic system (Latex 2-rGO based composite) because the high temperature explosive reduction regime cannot be accessed due to the NLR degradation. Subsequently, the electrical properties of the NLR system were studied using graphene as a filler. For NLR-rGO and graphene-based composites the electrical conductivity has similar values, but is markedly

different in the amount of filler needed to reach that value. It is clear that in order to obtain a similar value with graphene it is necessary to use more materials or more monolayer flakes. This implies that the reduction of the GO in situ is a highly effective method of creating conductive rubber composites. Subsequently, starting from the idea that graphene provides the opportunity to act as an impermeable barrier, a graphene glove was created in order to increase the permeability of the normal NLR glove. The permeation test was performed using different solvents such as acetone and IPA. Unfortunately, the permeation test displayed in Figure 6.11 shows that the permeability of the graphene glove is getting worse while using both solvents compared with the NLR glove itself. In this particular case, it is conceivable that graphene sheets are creating pores in the sample structure and are not acting as an impermeable barrier.

Chapter 7

Apollonian packing using a bimodal system

In this chapter results of a synthetic latex particle packing and percolation threshold for a bimodal system using graphene sheets are presented. It is well known that in order to enhance the electrical properties of polymer-based composites it is important to create a conducting network, and therefore play with the volume of filler that is required to reach the percolation threshold. Almost 2000 years ago Apollonius and Perga [232] proposed the concept of filling the interstices of large particles with smaller particles. Later, in 1920, Furnas [233][234] described the possibility for particles to pack in the same way as shown by Appollonius, using a bimodal particle system. In this way, he gave the possibility of creating composite materials that possess high density and low void fraction. In 2010, King [235] used a bimodal system to create CNTs-Latex composites. In her work, the bimodal system was used to maximise densities of the system and hence reduce the percolation threshold for electrical measurements. CNTs were forced to fill the reduced void space and form a connected network using lower volume of filler. It has been shown that there is a direct dependence of the percolation threshold on the void fraction of the polymer matrix, and it can be controlled through particle choice. Starting from these previous findings, a bimodal system of particles used to create graphene-based composites is illustrated in this chapter. The idea was to use bimodal system packing to maximise densities of the system and hence reduce the percolation threshold for electrical measurements. Moreover, understanding how the conductivity and the percolation threshold change while using different fillers was desirable. Therefore, graphene-based composites have been compared with the CNTs-Latex composites studied previously by King.

7.1. Bimodal system packing

For a long time, mixing different sized particles has remained an academic exercise through interest in geometric and theoretical modelling. In fact, almost 2000 years ago Apollonius of Perga [232] [236] proposed the concept of packing smaller particles into the interstices of large particles. The approach was a two-dimensional 'gasket' as shown in Figure 7.1.

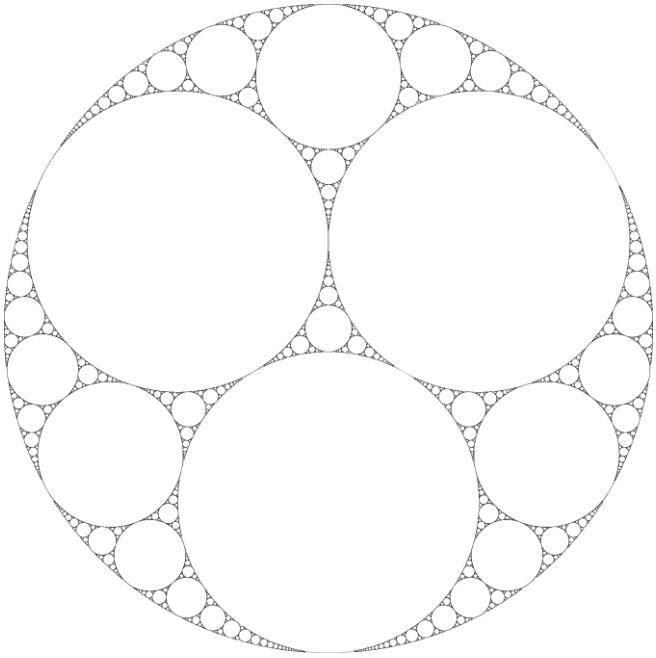

Figure 7.1 Apollonian gasket constructed from 10 million points. The smaller circles are filling the interstices of the previous sized circle [236].

This type of system can be used for some real world situations such as porosities in aggregates in oil drilling and for sands. Particles packing in bimodal systems have been studied for a long time. It has primarily been considered in two different ways. Experimental studies of particle packing to minimise the void space [237] and two-dimensional computer simulations to correlate the experimental results [238]. In 1920, Furnas [233][234] studied the density of grains in a furnace system as part of a study into gas flow through particle beds. He established a set of equations that defined the density of a bimodal system and he found that if two sets of particles are mixed with the small particles being small enough to fill the interstices of the large particles than the void fraction is always reduced, and the overall structure is not disturbed. To simplify the

calculation, he considered a bimodal distribution of homogeneous spheres. Latex particles can very closely approximate the same situation as seen in Figure 7.2.

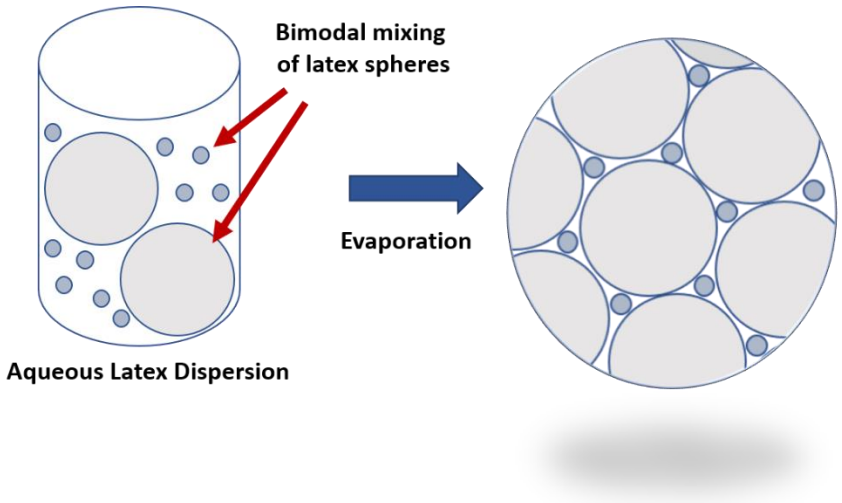

Figure 7.2 Schematic of a bimodal packing representation for different size latex particles.

The system can be defined by the volume fraction of large (C_l) and small particles (C_s), and by the ratio (u) between the two particles and the void fraction of the final mixture (h). He also found the saturation point of the system in which the small particles fill completely the interstices of the large particles. At the saturation point, there would be a maximum density and hence a minimum void fraction [234]. The only observation that must be made is that Furnas [233] considered a random close packing of particles in which the initial packing fraction is much lower than for close packed crystal-like structures such as the latex systems. For a completely random packed system, the initial void fraction is 0.5.

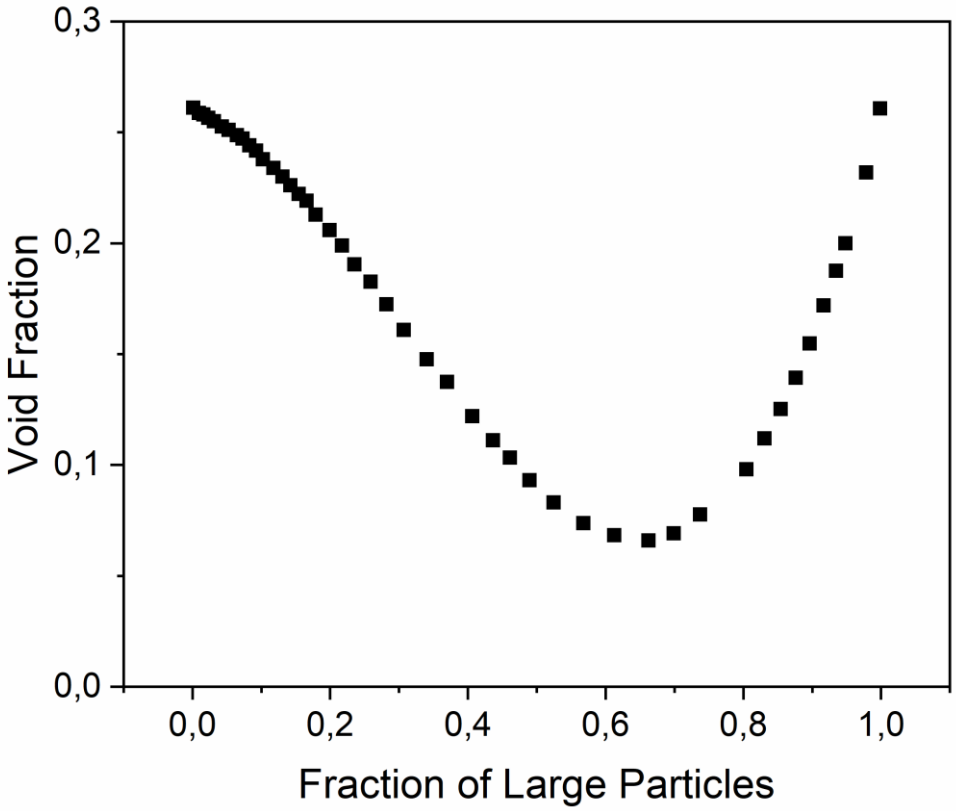

Figure 7.3 Curve of predicted void fraction for a bimodal system from Kister- Redlich [237].

Subsequently, Brouwers [226][227][228] defined a function for how the void fraction would vary for all the lattice systems that follow a Redlich-Kister [237] function, given as:

$$\frac{\eta}{f_1} = \frac{X_L(u^3-1)+1}{X_L(u^3-1)+1+\frac{1}{n}[1-X_L^n-(1-X_L)^n](u^3-1)} \qquad \text{(Equation 7.1)}$$

where f_1 is the initial packing fraction of the monodisperse system, X_L is the mole fraction of large particles, u is the ratio of the particle diameter (there is an optimum value of u as described above), η is the packing fraction of the bimodal system, and n denotes the number of spheres required to make up the basic crystal unit. In Figure 7.3 the curve of predicted void fraction for a bimodal system from Kister [237] is shown. From this graph

it is possible to see that the change in volume fraction goes with large particle fraction but is also affected by the ratio of large to small particles. Hence at some critical value of X_L the system reaches a minimum before being dominated by the small ball inclusion. In 2010, King [235] has done a similar study using a bimodal system to maximise densities and reduce the percolation threshold for electrical measurements with CNTs as a nanofiller. She was able to observe that the reduction in percolation threshold at different ratios of large to small experimentally calculated closely followed the theoretical trend in the void fraction as shown in Figure 7.4 a. [227]. The relationship between the percolation threshold and the void fraction is what is expected from following the traditional percolation theories using the Furnas packing regime.

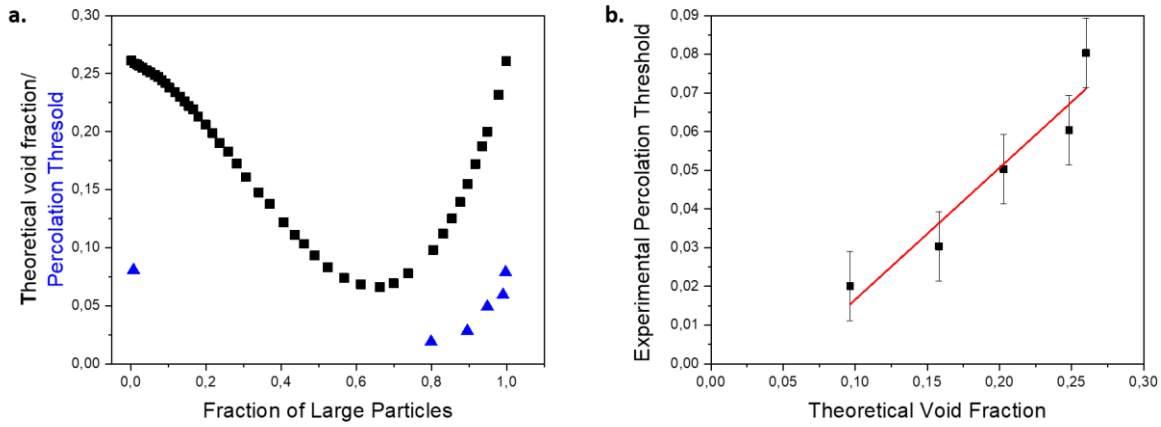

Figure 7.4 a. ■ Theoretical void fraction plot as obtained from the Redlitch-Kister function [237] and ▲ percolation threshold of the composites experimentally calculated from the CNTs system [235]. b. Graph of the experimental percolation threshold vs the theoretical void fraction at different concentration of CNTs with a linear fit [235].

This relationship can be confirmed by the presence of a linear fit among the void fraction and the percolation threshold described in Figure 7.4 b. Inspired by this previous work using CNTs, we present a bimodal system with graphene sheets.

7.2. Bimodal segregated network using graphene

The segregated network explained by Kusy [120] can be applied for a bimodal latex system. The self-assembly method explained in Chapter 5 is used to form a segregated network nanocomposite using a bimodal latex. The liquid exfoliated graphene is dispersed into the aqueous Latex 3 dispersion. While the water evaporates, the polymer spheres start to deform and form the apollonian structure (small particles into the interstices of the large particles), and the graphene sheets are forced to stay at the interstices of the small and the large polymer particles. The graphene based composite is then obtained after completing the drying. Figure 7.5 illustrates the preparation process of the composite.

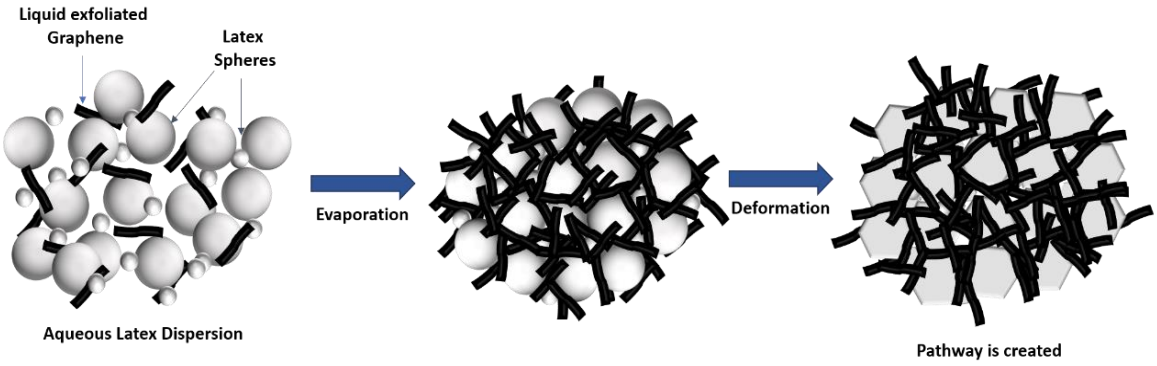

Figure 7.5 Schematic representation of latex- graphene based composite preparation.

The AFM image in topography (in Figure 7.6 a.) shows the morphology of Latex 3-graphene based composite using 0.2 % of small particles and 2 wt.% of graphene flakes. From the image, it is visible that a good aggregation of Latex 3 is achieved, and it is also possible to see for example in the circled area that the small particles are situated in the void fraction of the large particles. Moreover, there is also clearly a presence of graphene sheets in the interstices.

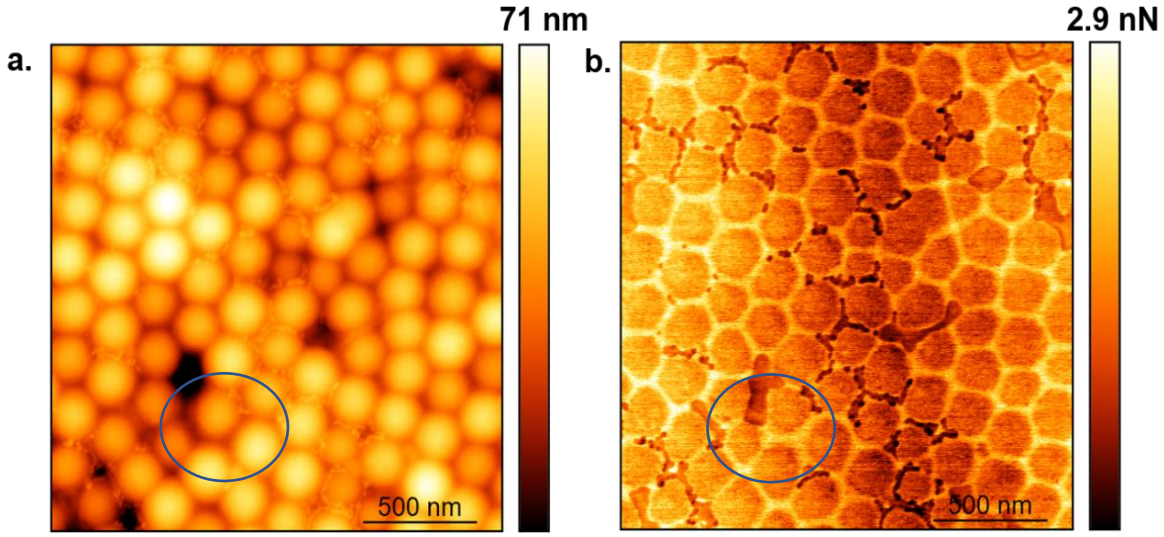

Figure 7.6 a. AFM height sensor image of Latex 3, 0.2 % of small particles and 2 wt.% of graphene and b. AFM images in adhesion mode showing a clear contrast between the polymer and the graphene sheets.

The graphene presence in the bimodal latex structure is confirmed by the AFM image in adhesion mode (in Figure 7.6 b.). It shows a large contrast between the latex spheres and the graphene nanoparticles due to the different interaction of the AFM probe with the two systems. Furthermore, the minimisation of the void space discussed previously is shown in Figure 7.7 A.B.C. From the SEM images is evident how this concept is affecting the assembly and the orientation of the graphene sheets. Indeed, it is noticeable that the graphene sheets wrap around the latex spheres in a network fashion. The low magnification electron micrograph of an uncoated sample in Figure 7.7 A. shows the segregated pathway created by the graphene filler. In Figure 7.7 B.C. a high magnification electron micrograph of Latex 3-graphene based composite is shown. In some areas at the interstices the presence of graphene sheets and how they avoid the small latex particles can be seen. Graphene sheets are actually arranging in a triangular-like assembled structure around the organised template created by the bimodal polymer particle packing, even though from SEM images it is not possible to see any particle spheres (as one might expect for a dielectric material).

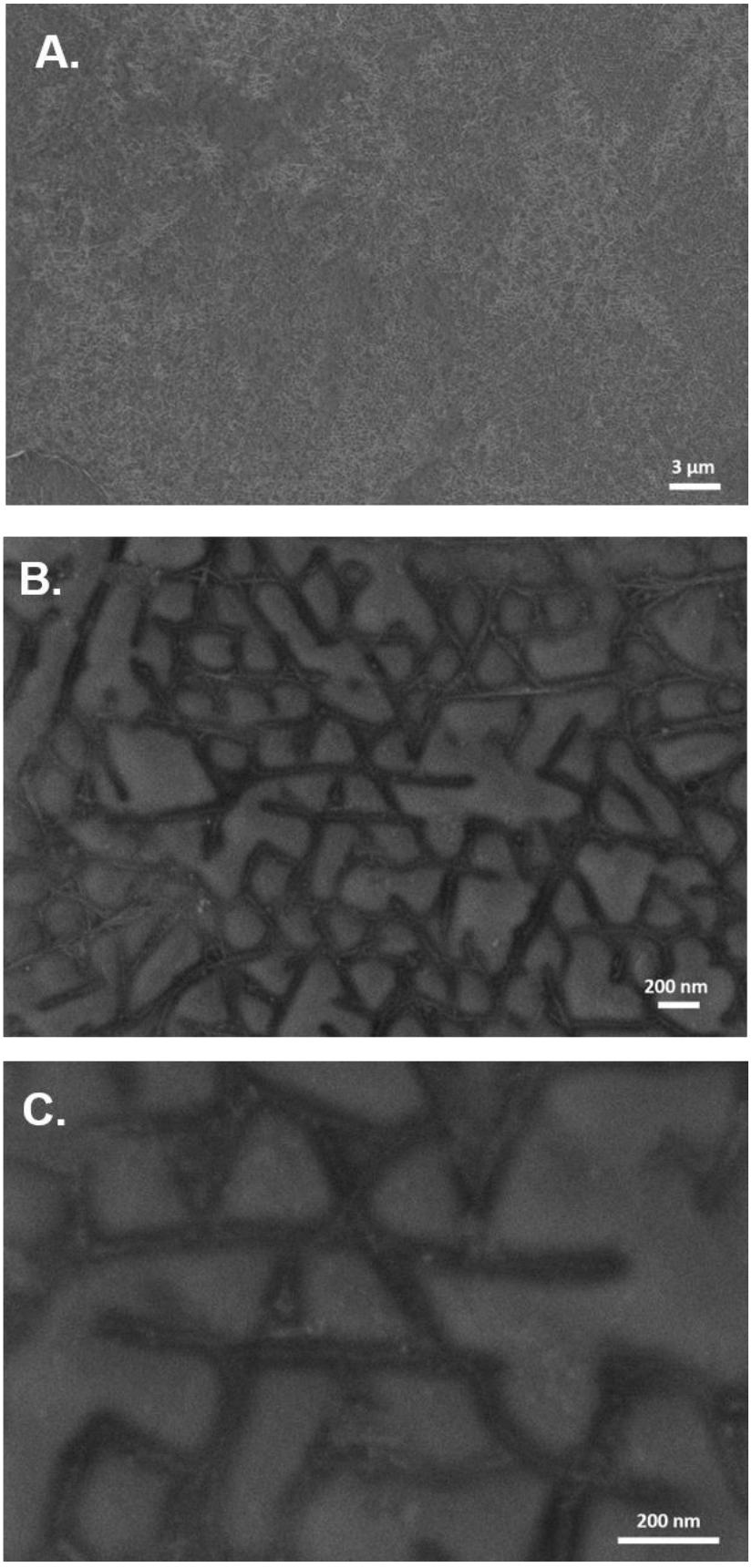

Figure 7.7 A.B.C. Scanning electron microscope images of an uncoated Latex 3-graphene based composite at different orders of magnification.

The volume available for the graphene is reduced and therefore the filler is forced to fill connecting networks at lower volume fractions. The reduction in the void fraction proposed by Furnas [233] can actually be responsible for the decrease of the percolation threshold for these composites. The electrical conductivity measurements were carried out as described in Chapter 3. In Figure 7.8 a.b.c.d.e. is shown the absolute conductivity at different weight fractions of graphene sheets in the Latex 3-graphene based composites using different volume % of small particles. The highest electrical conductivity is reached when the volume fraction of small particles is 25 % as seen in Figure 7.8 b. The conductivity is 2.3×10^{-5} S/m at 0.5 wt.% of graphene sheets and by fitting the measured conductivity data with Equation 5.5 in Chapter 5, the percolation threshold appears at 0.14 wt.% of graphene. The conductivity has been increased by four orders of magnitude compared to the pristine polymer matrix (Latex 3). There is a difference, compared to the latex 3-graphene based composite using 25 % of small particles, of one order of magnitude in terms of electrical conductivity when CNTs are used as a nanofiller. When the volume fraction of small particles is 20 % as reported here [235] the electrical conductivity is 5×10^{-4} S/m at 0.1 wt.% of CNTs. This difference increases when only large particles are used in the system. The highest value obtained in Latex 3-graphene based composite is 4×10^{-6} S/m while for Latex-CNTs system the highest value is 1×10^{-2} S/m. The fact that there is an enormous difference in terms of conductivity is probably a consequence of the fact that CNTs have a bigger aspect ratio, and also that when graphene is used as a filler there were difficulties in film preparation due to the solids content. In Figure 7.8 a.b.c.d.e. it is possible to see that the volume content of the small particles markedly affects the power law dependence of the change in conductivity with obvious modiifcations to the percolation threshold. Moreover, there is a drop in the conductivity by three orders of magnitude when small particles only are used to prepare the composite (Figure 7.8 e.). This can be explained by the impossibility of producing cohesive and smooth composite films at that volume % of small particles. In fact, there were some difficulties in film preparation, and the composite was presenting cracks and inhomogeneities on the surface. It is conceivable that as the volume content of small particles grows the composite must expand to make space for the small particles and this means that the particle packing is disrupted instead of minimised.

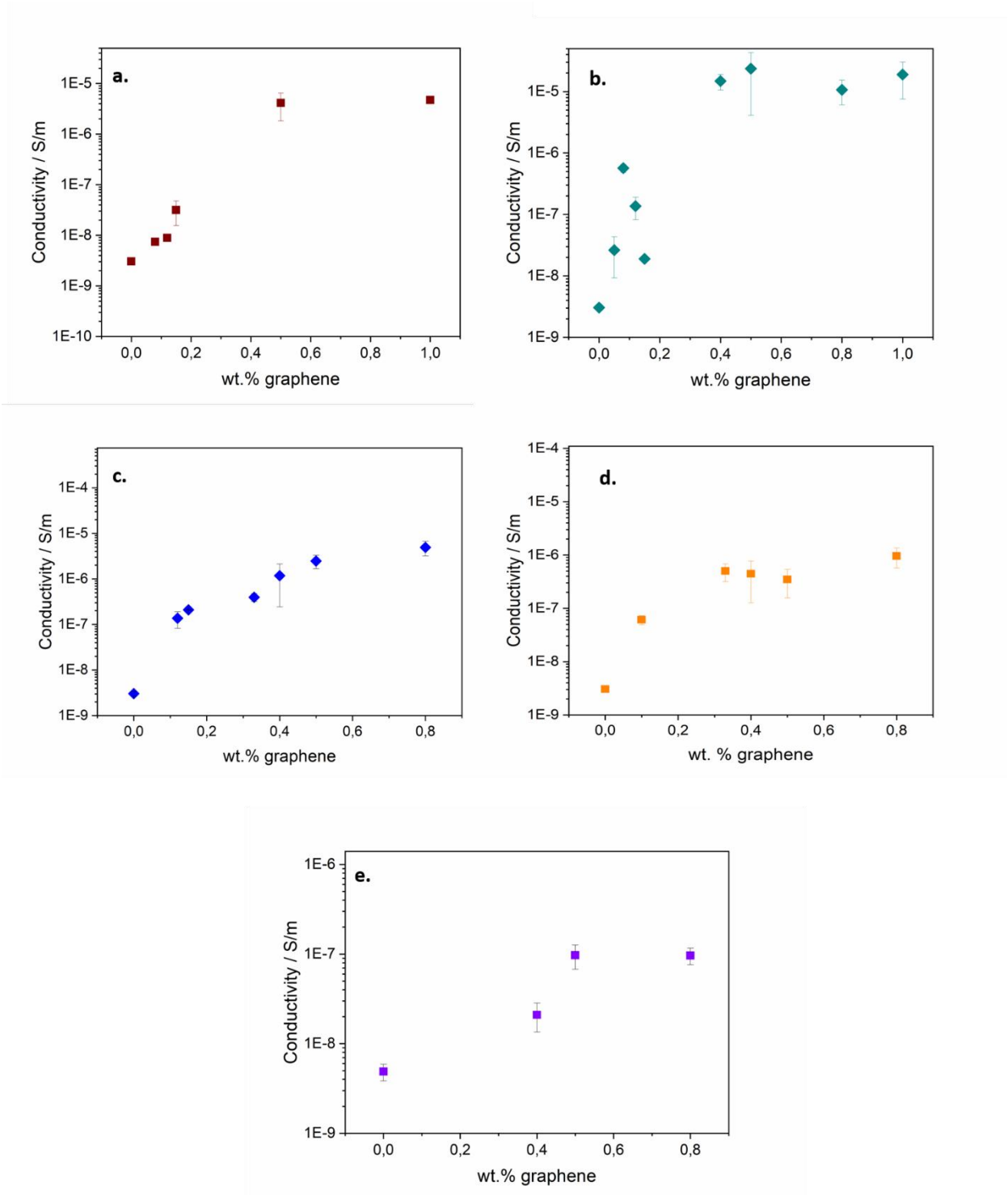

Figure 7.8 Absolute conductivity vs wt.% of graphene sheets of Latex 3-graphene based composites at different volume content a. large particles only; b. 25 % of small particles; c. 35 % of small particles; d. 50% of small particles e. small particles only.

Furthermore, it seems that graphene is more rigid and disrupts the composite structure as seen in Chapter 6. In table 7.1 the maximum conductivity reached for different volume fractions of small particles, and the respective percolation threshold, are reported. The percolation threshold is reduced as the volume of small particles increases, which also corresponds to a drop in conductivity. This behaviour is something that has generally been observed before in composite films [235]. This is important for the development of the theoretical model based upon the void fraction that has been shown before at the beginning of the chapter.

Table 7.1 Percolation threshold and maximum conductivity for different fractions of small particles.

Fraction of Small Particles /%	Percolation Threshold / wt.% of graphene	Maximum Conductivity / S/m
0	0.23	$4.1 \times 10^{-6} \pm 2.3 \times 10^{-6}$
25	0.14	$2.4 \times 10^{-5} \pm 1.9 \times 10^{-5}$
35	0.008	$4.9 \times 10^{-6} \pm 1.7 \times 10^{-6}$
5	0.07	$4.5 \times 10^{-7} \pm 3.2 \times 10^{-7}$
100	0.4	$9.7 \times 10^{-8} \pm 2.9 \times 10^{-8}$

The experimentally determined percolation threshold of Latex 3-graphene based composites using different volume fraction of small particles is shown in Figure 7.9. From the graph it is possible to see that the percolation threshold change follows the theoretical model plot of the composite void fraction as calculated from Kister- Redlich [237] shown before in Figure 7.3. This link is what is expected by following the combination of traditional theories with the Furnas packing regime [233]. The percolation threshold data

obtained when only small particles are used to prepare the composite is inconclusive as there is a large scatter in the data. This can be explained by the difficulties in sample preparation mentioned before. It is important to keep in mind that in order to obtain novel high-performance composites, it is essential to play with the volume fraction of small particles.

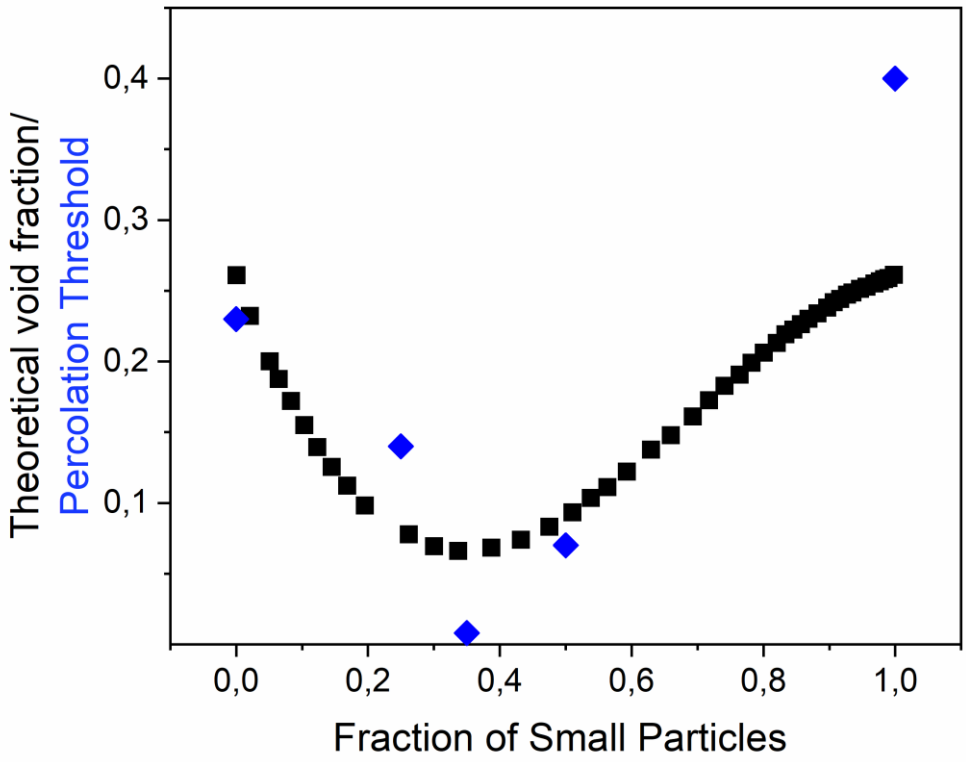

Figure 7.9 ■Theoretical void fraction plot as obtained from the Redlich-Kister function [237] and ◆ percolation threshold of Latex 3-graphene based composites at a different volume fraction of small particles experimentally calculated.

Hence, it is fundamental to understand how the morphology of the matrix can be reflected in the electrical performance of the system. The relationship between the theoretical void fraction and the experimental percolation threshold is confirmed by the presence of a linear fit shown in Figure 7.10. The intercept is assumed to be a measure of the experimental error and should be expected to pass through zero [235]. Indeed, in this particular case, there is a scaling relationship from the plot in Figure 7.10 of 0.35 ± 0.08 (value derived from the fitting to a linear relationship). In fact, if the void fraction is imaged as the space available for the graphene sheets to fill, then this scaling relationship

can be viewed as the fraction of the void space that must be filled to achieve percolation [235]. This linear relationship is something that has been previously studied by King [235] and it is shown in Figure 7.4 b.

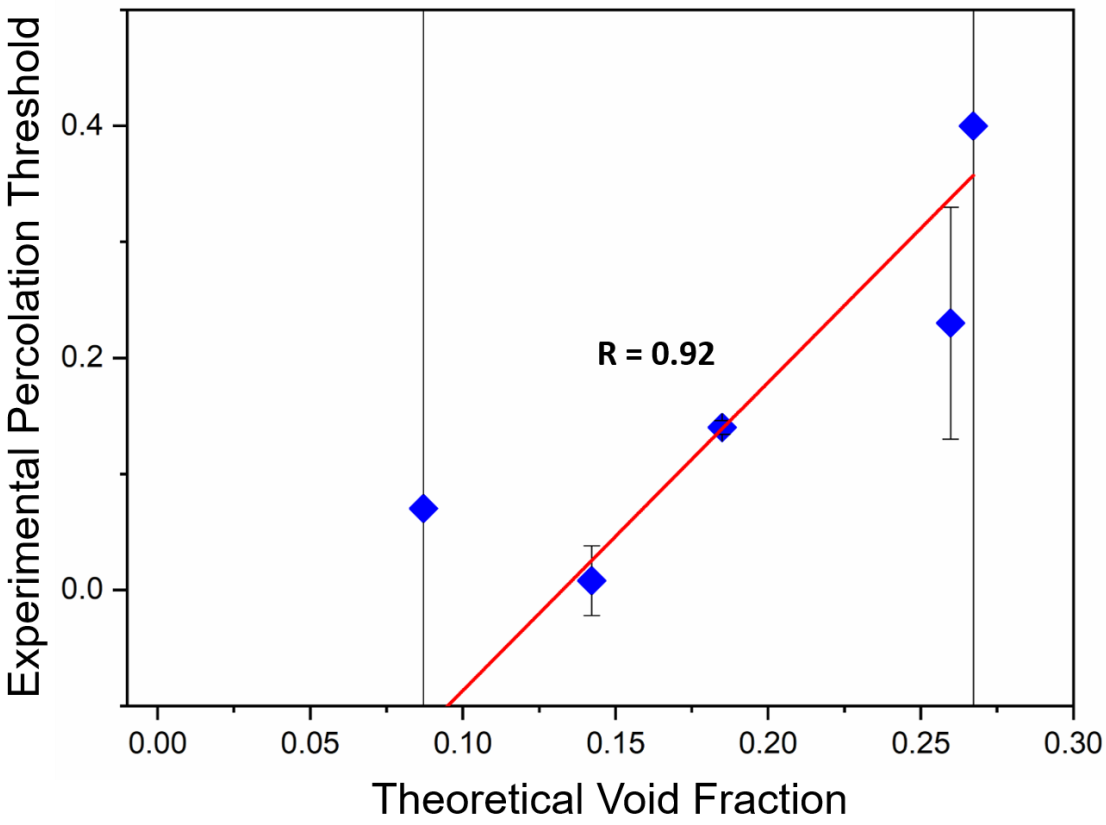

Figure 7.10 Graph of the experimental percolation threshold vs the theoretical void fraction at different concentration of graphene with a linear fit.

In Figure 7.10 it is clear that the error bars are quite high for the composites with higher volume fraction of small particles. This is correlated to some difficulties in sample preparation, which was presenting inhomogeneities and cracks on the surface. Another reason may be related to the increase in volume of small particles; as the volume of small particles rises, the composite expands in order to have more space for the small particles. This leads to a disruption of the particle packing instead of a minimisation.

7.3. Conclusions

This chapter contains the study of a bimodal system used to maximise densities and to reduce the percolation threshold for electrical measurements. The concept of using small particles to fill the interstices of large particles was proposed for the first time by Apollonius and Perga [232] almost 2000 years ago. Subsequently, Furnas [233][234] described the possibility of using a bimodal particle system to create materials with low void fraction and high density. Later, King [235] used a bimodal system to create Latex-CNTs based composites. In her work, CNTs were forced to fill the reduced void space and form a connected network using a lower volume of filler. It has been shown that a direct dependence of the percolation threshold on the void fraction of the polymer matrix exists. Inspired by these previous findings, in this chapter a bimodal system of particles used to create graphene based composite is described. AFM and SEM images are shown in Figure 7.6 a.b. and 7.7 A.B.C. respectively. They demonstrate the presence of graphene sheets networks in the bimodal latex. Graphene sheets were filling the void space between the polymer spheres and creating a triangular-like structure around the organised polymer template. This can be explained by the reduction of the volume available for the graphene sheets, which were forced to fill the connecting network at lower volume fractions. Therefore, the reduction of the void fraction proposed by Furnas can be responsible for the decrease of the percolation threshold for these composites. Subsequently, the electrical properties of Latex 3-graphene based and CNTs based composites were shown. These two systems have been compared in order to understand how the conductivity and the percolation threshold change using different nanoparticles. Graphene based composites have shown a maximum conductivity of 4.12×10^{-6} S/m (Figure 7.6.a.) while for the CNTs system the highest value is 1×10^{-2} S/m (reported in King's work [235]). The huge difference in terms of conductivity is probably a consequence of the fact that CNTs have a bigger aspect ratio, and also that with graphene filler some difficulties in film preparation have been encountered especially when small particles were used. It seems that graphene is more rigid and disrupts the structure. This can be also reconnected to the poor permeability performance of NLR-graphene based composites showed in Chapter 6. In this study it was possible to see that the change in the percolation threshold follows the theoretical plot of the composite void fraction as calculated from Kister-Redlich [237] shown in Figure 7.3. This is what was expected by following the combination of traditional theories with the Furnas packing regime [233]. The percolation

threshold data obtained when only small particles are used to prepare the composite are scattered, which is possibly explained by the difficulties encountered in sample preparation with cracks and inhomogeneities on the surface of the films clearly evident in many samples. However, the relationship between the theoretical void fraction and the experimental percolation threshold was confirmed by the presence of a linear fit (Figure 7.10). In conclusion, this study has demonstrated that in order to obtain novel high-performance composites, it is essential to play with the volume fraction of small particles while using a bimodal latex matrix.

Chapter 8

Studies of the modification of mechanical properties

In this chapter, the mechanical properties of Latex 2-GO and rGO based composites, NLR-GO; rGO and graphene based composites are investigated in detail. As discussed in Chapter 2, high modulus graphene is used to reinforce a low modulus polymer matrix [87][239]. For this reason, an enormous amount of research has been focused on the mechanical properties of graphene-based nanocomposites [87][239]. In graphene-based composites, the reinforcement evaluation is commonly carried out by the study of the stress-strain curves from which the change in elastic modulus, tensile strength, adhesion etc are examined [87]. In order to obtain a significant improvement of the mechanical properties, it is essential to create a homogeneous dispersion of the filler in the matrix and a strong filler-polymer matrix interaction at the interface [240][241]. The tensile strength is influenced by the aggregation of the filler and this explains why it saturates at lower filler percentages. It is also found that there exists a linear increase of the tensile modulus with increasing filler content. In general, there is a significant increase in the tensile strength and Young's modulus even with a very small amount of the filler [87]. Moreover, GO is often preferred due to the presence of some functional group that allows a better interaction between the polymer matrix and the filler even though its modulus is about 25 % of that of monolayer graphene [87][242]. In literature, there are several papers that investigate the mechanical properties of graphene, GO and rGO based composites and some examples are reported in Table 2 in the Appendix [112] [138][139][140] [243][244]. The purpose of this chapter is to see how the mechanical properties of Latex 2 change while using a different filler such as GO and rGO. It has been proved that GO can actually modify the mechanical properties of the latex matrix. Furthermore, the change of the mechanical properties of NLR matrix is shown while using different fillers such as GO, rGO and graphene.

8.1. Comparison of reinforcement efficiency and adhesion strength of various latex-based composites

8.1.1. Evaluation of mechanical properties of composites as a function of GO content and after the reduction treatment

It is well known that in order to obtain a significant enhancement of the mechanical properties, it is fundamental to create a homogeneous dispersion of the filler in the matrix and try to avoid the agglomeration of the filler in the solvent-polymer dispersion [240]. Zhou *et al.* [241] have found a method to prevent the agglomeration of GO during a direct reduction in PVA/GO aqueous solution, opening a new way to scale up the production of graphene nanocomposites using a simple reducing agent. In the first stage, they prepared PVA-GO based composite films and then they reduced the GO using $Na_2S_2O_4$. They have found an enhancement of 40% of the tensile strength of the PVA matrix by using 0.7 wt.% of rGO. Inspired by this work, Latex 2-GO based composites were first prepared and then reduced by using a thermal treatment of 150 °C. Sample preparation is described in Chapter 3 in the experimental section. After that, a series of mechanical tests in tension mode were conducted on Latex 2-GO based composites before and after reduction at 150 °C. Mechanical measurements of the composites let us determine whether the chemical processes inferred in Chapter 5 have significant impacts on the macroscopic properties of the system. Figure 8.1 shows representative stress-strain curves for Latex 2 composites with 0 and 2 wt% of GO before and after reduction.

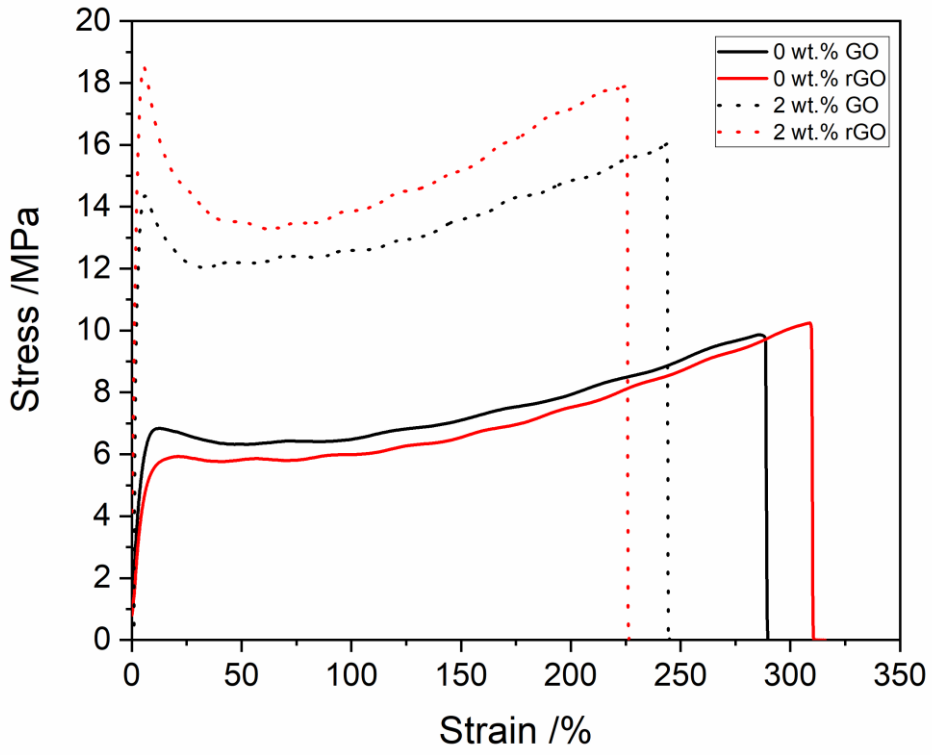

Figure 8.1 Stress-strain curves for Latex 2-GO based composites at two different GO weight fractions.

For the Latex 2 composite with 2 wt.% of GO and rGO, the stress-strain curves display a sharp initial linear growth ascribable to elastic deformation followed by an irreversible plastic deformation which terminates at a yield point. After the yield point, the sample experienced some instabilities as a result of intrinsic strain-softening. This means that there is a decrease in the stress resulting from increasing the strain and then subsequent strain hardening is shown. At a certain point, the curve reaches a critical position where the material fractures. Conversely, pristine Latex 2 has a significantly weaker linear growth, followed by plastic deformation, intrinsic strain softening and strain hardening before fracture before and after reduction. In general, the incorporation of GO at low weight fractions was found to greatly enhance the Young's modulus of elasticity of the polymer latex 2 as shown in Figure 8.2 a. Without any thermal treatment, Young's modulus increases linearly with increasing mass fraction of GO to approximately 3.5 times the base value for 2.0 wt% GO addition. The pristine polymer latex 2 was found to have Young's modulus of (156 ± 20) MPa. The values are listed in Table 8.1. After

reduction, Young's modulus of the composites showed no statistically significant deviation from the unreduced trend. The highest Young's Modulus achieved overall is at 2 wt % after the GO reduction and is equal to (500 ± 20 MPa). Extrapolating the fitted trend to 100 wt%, we can estimate the mechanical properties of the filler network. This produces a Young's Modulus of ~25 GPa; a value approximately 10 times smaller than that of graphene oxide sheets [245]. There is also an enhancement of the yield stress of the composites, which seemingly increases quadratically with the concentration of the filler (as seen in Figure 8.2 b.). The important feature, again, is that the reduction process appears to have no significant impact on the macroscopic mechanical properties. This suggests, as the microscopic and chemical measurements do, that the modifications to the polymer matrix are strongly localised rather than throughout the bulk.

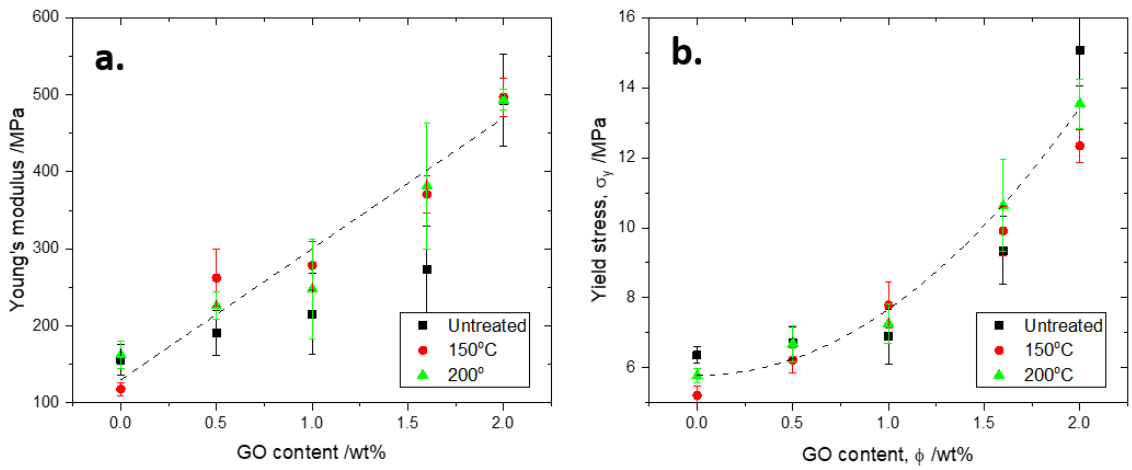

Figure 8.2 Mechanical properties of Latex 2 composite as a function of GO vs rGO (at 150 and 200 °C) weight fraction (a.) Young's modulus, (b.) Yield stress.

After testing the stress-strain behaviour, it was necessary to evaluate the adhesion strength of these composites in order to understand if it is possible to use them for adhesion strength sensors. Sample preparation and adhesion measurements are described in Chapter 3.

Table 8.1 Mechanical properties of Latex 2 composites with 2 wt.% of GO, 2 wt.% of rGO after thermal reduction at 150 and 200 °C.

	Latex 2-GO 2 wt.% of GO	Latex 2-rGO 2 wt.% of rGO_150 °C	Latex 2-rGO 2 wt.% of rGO_200 °C
Young's modulus / MPa	273 ± 55.8	496 ± 24.5	493 ± 13.4
Yield stress / MPa	15 ± 0.9	12.3 ± 0.5	13.5 ± 0.7

In Figure 8.3 a. some representative AAT profiles for the Latex 2 composites as a function of the GO content are shown. They exhibit only one peak in which the height is related to the tack performance of the adhesives. The force increases with the probe displacement following Hooke's law to a yield point. After the yield point (maximum height in the force-displacement curve), the force starts to decrease [177]. The Latex 2 composite with 0.2 wt.% of GO possesses the highest yield point in the AAT profiles compared to the other samples with a lower concentration of GO. In Figure 8.3.b the AAT profile curves for the Latex 2 composite with different rGO concentration after the thermal reduction at 150 °C are shown. Similarly, the AAT profile curve exhibits one peak as seen before for the untreated one. The highest yield point belongs to Latex 2 composite at 0.2 wt.% if rGO and is equal to (~0.5 N). From the AAT profile curves, it is also possible to see that there is a clear increase in the yield point as a function of GO content (from 0.04 to 0.2 wt.%) which then approximately doubles for each sample when reduced.

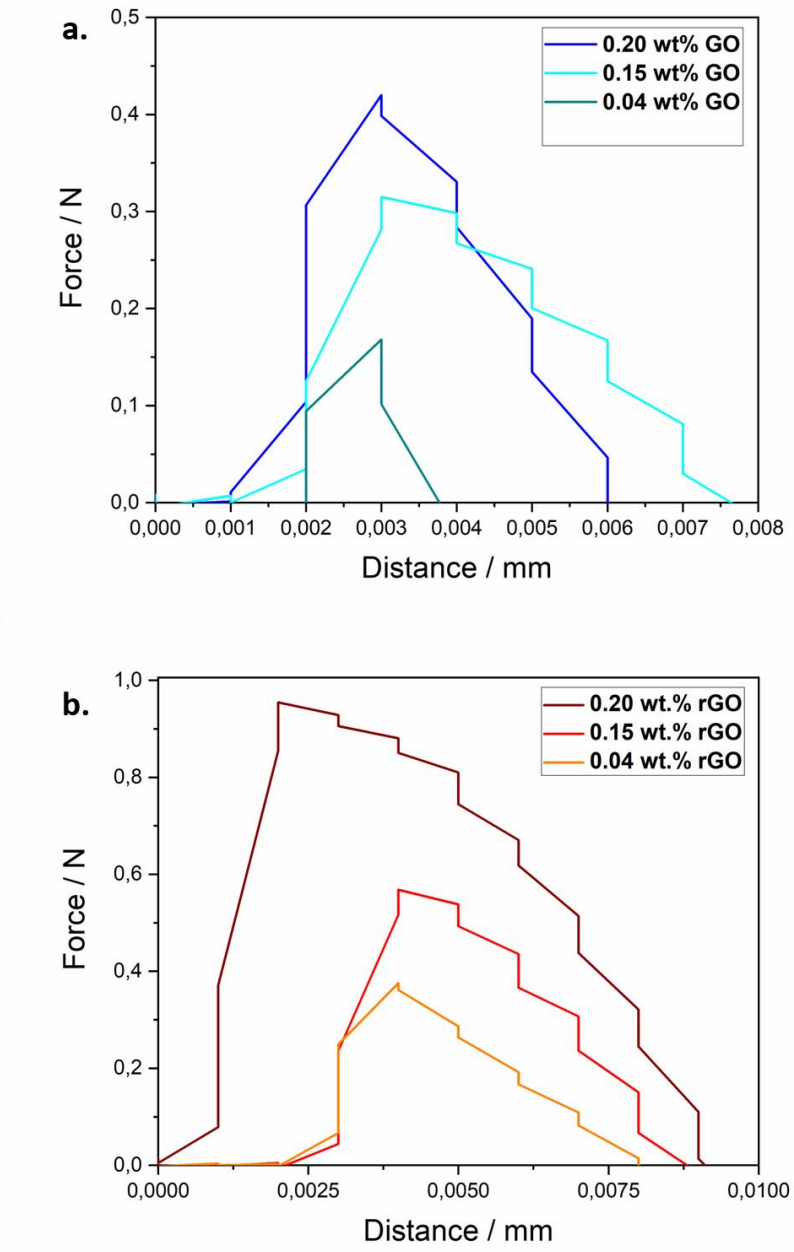

Figure 8.3 a. AAT profiles for Latex 2 composites with different weight fractions of GO and b. rGO after the thermal reduction.

A study of the adhesion energy of Latex 2 composites at different loadings of GO (0-0.3 wt.%) before and after reduction at 150 °C is reported in Figure 8.4 while a force of a. 0.5 N, c. 1.5 N, e. 2 N and g. 3 N is applied.

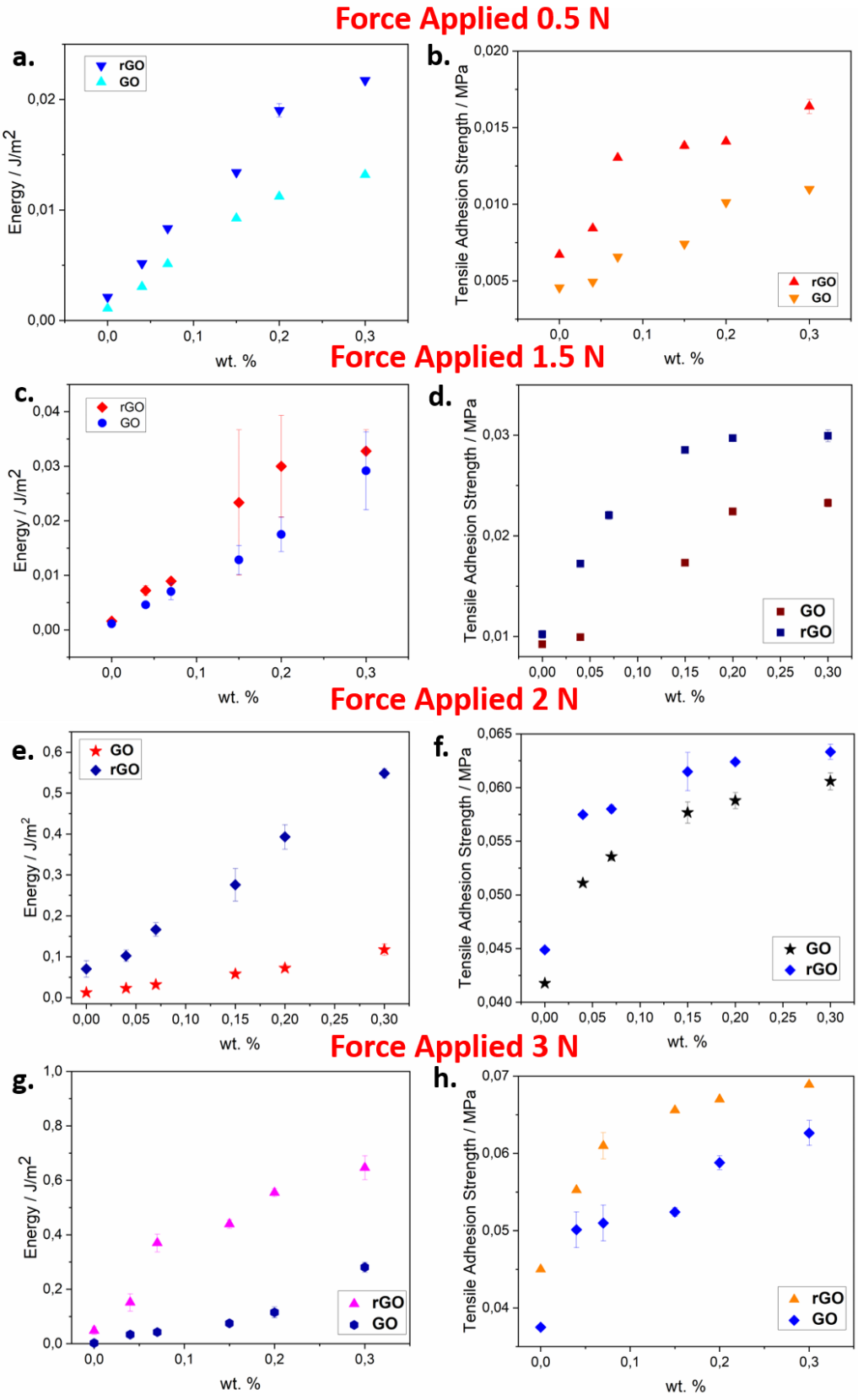

Figure 8.4 a.c.e.g Energy vs GO and rGO weight fraction at 0.5, 1.5, 2 and 3 N respectively for Latex 2 based composites and b.d.f.h. Tensile adhesion strength vs GO and rGO weight fraction at 0.5, 1.5, 2 and 3 N respectively for Latex 2 based composites.

As expected when adding a stiff filler to a soft matrix, the energy increases with increasing GO concentration as seen elsewhere [246]. In Figure 8.4 a. the adhesion energy has increased by ~0.01 J/m^2 compared to the pristine polymer latex. The same behaviour is shown when GO is reduced at 150 °C, in fact, there is an enhancement of ~0.02 J/m^2. Similarly, there is an enhancement of adhesion energy when the force applied is increased. All the values for Latex 2-GO at 0.3 wt.% of GO before and after reduction are reported in Table 8.2 below. From Table 8.2, it can be seen that when a force of 0.5 N is applied to the Latex 2-GO and rGO composites the error values are very large, and this is probably due to the fact that the applied force was not sufficient to get reliable results. Furthermore, the highest energy values are obtained using a force of 3 N. There is, indeed, an enhancement of ~0.28 J/m^2 when GO is used as a filler and ~0.65 J/m^2 after the reduction at 150 °C. The fact that the Latex 2-rGO based composites show higher adhesion energy is probably ascribable to a chemical modification of the Latex 2 after reduction as discussed in Chapter 5. This chemical modification allows for a higher adhesion energy value and therefore the composites become stickier compared to the untreated specimens.

Table 8.2 Adhesion energy of Latex 2-GO based composites with 0.3 wt.% of GO before and after reduction at 150 °C, when different forces are applied.

	0.3 wt.% GO	**0.3 wt.% rGO**
Energy / J/m^2, 0.5 N Force Applied	0.01 ± 1.13	0.02 ± 8.4
Energy / J/m^2, 1.5 N Force Applied	0.03 ± 0.007	0.03 ± 0.004
Energy / J/m^2, 2 N Force Applied	0.12 ± 0.014	0.55 ± 0.012
Energy / J/m^2, 3 N Force Applied	0.28 ± 0.02	0.65 ± 0.04

In figure 8.4 the tensile adhesion strength for Latex 2 composites at different weight fractions of GO (0-0.3 wt.%) before and after reduction at 150 °C is shown while a force of b. 0.5 N, d. 1.5 N, f. 2 N and h. 3N is applied. Similarly to the adhesion energy, the tensile adhesion strength increases with the concentration and the applied forces. For the untreated sample with GO concentration of 0.3 wt% and applied force of 0.5 N, there is a difference of ~0.005 MPa compared to the pristine latex. The difference gets higher after the reduction, indeed, there is an improvement of 0.011 MPa. Table 8.3 reports the tensile adhesion strength data related to Latex 2-GO based composites at 0.3 wt.% before and after thermal reduction at 150 °C. In this case again, the errors are quite large and for this reason, are not reliable. Summarising graphs are reported in Figure 8.5 A.B., in order to better understand how the adhesion energy and strength increase with applied force. In Figure 8.5 A. the energy values while increasing the applied force from 0.5 N to 3N for Latex 2-GO composites before and after reduction at 0.04 and 0.3 wt.% of GO are shown. When a force of 0.5 N is applied to the specimen the energy change is very minor.

Table 8.3 Tensile adhesion strength of Latex 2-GO based composites with 0.3 wt.% of GO before and after reduction at 150 °C, when different forces are applied.

	0.3 wt.% GO	**0.3 wt.% rGO**
Tensile adhesion strength / MPa, 0.5 N Force Applied	0.01 ± 1.55	0.01 ± 4.63
Tensile adhesion strength / MPa, 1.5 N Force Applied	0.02 ± 3.96	0.03 ± 5.94
Tensile adhesion strength / MPa, 2 N Force Applied	0.061 ± 7.8	0.063 ± 6.9
Tensile adhesion strength / MPa, 3 N Force Applied	0.063 ± 0.001	0.069 ± 1.8

The energy difference starts to be higher while a force of 2 N is applied. In fact, at 2 N, Latex 2-rGO with 0.3 wt.% of rGO displays an energy value that is ~0.6 times higher compared to the untreated sample at 0.04 wt.% of GO. An equivalent behaviour is observable when a force of 3 N is applied to the specimen. The highest energy value is ~0.65 J/m^2 for the composite with 0.3 wt.% of rGO. This can be explained by the fact that after the thermal treatment at 150 °C there is an intimate bonding between the Latex 2 and the rGO flakes. Indeed, as seen previously in Chapter 5 the polymer experiences chemical modification due the explosive reaction of GO after reduction. Therefore, this chemical modification leads to a higher adhesion energy value and indeed the Latex 2-rGO composites become stickier compared to the untreated specimens. In Figure 8.5 B. are shown the adhesion strength values for Latex 2-GO based composites at 0.04 wt.% and 0.3 wt.% of GO before and after the thermal reduction at 150 °C while different forces (from 0.5 N to 3 N) are applied. In this case, there is an increase in adhesion strength while increasing the applied force even at 0.5 N. As expected, the lowest value is reached when 0.04 wt.% of GO is used and instead when 0.3 wt.% of rGO is used the adhesion strength increases. The difference is more than double the energy for the same loading level. The rGO flakes are effectively changing the adhesion properties of the matrix more than the untreated GO as previously discussed. Curiously, it is important to highlight that when the tensile adhesion strength vs wt.% of GO and rGO is plotted, the system reaches a maximum value and then decrease while using a higher concentration of filler. There is a maximum value at 0.3 wt.% of GO and after this value the tensile adhesion strength starts to decrease when the concentration of GO is growing from 0.5 to 2 wt.%. It appears that after 0.3 wt.% the systems reach a saturation point and after that the samples become stiffer and therefore, they can not be used as pressure sensitive adhesives materials. This behaviour is shown in Figure 8.6 while different forces a. 0.5 N, b. 1.5 N, c. 2 N and d. 3 N are applied.

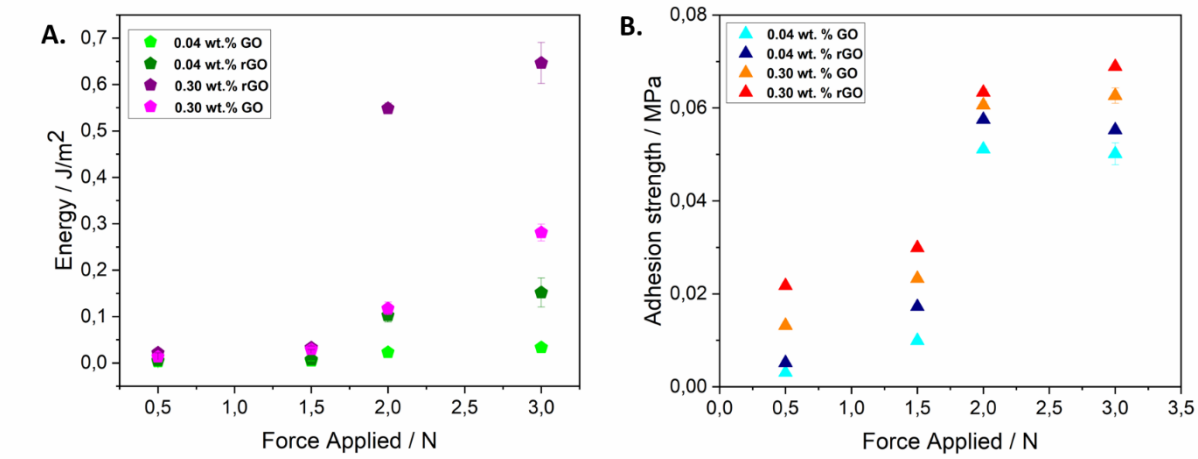

Figure 8.5 A. Energy vs Force Applied for Latex 2-GO composites at 0.04 and 0.3 wt.% of GO before and after reduction. B. Adhesion strength vs Force Applied for Latex 2-GO composites at 0.04 and 0.3 wt.% of GO before and after reduction.

At this point, it is clear that the rGO flakes change the mechanical properties of the latex matrix, in terms of stress-strain measurements and adhesion. The latex becomes more flexible and tackier which is potentially useful for applications such as pressure sensitive adhesives materials. The increased energy and adhesion strength are likely due to the intimate bonding between the rGO and the polymer after reduction. In general, the interface is the usual point of failure in a composite, and excellent energy transfer between matrix and filler is needed to improve mechanical performance. The chemical nature of the filler/matrix interface after reduction is, therefore, improving this interfacial energy transfer.

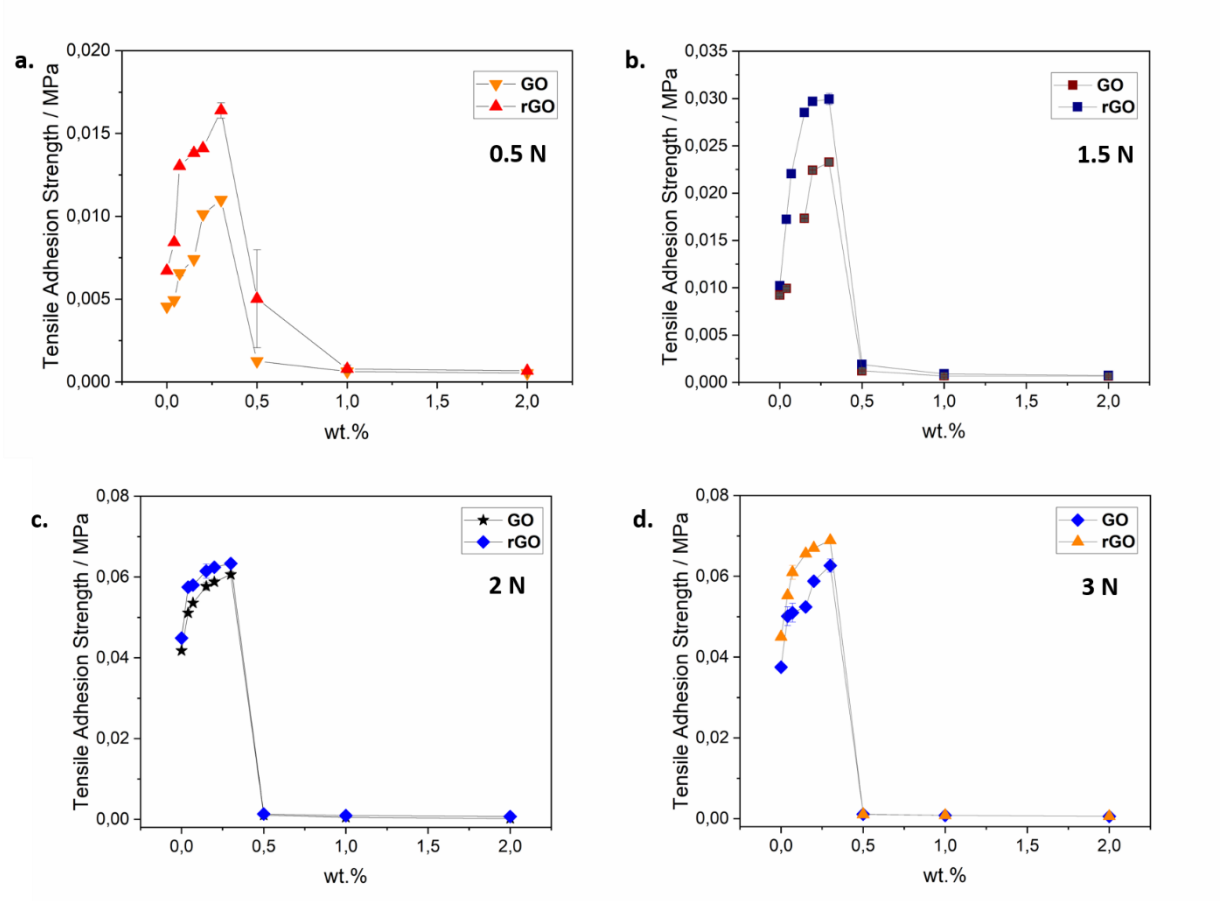

Figure 8.6 Tensile Adhesion Strength vs wt.% of GO and rGO when a force of a. 0.5 N, b. 1.5 N, c. 2 N and d. 3 N is applied. There is a drop off of the adhesion from 0.5 to 2 wt.%.

Thus, these composites turn out to have potential applications for pressure sensitive adhesives, as the rGO strongly influences the tackiness of the polymer system. The addition of the rGO greatly alters the adhesion of the polymer, and so we can create composites with a specific tackiness.

8.2. Evaluation of mechanical properties of NLR composites as a function of rGO and graphene content

In this section the mechanical properties of NLR composites as a function of different fillers such as rGO and graphene are evaluated. The two systems are then compared to see how the filler can influence the mechanical response of the NLR composites. Sample preparation and mechanical measurements are explained in Chapter 3. Figure 8.7 presents the stress-strain curves for NLR-rGO composites with different loadings (from 0 to 0.56 wt.%) of rGO. The curves do not show any stress drop, as seen before for the Latex 2-GO based composites after reduction at 150 °C. However, they do exhibit strain hardening behaviour and at a certain point, the curves reach a critical position where the material fractures.

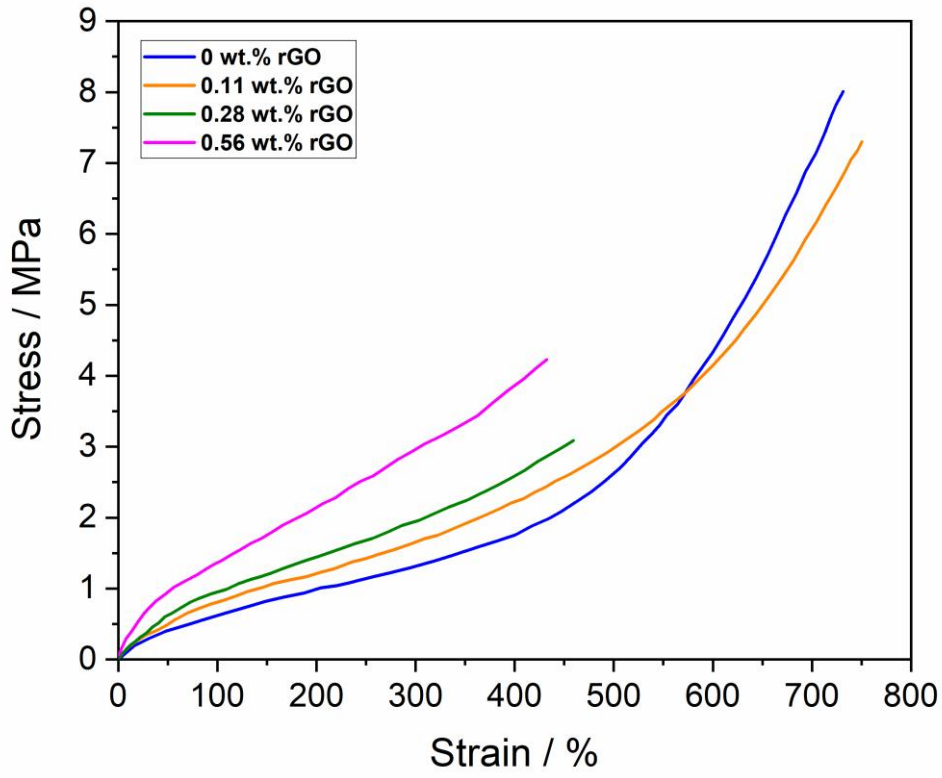

Figure 8.7 Stress-strain curves for NLR composite containing different weight fraction of rGO.

In Figure 8.8 a. it is shown that there is a linear increase of Young's modulus with increasing filler content for NLR-rGO composite, confirming what is found elsewhere [87]. The highest value is reached for NLR-rGO composites with 0.56 wt.% of rGO. The

Young's modulus is increased by 0.45 MPa compared to the pristine NLR matrix itself. In Figure 8.8 b. the graph of stress vs wt.% of rGO when a strain of 100% is applied is displayed. In this case, again, a linear enhancement of the stress as the weight fraction of rGO grows is visible. This confirms the fact that it has been achieved a homogeneous dispersion of the filler in the matrix, and that there is an intimate bonding between the rGO flakes and the NLR matrix. The stress achieved for NLR-rGO based composites is 1.26 MPa higher compared to the pristine NLR matrix. At this point it was also important to see if the deformation energy as a function of different loading of rGO was also following a linear behaviour.

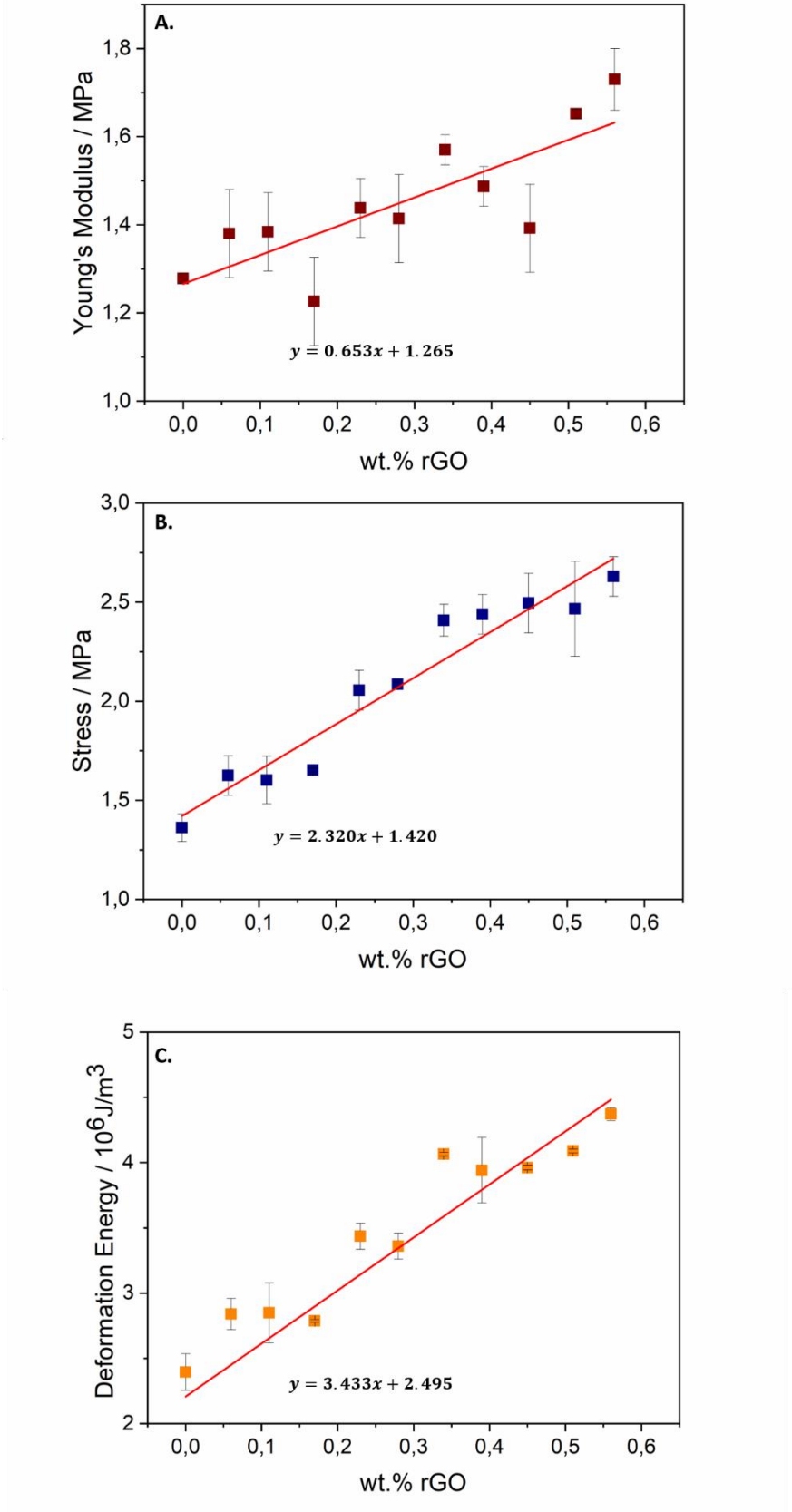

Figure 8.8 Mechanical properties of NLR composite as a function of rGO weight fraction (A.) Young's modulus, (B.) Stress at 100% of strain, (C.) Deformation energy at 300% of strain.

The deformation energy as a function of different weight percent of rGO is illustrated in Figure 8.8 c. The deformation energy values have been obtained when a strain of 300 % is applied. The deformation energy increases with the concentration of rGO. The deformation energy for NLR-rGO based composite at 0.56 wt.% of rGO is increased by ~2 x 10^6 J/m^3 compared to the polymer itself. This confirms the fact that the composites film are homogenous and that there is good interaction between the matrix and the filler. Indeed, in a composite material, the interface is usually a point of failure, and thus to improve the mechanical properties of the matrix is essential in providing excellent energy transfer between the matrix and the filler. All the mechanical data for pristine NLR and NLR-rGO based composites are summarised in Table 8.4 below. These changes in mechanical properties are ascribable to the reduction of rGO that happens when the sample is treated at 130 °C for 30 minutes as discussed in Chapter 6. The rGO flakes are modulating the properties of the pristine polymer.

Table 8.4 Mechanical properties of pristine NLR and of the composites at 0.56 weight fraction after treatment at 130 °C for 30 min.

	Pristine NLR	**0.56 wt.% rGO at 130 °C**
Young Modulus / MPa	1.27±0.012	1.73±0.07
Stress / MPa 100% strain	1.36±0.07	2.62±0.24
Deformation Energy / 10^6J/m^3 300% strain	2.39±0.14	4.37±0.05

At this point, it is necessary to compare the Latex 2-rGO composites described in section 8.1, with the NLR-rGO composites. The Young's modulus of the Latex 2-rGO composite is higher compared to the NLR-rGO system. There is a difference of 170 MPa when the

specimen is treated at 150°C and 250 MPa when reduced at 200 °C. This difference can be explained by the fact that Latex 2-rGO based composites have experienced a chemical modification of the matrix due to the explosive reduction of GO at 150 °C shown in Chapter 5. Furthermore, the Latex 2 matrix becomes aromatic after the thermal reduction at 150 °C and this is probably reflected by the better mechanical performance. It is conceivable that NLR-rGO based composites are not performing as well as Latex 2-rGO because the thermal treatment is performed at 130 °C which may not be enough to obtain the complete reduction of the GO flakes. Subsequently, it was also interesting to see if adding graphene instead of rGO could have modified the mechanical properties in the same way as the rGO does. For that several measurements have been done with NLR using graphene as filler. The stress-strain curves for the sample at 0 and 0.75 wt.% of graphene are represented in Figure 8.9. The curves possess the same behaviour as the NLR-rGO based composite. After a sharp initial linear growth corresponding to elastic deformation, irreversible plastic deformation occurs, and after that, there is a strain hardening of the material.

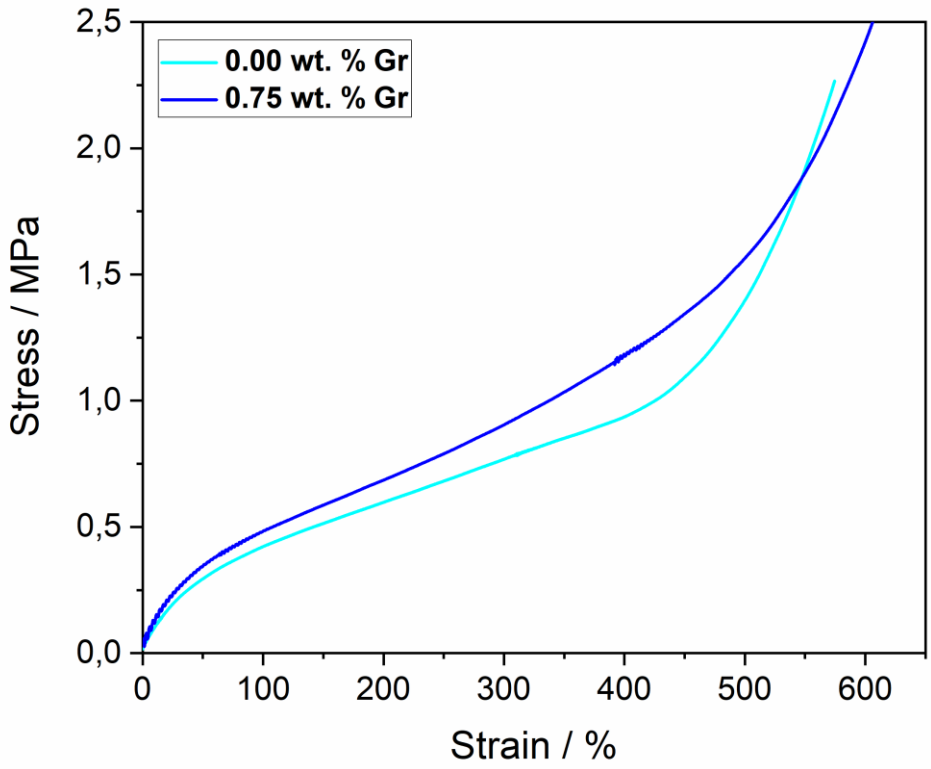

Figure 8.9 Stress-strain curves for NLR composite containing different graphene weight fraction.

Figure 8.10 A. shows the Young's modulus as a function of the weight fraction of graphene. Likewise, for this composite, the Young's modulus exhibits a linear increase as the concentration of graphene increases. NLR-graphene based composite at 2 wt.% of graphene has Young's modulus of 0.995 MPa that is much lower than the value obtained for NLR-rGO based composite at 0.56wt.%. This can be explained by the presence of weak interactions between the NLR polymer and the graphene sheets, indeed, the change in mechanical properties is not significant.

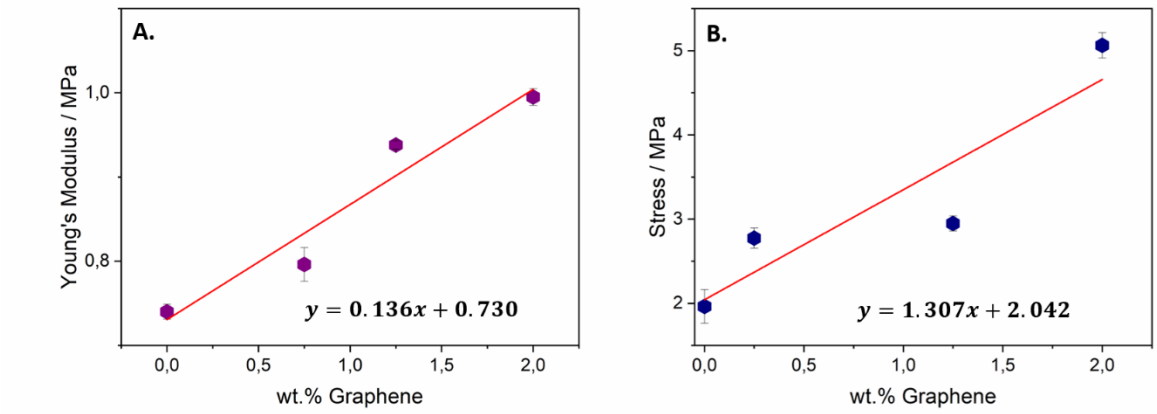

Figure 8.10 Mechanical properties of NLR composite as a function of graphene weight fraction (A.) Young's modulus, (B.) Stress at 600% of strain.

In Figure 8.10 B. the stress as a function of weight fraction of graphene (from 0 to 2 wt.%), is displayed while a strain of 600 % is applied. It is increased by ~3 MPa when 2 wt.% of graphene is added to the pristine NLR matrix. The data for pristine NLR and NLR-graphene based composites are shown in Table 8.5 below. In this case, again, the mechanical change in stress is ascribable to the presence of graphene sheets. Even though they are not changing in an extraordinary way. This can be explained by the fact that graphene sheets are too rigid to conform to the particle packing and are not forming a homogeneous film.

Table 8.5 Mechanical properties of pristine NLR and graphene at 2 weight fractions.

	Pristine NLR	**Graphene 2 wt.%**
Young's Modulus / MPa	0.74±0.009	0.99±0.01
Stress / MPa 600% strain	1.96±0.20	5.06±0.15

8.3. Conclusions

This chapter was aimed at studying the mechanical properties of Latex 2-GO based composites before and after reduction, and NLR-rGO and graphene based composites. It is well known that in order to obtain an enhancement of the mechanical properties, it is important to create a homogeneous dispersion of the filler in the matrix and a strong filler-polymer matrix interaction at the interface [240][241]. In the first section the stress-strain and adhesion measurements for Latex 2-GO based composites before and after reduction at 150 and 200 °C were evaluated. It has been shown that the incorporation of a low weight fraction of GO greatly enhances the Young's modulus of the Latex 2. Moreover, it has been seen that the Young's modulus increases linearly with increasing mass fraction of GO to approximately 3.5 times the base value for 2.0 wt% GO addition. The pristine Latex 2 was found to have Young's modulus of (156 ± 20) MPa. After reduction, the Young's modulus of the composites showed no statistically significant deviation from the unreduced trend. The highest Young's Modulus achieved overall is at 2 wt % after the GO reduction and is equal to (500 ± 20 MPa). Thus, the reduction process seems to have no significant impact on the macroscopic mechanical properties. This suggests, that the modifications to the polymer matrix are strongly localised rather than throughout the bulk. After that, the adhesion strength of Latex 2-GO based composites before and after reduction at 150 °C has been evaluated in order to understand if it was possible to use them for adhesion strength sensors. It has been shown that Latex 2-rGO based composites have shown higher adhesion energy and tensile adhesion strength at a lower weight fraction of rGO. Thus, after the thermal reduction, the composites have become stickier due to a chemical modification of the Latex 2 after the explosive reduction of GO at 150 °C. They can be potentially useful for applications such as pressure sensitive adhesives materials. The increased energy and adhesion strength are likely due to the intimate bonding between the rGO and the polymer after reduction. Furthermore, in the second section the mechanical properties of NLR composites as a function of different fillers such as rGO and graphene were described. The two systems are then compared to see how the filler can influence the mechanical response of the NLR composites. It has been shown that rGO has enhanced the Young's modulus by 0.45 MPa while using graphene the Young's Modulus rise is much lower compared to the previous system and it was only ~0.20 MPa. It is obvious that in Latex 2-rGO based composites there is greater interaction between the filler and the matrix. That brings to the conclusion that Latex 2-rGO based

composites are the best composites compared to the other 2 systems in terms of Young's Modulus elongation. Therefore this can be explained by the fact that when graphene is used as a filler this follows a rule of mixtures type behaviour, of adding a hard material to a soft one, whereas the GO and subsequent reduction has a more significant effect on the properties, due to the involved chemistry.

Chapter 9

Summary and Future Work

9.1. Summary

The purpose of this research work was the development of highly ordered polymer particle matrices, which act as a template for the assembly of different fillers such as GO and graphene into three-dimensional hexagonal arrangements. During film formation, the polymer spheres deform into rhombic dodecahedra arrays due to capillary forces and convective particle flux by water evaporation. The fillers are then assembled and located at the interstitial space between the polymer latex spheres resulting in a honeycomb-like structure. This method has the advantage of being environmentally friendly compared to the solvent-based alternatives; it is inexpensive in terms of equipment or materials and it is facile to assemble. Indeed, it is a promising way to open up pathways to tunable electronic composite materials on a large scale. Obtaining a segregated percolating network using low loadings of nanoparticles to attain the maximum enhancement of electrical and mechanical properties, can be useful to reduce the cost for possible industrial applications. Using this method, highly structured GO based nanocomposites were produced and after in-situ thermal reduction of the GO nanoparticles, a modification to the polymer in proximity to the particles was observed, which resulted in extraordinarily high values of conductivity in the resulting composites. These composites have shown the highest conductivity value of 1808 S/m with and a percolation threshold of 0.4 wt.% of rGO. Moreover, the reduction can be controlled by modifying the thermal treatment. In fact, higher temperatures can be used to increase the rate of reduction, or an almost room temperature process can be used over a longer period, where heating may be undesirable. This time and temperature dependence of the composites can make them excellent sensors (time-temperature indicators). Furthermore, the physical properties of these composites have been tailored using different matrices such as natural latex rubber, or a bimodal particle system, to create materials with high density and low void fractions,

and hence very low percolation thresholds. By the use of NLR with a bimodal particle size distribution, NLR-GO-based composites were fabricated. In order to regain much of the electrical properties of graphene, a simple reduction step has been performed using mild temperatures after the dipping process. The AFM and SEM images have shown that in the solid composite no structured morphology is displayed due to the significantly lower Tg of the NLR compared to the room temperature synthetic latex, but the fact that in SEM it is possible to see a contrast effect indicates that there is a conductivity within the system, as otherwise there would be charging. This means there must be some conductive network within the matrix that is not visible as the particles coalesce and the packing must happen when the NLR particles are dispersed with the GO flakes before the film forming and the fillers are trapped. The differences in morphology compared to the synthetic system are reflected in the electrical conductivity performance. The NLR-rGO composite does not reach the same level of conductivity reached by the latex 1, the highest conductivity is $\sim 10^{-4}$ S/m using 0.06 wt.% of rGO content. The percolation threshold appears at approximately 0.002 wt.%. The value at such mass fraction is very low, near to Apollonian packing due to the fact that the NLR dispersion is a bimodal system and contains small particles of 60 nm and big particles of 400 nm and this gives a size ratio of 6.7 which is the theoretical value for the perfect filling of the voids between the large particles, with the small particles. This feature allows the rGO flakes to form a conductive pathway in the composite. There are some differences when graphene is used as a filler. The NLR-graphene-based composites exhibit the same conductivity value of $\sim 10^{-4}$ S/m as the NLR-GO composites, but in this case, using 5 wt.% of graphene compared to the 0.06 wt.% to the other system. It is clear that in order to obtain a similar value with graphene it is necessary to use more materials and it implies that the reduction of the GO in situ is a highly effective method of creating conductive rubber composites. The fact that graphene composite does not outperform the rGO composite can be ascribable to the hydrophobicity of the graphene compared to the water dispersibility of the GO, and it is reflected in the homogeneity of the dispersion. Therefore, the reduction process creates an intimate bond between the matrix and the filler, with a region of modified polymer binding the flakes and the polymer matrix, thus the reduction process provides better pathways for electron transport. Subsequently, graphene based nanocomposites were prepared using a bimodal system packing to study changes in conductivity and modifications to the percolation threshold and how it changes compared to the NLR

system. Adding a conductive nanoparticle to a high density bimodal system means that the filler is forced to fill the void space and so form a network at a much lower volume. The density is maximised by the use of particle mixing to fill the interstices of the larger particles with smaller ones. From AFM images it was possible to see the graphene sheets wrapping around the particle network and forced to take up only the limited space and so form a connected network at much lower volume fraction. The typical percolation curves, for the conductivity behaviour of the films, was measured for different particle mixtures. With graphene, the maximum conductivity reached is $\sim 10^{-5}$ S/m and the percolation threshold is 0.14 wt.%. Although the conductivity is one order of magnitude lower compared to the NLR, this might be due to difficulties in film preparation, whereby film stratification caused cracks and inhomogeneities on the surface due to phase separation in the dispersion while film formation was happening. This matter can also explain why the NLR-graphene-based composites were failing in the permeability performance, as the disruption creates pores. The mechanical properties of some of these composites (latex-rGO, NLR-rGO and NLR-graphene based composites) were studied showing changes when different fillers are added into the pristine matrix polymer. The Young's modulus of Latex-rGO-based composite at 2wt. % of rGO experienced an increase of ~ 370 MPa compared to the polymer latex itself, while for the NLR-rGO composite at 0.56 wt.% of rGO the increment is only 0.45 MPa, and the Young's Modulus rise is much lower while using 2 wt.% of graphene (~0.20 MPa). It is obvious that in the first system there is greater interaction between the filler and the matrix as described above. That brings us to the conclusion that it is the best composite compared to the other 2 systems in terms of Young's Modulus elongation. Furthermore, the adhesion properties of latex-rGO based composites were studied in order to use them as possible pressure sensitive adhesives. The electrical conductivity is the highest reported for such composite materials.

9.2. Potential future work

Future work might focus on exploring the bimodal system further. Specifically, the relationship between the packing density of the spheres and the aspect ratio of the platelet is critical. Ultimately, it would be very interesting to repeat the in situ-reduction to produce highly conducting composites at extraordinarily low weight fractions. By using GO there will be better compatibility with the matrix during sample preparation because

it is highly hydrophilic and forms stable aqueous colloids as seen for the latex-GO based composite and the NLR-GO based composite. In terms of permeation performance, another possibility is to try using other solvents such as water and ethanol and see if the graphene will give better results compared to the NLR itself, and then try to see how it will change using rGO instead. Furthermore, using rGO after the reduction in situ will lead to the creation of a composite with better permeation performance compared to the graphene based composite as a consequence of the high effectivity of creating conductive rubber composites. It would be also interesting to consider the use of larger and non-deformable matrices, such as glass or silica beads with the possibility of being able to remove the matrix later, which was impossible to do with the present system. Some trials have been performed to essentially produce inverse structures by removing the polymeric matrix, but unfortunately, in these studies, the range of solvents used destroyed the segregated network. By continuing to investigate the interface between chemically different nanomaterials and polymer latexes I am hoping to understand the mechanism that is determining the interfacial interaction at the nanoscale, and how this relates to the macroscale properties. By understanding this interaction, it should be possible to design hybrids composite systems for various applications, such as solar cells, batteries, supercapacitors and others. For example, rGO-TiO_2 or rGO-MoS_2 composites could be used for photo-electrocatalytic applications and so if we can optimise their inclusion in our system we can develop solar cells that can absorb a fraction of the solar spectrum, and of course, the combination of different semiconductors can enhance the performance of the system.

Appendix

In table 1 are shown all the electrical conductivity data of different composites that I have used in Figure 5.17 A.B. in Chapter 5.

Table 1. Electrical Conductivity of polymer nanocomposites with different conductive fillers.

Polymer nanocomposite	Method	Percolation Threshold	Highest reported conductivity
PVAc-carbon black [125]	Latex technology	~ 2.0 vol.%	33.8 S/m at 20 vol.%
Poly(MMA-co-BA)-carbon black [126]	Latex technology	~ 1.45 vol.%	~10 S/m at 12 vol.%
PMMA/NanoG [127]	In-situ polymerization	~ 0.3 vol. %	~ 1.0 S/m at 2 vol.%
PVAc- SWNTs [128]	Latex technology	< 0.1 wt.%	~25 S/m at 4.0 wt.%
PS-MWNTs [247]	Latex technology	~ 1.5 wt.%	~1.0 S/m at 5.5 wt.%
BA:MMA:AAEM-SWNTs [131]	Latex technology	~ 0.12 wt. %	~10 S/m at 1 wt.%
PS/ CCG [132]	Latex technology	0.60 wt.%	~15 S/m at 2.0 wt.%
Polycarbonate-FGS [129]	Latex technology	0.14 vol.%	~51.2 S/m at 2.2 vol.%
PS-RGO [248]	Latex technology	0.9 wt.%	12 S/m at 2wt. %

PP-RGO [248]	Latex technology	0.4 wt.%	0.4 S/m at 2wt.%
PMMA-RGO [133]	Latex technology	0.16 vol.%	~64.1 S/m at 2.7 vol.%
PMMA-co-BA-CB [126]	Latex technology	2.9 wt.%	10 S/m at 24 wt%
PP-CB [249]	Latex technology	4.5 wt.%	1.5 S/m at 10 wt%
PS-MWNTs [247]	Latex technology	1.5 wt.%	1 S/m at 5.5.wt%
PP-MWNTs [249]	Latex technology	0.3 wt.%	1.5 S/m at 1wt%
PMMA-rGO [216]	Emulsion polymerisation	0.32 wt.%	64 S/m at 5.4 wt%
PS-rGO [250]	Mixing technique	0.16 wt.%	20.5 S/m at 8wt%
PVP-rGO [251]	In situ-polymerisation	0.6 wt.%	0.23 S/m at 0.9 wt%
PTFE-rGO [252]	Latex technology	0.5 wt.%	1.4 S/m at 2 wt%
Polycarbonate-FGS [129]	Solution blending	0.28 wt.%	51.2 S/m at 4.4 wt%
PS-CCG [132]	Latex technology	0.6 wt.%	15 S/m at 2 wt%

PP-graphene [249]	Latex technology	1.2 wt.%	1.5 S/m at 3.5 wt%
PS-GNs [109]	Latex technology	0.18 wt.%	25.2 S/m at 2.4 wt%
PS-EVA-GSs [134]	Solvent mixing	0.3 wt.%	1024 S/m at 9.6 wt%
PA6-mGNSs [217]	Mixing technique	0.064 wt.%	60 S/m at 4.9wt%
Cellulose-CC GSs [95]	Filtering emulsion	0.3 wt.%	71.8 S/m at 10 wt%
PMMA-co-BA-NMG [104]	Latex technology	0.8 wt.%	700 S/m at 22 wt%
PMMA- NanoG [253]	In situ polymerization	0.6 wt.%	1 S/m at 4 wt%
PP-graphite [249]	Latex technology	7 wt.%	0.1 S/m at 10 wt%

In table 2 are shown the mechanical data for different composites that I have found in the literature to compare the results that I have explained in Chapter 8.

Table 2. Mechanical properties of graphene-based composites.

Polymer nanocomposite	Method	Optimum loading	Matrix modulus E_m/GPa	Tensile modulus increase /%	Graphene modulus E_f / GPa	Tensile strength increase /%
PMMA-Gr [112]	In situ polymerization	0.5 wt.%	2.1	150	1262	114

PMMA-GO [139]	Melt mixing	1 wt.%	2.2	35	152	21
rGO-g-PMMA [140]	Emulsion polymerization	1wt%	3.12	42	265	15
PVA-GO [138]	Solution blending	0.3 wt.%	2.3	150	2335	149
PVA-rGO [137]	Solution blending	0.7 wt.%	4	37	379	40
PVA-fGr [254]	Solution blending	5 wt.%	2.9	150	177	153
PP-frGO [243]	Solution blending	0.5 wt.%	1.15	16.5	65	19
PP-GNP [244]	In situ polymerization	4 wt. %	1.6	23	21	12
PP-Gr [136]	Melt mixing	0.42 wt.%	1	74	181	54

References

[1] B. O. D. Velev and E. W. Kaler, “Structured Porous Materials via Colloidal Crystal Templating : From Inorganic Oxides to Metals,” *Adv. Mater.*, vol. 12, pp. 531–534, 2000.

[2] S. K. Bhattacharya, *Metal filled polymers*, vol. 11. CRC Press, 1986.

[3] http://www.robaid.com/bionics/computation-3d-printing-and-testing-of-bone-inspired-composites.htm, http://www.mastour.com/blog/what-is-ready-mix-concrete-composed-of/composition-of-concrete-4/, https://www.asiapapermarkets.com/researchers-make-breakthroug.

[4] V. Nicolosi, M. Chhowalla, M. G. Kanatzidis, M. S. Strano, and J. N. Coleman, “Liquid Exfoliation of Layered Materials Liquid Exfoliation of Layered Materials,” *Science (80-.).*, vol. 340, 2013.

[5] R. Mas-Ballesté, C. Gómez-Navarro, J. Gómez-Herrero, and F. Zamora, “2D materials: To graphene and beyond,” *Nanoscale*. pp. 20–30, 2011.

[6] K. S. Novoselov *et al.*, “Electric Field Effect in Atomically Thin Carbon Films,” *Science (80-.).*, vol. 306, no. 5696, pp. 666–669, 2004.

[7] X. Gu and R. Yang, “Phonon transport and thermal conductivity in two-dimensional materials,” *Annu. Rev. Heat Transf.*, vol. 19, pp. 1–67, 2016.

[8] X. Geng and J. Yi, *The Development of High-Temperature Superconductors and 2D Iron-Based Superconductors*. Elsevier Inc., 2019.

[9] C. Anichini *et al.*, “Chemical sensing with 2D materials,” *This J. is Cite this Chem. Soc. Rev*, vol. 4860, p. 4860, 2018.

[10] A. A. Balandin *et al.*, “Superior thermal conductivity of single-layer graphene,” *Nano Lett.*, vol. 8, no. 3, pp. 902–907, 2008.

[11] K. S. Novoselov *et al.*, “Room-temperature quantum hall effect in graphene,” *Science (80-.).*, vol. 315, no. 5817, p. 1379, 2007.

[12] J. W. K. and J. H. Changgu Lee, Xiaoding Wei, “Measurement of the Elastic Properties and Intrinsic Strength of Monolayer Graphene,” *Science (80-.).*, vol. 321, no. 5887, pp. 382–385, 2008.

[13] V. Berry, “Impermeability of graphene and its applications,” *Carbon N. Y.*, vol. 62, pp. 1–10, 2013.

[14] G. Mittal, V. Dhand, K. Y. Rhee, S. J. Park, and W. R. Lee, “A review on carbon nanotubes and graphene as fillers in reinforced polymer nanocomposites,” *J. Ind. Eng. Chem.*, vol. 21, no. November 2017, pp. 11–25, 2015.

[15] Q. Yu, J. Lian, S. Siriponglert, H. Li, Y. P. Chen, and S. S. Pei, “Graphene segregated on Ni surfaces and transferred to insulators,” *Appl. Phys. Lett.*, vol. 93, no. 11, pp. 1–4, 2008.

[16] X. Li *et al.*, “33.Large-area synthesis of high-quality and uniform graphene films on copper foils.,” *Science (80-.).*, vol. 324, no. 5932, pp. 1312–1314, 2009.

[17] Y. Wang *et al.*, “Toward High Throughput Interconvertible Graphane-to-Graphene Growth and Patterning,” *ACS Nano*, vol. 4, no. 10, pp. 6146–6152, 2010.

[18] C. Berger *et al.*, “Ultrathin epitaxial graphite: 2D electron gas properties and a route toward graphene-based nanoelectronics,” *J. Phys. Chem. B*, vol. 108, no. 52, pp. 19912–19916, 2004.

[19] M. Choucair, P. Thordarson, and J. A. Stride, “Gram-scale production of graphene based on solvothermal synthesis and sonication,” *Nat. Nanotechnol.*, vol. 4, no. 1, pp. 30–33, 2009.

[20] X. Wang, L. Zhi, N. Tsao, Ž. Tomović, J. Li, and K. Müllen, “Transparent carbon films as electrodes in organic solar cells,” *Angew. Chemie - Int. Ed.*, vol. 47, no. 16, pp. 2990–2992, 2008.

[21] Y. Hernandez *et al.*, “High-yield production of graphene by liquid-phase exfoliation of graphite,” *Nat. Nanotechnol.*, vol. 3, no. 9, pp. 563–568, 2008.

[22] M. Lotya *et al.*, “Liquid Phase Production of Graphene by Exfoliation of Graphite in Surfactant / Water Solutions Liquid Phase Production of Graphene by Exfoliation of Graphite in Surfactant / Water Solutions,” no. 11, pp. 3611–3620, 2009.

[23] X. Li *et al.*, “Highly conducting graphene sheets and Langmuir-Blodgett films,”

Nat. Nanotechnol., vol. 3, no. 9, pp. 538–542, 2008.

[24] N. Liu, F. Luo, H. Wu, Y. Liu, C. Zhang, and J. Chen, "One-step ionic-liquid-assisted electrochemical synthesis of ionic-liquid-functionalized graphene sheets directly from graphite," *Adv. Funct. Mater.*, vol. 18, no. 10, pp. 1518–1525, 2008.

[25] D. Li, M. B. Müller, S. Gilje, R. B. Kaner, and G. G. Wallace, "Processable aqueous dispersions of graphene nanosheets," *Nat. Nanotechnol.*, vol. 3, no. 2, pp. 101–105, 2008.

[26] W. S. Hummers and R. E. Offeman, "Preparation of Graphitic Oxide," *J. Am. Chem. Soc.*, vol. 80, no. 6, p. 1339, 1958.

[27] J. Mattei, "Crosslinking graphene oxide and chitosan to form scalable water treatment membranes." 2017.

[28] D. W. Boukhvalov and M. I. Katsnelson, "Modeling of Graphite Oxide," *J.Am. Chem. Soc.*, vol. 130, no. July, pp. 10697–10701, 2008.

[29] H. Becerril, J. Mao, Z. Liu, R. Stoltenberg, Z. Bao, and Y. Chen, "Evaluation of Solution-Processed Reduced Graphene Oxide Films as Transparent Conductors," *ACS Nano*, vol. 2, no. 3, pp. 463–470, 2008.

[30] G. Eda, C. Mattevi, H. Yamaguchi, H. Kim, and M. Chhowalla, "Insulator to semimetal transition in graphene oxide," *J. Phys. Chem. C*, vol. 113, no. 35, pp. 15768–15771, 2009.

[31] K. P. Loh, Q. Bao, G. Eda, and M. Chhowalla, "Graphene oxide as a chemically tunable platform for optical applications," *Nat. Chem.*, vol. 2, no. 12, pp. 1015–1024, 2010.

[32] X. Zuo *et al.*, "Graphene oxide-facilitated electron transfer of metalloproteins at electrode surfaces," *Langmuir*, vol. 26, no. 3, pp. 1936–1939, 2010.

[33] https://www.utu.fi/en/units/sci/units/chemistry/research/mcca/PublishingImages/GO rGO.jpg.

[34] S. Stankovich *et al.*, "Synthesis of graphene-based nanosheets via chemical

reduction of exfoliated graphite oxide," *Carbon N. Y.*, vol. 45, no. 7, pp. 1558–1565, 2007.

[35] S. Stankovich, R. D. Piner, X. Chen, N. Wu, S. T. Nguyen, and R. S. Ruoff, "Stable aqueous dispersions of graphitic nanoplatelets via the reduction of exfoliated graphite oxide in the presence of poly(sodium 4-styrenesulfonate)," *J. Mater. Chem.*, vol. 16, no. 2, pp. 155–158, 2006.

[36] H. J. Shin *et al.*, "Efficient reduction of graphite oxide by sodium borohydride and its effect on electrical conductance," *Adv. Funct. Mater.*, vol. 19, no. 12, pp. 1987–1992, 2009.

[37] M. Periasamy and M. Thirumalaikumar, "Methods of enhancement of reactivity and selectivity of sodium borohydride for applications in organic synthesis," *J. Organomet. Chem.*, vol. 609, no. 1–2, pp. 137–151, 2000.

[38] M. J. Fernández-Merino *et al.*, "Vitamin C Is an Ideal Substitute for Hydrazine in the Reduction of Graphene Oxide Suspensions," *J. Phys. Chem. C*, vol. 114, no. 14, pp. 6426–6432, 2010.

[39] I. K. Moon, J. Lee, R. S. Ruoff, and H. Lee, "Reduced graphene oxide by chemical graphitization," *Nat. Commun.*, vol. 1, no. 6, pp. 1–6, 2010.

[40] S. Pei, J. Zhao, J. Du, W. Ren, and H. M. Cheng, "Direct reduction of graphene oxide films into highly conductive and flexible graphene films by hydrohalic acids," *Carbon N. Y.*, vol. 48, no. 15, pp. 4466–4474, 2010.

[41] X. Fan *et al.*, "Deoxygenation of exfoliated graphite oxide under alkaline conditions: a green route to graphene preparation," *Adv. Mater.*, vol. 20, no. 23, pp. 4490–4493, 2008.

[42] Z. S. Wu *et al.*, "Synthesis of graphene sheets with high electrical conductivity and good thermal stability by hydrogen arc discharge exfoliation," *ACS Nano*, vol. 3, no. 2, pp. 411–417, 2009.

[43] Z. S. Wu, W. Ren, L. Gao, B. Liu, C. Jiang, and H. M. Cheng, "Synthesis of high-quality graphene with a pre-determined number of layers," *Carbon N. Y.*, vol. 47, no. 2, pp. 493–499, 2009.

[44] H. C. Schniepp *et al.*, “Functionalized single graphene sheets derived from splitting graphite oxide,” *J. Phys. Chem. B*, vol. 110, no. 17, pp. 8535–8539, 2006.

[45] X. Wang, L. Zhi, and K. Müllen, “Transparent, conductive graphene electrodes for dye-sensitized solar cells,” *Nano Lett.*, vol. 8, no. 1, pp. 323–327, 2008.

[46] X. Li, H. Wang, J. T. Robinson, H. Sanchez, G. Diankov, and H. Dai, “Simultaneous Nitrogen Doping and Reduction of Graphene Oxide,” *J. Am. Chem. Soc.*, vol. 131, no. 43, pp. 15939–15944, 2009.

[47] Z. S. Wu *et al.*, “Synthesis of Graphene Sheets with High Electrical Conductivity and Good Thermal Stability by Hydrogen Arc Discharge Exfoliation94,” *ACS Nano*, vol. 3, no. 2, pp. 411–417, 2009.

[48] D. Voiry *et al.*, “High-quality graphene via microwave reduction of solution-exfoliated graphene oxide,” *Science (80-.).*, vol. 353, no. 6306, pp. 1413–1416, 2016.

[49] Y. Zhu, S. Murali, M. D. Stoller, A. Velamakanni, R. D. Piner, and R. S. Ruoff, “Microwave assisted exfoliation and reduction of graphite oxide for ultracapacitors,” *Carbon N. Y.*, vol. 48, no. 7, pp. 2118–2122, 2010.

[50] H. M. A. Hassan *et al.*, “Microwave synthesis of graphene sheets supporting metal nanocrystals in aqueous and organic media,” *J. Mater. Chem.*, vol. 19, no. 23, pp. 3832–3837, 2009.

[51] L. J. Cote, R. Cruz-Silva, and J. Huang, “Flash Reduction and Patterning of Graphite Oxide and Its Polymer Composite,” *J. Am. Chem. Soc.*, vol. 131, no. 17, pp. 11027–11032, 2009.

[52] H. Guo, X. Wang, Q. Qian, F. Wang, and X. Xia, “A Green Approach to the Synthesis of graphene nanosheets,” *ACS Nano*, vol. 3, no. 9, pp. 2653–2659, 2009.

[53] Z. Wang, X. Zhou, J. Zhang, F. Boey, and H. Zhang, “Direct Electrochemical Reduction of Single-Layer Graphene Oxide and Subsequent Functionalization with Glucose Oxidase,” *J. Phys. Chem. C*, vol. 113, no. 32, pp. 14071–14075, 2009.

[54] S. J. An *et al.*, “Thin film fabrication and simultaneous anodic reduction of deposited graphene oxide platelets by electrophoretic deposition,” *J. Phys. Chem. Lett.*, vol. 1, no. 8, pp. 1259–1263, 2010.

[55] G. K. Ramesha and S. Sampath, “Electrochemical Reduction of Oriented Graphene Oxide Films : An in Situ Raman Spectroelectrochemical Study,” *Phys. Chem C*, vol. 113, no. 19, pp. 7985–7989, 2009.

[56] X. Zhao *et al.*, “Photocatalytic Reduction of Graphene Oxide-TiO 2 Nanocomposites for Improving Resistive-Switching Memory Behaviors,” *Small*, vol. 14, no. 29, p. 1801325, 2018.

[57] W. D. Yang, Y. R. Li, and Y. C. Lee, “Synthesis of r-GO/TiO2composites via the UV-assisted photocatalytic reduction of graphene oxide,” *Appl. Surf. Sci.*, vol. 380, pp. 249–256, 2016.

[58] G. Williams, B. Seger, and P. V Kamat, “UV-Assisted Photocatalytic Reduction of Graphene Oxide,” *ACS Nano*, vol. 2, no. 7, pp. 1487–1491, 2008.

[59] G. Williams and P. V. Kamat, “Graphene-semiconductor nanocomposites: Excited-state interactions between ZnO nanoparticles and graphene oxide,” *Langmuir*, vol. 25, no. 24, pp. 13869–13873, 2009.

[60] P. Afzali, Y. Abdi, and E. Arzi, “Directional reduction of graphene oxide sheets using photocatalytic activity of ZnO nanowires for the fabrication of a high sensitive oxygen sensor,” *Sensors Actuators, B Chem.*, vol. 195, pp. 92–97, 2014.

[61] Y. H. Ng, A. Iwase, A. Kudo, and R. Amal, “Reducing graphene oxide on a visible-light BiVO4 photocatalyst for an enhanced photoelectrochemical water splitting,” *J. Phys. Chem. Lett.*, vol. 1, no. 17, pp. 2607–2612, 2010.

[62] G. Demazeau, “Solvothermal processes-A route to the stabilization of new materials,” *J Mater Chem*, vol. 9, no. 1, pp. 15–18, 1999.

[63] Y. Zhou, Q. Bao, L. A. L. Tang, Y. Zhong, and K. P. Loh, “Hydrothermal dehydration for the ‘green’ reduction of exfoliated graphene oxide to graphene and demonstration of tunable optical limiting properties,” *Chem. Mater.*, vol. 21, no. 13, pp. 2950–2956, 2009.

[64] S. Dubin *et al.*, “A one-step, solvothermal reduction method for producing reduced graphene oxide dispersions in organic solvents,” *ACS Nano*, vol. 4, no. 7, pp. 3845–3852, 2010.

[65] S. Iijima, “Helical microtubules of graphitic carbon,” *Nature*, vol. 354, no. 6348, pp. 56–58, 1991.

[66] T.-W. C. Erik T. Thostenson, Zhifeng Ren, “Advances in the science and technology of carbon nanotubes and their composites: a review,” *Compos. Sci. Technol.*, vol. 61, pp. 1899–1912, 2001.

[67] T. Belin and F. Epron, “Characterization methods of carbon nanotubes: A review,” *Mater. Sci. Eng. B Solid-State Mater. Adv. Technol.*, vol. 119, no. 2, pp. 105–118, 2005.

[68] S. lljima & T. Ichihashi, “Single-shell carbon nanotubes of 1-nm diameter,” *Nature*, vol. 363, pp. 603–605, 1993.

[69] S. Fan *et al.*, “Self-Oriented Regular Arrays of Carbon Nanotubes and Their Field Emission Properties,” *Science (80-.).*, vol. 283, pp. 512–514, 1999.

[70] A. G. Rinzler *et al.*, “Large-scale purification ofsingle-wall carbon nanotubes: process, product, and characterization,” *Appl. Phys. A*, vol. 37, no. 1, pp. 29–37, 1998.

[71] and J. H. W. Z. P. Huang, J. W. Xu, Z. F. Ren, “Growth of highly oriented carbon nanotubes by plasma-enhanced hot filament chemical vapor deposition,” *Appl. Phys. Lett.*, vol. 73, no. 26, pp. 3845–3847, 1998.

[72] J. Prasek *et al.*, “Methods for carbon nanotubes synthesis - Review,” *J. Mater. Chem.*, vol. 21, no. 40, pp. 15872–15884, 2011.

[73] S. Imtiaz, M. Siddiq, A. Kausar, S. T. Muntha, J. Ambreen, and I. Bibi, “A Review Featuring Fabrication, Properties and Applications of Carbon Nanotubes (CNTs) Reinforced Polymer and Epoxy Nanocomposites,” *Chinese J. Polym. Sci. (English Ed.*, vol. 36, no. 4, pp. 445–461, 2018.

[74] C. L. C. & C. M. L. Stanislaus S. Wong, Ernesto Joselevich, Adam T. Woolley, “Covalently functionalized nanotubes as nanometre- sized probes in chemistry

and biology," *Nature*, vol. 394, pp. 52–55, 1998.

[75] S. H. Kim *et al.*, "Synthesis of polystyrene/poly(butyl acrylate) core-shell latex and its surface morphology," *J. Appl. Polym. Sci.*, vol. 88, no. 3, pp. 595–601, 2003.

[76] M. . Paridah, A. Moradbak, A. . Mohamed, F. abdulwahab taiwo Owolabi, M. Asniza, and S. H. . Abdul Khalid, "Emulsion Polymerization Mechanism," *IntechOpen*, pp. 4–13, 2016.

[77] S. Mondal, B. Gupta, and H. Singh, "Acrylic monomers based emulsion copolymer for coating application," *Indian J. Fibre Text. Res.*, vol. 30, no. 2, pp. 184–189, 2005.

[78] G. Riess and C. Labbe, "Block Copolymers in Emulsion and Dispersion Polymerization," *Macromol. Rapid Commun.*, vol. 25, no. 2, pp. 401–435, 2004.

[79] V. I. Eliseeva, S. S. Ivanchev, S. I. Kuchanov, and A. V Lebedev, *Emulsion polymerization and its applications in industry*. Springer Science & Business Media, 2012.

[80] J. C. Padget, "Polymers for water-based coatings — a systematic overview," *J. Coat. Technol.*, vol. 66, no. 839, pp. 89–105, 1994.

[81] M. S. E.-A. Peter A. Lovell, *Emulsion polymerization and emulsion polymers*. 1997.

[82] A. Tzitzinou, "Physical Characterisation Acrylic of Latex Film Formation," 1999.

[83] J. L. Jacob, J. d'Auzac, and J. C. Prevôt, "The composition of natural latex from Hevea brasiliensis," *Clin. Rev. Allergy*, vol. 11, no. 3, pp. 325–337, 1993.

[84] C. Zhang, T. Zhai, Y. Dan, and L. S. Turng, "Reinforced natural rubber nanocomposites using graphene oxide as a reinforcing agent and their in situ reduction into highly conductive materials," *Polym. Compos.*, vol. 38, pp. E199–E207, 2017.

[85] R. P. Dinsmore, "Rubber Chemistry," *Ind. Eng. Chem.*, vol. 43, no. 4, pp. 795–803, 1951.

[86] J. Zainon, “Presentation of natural rubber.” [Online]. Available: https://www.slideshare.net/jannahbest/natural-rubber-latex.

[87] D. G. Papageorgiou, I. A. Kinloch, and R. J. Young, “Mechanical properties of graphene and graphene-based nanocomposites,” *Prog. Mater. Sci.*, vol. 90, pp. 75–127, 2017.

[88] X. Huang, X. Qi, F. Boey, and H. Zhang, “Graphene-based composites,” *Chem. Soc. Rev.*, vol. 41, no. 2, pp. 666–686, 2012.

[89] K. H. Liao, Y. T. Park, A. Abdala, and C. Macosko, “Aqueous reduced graphene/thermoplastic polyurethane nanocomposites,” *Polym. (United Kingdom)*, vol. 54, no. 17, pp. 4555–4559, 2013.

[90] T. Ramanathan *et al.*, “Functionalized graphene sheets for polymer nanocomposites.,” *Nat. Nanotechnol.*, vol. 3, no. 6, pp. 327–331, 2008.

[91] X. Zhao, Q. Zhang, D. Chen, and P. Lu, “Enhanced mechanical properties of graphene-based polyvinyl alcohol composites,” *Macromolecules*, vol. 43, no. 5, pp. 2357–2363, 2010.

[92] S. Mo *et al.*, “Enhanced properties of poly(vinyl alcohol) composite films with functionalized graphene,” *RSC Adv.*, vol. 5, no. 118, pp. 97738–97745, 2015.

[93] H. Kim *et al.*, “Graphene/polyethylene nanocomposites: Effect of polyethylene functionalization and blending methods,” *Polymer (Guildf).*, vol. 52, no. 8, pp. 1837–1846, 2011.

[94] D. Galpaya, M. Wang, M. Liu, N. Motta, E. Waclawik, and C. Yan, “Recent Advances in Fabrication and Characterization of Graphene-Polymer Nanocomposites,” *Graphene*, vol. 01, no. 02, pp. 30–49, 2012.

[95] N. D. Luong *et al.*, “Graphene/cellulose nanocomposite paper with high electrical and mechanical performances,” *J. Mater. Chem.*, vol. 21, no. 36, pp. 13991–13998, 2011.

[96] I. H. Kim and Y. G. Jeong, “Polylactide/exfoliated graphite nanocomposites with enhanced thermal stability, mechanical modulus, and electrical conductivity,” *J. Polym. Sci. Part B Polym. Phys.*, vol. 48, no. 8, pp. 850–858, 2010.

[97] H. Bin Zhang *et al.*, “Electrically conductive polyethylene terephthalate/graphene nanocomposites prepared by melt compounding,” *Polymer (Guildf).*, vol. 51, no. 5, pp. 1191–1196, 2010.

[98] V. Singh, D. Joung, L. Zhai, S. Das, S. I. Khondaker, and S. Seal, “Graphene based materials: Past, present and future,” *Prog. Mater. Sci.*, vol. 56, no. 8, pp. 1178–1271, 2011.

[99] H. Kim and C. W. Macosko, “Processing-property relationships of polycarbonate/graphene composites,” *Polymer (Guildf).*, vol. 50, no. 15, pp. 3797–3809, 2009.

[100] K. Kalaitzidou, H. Fukushima, and L. T. Drzal, “A new compounding method for exfoliated graphite-polypropylene nanocomposites with enhanced flexural properties and lower percolation threshold,” *Compos. Sci. Technol.*, vol. 67, no. 10, pp. 2045–2051, 2007.

[101] C. Bao *et al.*, “Preparation of graphene by pressurized oxidation and multiplex reduction and its polymer nanocomposites by masterbatch-based melt blending,” *J. Mater. Chem.*, vol. 22, no. 13, pp. 6088–6096, 2012.

[102] A. Noël, J. Faucheu, M. Rieu, J. P. Viricelle, and E. Bourgeat-Lami, “Tunable architecture for flexible and highly conductive graphene-polymer composites,” *Compos. Sci. Technol.*, vol. 95, pp. 82–88, 2014.

[103] C. Tang *et al.*, “Conductive polymer nanocomposites with hierarchical multi-scale structures via self-assembly of carbon-nanotubes on graphene on polymer-microspheres,” *Nanoscale*, vol. 6, no. 14, pp. 7877–7888, 2014.

[104] A. Noël, J. Faucheu, J. M. Chenal, J. P. Viricelle, and E. Bourgeat-Lami, “Electrical and mechanical percolation in graphene-latex nanocomposites,” *Polym. (United Kingdom)*, vol. 55, no. 20, pp. 5140–5145, 2014.

[105] E. Bourgeat-Lami, J. Faucheu, and A. Noël, “Latex routes to graphene-based nanocomposites,” *Polym. Chem.*, vol. 6, no. 30, pp. 5323–5357, 2015.

[106] K. Hu, D. D. Kulkarni, I. Choi, and V. V. Tsukruk, “Graphene-polymer nanocomposites for structural and functional applications,” *Prog. Polym. Sci.*, 2014.

[107] N. Yousefi, M. M. Gudarzi, Q. Zheng, S. H. Aboutalebi, F. Sharif, and J. K. Kim, "Self-alignment and high electrical conductivity of ultralarge graphene oxide-polyurethane nanocomposites," *J. Mater. Chem.*, vol. 22, no. 25, pp. 12709–12717, 2012.

[108] W. L. Zhang, Y. D. Liu, H. J. Choi, and Y. Seo, "Core-shell structured graphene oxide-adsorbed anisotropic poly(methyl methacrylate) microparticles and their electrorheology," *RSC Adv.*, vol. 3, no. 29, pp. 11723–11731, 2013.

[109] P. Zhao *et al.*, "Electrically conductive graphene-filled polymer composites with well organized three-dimensional microstructure," *Mater. Lett.*, vol. 121, pp. 74–77, 2014.

[110] M. M. Gudarzi and F. Sharif, "Molecular level dispersion of graphene in polymer matrices using colloidal polymer and graphene," *J. Colloid Interface Sci.*, vol. 366, no. 1, pp. 44–50, 2012.

[111] Z. Xu and C. Gao, "In situ polymerization approach to graphene-reinforced nylon-6 composites," *Macromolecules*, vol. 43, no. 16, pp. 6716–6723, 2010.

[112] J. Wang, Z. Shi, Y. Ge, Y. Wang, J. Fan, and J. Yin, "Solvent exfoliated graphene for reinforcement of PMMA composites prepared by in situ polymerization," *Mater. Chem. Phys.*, vol. 136, no. 1, pp. 43–50, 2012.

[113] J. Y. Wang, S. Y. Yang, Y. L. Huang, H. W. Tien, W. K. Chin, and C. C. M. Ma, "Preparation and properties of graphene oxide/polyimide composite films with low dielectric constant and ultrahigh strength via in situ polymerization," *J. Mater. Chem.*, vol. 21, no. 35, pp. 13569–13575, 2011.

[114] C. C. Teng *et al.*, "Thermal conductivity and structure of non-covalent functionalized graphene/epoxy composites," *Carbon N. Y.*, vol. 49, no. 15, pp. 5107–5116, 2011.

[115] Z. L. Mo, T. T. Xie, J. X. Zhang, Y. X. Zhao, and R. Bin Guo, "Synthesis and characterization of NanoGs-PPy/epoxy nanocomposites by in situ polymerization," *Synth. React. Inorganic, Met. Nano-Metal Chem.*, vol. 42, no. 8, pp. 1172–1176, 2012.

[116] F. Zhang, B. Wang, R. Man, and Zhiyuan Peng, "Isothermal crystallization

kinetics of in situ Nylon 6/graphene composites by differential scanning calorimetry," *Polym. Eng. Sci.*, vol. 54, no. 11, pp. 2610–2616, 2014.

[117] J. R. Potts *et al.*, "Thermomechanical properties of chemically modified graphene/poly(methyl methacrylate) composites made by in situ polymerization," *Carbon N. Y.*, vol. 49, no. 8, pp. 2615–2623, 2011.

[118] X. Wang, Y. Hu, L. Song, H. Yang, W. Xing, and H. Lu, "In situ polymerization of graphene nanosheets and polyurethane with enhanced mechanical and thermal properties," *J. Mater. Chem.*, vol. 21, no. 12, pp. 4222–4227, 2011.

[119] W. Thongruang, R. J. Spontak, and C. M. Balik, "Bridged double percolation in conductive polymer composites: an electrical conductivity, morphology and mechanical property study," *Polymer (Guildf).*, vol. 43, no. 13, pp. 3717–3725, 2002.

[120] R. P. Kusy, "Influence of particle size ratio on the continuity of aggregates," *J. Appl. Phys.*, vol. 48, no. 12, pp. 5301–5305, 1977.

[121] R. Taherian, M. J. Hadianfard, and A. N. Golikand, "A new equation for predicting electrical conductivity of carbon-filled polymer composites used for bipolar plates of fuel cells," *J. Appl. Polym. Sci.*, vol. 128, no. 3, pp. 1497–1509, 2013.

[122] D. Stauffer and A. Aharony, *Introduction to percolation theory: revised second edition*. CRC press, 2014.

[123] P. Pötschke, S. M. Dudkin, and I. Alig, "Dielectric spectroscopy on melt processed polycarbonate - Multiwalled carbon nanotube composites," *Polymer (Guildf).*, vol. 44, no. 17, pp. 5023–5030, 2003.

[124] B. E. Kilbride *et al.*, "Experimental observation of scaling laws for alternating current and direct current conductivity in polymer-carbon nanotube composite thin films," *J. Appl. Phys.*, vol. 92, no. 7, pp. 4024–4030, 2002.

[125] J. C. Grunlan, W. W. Gerberich, and L. F. Francis, "Electrical and Mechanical Behavior of Carbon Black-Filled Poly(Viny1 Acetate) Latex-Based Composites," vol. 41, no. 11, pp. 1523–1526, 2001.

[126] J. C. Grunlan, Y. Ma, M. A. Grunlan, W. W. Gerberich, and L. F. Francis, “Monodisperse latex with variable glass transition temperature and particle size for use as matrix starting material for conductive polymer composites,” *Polymer (Guildf).*, vol. 42, no. 16, pp. 6913–6921, 2001.

[127] G. Chen, W. Weng, D. Wu, and C. Wu, “PMMA/graphite nanosheets composite and its conducting properties,” *Eur. Polym. J.*, vol. 39, no. 12, pp. 2329–2335, 2003.

[128] J. C. Grunlan, A. R. Mehrabi, M. V. Bannon, and J. L. Bahr, “Water-based single-walled-nanotube-filled polymer composite with an exceptionally low percolation threshold,” *Adv. Mater.*, vol. 16, no. 2, pp. 150–153, 2004.

[129] M. Yoonessi and J. R. Gaier, “Highly conductive multifunctional graphene polycarbonate nanocomposites,” *ACS Nano*, vol. 4, no. 12, pp. 7211–7220, 2010.

[130] I. Jurewicz *et al.*, “Colloid-assisted self-assembly of robust, three-dimensional networks of carbon nanotubes over large areasa,” *Macromol. Rapid Commun.*, vol. 31, no. 7, pp. 609–615, 2010.

[131] I. Jurewicz, P. Worajittiphon, A. A. K. King, P. J. Sellin, J. L. Keddie, and A. B. Dalton, “Locking carbon nanotubes in confined lattice geometries - A route to low percolation in conducting composites,” *J. Phys. Chem. B*, vol. 115, no. 20, pp. 6395–6400, 2011.

[132] E. Tkalya, M. Ghislandi, A. Alekseev, C. Koning, and J. Loos, “Latex-based concept for the preparation of graphene-based polymer nanocomposites,” *J. Mater. Chem.*, vol. 20, no. 15, pp. 3035–3039, 2010.

[133] V. H. Pham, T. T. Dang, S. H. Hur, E. J. Kim, and J. S. Chung, “Highly conductive poly (methyl methacrylate)(PMMA)-reduced graphene oxide composite prepared by self-assembly of PMMA latex and graphene oxide through electrostatic interaction,” *ACS Appl. Mater. Interfaces*, vol. 4, no. 5, pp. 2630–2636, 2012.

[134] C. Wu *et al.*, “Highly conductive nanocomposites with three-dimensional, compactly interconnected graphene networks via a self-assembly process,” *Adv. Funct. Mater.*, vol. 23, no. 4, pp. 506–513, 2013.

[135] R. Verdejo, M. M. Bernal, L. J. Romasanta, and M. A. Lopez-Manchado, "Graphene filled polymer nanocomposites," *J. Mater. Chem.*, vol. 21, no. 10, pp. 3301–3310, 2011.

[136] P. Song, Z. Cao, Y. Cai, L. Zhao, Z. Fang, and S. Fu, "Fabrication of exfoliated graphene-based polypropylene nanocomposites with enhanced mechanical and thermal properties," *Polymer (Guildf).*, vol. 52, no. 18, pp. 4001–4010, 2011.

[137] T. Zhou *et al.*, "The preparation of high performance and conductive poly (vinyl alcohol)/graphene nanocomposite via reducing graphite oxide with sodium hydrosulfite," *Compos. Sci. Technol.*, vol. 71, no. 9, pp. 1266–1270, 2011.

[138] S. Kashyap, S. K. Pratihar, and S. K. Behera, "Strong and ductile graphene oxide reinforced PVA nanocomposites," *J. Alloys Compd.*, vol. 684, pp. 254–260, 2016.

[139] C. Vallés, I. A. Kinloch, R. J. Young, N. R. Wilson, and J. P. Rourke, "Graphene oxide and base-washed graphene oxide as reinforcements in PMMA nanocomposites," *Compos. Sci. Technol.*, vol. 88, pp. 158–164, 2013.

[140] L. X. Gong *et al.*, "Polymer grafted reduced graphene oxide sheets for improving stress transfer in polymer composites," *Compos. Sci. Technol.*, vol. 134, pp. 144–152, 2016.

[141] C. Gay and L. Leibler, "Theory of tackiness," *Phys. Rev. Lett.*, vol. 82, no. 5, pp. 936–939, 1999.

[142] I. Minkoff, "Applications of the scanning electron microscope in materials science," *J. Mater. Sci.*, vol. 2, no. 4, pp. 388–394, 1967.

[143] L. Reimer, "Introduction," in *Scanning Electron Microscopy: Physics of Image Formation and Microanalysis*, Berlin, Heidelberg: Springer Berlin Heidelberg, 1998, pp. 1–12.

[144] S. Nasrazadani and S. Hassani, *Modern analytical techniques in failure analysis of aerospace, chemical, and oil and gas industries*. Elsevier Ltd., 2015.

[145] https://en.wikipedia.org/wiki/Scanning_electron_microscope.

[146] "Introduction," in *Transmission Electron Microscopy: Physics of Image*

Formation, New York, NY: Springer New York, 2008, pp. 1–15.

[147] G. Haugstad, *Atomic Force Microscopy: Understanding Basic Modes and Advanced Applications*. Wiley, 2012.

[148] B. Cappella and G. Dietler, "Force-distance curves by atomic force microscopy," *Surf. Sci. Rep.*, vol. 34, no. 1–3, pp. 1–104, 1999.

[149] https://commons.wikimedia.org/wiki/File:AFM_schematic_(EN).svg.

[150] E. Meyer, "Atomic force microscopy," *Prog. Surf. Sci.*, vol. 41, no. 1, pp. 3–49, 1992.

[151] W. Melitz, J. Shen, A. C. Kummel, and S. Lee, "Kelvin probe force microscopy and its application," *Surf. Sci. Rep.*, vol. 66, no. 1, pp. 1–27, 2011.

[152] D. Harvey, "Analytical Chemistry 2.0: Chapter 10 - Spectroscopic Methods," *Anal. Bioanal. Chem.*, pp. 543–666, 2011.

[153] R. L. McCreery, *Raman Spectroscopy for Chemical Analysis*. 2000.

[154] https://en.wikipedia.org/wiki/Raman_spectroscopy.

[155] N. B. Colthup, L. H. Daly, and S. E. Wiberley, *Introduction to Infrared and Raman Spectroscopy*. 1990.

[156] Y. P. C. Isaac Childres, Luis A. Jauregui, Wonjun Park, Helin Cao, "Raman Spectroscopy of Graphene and Related Materials," in *New developments in photon and materials research 1*, 2013.

[157] https://www.azom.com/article.aspx?ArticleID=5958.

[158] H.-H. Perkampus, *UV-VIS Spectroscopy and its Applications*. Springer Science & Business Media, 2013.

[159] M. E. Brown, "Differential thermal analysis (DTA) and differential scanning calorimetry (DSC)," in *Introduction to Thermal Analysis. Springer, Dordrecht*, 1988.

[160] https://pslc.ws/macrog/dsc.htm.

[161] A. H. D. V.S. Ramachandran, Ralph M. Paroli, James J. Beaudoin, "Handbook of Thermal Analysis of Construction Materials," in *Norwich, N.Y.: Noyes*

Publications/William Andrew Pub, 2003.

[162] S. Gaisford, V. Kett, and P. Haines, *Principles of thermal analysis and calorimetry*. Royal society of chemistry, 2016.

[163] A.K.Chatterjee, "X-Ray Diffraction," in *Handbook of Analytical Techniques in Concrete Science and Technology Principles, Techniques, and Applications*, 2001, pp. 275–332.

[164] https://commons.wikimedia.org/w/index.php?curid=17543875.

[165] H. M. Rietveld, "The Rietveld method," *Phys. Scr.*, vol. 89, 2014.

[166] S. J. Kerber, T. L. Barr, G. P. Mann, W. A. Brantley, E. Papazoglou, and J. C. Mitchell, "The Complementary Nature of X-Ray Photoelectron Spectroscopy and Angle-Resolved X-Ray Diffraction Part I: Background and Theory," *J. Mater. Eng. Perform.*, vol. 7, no. 3, pp. 329–333, 1998.

[167] https://lsinstruments.ch/en/technology/dynamic-light-scattering-dls.

[168] M. Lotya, A. Rakovich, J. F. Donegan, and J. N. Coleman, "Measuring the lateral size of liquid-exfoliated nanosheets with dynamic light scattering," *Nanotechnology*, vol. 24, no. 26, 2013.

[169] J. R. Davis, "Introduction of tensile testing," in *Tensile Testing, 2nd Edition*, 2004.

[170] T. H. G. Megson, *Structural and Stress Analysis 2nd Edition*. 2005.

[171] http://polymerdatabase.com/polymer physics/Mechanical Properties.html.

[172] http://polymerdatabase.com/polymer physics/Stress-Strain Behavior.html.

[173] V. G. Rostiashvili and T. A. Vilgis, "Statistical Thermodynamics of Polymeric Networks," *Encycl. Polym. Nanomater.*, vol. 12, no. 2, pp. 1–18, 2007.

[174] A. A. Shabana, *Computational continuum mechanics*. John Wiley & Sons, 2018.

[175] A. Lindner *et al.*, "Adhesive and rheological properties of lightly crosslinked model acrylic networks," *J. Adhes.*, vol. 82, no. 3, pp. 267–310, 2006.

[176] R. Jovanović and M. A. Dubé, "Emulsion-Based Pressure-Sensitive Adhesives: A Review," *J. Macromol. Sci. - Polym. Rev.*, vol. 44, no. 1, pp. 1–51, 2004.

[177] H. K. Chuang, C. Chiu, and R. Paniagua, “Avery Adhesive Test Yields More Performance Data Than Traditional Probe,” *Adhes. Age*, vol. 40, no. 10, pp. 18–23, 1997.

[178] J. Keddie and A. F. Routh, “An introduction to Latex and the Principles of Colloidal Stability,” in *Fundamentals of latex film formation: processes and properties*, Springer Science & Business Media, 2010, pp. 1–26.

[179] P. R. Sperry, B. S. Snyder, M. L. O’Dowd, and P. M. Lesko, “Role of Water in Particle Deformation and Compaction in Latex Film Formation,” *Langmuir*, vol. 10, no. 8, pp. 2619–2628, 1994.

[180] H. Jiang, K. Yu, and Y. Wang, “Antireflective structures via spin casting of polymer latex.,” *Opt. Lett.*, vol. 32, no. 5, pp. 575–7, 2007.

[181] J. L. Keddie, “Reports : A Review Journal Film formation of latex,” *Mater. Sci. Eng.*, vol. 21, no. 97, pp. 101–170, 1997.

[182] L. A. Felton, “Introduction to Aqueous-Based Polymeric Coating,” in *Aqueous Polymeric Coatings for pharmaceutical dosage forms, fourth Edition*, 2017, pp. 1–10.

[183] K. Nollenberger and J. Albers, “Poly(meth)acrylate-based coatings,” *Int. J. Pharm.*, vol. 457, no. 2, pp. 461–469, 2013.

[184] http://www.substech.com/dokuwiki/doku.php?id=elastomer_polyisoprene_natural_rubber.

[185] C. Vallés, J. David Núñez, A. M. Benito, and W. K. Maser, “Flexible conductive graphene paper obtained by direct and gentle annealing of graphene oxide paper,” *Carbon N. Y.*, vol. 50, no. 3, pp. 835–844, 2012.

[186] D. C. Marcano *et al.*, “Improved synthesis of graphene oxide,” *ACS Nano*, vol. 4, no. 8, pp. 4806–4814, 2010.

[187] and G. M. F. Sette, G.K. Wertheim, Y.Ma, “Lifetime and screening of the C 1s photoemission in graphite,” *Phys. Rev. B*, vol. 41, no. 14, pp. 9766–9770, 1990.

[188] https://www.khanacademy.org/test-prep/mcat/physical-sciences-practice/physical-sciences-practice-tut/e/elasticity-and-kinetics-of-vulcanized-

rubber.

[189] A. C. Ferrari, “Raman spectroscopy of graphene and graphite: Disorder, electron-phonon coupling, doping and nonadiabatic effects,” *Solid State Commun.*, vol. 143, no. 1–2, pp. 47–57, 2007.

[190] A. Kaniyoor and S. Ramaprabhu, “A Raman spectroscopic investigation of graphite oxide derived graphene,” *AIP Adv.*, vol. 2, no. 032183, 2012.

[191] F. P. and N. Armata, “Chapter 2: Synthesis , Characterization and Models of Graphene Oxide,” in *Graphene Oxide in Environmental Remediation Process, SpringerBriefs in Applied Sciences and Technology*, 2017.

[192] M. Z. and Z.-Z. Y. Youwei Zhang, Hui-Ling Ma, Qilu Zhang, Jing Peng, Jiuqiang Li, “Facile synthesis of well-dispersed graphene by g-ray induced reduction of graphene oxide,” *J. Mater. Chem.*, vol. 22, pp. 13064–13069, 2012.

[193] A. Bagri, C. Mattevi, and M. C. and V. B. S. , MugeAcik , Yves J. Chabal, “Structural evolution during the reduction of chemically derived graphene oxide,” *Nat. Chem.*, vol. 2, no. 7, pp. 581–587, 2010.

[194] H. Yang, H. Li, J. Zhai, L. Sun, and H. Yu, “Simple synthesis of graphene oxide using ultrasonic cleaner from expanded graphite,” *Ind. Eng. Chem. Res.*, vol. 53, no. 46, pp. 17878–17883, 2014.

[195] M. M. Storm *et al.*, “Reduced graphene oxide for Li-air batteries: The effect of oxidation time and reduction conditions for graphene oxide,” *Carbon N. Y.*, vol. 85, pp. 233–244, 2015.

[196] T. F. Yeh, F. F. Chan, C. Te Hsieh, and H. Teng, “Graphite oxide with different oxygenated levels for hydrogen and oxygen production from water under illumination: The band positions of graphite oxide,” *J. Phys. Chem. C*, vol. 115, no. 45, pp. 22587–22597, 2011.

[197] Sandra Víctor-Román, “Synthesis and characterization of GO-based composites for water splitting applications,” 2019.

[198] F. T. and J. L. Koenig, “Raman Spectrum of Graphite,” *J. Chem. Phys.*, vol. 53, no. 3, p. 1126, 1970.

[199] C. Thomsen and S. Reich, “Double Resonant Raman Scattering in Graphite,” *Phys. Rev. Lett.*, vol. 85, no. 24, pp. 5214–5217, 2000.

[200] A. C. Ferrari *et al.*, “Raman Spectrum of Graphene and Graphene Layers,” *Phys. Rev. Lett.*, vol. 97, p. 187401, 2006.

[201] T. Yu, Z. Ni, C. Du, Y. You, Y. Wang, and Z. Shen, “Raman Mapping Investigation of Graphene on Transparent Flexible Substrate : The Strain Effect,” *J. Phys. Chem. C*, vol. 112, no. 33, pp. 12602–12605, 2008.

[202] C. Backes *et al.*, “Spectroscopic metrics allow in situ measurement of mean size and thickness of liquid-exfoliated few-layer graphene nanosheets,” *Nanoscale*, vol. 8, no. 7, pp. 4311–4323, 2016.

[203] J. C. Grunlan, W. W. Gerberich, and L. F. Francis, “Lowering the percolation threshold of conductive composites using particulate polymer microstructure,” *J. Appl. Polym. Sci.*, vol. 80, no. 4, pp. 692–705, 2001.

[204] Y. Qiu, F. Guo, R. Hurt, and I. Külaots, “Explosive thermal reduction of graphene oxide-based materials: Mechanism and safety implications,” *Carbon N. Y.*, vol. 72, pp. 215–223, 2014.

[205] O. M. Slobodian *et al.*, “Low-Temperature Reduction of Graphene Oxide : Electrical Conductance and Scanning Kelvin Probe Force Microscopy,” *Nanoscale Res. Lett.*, vol. 13, pp. 1–11, 2018.

[206] Y. Qiu, F. Collin, R. H. Hurt, and I. Külaots, “Thermochemistry and kinetics of graphite oxide exothermic decomposition for safety in large-scale storage and processing,” *Carbon N. Y.*, vol. 96, pp. 20–28, 2016.

[207] A. Hussein, S. Sarkar, and B. Kim, “Low Temperature Reduction of Graphene Oxide Using Hot-plate for Nanocomposites Applications,” *J. Mater. Sci. Technol.*, vol. 32, no. 5, pp. 411–418, 2016.

[208] R. Potts, O. Shankar, L. Du, R. S. Ruo, E. D. K. St, and U. States, “Processing − Morphology − Property Relationships and Composite Theory Analysis of Reduced Graphene Oxide / Natural Rubber Nanocomposites,” *Macromolecules*, vol. 45, p. 6045−6055, 2012.

[209] B. Mutel, P. Goudmand, L. Gengembre, and J. Grimblot, “Energy Consumption and Kinetic Evolution of Nitrogen Fixation on Polyethylene Terephthalate by Remote Nitrogen Plasma : XPS Study,” *Surf. Interface Anal.*, vol. 20, pp. 283–289, 1993.

[210] H. M. J. F. Bodino, G. Baud, M. Benmalek, J. P. Besse, “Alumina coating on polyethylene terephthalate,” *Thin Solid Films*, vol. 241, pp. 21–24, 1994.

[211] W. Bauhofer, J. Z. Kovacs, T. Swan, T. Swan, and T. Swan, “A review and analysis of electrical percolation in carbon nanotube polymer composites,” *Compos. Sci. Technol.*, vol. 69, no. 10, pp. 1486–1498, 2008.

[212] L. Sygellou, G. Paterakis, C. Galiotis, and D. Tasis, “Work Function Tuning of Reduced Graphene Oxide Thin Films,” *J. Phys. Chem. C*, vol. 120, no. 1, pp. 281–290, 2016.

[213] J. F. Douglas and F. Thorpe, “Geometrical percolation threshold ofoverlapping ellipsoids,” *Phys. Rev. E*, vol. 52, no. 1, pp. 819–828, 1995.

[214] Dimitris Achlioptas and Joel Spencer, “Explosive Percolation in Random Networks,” *Science (80-.).*, vol. 323, no. 5920, pp. 1453–1456, 2009.

[215] R. A. Da Costa, S. N. Dorogovtsev, A. V. Goltsev, and J. F. F. Mendes, “Explosive percolation transition is actually continuous,” *Phys. Rev. Lett.*, vol. 105, no. 25, 2010.

[216] V. H. Pham, T. T. Dang, S. H. Hur, E. J. Kim, and J. S. Chung, “Highly conductive poly(methyl methacrylate) (PMMA)-reduced graphene oxide composite prepared by self-assembly of PMMA latex and graphene oxide through electrostatic interaction,” *ACS Appl. Mater. Interfaces*, 2012.

[217] P. Wang, H. Chong, J. Zhang, and H. Lu, “Constructing 3D Graphene Networks in Polymer Composites for Significantly Improved Electrical and Mechanical Properties,” *ACS Appl. Mater. Interfaces*, vol. 9, no. 26, pp. 22006–22017, 2017.

[218] N. Rattanasom, T. Saowapark, and C. Deeprasertkul, “Reinforcement of natural rubber with silica/carbon black hybrid filler,” *Polym. Test.*, vol. 26, no. 3, pp. 369–377, 2007.

[219] X. F. Xin Xiong, Jingyi Wang, Hongbing Jia, Lifeng Ding, Xiu Dai, “Synergistic Effect of Carbon Black and Carbon–Silica Dual Phase Filler in Natural Rubber Matrix,” *Polym. Compos.*, pp. 1466–1472, 2014.

[220] C. H. Chan, J. Joy, H. J. Maria, and S. Thomas, *CHAPTER 1. Natural Rubber-Based Composites and Nanocomposites: State of the Art, New Challenges and Opportunities*, vol. 2, no. 8. 2014.

[221] H. Ismail, A. F. Ramly, and N. Othman, “Effects of silica/multiwall carbon nanotube hybrid fillers on the properties of natural rubber nanocomposites,” *J. Appl. Polym. Sci.*, vol. 128, no. 4, pp. 2433–2438, 2013.

[222] Y. Zhan, J. Wu, H. Xia, N. Yan, G. Fei, and G. Yuan, “Dispersion and exfoliation of graphene in rubber by an ultrasonically- assisted latex mixing and in situ reduction process,” *Macromol. Mater. Eng.*, vol. 296, no. 7, pp. 590–602, 2011.

[223] Y. Zhan, M. Lavorgna, G. Buonocore, and H. Xia, “Enhancing electrical conductivity of rubber composites by constructing interconnected network of self-assembled graphene with latex mixing,” *J. Mater. Chem.*, vol. 22, no. 21, pp. 10464–10468, 2012.

[224] M. Hernández, M. del M. Bernal, R. Verdejo, T. A. Ezquerra, and M. A. López-Manchado, “Overall performance of natural rubber/graphene nanocomposites,” *Compos. Sci. Technol.*, vol. 73, no. 1, pp. 40–46, 2012.

[225] M. Acik *et al.*, “The role of oxygen during thermal reduction of graphene oxide studied by infrared absorption spectroscopy,” *J. Phys. Chem. C*, vol. 115, no. 40, pp. 19761–19781, 2011.

[226] H. J. H. Brouwers, “Packing of crystalline structures of binary hard spheres : An analytical approach and application to amorphization,” *Phys. Rev. E*, vol. 76, 2007.

[227] H. J. H. Brouwers, “Particle-size distribution and packing fraction of geometric random packings,” *Phys. Rev. E*, vol. 74, 2006.

[228] H. J. H. Brouwers, “Packing fraction of crystalline structures of binary hard spheres: A general equation and application to amorphization,” *Phys. Rev. E* -

Stat. Nonlinear, Soft Matter Phys., vol. 78, no. 1, pp. 1–7, 2008.

[229] C. D. Lorenz and R. M. Ziff, "Precise determination of the critical percolation threshold for the three-dimensional 'Swiss cheese' model using a growth algorithm," *J. Chem. Phys.*, vol. 114, no. 8, pp. 3659–3661, 2001.

[230] S. C. Van der Marck, "Network approach to void percolation in a pack of unequal spheres," *Phys. Rev. Lett.*, vol. 77, no. 9, pp. 1785–1788, 1996.

[231] M. A. Worsley, P. J. Pauzauskie, T. Y. Olson, J. Biener, J. H. Satcher, and T. F. Baumann, "Synthesis of graphene aerogel with high electrical conductivity," *J. Am. Chem. Soc.*, vol. 132, no. 40, pp. 14067–14069, 2010.

[232] A. of P. T. L.Heath, "Treatise on Conic Sections," *Cambridge Cambridge Univ. Press*, vol. 54, pp. 314–315, 1896.

[233] C. Furnas, "Flow of gases through beds of broken solids," *J. Franklin Inst.*, vol. 209, no. 2, pp. 269–270, 1930.

[234] C. C. Furnas, "Heat Transfer from a Gas Stream to Broken Solids Bed of Broken Solids," *Ind. Eng. Chem.*, vol. 22, no. 1, pp. 26–31, 1930.

[235] A. King, "Fabrication of Novel, Structured, Bimodal Particle and CNT Composites, with Low Percolation Thresholds.," 2010.

[236] P. Bourke, "An Introduction to the Apollonian Fractal." 2006.

[237] O. R. and A. T. Kister, "On the Thermodynamics of Solutions. IV. The Determination of Liquid-Vapor Equilibria by Measuring the Total Pressure.," *Ind Eng Chem*, vol. 71, 1949.

[238] F. G. R. Gauthier and S. C. Danforth, "Packing of bimodal mixtures of colloidal silica," *J. Mater. Sci.*, vol. 26, no. 22, pp. 6035–6043, 1991.

[239] T. Kuilla, S. Bhadra, D. Yao, N. H. Kim, S. Bose, and J. H. Lee, "Recent advances in graphene based polymer composites," *Prog. Polym. Sci.*, vol. 35, no. 11, pp. 1350–1375, 2010.

[240] A. G. Arani, G. S. Jafari, and R. Kolahchi, "Vibration Analysis of Nanocomposite Microplates Integrated With Sensor and Actuator Layers Using," *Polym. Compos.*, pp. 1–14, 2016.

[241] T. Zhou *et al.*, “The preparation of high performance and conductive poly (vinyl alcohol)/graphene nanocomposite via reducing graphite oxide with sodium hydrosulfite,” *Compos. Sci. Technol.*, vol. 71, no. 9, pp. 1266–1270, 2011.

[242] D. G. Papageorgiou, I. A. Kinloch, and R. J. Young, “Graphene/elastomer nanocomposites,” *Carbon N. Y.*, vol. 95, pp. 460–484, 2015.

[243] X. Yang, X. Wang, J. Yang, J. Li, and L. Wan, “Functionalization of graphene using trimethoxysilanes and its reinforcement on polypropylene nanocomposites,” *Chem. Phys. Lett.*, vol. 570, pp. 125–131, 2013.

[244] B. M. Cromer, S. Scheel, G. A. Luinstra, E. B. Coughlin, and A. J. Lesser, “In-situ polymerization of isotactic polypropylene-nanographite nanocomposites,” *Polym. (United Kingdom)*, vol. 80, pp. 275–281, 2015.

[245] L. Liu, J. Zhang, and F. Liu, “Mechanical properties of graphene oxides,” *Nanoscale*, vol. 4, pp. 5910–5916, 2012.

[246] T. Wang *et al.*, “Waterborne, nanocomposite pressure-sensitive adhesives with high tack energy, optical transparency, and electrical conductivity,” *Adv. Mater.*, vol. 18, no. 20, pp. 2730–2734, 2006.

[247] J. Yu, K. Lu, E. Sourty, N. Grossiord, C. E. Koning, and J. Loos, “Characterization of conductive multiwall carbon nanotube/polystyrene composites prepared by latex technology,” *Carbon N. Y.*, vol. 45, no. 15, pp. 2897–2903, 2007.

[248] Y. V. Syurik *et al.*, “Graphene network organisation in conductive polymer composites,” *Macromol. Chem. Phys.*, vol. 213, no. 12, pp. 1251–1258, 2012.

[249] M. Ghislandi, E. Tkalya, B. Marinho, C. E. Koning, and G. De With, “Electrical conductivities of carbon powder nanofillers and their latex-based polymer composites,” *Compos. Part A Appl. Sci. Manuf.*, vol. 53, pp. 145–151, 2013.

[250] G. Long *et al.*, “Resolving the dilemma of gaining conductivity but losing environmental friendliness in producing polystyrene/graphene composites via optimizing the matrix-filler structure,” *Green Chem.*, vol. 15, no. 3, pp. 821–828, 2013.

[251] A. Arzac, G. P. Leal, R. Fajgar, and R. Tomovska, “Comparison of the emulsion mixing and in situ polymerization techniques for synthesis of water-borne reduced graphene oxide/polymer composites: Advantages and drawbacks,” *Part. Part. Syst. Charact.*, vol. 31, no. 1, pp. 143–151, 2014.

[252] H. Jiang, L. Chen, S. Chai, X. Yao, F. Chen, and Q. Fu, “Facile fabrication of poly (tetrafluoroethylene)/graphene nanocomposite via electrostatic self-assembly approach,” *Compos. Sci. Technol.*, vol. 103, pp. 28–35, 2014.

[253] G. Chen, W. Weng, D. Wu, and C. Wu, “PMMA/graphite nanosheets composite and its conducting properties,” *Eur. Polym. J.*, vol. 39, pp. 2329–2335, 2003.

[254] A. Abdolmaleki, S. Mallakpour, and S. Borandeh, “Improving interfacial interaction of L-phenylalanine-functionalized graphene nanofiller and poly(vinyl alcohol) nanocomposites for obtaining significant membrane properties: morphology, thermal, and mechanical studies,” *Polym. Compos.*, vol. 37, no. 6, pp. 1924–1935, 2016.